2022

Stable Zinc Metal Anode for High-performance Aqueous Zn-ion Batteries

Xiaohui Zeng

UNIVERSITY OF WOLLONGONG AUSTRALIA

Stable Zinc Metal Anode for High-performance Aqueous Zn-ion Batteries

Xiaohui Zeng

Supervisors:

Wei Kong Pang, Zaiping Guo, Jianfeng Mao

This thesis is presented as part of the requirement for the conferral of the degree:

Doctor of Philosophy

Institute for Superconducting and Electronic Materials

Faculty of Engineering and Information Sciences

University of Wollongong, NSW, Australia

April 2022

Certification

I, Xiaohui Zeng, declare that the original work presented in this thesis was carried out in the laboratories of the Institute for Superconducting and Electronics Materials, at the University of Wollongong, Australia, and has not been submitted for qualifications to any other academic institution for higher education.

Xiaohui Zeng

April 2022

DEDICATION

To my dear family and friends who stand by me all the time.

Acknowledgements

Both the study career in University of Wollongong and the life experience in Australia are a wonderful, valuable and memorable journey, and will have a profound effect to my entire lifetime. Studying abroad is my dream when I was an undergraduate. The beginning of the dream was difficult, because the visa processing had taken almost one year before I arrived at Australia. With all the supports from my supervisors, family members and colleagues, I complete my Ph.D. study at the University of Wollongong successfully and smoothly. I would like to take this great opportunity to express my sincere gratitude to everyone who assisted and accompanied me.

Firstly, I would like to pay my deepest appreciation and gratitude to my academic supervisor, Distinguished Prof. Zaiping Guo. Prof. Guo offered me a precious learning opportunity in the big research group in Institute for Superconducting and Electronic Materials in 2017. The most sincere acknowledgement to Prof. Guo for her professional guidance and kindly encouragement to me since then, whenever I encounter difficulties and doubts in my doctoral research work. Prof. Guo acts as not only a knowledgeable supervisor to teach me how to be a qualified and independent researcher in the academic field, but also a close friend who gives me many valuable life advices and presents my wedding ceremony as one of the marriage witnesses. I am grateful for her continuous supports to my Ph.D. project, career development as well as life planning.

I would also like to thank Dr. Jianfeng Mao very much here. Dr. Mao gives me many valuable academic guidance, including creative thinking, experimental design and research paper writing. His generous help and encouragement always give me lots of positive energy to face experiment failure or paper rejection. Without his continuous guidance and support, my Ph.D. project would not be completed such smoothly. Besides,

I am also very grateful to Prof. Wei Kong Pang, for his great supervision and guidance to my doctoral study, for his valuable advices to my research career. I am deeply grateful to Prof. Shixue Dou, Prof. Huakun Liu, Prof. Xiaolin Wang and Prof. Konstantin Kostaninov, for their great contribution to our institute. I also wish to thank Prof. Chunsheng Wang, Prof. Chris Ling, Prof. Qinghong Wang, Prof. Tengfei Zhou and Prof. Jianwen Liu for their valuable academic guidance and suggestions to my research works.

Moreover, I acknowledge Dr. Germanas Peleckis, Dr. Dongqi Shi, Dr. Tony Romeo, Dr. Yunxiao Wang, Dr. Weijie Li, Prof. Jiazhao Wang, and Dr. Chao Wu for their patiently training for experimental instruments. I appreciate kindly help and supports from Dr. Joanne George, Dr. Candace Gabelish, Mr. Wayne Ireland, Mrs. Crystal Mahfouz, Mrs. Narelle Badger, and Mrs. Naomi Davies. I acknowledge Dr. Qiang Zhu, Dr. Dave Mitchell, Dr. Tian Zheng, Dr. Jitraporn Pimm Vongsvivut and Dr. Qinfen Gu for their assistance with material characterizations and data analyses. I would like to thank Dr. Tania Silver for her careful language revision for paper manuscripts and this thesis.

I would like to take this opportunity to show my gratitude to my dear friends, co-workers, and colleagues, who offer me numerous help and spiritual support, and share many happy moments with me. Many thanks to Mrs. Chun Yang, Mrs. Fangling You, Mrs. Lisha Li, Mr. Junzhuo Zhang, Dr. Hanna He, Dr. Jing Cuan, Dr. Qing Zhang, Dr. Yan Lu, Mrs. Sailin Liu, Miss Yanyan Wang, Miss Yameng Fan, Mrs. Fangli Zhang, Miss Qiuran Yang, Dr. Guanglin Xia, Dr. Wenchao Zhang, Dr. Christophe Didier, Dr. Junnan Hao, Dr. Xiaolong Li, Dr. Qingbing Xia, Dr. Shilin Zhang, Dr. Gemeng Liang, Dr. Fuhua Yang, Dr. Zhibin Wu, Mr. Qining Fan, Mr. Zhijie Wang, Mr. Jingxin Wu, Dr. Xinyu Zhao, Dr. Xiaobo Zheng.

Finally, I would like to show great gratitude to my dear husband, beloved parents, brothers and sisters, for their selfless devotion and great moral support throughout the whole period of doctoral study. Special thanks to my husband, Mr. Jiatu Liu, for his company, care and love all the time, for his giving and tolerance, for his sustained efforts for the very moment and the wonderful future. Also special thanks to my dear son, Yipi Liu (Albert), for his big smiles and lovely face. I could not have completed my Ph.D. study successfully without the strong support and encouragement from my beloved family. I also do appreciate the financial support from the China Scholarship Council (CSC) and the Australian Research Council (ARC).

Abstract

Owing to the high capacity of metallic Zn anode and intrinsically safe aqueous electrolyte, aqueous Zn-ion batteries (AZIBs) have become advanced energy storage alternatives beyond the lithium-ion batteries by providing cost benefit, high safety, and competitive energy density. There has been a new wave of research interest across AZIBs, however, the state-of-the-art AZIBs are still far from satisfactory. One important reason is that Zn anode still suffers from low Coulombic efficiency (CE) and inferior cycling stability, due to its notorious dendrite formation and side reactions (e.g. corrosion, passivation, and H_2 evolution) in aqueous electrolytes. Accordingly, my doctoral project is focused on improving the electrochemical performance of AZIBs via enabling highly stable and reversible Zn metal anode, including three subprojects (1) *in situ* construction of highly Zn^{2+}-conductive solid electrolyte interphase for stable Zn anode; (2) an *in situ* polymeric interface on Zn anode towards high-performance aqueous Zn-ion batteries; (3) boosting advanced aqueous Zn/MnO_2 batteries via electrolyte salt chemistry.

In the first subproject, an *in-situ* formation of a dense, stable, and highly Zn^{2+}-conductive SEI layer (hopeite) was demonstrated in aqueous Zn chemistry, by introducing $Zn(H_2PO_4)_2$ salt into the electrolyte. The hopeite SEI enables uniform and rapid Zn-ion transport kinetics for dendrite-free Zn deposition, and restrains the side reactions via isolating active Zn from the bulk electrolyte. Under practical testing conditions with an ultrathin Zn anode, a low negative/positive capacity ratio, and lean electrolyte, the Zn/V_2O_5 full cell retained 94.4 % of its original capacity after 500 cycles. This work provides a simple yet practical solution to high-performance aqueous battery technology via building *in-situ* SEI layers.

As for the second subproject, inspired by the bio-adhesion principle, a stable SEI of

polydopamine is constructed successfully on Zn anode via an *in-situ* electrochemical polymerization process of dopamine additive. This *in-situ* polymeric SEI offers multifunctional features with abundant functional groups and prominent hydrophilicity for regulating Zn nucleation to achieve dendrite-free Zn deposition, high Zn-ion conductivity for fast Zn^{2+} transport, and strong adhesion capability for blocking interfacial side reactions. Consequently, the Zn electrodes exhibit high reversibility with 99.5 % Coulombic efficiency and outstanding stability, even at ultrahigh current density and areal capacity (30 mA cm^{-2}, 30 mA h cm^{-2}). Moreover, a prolonged lifespan of the Zn/V_2O_5 full cell can be attained under lean electrolyte (9 μL mAh^{-1}) and with a low capacity ratio of negative electrode to positive electrode (~ 2). This work provides inspiration on SEI design for aqueous battery chemistry and promotes the practical application of AZIBs.

The third subproject is focused on a novel adoption of a near-neutral acetate-based electrolyte, which promotes the two-electron Mn^{4+}/Mn^{2+} redox reaction and simultaneously enables a stable Zn anode. The acetate anion triggers a highly reversible MnO_2/Mn^{2+} reaction, which ensures high capacity and avoids the issue of structural collapse of MnO_2. Meanwhile, the anode-friendly electrolyte enables a dendrite-free Zn anode with outstanding stability and high plating/stripping Coulombic efficiency. Hence, a high capacity of 556 mA h g^{-1}, a lifetime of 4000 cycles without decay, and excellent rate capability up to 70 mA cm^{-2} are demonstated in this new near-neutral aqueous Zn/MnO_2 battery by simply manipulating the salt anion in the electrolyte. The acetate anion not only modifies the surface properties of MnO_2 cathode but also creates a highly compatible environment for the Zn anode. This work provides a new opportunity for developing high-performance Zn/MnO_2 and other aqueous batteries based on the salt anion chemistry.

In conclusion, AZIBs have been regarded as a promising alternative for large-scale application due to their advantages of low cost, high performance, inherent safety, and environmental benignity. Nevertheless, because of the poor reversibility and stability of the Zn anode in aqueous electrolyte. the development of AZIBs is still far from meeting our ever-increasing large-scale energy demands. To optimize Zn electrode and further improve the battery performance, this doctoral project proposes both interfacial engineering and electrolyte salt strategy via deeply understanding Zn surface chemistry. This doctoral project offers effective strategies to address Zn issues towards the practical application of AZIBs.

Table of Contents

List of Figures, Tables, Abbreviations, and Organizations

Zn dendrites would pierce the separator after a certain number of cycles. (Reprinted with permission from ref. 55. Copyright 2017, AAAS). (b) Three-dimensional volume-rendered X-ray tomograms of Zn_{20} and Zn_{30} sponges. (Reprinted with permission from ref. 57. Copyright 2018, American Chemical Society)

Figure 2.5 *In-situ* optical microscope images of Zn electrode after Zn deposition for 30 min. The electrolyte contains 0.1 M ZnO + 4.0 M KOH with various concentrations of PEI: (a) 0 ppm, (b) 10 ppm, (c) 50 ppm, and (d) 100 ppm. SEM images of Zn deposition morphology: (e) in the additive-free electrolyte, (f) in the electrolyte containing 10 ppm PEI additive. (Reprinted with permission from ref. 58. Copyright 2015, Elsevier)

Figure 2.6 (a) Synthesis of the PANa gel electrolyte, which consists of acrylic acid (AA) monomer, NaOH, ammonium persulfate, $Zn(CH_3COO)_2$, and KOH (water and ion content regulator). (b) Schematic illustration of the quasi-SEI formation between Zn anode and PANa electrolyte. (Reprinted with permission from ref. 81. Copyright 2018, John Wiley and Sons). (c) Schematic illustration of the preparation process for the porous PVA-based gel electrolyte along with its inner structure for the Zn–air battery. (Reprinted with permission from ref. 82. Copyright 2019, Elsevier)

Figure 2.7 (a) Schematic diagram of charging behaviour of a PBI membrane with the ultra-high mechanical stability and a 3D porous carbon felt coating for the alkaline Zn battery. (b) The transportation mechanism of OH^- ions in a PBI membrane. (Reprinted with permission from ref. 90. Copyright 2018, Elsevier). (c) Operating principle of the porous polyolefin membrane for the alkaline Zn battery. (d) Schematic illustration of the self-healing process. (Reprinted with permission from ref. 91. Copyright 2018, John Wiley and Sons). (e) Schematic diagram of a cell with the conventional frontside-plating configuration. (f) Schematic representation of a cell with the backside-plating configuration for avoiding internal short circuits. (Reprinted with permission from ref.

96. Copyright 2016, Springer Nature)

Figure 2.8 Summary of the strategies for addressing the problematic issues for Zn electrode in alkaline electrolyte.

Figure 2.9 (a) DEMS tests on the symmetrical Zn cells to monitor the electrochemical H_2 evolution. (Reprinted with permission from ref. 104. Copyright 2019, Elsevier) (b) H_2 gas evolution accompanied by the chemical corrosion of Zn electrode in 3 M $ZnSO_4$ electrolyte (Reprinted with permission from ref. 105. Copyright 2020, Elsevier). (c) *In-situ* optical microscope images of H_2 gas evolution during the Zn electrodeposition process at 0.2 mA cm^{-2}. (d) Zn foil soaked in 1 M $ZnSO_4$ electrolyte and photographic comparison of Zn foil before/after soaking in electrolyte for 7 days. (e) SEM image of $Zn_4SO_4(OH)_6{\cdot}xH_2O$ by-product on Zn foil and its crystal structure. (Reprinted with permission from ref. 112. Copyright 2020, John Wiley and Sons).

Figure 2.10 (a) Linear polarization curves of the synthesized zinc with and without organic additives and commercial zinc foil when in contact with the battery's electrolyte. (Reprinted with permission from ref. 117. Copyright 2017, American Chemical Society) Cyclic voltammograms of Zn electrode in aqueous electrolyte containing (b) 1 M $Zn(CF_3SO_3)_2$ and (c) 1 M $ZnSO_4$ at the scan rate of 0.5 mV s^{-1} between –0.2 and 2.0 V. (Reprinted with permission from ref. 69. Copyright 2016, American Chemical Society) (d) Snapshot of the molecular dynamics (MD) simulation cell for highly-concentrated electrolyte (HCZE) (1 m $Zn(TFSI)_2$ + 20 m LiTFSI) at 363 K. (e) Representative Zn^{2+}-solvation structures in the electrolytes with 1 m $Zn(TFSI)_2$ and three concentrations of LiTFSI (5 m, 10 m and 20 m). (Reprinted with permission from ref. 54. Copyright 2018, Springer Nature) (f) Schematic diagram for the fabrication of the cross-linked polyacrylamide (PAM)-based electrolyte. (g) SEM image of the free-standing PAM. (Reprinted with permission from ref. 146. Copyright 2018, American Chemical Society)

Figure 2.11 (a) Differential charge density distribution of Zn@ZnO-3D from first-principles calculations. (b) Electric double layer structure in the vicinity of the anode and the corresponding energy barriers. (Reprinted with permission from ref. 149. Copyright 2020, Royal Society of Chemistry) *In-situ* optical microscope images of cross-sectional Zn deposition morphology on (c) bare Zn plate and (d) PA-coated Zn plate in a symmetrical Zn cell at a current density of 10 mA cm^{-2}. (Reprinted with permission from ref. 102. Copyright 2019, Royal Society of Chemistry) (e) SEM images of Zn deposits on ZIF-8-500 electrode at a current density of 1.0 mA cm^{-2} for different capacities. Scale bars, 2 mm. (f) Schematic illustration of the Zn plating. (Reprinted with permission from ref. 157. Copyright 2019, Elsevier.)

Figure 2.12 Summary of the strategies for addressing the problematic issues for Zn electrode in mild electrolyte.

Figure 4.1 Schematic illustration of the Zn surface evolution and characterization of Zn electrodes in the baseline and designed electrolytes. (a) Schematic illustration of Zn surface evolution and the SEI formation mechanism. SEM images of Zn electrodes after 20 cycles in (b, c) the baseline electrolyte and (d, e) the designed electrolyte. The Zn electrodes were stripped out of their symmetrical cells after 20 cycles in 1 M $Zn(CF_3SO_3)_2$ with/without 25 mM $Zn(H_2PO_4)_2$ as electrolyte, respectively. The applied current density was 1 mA cm^{-2}, and the areal capacity was 1 mA h cm^{-2}. (f) XRD patterns of Zn electrode before and after 20 cycles in the designed electrolyte, with enlargement in the inset. (g) EDX mapping of the SEI-Zn electrode in the designed electrolyte.

Figure 4.2 Cross-sectional focused ion beam (FIB)-SEM images of the SEI-Zn electrode after (a, b) 10 cycles, (c, d) 20 cycles, (e, f) 30 cycles, and (g, h) 50 cycles. The Zn electrodes were stripped out of symmetrical cells after specific cycles (1 mA

cm^{-2}, 1 mA h cm^{-2}) in the designed electrolyte.

Figure 4.3 Raman spectra of the SEI-Zn electrode and bare Zn. The Zn electrode was stripped out of its symmetrical cell (1 mA cm^{-2}, 1 mA h cm^{-2}) after 20 cycles in the designed electrolyte.

Figure 4.4 FTIR characterization of the SEI-Zn electrode. (a) FTIR mapping of the SEI-Zn electrode, (b) FTIR spectra of a bare Zn electrode and the SEI-Zn electrode for the marked point in A. The Zn electrode was stripped out of its symmetrical cell after 20 cycles (1 mA cm^{-2}, 1 mA h cm^{-2}) in the designed electrolyte.

Figure 4.5 SEM images of cycled Zn electrodes in electrolytes consisting of 1 M $Zn(CF_3SO_3)_2$ with different $Zn(H_2PO_4)_2$ concentrations. (a) 10 mM, (b) 25 mM, (c) 50 mM, and (d) 100 mM. The Zn electrodes were stripped out of the symmetrical cells after 20 cycles at 1 mA cm^{-2} with areal capacity of 1 mA h cm^{-2}.

Figure 4.6 Comparison of the cycling stability of Zn electrodes in 1 M $Zn(CF_3SO_3)_2$ with different concentrations of $Zn(H_2PO_4)_2$. The Zn symmetric cells were cycled at 1 mA cm^{-2} with the areal capacity of 1 mA h cm^{-2}.

Figure 4.7 Interfacial stability and Zn-ion transport property of the *in-situ* SEI layer. (a) Linear polarization curves showing the corrosion on bare Zn and SEI-Zn electrodes. The SEI-Zn electrode was stripped out of its symmetrical cell after 20 cycles in the designed electrolyte. (b) EIS spectra of the Zn symmetric cells (cycled for 20 cycles at 1 mA cm^{-2}) in the baseline and designed electrolytes before and after rest for 3 days. (c) Comparison of the Zn-ion transference number of a bare Zn electrode and a SEI-Zn electrode. Calculated models of the interaction between a foreign zinc ion and the surfaces of (d) the SEI layer and (e) the bare Zn electrode. First-principles calculations of (f) the optimum Zn-ion diffusion pathway in the SEI layer and (g) the corresponding migration energy barrier.

Figure 4.23 SEM images of Zn deposition on Cu foil. (a, b) In the baseline electrolyte, (c, d) in the designed electrolyte. The applied current density was 5 mA cm^{-2}, and the areal capacity was 0.5 mA h cm^{-2}. The Cu foil was pre-cycled in Cu/Zn cells with the respective electrolytes for 10 cycles.

Figure 4.24 SEM images (a, b) and XRD pattern (c) of commercial V_2O_5 cathode.

Figure 4.25 Electrochemical behaviour of AZIBs with lean electrolyte and low N/P ratio. (a) Cyclic voltammograms for the Zn/V_2O_5 full cell in the designed electrolyte at a scan rate of 1 mV s^{-1}. (b) Rate capability and (c) the corresponding discharge/charge profiles of Zn/V_2O_5 cells at various current densities. (d, e) Long-term cycling stability and efficiency of Zn/V_2O_5 cells at a current density of 0.8 A g^{-1}. The electrolyte-to-capacity ratio (E/C) used here was controlled at 9 μL mA h^{-1}, and the Zn electrodes were ultrathin (10 μm thickness, ~ 5.85 mA h cm^{-2}). All the Zn/V_2O_5 cells were pre-activated at 0.1 A g^{-1} for 10 cycles.

Figure 4.26 Ex-situ XRD patterns of the V_2O_5 cathode at different voltage states during the first cycle in (a) the designed electrolyte and (b) the baseline electrolyte, respectively.

Figure 4.27 Long-term cycling stability and efficiency of Zn/V_2O_5 cells at 0.4 A g^{-1}. The Zn/V_2O_5 cells were assembled with lean electrolyte (9 μL mAh^{-1}) and low N/P (~ 4).

Figure 5.1 Schematic illustration of the polymeric SEI formation and characterization of Zn electrodes. (a) Schematic illustration of the *in-situ* formation of the multifunctional PDA SEI and its effective mechanism for dendrite-free Zn anode. (b) *In-situ* Raman spectra of the Zn electrode during cycling in the electrolyte (1 M $Zn(CF_3SO_3)_2$) with DA additive. (c) Representative polymerization procedure for PDA. SEM images and three-dimensional AFM images of Zn electrodes after 10 cycles in the electrolyte (d, f) with DA and (e, g) without DA. Comparison of galvanostatic cycling

properties of Zn symmetrical cells in the electrolytes with and without DA at (h) 1 mA cm^{-2}, 1 mA h cm^{-2}; (i) 10 mA cm^{-2}, 10 mA h cm^{-2}; and (j) 30 mA cm^{-2}, 30 mA h cm^{-2}.

Figure 5.2 Geometrical configuration and adsorption energy of polydopamine (PDA) on the Zn (002) plane.

Figure 5.3 Comparison of the Coulombic efficiency of Zn plating/stripping on Cu in electrolytes consisting of 1 M $Zn(CF_3SO_3)_2$ with different DA concentrations. The applied current density was 1 mA cm^{-2}, and the areal capacity was 1 mA h cm^{-2}.

Figure 5.4 Characterization of the *in situ* polymeric SEI layer on Zn electrode. (a) Top-view and (b, c) side-view focused ion beam (FIB)-SEM images of the Zn electrode after 10 cycles in the electrolyte with DA. To protect the *in-situ* PDA layer from incurring electron/ion beam induced damage, the Zn electrode was coated with a Pt/C protective layer. (d) Low-resolution and (e) high-resolution cryo-EM images of Zn electrode with the PDA layer (the PDA-Zn electrode). (f) Corresponding elemental mapping images. High-resolution X-ray photoelectron spectroscopy (XPS) spectra of (g) C 1s and (h) N 1s orbitals for the PDA-Zn electrode. XPS depth profiles of (i) C 1s and (j) N 1s for the PDA-Zn electrode with various Ar sputtering times. (k) FTIR mapping and (l) the corresponding spectrum of the PDA-Zn electrode. The PDA-Zn electrodes were stripped out of the Zn symmetrical cells after 10 cycles in the electrolyte consisting of 1 M $Zn(CF_3SO_3)_2$ with DA additive.

Figure 5.5 Multifunctional features of the polymeric SEI. (a) Schematic illustration of the PDA SEI layer on Zn electrode. Contact angle measurements of the electrolyte on (b) bare Zn electrode and (c) PDA-Zn electrode. (d) Linear polarization curves of bare Zn and PDA-Zn electrodes. (e) EIS spectra of the Zn symmetrical cells. (f) Voltage response of bare Zn and PDA-Zn electrodes. DFT calculation of the interactions of a foreign Zn^{2+} ion on (g) bare Zn electrode and (h) the PDA layer.

Figure 5.6 XRD patterns of bare Zn electrode and PDA-Zn electrode after immersion in aqueous electrolyte for 3 days.

Figure 5.7 Linear sweep voltammograms (LSVs) of 1 M Zn $(CF_3SO_3)_2$ electrolyte with and without DA additive measured in a Zn/Ti half-cell at 0.1 mV s^{-1}.

Figure 5.8 Arrhenius curves and activation energies of bare Zn and PDA-Zn, determined by EIS of symmetric cells at different temperatures. The symmetric cells were cycled for 20 cycles in the electrolyte with or without DA additive at room temperature.

Figure 5.9 First-principles calculations of (a) the Zn-ion migration path in the PDA SEI layer and (b) the corresponding migration energy barrier.

Figure 5.10 Effect of the polymeric SEI layer on Zn plating behavior and reversibility. *In-situ* optical microscope images of Zn plating on (a) bare Zn electrode and (b) PDA-Zn electrode. XRD characterization of Zn electrodes after specific cycles in 1 M $Zn(CF_3SO_3)_2$ (c) without and (d) with DA. (e) Coulombic efficiency (CE) measurements and (f) corresponding voltage profiles of Cu/Zn cells in the electrolytes with and without DA.

Figure 5.11 SEM images of Zn deposition morphology on Cu foil. (a-c) 1 M $Zn(CF_3SO_3)_2$, (d-f) 1 M $Zn(CF_3SO_3)_2$ with DA as electrolyte. The applied current density was 1 mA cm^{-2}, and the areal capacity was 1 mA h cm^{-2}. The Cu foil was pre-cycled in Cu/Zn cells with the respective electrolytes for 5 cycles.

Figure 5.12 (a) SEM image and (b-d) corresponding EDX mapping of the Zn electrode after 400 h of plating/stripping in electrolyte with DA.

Figure 5.13 Raman spectra of pristine Zn and Zn electrode after long cycling in electrolyte with DA. The cycled Zn electrode was stripped out of its symmetrical cell (1 mA cm^{-2}, 1 mA h cm^{-2}) after 400 h of plating/stripping in electrolyte with DA. The

Raman spectrum of long-cycled Zn still shows the typical stretching and deformation peaks of aromatic rings in PDA.

Figure 5.14 Top-view SEM images of Zn electrodes after 400 h of plating/stripping. (a) 1 M $Zn(CF_3SO_3)_2$, (b) 1 M $Zn(CF_3SO_3)_2$ with DA as electrolyte.

Figure 5.15 Side-view SEM images of Zn electrodes after 400 h of plating/stripping. (a, b) 1 M $Zn(CF_3SO_3)_2$, (c, d) 1 M $Zn(CF_3SO_3)_2$ with DA as electrolyte.

Figure 5.16 Digital images of Zn electrodes and glass fiber separators stripped from symmetrical cells after 400 h. (a) Glass fiber separator and (b) Zn electrode after cycling in the 1 M $Zn(CF_3SO_3)_2$ electrolyte. (c) Glass fiber separator and (d) Zn electrode after cycling in the electrolyte with DA. The applied current density was 1 mA cm^{-2}, and the areal capacity was 1 mA h cm^{-2}. In 1 M $Zn(CF_3SO_3)_2$ without DA, significant pulverization and corrosion of the Zn electrode could be observed after long-term cycling.

Figure 5.17 Electrochemical performances of RAZBs under practical conditions. (a) CV curves of Zn/V_2O_5 full cells. (b) Comparison of rate performances of Zn/V_2O_5 full cells in the electrolyte with and without DA additive. (c) Corresponding voltage profiles of Zn/V_2O_5 full cells in the electrolyte with DA at different current densities. (d, e) Comparison of the cycling performances of Zn/V_2O_5 full cells at 1 A g^{-1} under lean electrolyte and low N/P ratios.

Figure 5.18 XPS characterization of V_2O_5 cathode after cycling. (a, b) 1 M $Zn(CF_3SO_3)_2$, (c, d) 1 M $Zn(CF_3SO_3)_2$ with DA additive as electrolyte**.**

Figure 5.19 Raman spectra of V_2O_5 cathode before and after cycling.

Figure 5.20 SEM images of cycled V_2O_5 cathodes and digital images of glass fiber separators (insets) stripped from Zn/V_2O_5 full cells after cycling at 1 A g^{-1} for 200 cycles.

(a, b) Cycling in 1 M $Zn(CF_3SO_3)_2$ electrolyte. (c, d) Cycling in 1 M $Zn(CF_3SO_3)_2$ electrolyte with 50 mM DA.

Figure 5.21 Long-term cycling stability of Zn/V_2O_5 full cells with high excess Zn (thickness 60 μm) and electrolyte with and without DA. The applied current density was 1 A g^{-1}.

Figure 5.22 SEM images of ultrathin Zn electrodes (10 μm) after cycling for 200 cycles in Zn/V_2O_5 full cells. (a, b) Cycling in 1 M $Zn(CF_3SO_3)_2$ as electrolyte, (c, d) cycling in 1 M $Zn(CF_3SO_3)_2$ with 50 mM DA.

Figure 6.1 Electrochemical behavior of MnO_2 cathode in different aqueous electrolytes. (a) Different pH ranges of representative aqueous electrolytes in reported Zn/MnO_2 batteries. The star represents strongly acidic $ZnSO_4$ + $MnSO_4$ + H_2SO_4 aqueous electrolyte. The rectangle represents mildly acidic $ZnSO_4$, $ZnCl_2$, $Zn(NO_3)_2$, $Zn(TFSI)_2$ + $Mn(TFSI)_2$, $ZnSO_4$ + $MnSO_4$, and $Zn(CF_3SO_3)_2$ + $Mn(CF_3SO_3)_2$ electrolytes. The triangle represents near-neutral $Zn(CH_3COO)_2$ + $Mn(CH_3COO)_2$ electrolyte. The rhombus represents strongly alkaline KOH and NaOH electrolytes. (b) Schematic illustration of the aqueous rechargeable Zn/MnO_2 energy storage system in the acetate-based electrolyte. (c) CV curves in different electrolytes at 0.1 mV s^{-1} from 1.0 V to 1.8 V, and (d-f) galvanostatic discharge curves (5 mA cm^{-2}, charge to 0.5 mA h cm^{-2} at 1.8 V) of the Zn/MnO_2 battery in sulfate-based, sulfonate-based and acetate-based aqueous electrolytes, respectively.

Figure 6.2 Working potential window analysis of the Zn/MnO_2 battery in a three-electrode system.

Figure 6.3 Characterization of the cathode in the acetate-based electrolyte. (a, b) SEM images of the cathode after the first charge to 0.5 mA h cm^{-2}. (c, d) SEM images of the cathode after the first discharge to 1.4 V at 5 mA cm^{-2}. (e, f) SEM images of the cathode

after the first discharge to 1.0 V. (g, h) TEM images and the corresponding SAED pattern (inset of h) of the MnO_2 cathode after charge. (i) Elemental mapping images of the cathode after charge.

Figure 6.4 SEM images of the electrodeposited MnO_2 cathode in the Zn/MnO_2 cell after the first charge to 0.5 mA h cm^{-2}.

Figure 6.5 Investigation of the reaction mechanism. (a) *Ex situ* XRD patterns of the MnO_2 cathode at different charge/discharge states in the acetate-based electrolyte. (b) Mn 3s XPS spectrum of the MnO_2 cathode in the charged state. (c) Atomic structures for the dissolution reaction on MnO_2 with a bare surface and with an acetate-rich surface. (d) Energy diagram of the dissolution reaction on MnO_2 with a bare surface and with an acetate-rich surface. (e) Differential charge density of an acetate ion adsorbed on MnO_2, with yellow and blue colors representing electron accumulation and depletion regions, respectively, with an isosurface value of 0.002 e/$Å^3$.

Figure 6.6 Raman spectra of the MnO_2 cathode on carbon cloth at different charge/discharge states.

Figure 6.7 XPS spectra of (a) Mn 3s and (b) Mn 2p for the cathode at different charge/discharge states.

Figure 6.8 *Ex-situ* XRD patterns of MnO_2 cathode in the sulfate-based electrolyte.

Figure 6.9 SEM images of the MnO_2 cathode in the sulfate-based electrolyte. (a, b) After the first charge to 0.5 mA h cm^{-2}. (c, d) After the first discharge to 1.0 V.

Figure 6.10 High-resolution TEM (HRTEM) image of the electrodeposited MnO_2 cathode.

Figure 6.11 Electrochemical behaviour of the Zn/MnO_2 battery in the acetate-based electrolyte with added H_2SO_4 (pH ≈ 3.8). (a) Cycling performance. (b) Corresponding galvanostatic discharge curves.

Figure 6.12 Electrochemical stability and reversibility of Zn metal anode. (a) Zn plating/ stripping test of Zn/Zn symmetrical cells at a current density of 1 mA cm^{-2} in the acetate-based electrolyte, the sulfonate-based electrolyte, and the sulfate-based electrolyte. The plating/stripping capacities of the Zn electrodes (0.1 mm) were 1 mA h cm^{-2} in each cycle. (b) Coulombic efficiency of a Zn/Ti cell in the acetate-based electrolyte at 1 mA cm^{-2}. The cut-off potential was 0.5 V, and the inset shows the corresponding voltage profiles. (c-f) SEM images of c the pristine Zn anode and the Zn anodes from the Zn/Zn symmetrical cells after plating/stripping for 100 h in d the acetate-based electrolyte, e the sulfonate-based electrolyte, and f the sulfate-based electrolyte.

Figure 6.13 Long-term cyclability and rate performance of Zn/Zn symmetric cell in the acetate-based electrolyte. (a) Long-term cyclability at 0.5 mA cm^{-2}. (b) Rate performance at current densities from 0.5 to 5 mA cm^{-2}. (c) Corresponding voltage profiles at each current density. The areal capacity was 1.0 mA h cm^{-2}.

Figure 6.14 Coulombic efficiency of Zn/Ti cells at 1 mA cm^{-2} in different electrolytes. (a) The sulfonate-based electrolyte. (b) The sulfate-based electrolyte. (c) The sulfate-based electrolyte with 0.1 M H_2SO_4. The insets show the corresponding voltage profiles.

Figure 6.15 SEM images of electrodeposited Zn on Ti foil in different electrolytes. (a, b) The acetate-based electrolyte. (c, d) The sulfonate-based electrolyte. (e, f) The sulfate-based electrolyte.

Figure 6.16 XRD patterns of Zn electrodes cycled in different electrolytes. The Zn electrodes were measured after plating/stripping in Zn/Zn symmetrical cells at 1 mA cm^{-2} for 100 h.

Figure 6.17 Optical images of Zn electrodes and separators after cycling in different electrolytes. (a) The acetate-based electrolyte. (b) The sulfonate-based electrolyte. (c)

Table 5.1 Comparison of the electrochemical stability of state-of-the-art Zn metal electrodes at high current densities and areal capacities.

Abbreviations

Abbreviation	Full name
LIB	Lithium-ion battery
AZIB	aqueous Zn-ion batteries
CE	Coulombic efficiency
AFM	Atomic force microscope
TEM	Transmission electron microscopy
Fθ_A	Contact angle
PVDF	Polyvinylidene fluoride
CV	Cyclic voltammetry
E_a	Activation energy
EDS	Energy dispersive X-ray spectroscopy
EIS	Electrochemical impedance spectroscopy
FE-SEM	Field emission scanning electron microscopy
JCPDS	Joint Committee on Powder Diffraction Standards
(h k l)	Miller indices
Raman	Raman Spectroscopy
Li^+	Lithium ions
Zn^{2+}	Zinc ions
mA	Milliampere
h	Hour
g	gram

SAED	Selected area electron diffraction
SEI	Solid electrolyte interphase
SEM	Scanning electron microscopy
SHE	Standard hydrogen electrode
DFT	Density Functional Theory
VASP	Vienna *Ab-Initio* Simulation Package
GGA	Generalized gradient approximation
D	Diffusion coefficient
XPS	X-ray photoelectron spectroscopy
XRD	X-ray diffraction
FTIR	Fourier transform infrared spectroscopy
σ	Conductivity
$t_{Zn^{2+}}0$	Transference number

Organizations

Abbreviation	Full name
CSC	China Scholarship Council
ARC	Australian Research Council
ANSTO	Australia's Nuclear Science and Technology Organisation
UOW	University of Wollongong
AIIM	Australian Institute of Innovative Materials
ISEM	Institute for Superconducting and Electronic Materials
EMC	Electron Microscopy Centre

Chapter 1

Introduction

1.1 Research Background

Rechargeable batteries have been regarded as the preferred energy storage solution for next-generation sustainable energy suppliers by storing the energy harnessed from these intermittent energy sources.[1-3] Lithium–ion batteries (LIBs), as the most widely studied rechargeable batteries, have undoubtedly dominated the energy storage market for decades due to their high energy density, long cycling stability, and high energy efficiency.[4] Nevertheless, some intrinsic characteristics render the current LIB technology less feasible for large-scale energy storage, in which the requirements of safety, cost, and environmental friendliness are relatively more critical than that of energy density.[5, 6] It is now generally accepted that designing water-based battery systems with low cost and high safety is in great demand to address many of these concerns, especially for the grid-scale energy storage.[7]

Aqueous rechargeable batteries have been regarded as promising alternatives to conventional LIBs due to their underlying advantage of suitability for water-based electrolytes.[8] Compared to the flammable organic solvents, water solvent is a flame retardant, which enables the water-based batteries to effectively avoid the dangers of catching fire or explosion.[9-11] In addition, water and water-soluble electrolyte salts are relatively cost-efficient, so that they help to reduce the overall cost of aqueous batteries.[12] Furthermore, instead of the strict manufacturing conditions, aqueous batteries can be assembled in air, benefiting from the insensitivity of water-based electrolyte. Another significant advantage of water-based electrolytes is their ionic conductivity (~0.1 S cm^{-1}), which is much higher than that of organic electrolytes (~1-10 mS cm^{-1}), resulting in outstanding rate capability and high power density.[13]

Furthermore, water, as an ideal electrolyte solvent, is totally non-toxic and environmentally benign, which brings huge superiority in terms of the ability to recycle discarded aqueous batteries.[14]

To date, a variety of aqueous rechargeable batteries based on mono-valent charge carriers (*e.g.* Li^+, Na^+, and K^+) and multivalent cations (*e.g.* Mg^{2+}, Ca^{2+}, Zn^{2+}, and Al^{3+}) have been widely reported because of their abundant resources, environmental friendliness, intrinsic safety, and even their comparable capacities to those of organic rechargeable batteries.[14-16] Among the anode candidates, metallic Zn offers good tolerance to O_2 and humid atmosphere than other active metals.[17] It thus can be directly adopted as a stable anode due to its intrinsic features, which significantly simplifies the battery configuration and lowers the processing and assembling costs.[9, 18-23] Apart from Zn metal, however, other metals cannot directly serve as anode in aqueous electrolytes, since their electrochemical redox voltages are beyond the stable potential window of water solvent.[24-26] Meanwhile, metallic Zn shows low redox potential and high over-potential for hydrogen (H_2) evolution, which enables the wide working voltage window of Zn batteries (~1.8 V).[27] Furthermore, its theoretical capacity (gravimetric capacity of 820 mA h g^{-1} and volumetric capacity of 5855 mA h cm^{-3}) is also much higher than those of the intercalation type anode materials that could be used in aqueous electrolyte.[28, 29]

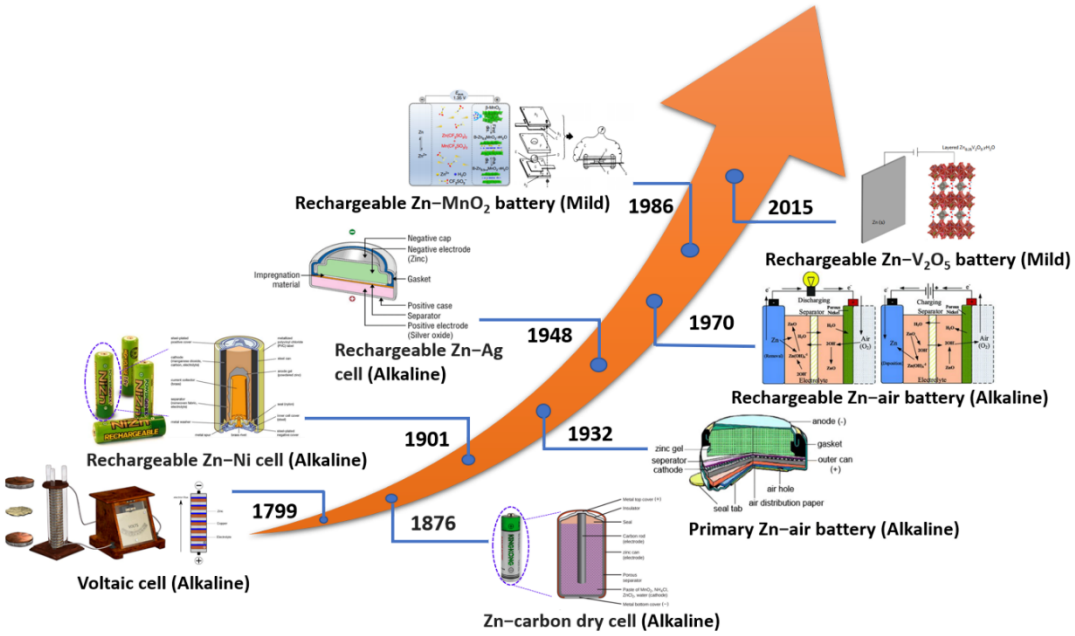

Figure 1.1 Schematic illustration of the development of Zn metal electrodes used in various alkaline and mild batteries.[18-22, 37, 38]

Current aqueous Zn-based batteries could be classified into two major categories based on their electrolytes (Figure 1). One is the class of Zn-based batteries using alkaline electrolyte (*e.g.,* KOH solution), typically Zn-air, Zn-Ag, and Zn-Ni batteries.[30-33] In recent decades, the rechargeable Zn-air batteries have undergone rapid development due to their relatively high specific energy (1218 W h kg^{-1}) and volumetric energy density (6136 W h L^{-1}), which is even comparable to that of Li-air batteries.[34, 35] The other category is the class of Zn-ion batteries (ZIBs) using mild electrolytes (including slightly acidic electrolyte, *e.g.*, $ZnSO_4$ solution), such as Zn-MnO_2 and Zn-V_2O_5 batteries.[36, 37] This kind of battery could be traced back to as early as the 1986, when Yamamoto *et al.* first developed the Zn/$ZnSO_4$/MnO_2 system by replacing KOH electrolyte with $ZnSO_4$ electrolyte.[38] In the last five years, ZIBs with mild electrolyte have sparked tremendous research interests again. Intensive efforts have also been spent on the exploration of high-performance cathode candidates and optimization of Zn metal anodes as well as electrolyte components, which have laid the foundation for

the practical development of ZIBs.[39] At present, the state-of-the-art aqueous Zn-based batteries are still far from satisfactory, no matter whether they contain an alkaline or a mild electrolyte.[40, 41] The main challenge is that Zn anode still suffers from low Coulombic efficiency (CE) due to its poor irreversibility in aqueous electrolyte, which is greatly hampering the further development of Zn-based batteries.[42]

1.2 Objectives of the Research

Herein, this doctoral thesis focuses on developing stable zinc metal anode for high-performance aqueous Zn-ion batteries. The Zn metal anode suffers from the dendrite growth and side reactions, which gravely restrains the development of aqueous Zn-ion batteries. The purpose of the research is to explore a feasible strategy to ensure side reaction-free and dendrite-free Zn metal anode. The critical issue rooted in Zn metal in aqueous electrolytes is the absence of an appropriate solid electrolyte interphase (SEI) layer. Building an SEI layer in situ on Zn electrode in water-based electrolyte is highly challenging, due to the relatively high reduction potential of Zn deposition and restricted voltage windows of water. Although the parasitic H_2 evolution during Zn deposition triggers the formation of passivation layers, the thus-formed passivation layers are insulating and loose, and cannot be used as the functional SEI layer. Achieving in-situ SEI layers to restrain Zn dendrite growth and side reactions is in great demand for stable Zn metal anode. In this doctoral thesis, in-situ SEI layers have been established on Zn anode via rational electrolyte design principle. The in-situ SEI protective layer at the electrode-electrolyte interface not only restrains the side reactions via isolating the active Zn from the bulk electrolyte, but also ensures uniform and rapid Zn-ion transport kinetics for dendrite-free Zn deposition. In addition, the issues of the dendrites and the side reactions stem directly or indirectly from the interaction between

the Zn metal and the electrolyte. Strongly alkaline and acidic electrolytes for aqueous Zn-ion batteries are responsible for inherent corrosion issues, the growth of Zn dendrites and low Coulombic efficiency (CE) for Zn plating/stripping, adversely affecting the overall electrochemical performance. Although mildly acidic electrolytes have been intensively investigated, the goal of high stability and CE of Zn electrodes remains a challenge. In this doctoral thesis, a highly compatible and friendly near-neutral electrolyte has been proposed to enhance stability and reversibility of Zn metal anode, which promotes a two-electron cathode reaction simultaneously.

1.3 Thesis Structure

The structure of this doctoral thesis is shown as follows.

Chapter 1 briefly introduces the background knowledge of aqueous rechargeable batteries and current aqueous Zn-based batteries.

Chapter 2 provides a comprehensive literature review on Zn anode behavior and corresponding improvement strategies in different aqueous Zn-based batteries.

Chapter 3 presents the experimental details and characterization methods, including preparation of electrolytes and electrodes, materials characterization, and electrochemical measurements.

Chapter 4 illustrates a unique electrolyte design strategy for in-situ solid-electrolyte interphase (SEI) construction to stabilize the Zn-electrolyte interface.

Chapter 5 demonstrates an *in situ* polymeric SEI interface on Zn anode towards high-performance aqueous Zn-ion batteries.

Chapter 6 displays a novel adoption of a near-neutral acetate-based electrolyte for boosting advanced aqueous Zn/MnO_2 batteries via electrolyte salt chemistry.

Chapter 7 summarizes potential prospects for the industrial application of high-

performance aqueous Zn-based batteries.

1.4 References

1. J. Lu, T. Wu and K. Amine, *Nat. Energy*, 2017, **2**, 1-13.
2. S. Zhang, Q. Fan, Y. Liu, S. Xi, X. Liu, Z. Wu, J. Hao, W. K. Pang, T. Zhou and Z. Guo, *Adv. Mater.*, 2020, **32**, 2000380.
3. S. Chen, C. Wu, L. Shen, C. Zhu, Y. Huang, K. Xi, J. Maier and Y. Yu, *Adv. Mater.*, 2017, **29**, 1700431.
4. F. Wu, J. Maier and Y. Yu, *Chem. Soc. Rev.*, 2020, **49**, 1569-1614.
5. H. Kim, J. Hong, K. Y. Park, H. Kim, S. W. Kim and K. Kang, *Chem. Rev.*, 2014, **114**, 11788-11827.
6. G. Liang, Z. Wu, C. Didier, W. Zhang, J. Cuan, B. Li, K. Y. Ko, P. Y. Hung, C. Z. Lu, Y. Chen, Grzegorz Leniec, Sławomir Maksymilian Kaczmarek, Bernt Johannessen, Lars Thomsen, Vanessa K Peterson, Wei Kong Pang and Z. Guo, *Angew. Chem. Int. Ed.*, 2020, **29**, 10594 -10602.
7. J. Hao, Y. Liao, Y. Zhong, D. Shu, C. He, S. Guo, Y. Huang, J. Zhong and L. Hu, *Carbon*, 2015, **94**, 879-887.
8. G. Wang, L. Fu, N. Zhao, L. Yang, Y. Wu and H. Wu, *Angew. Chem. Int. Ed.*, 2007, **46**, 295-297.
9. D. Kundu, B. D. Adams, V. Duffort, S. H. Vajargah and L. F. Nazar, *Nat. Energy*, 2016, **1**, 1-8.
10. L. Hu and K. Xu, *Proc. Natl. Acad. Sci. U.S.A.*, 2014, **111**, 3205-3206.
11. D. Chao, W. Zhou, F. Xie, C. Ye, H. Li, M. Jaroniec and S. Z. Qiao, *Sci. Adv.*, 2020, **6**, eaba4098.
12. J. Zhou, L. Shan, Z. Wu, X. Guo, G. Fang and S. Liang, *Chem. Commun.*, 2018, **54**, 4457-4460.

13. N. Alias and A. A. Mohamad, *J. Power Sources*, 2015, **274**, 237-251.

14. F. Beck and P. Rüetschi, *Electrochim. Acta*, 2000, **45**, 2467-2482.

15. X. Zeng, J. Hao, Z. Wang, J. Mao and Z. Guo, *Energy Storage Mater.*, 2019, **20**, 410-437.

16. X. Ji, *Energy Environ. Sci.*, 2019, **12**, 3203-3224.

17. C. Xia, J. Guo, P. Li, X. Zhang and H. N. Alshareef, *Angew. Chem. Int. Ed.*, 2018, **57**, 3943-3948.

18. Y. Li and H. Dai, *Chem. Soc. Rev.*, 2014, **43**, 5257-5275.

19. R. S. Balog and A. Davoudi, in *Encyclopedia of Sustainability Science and Technology*, Springer, 2012, pp. 671-706.

20. J. Phillips, S. Mohanta, M. Geng, J. Barton, B. McKinney and J. Wu, *ECS Transactions*, 2009, **16**, 11.

21. F. von Sturm, in *Comprehensive Treatise of Electrochemistry*, Springer, 1981, pp. 407-419.

22. X. Chen, Z. Zhou, H. E. Karahan, Q. Shao, L. Wei and Y. Chen, *Small*, 2018, **14**, 1801929.

23. T. Shoji, M. Hishinuma and T. Yamamoto, *J. Appl. Electrochem.*, 1988, **18**, 521-526.

24. J. Muldoon, C. B. Bucur and T. Gregory, *Chem. Rev.*, 2014, **114**, 11683-11720.

25. L. Zhang, L. Chen, X. Zhou and Z. Liu, *Adv. Energy Mater.*, 2015, **5**, 1400930.

26. X. Wang, Y. Hou, Y. Zhu, Y. Wu and R. Holze, *Sci. Rep.*, 2013, **3**, 1401.

27. D. Chao and S.Z. Qiao, *Joule*, 2020. https://doi.org/10.1016/j.joule.2020.07.023.

28. S. Higashi, S. W. Lee, J. S. Lee, K. Takechi and Y. Cui, *Nat. Commun.*, 2016, **7**, 1-6.

29. L. E. Blanc, D. Kundu and L. F. Nazar, *Joule*, 2020, **4,** 771-799

30. J. McBreen, *J. Power Sources*, 1994, **51**, 37-44.

31. P. Tan, B. Chen, H. Xu, W. Cai, W. He, H. Zhang, M. Liu, Z. Shao and M. Ni, *ACS Appl. Mater. Interfaces*, 2018, **10**, 36873-36881.

32. P. C. Li, C. C. Hu, T. H. You and P. Y. Chen, *Carbon*, 2017, **111**, 813-821.

33. W. Zhou, D. Zhu, J. He, J. Li, H. Chen, Y. Chen and D. Chao, *Energy Environ. Sci.*, 2020. DOI: 10.1039/d0ee01221a

34. J. S. Lee, S. Tai Kim, R. Cao, N. S. Choi, M. Liu, K. T. Lee and J. Cho, *Adv. Energy Mater.*, 2011, **1**, 34-50.

35. A. Kraytsberg and Y. Ein-Eli, *Nano Energy*, 2013, **2**, 468-480.

36. W. Sun, F. Wang, S. Hou, C. Yang, X. Fan, Z. Ma, T. Gao, F. Han, R. Hu and M. Zhu, *J. Am. Chem. Soc.*, 2017, **139**, 9775-9778.

37. N. Zhang, Y. Dong, M. Jia, X. Bian, Y. Wang, M. Qiu, J. Xu, Y. Liu, L. Jiao and F. Cheng, *ACS Energy Lett.*, 2018, **3**, 1366-1372.

38. T. Yamamoto and T. Shoji, *Inorg. Chim. Acta*, 1986, **117**, L27-L28.

39. L. Chen, Q. An and L. Mai, *Adv. Mater. Interfaces*, 2019, **6**, 1900387.

40. J. Liu, C. Xu, Z. Chen, S. Ni and Z. X. Shen, *Green Energy Environ.*, 2018, **3**, 20-41.

41. D. Yang, H. Tan, X. Rui and Y. Yu, *Electrochem. Energy Rev.*, 2019, **22,** 1-33.

42. F. Wang, O. Borodin, T. Gao, X. Fan, W. Sun, F. Han, A. Faraone, J. A. Dura, K. Xu and C. Wang, *Nat. Mater.*, 2018, **17**, 543-549.

Chapter 2

Literature Review

2.1 Issues for Zn electrode in alkaline electrolyte

Zn electrode has been used and studied in alkaline electrolyte for a long time. Different issues for Zn electrode have been found to seriously limit the development of high-performance alkaline Zn-based batteries. According to the previous studies, Zn electrode issues in alkaline electrolyte can be classified into five types, namely Zn electrode corrosion, passivation, shape change, dendrite growth, and H_2 evolution. Each of them has been thoroughly analyzed as follows.

2.1.1 Zn electrode corrosion

Currently, the real energy density of the reported alkaline Zn-air batteries is only approximately 250 Wh kg^{-1}, which is far below the theoretical value (1086 Wh kg^{-1}).[1, 2] Self-corrosion of Zn electrode caused by its high solubility in strong alkaline media (pH ~ 14) is one of the important reasons for the difference between the actual and theoretical energy density. Zn corrosion in the alkaline electrolyte leads to the formation of saturated or supersaturated $Zn(OH)_4^{2-}$ solution, which not only causes gradual loss of active material but also triggers shape change of the Zn electrode and Zn dendrite growth.[3] Different Zn corrosion mechanisms as well as their factors have been studied.[4-8] To date, the most accepted mechanism of Zn dissolution in alkaline electrolyte involves two steps. The first step is the oxidation of metallic Zn to $Zn(OH)_4^{2-}$ (Reaction (1)). The other one is the precipitation of ZnO on the Zn surface once the dissolved $Zn(OH)_4^{2-}$ saturates the solution (Reaction (2)). Thus, the overall Zn corrosion should be expressed as follows (Reaction (3)). To the best of our knowledge, the H_2 evolution reaction is unlikely to occur during the Zn corrosion process, as the concentration of H^+

ions near the Zn electrode is very low (~10^{-14} mol L^{-1}). In this case, the O_2 absorption reaction (corrosion) is more likely to occur in the alkaline electrolyte, especially in the open Zn-air battery system.

$$Zn - 2e^- + 4OH^- \rightarrow Zn(OH)_4^{2-} \quad (1)$$

$$Zn(OH)_4^{2-} \rightarrow ZnO + H_2O + 2OH^- \quad (2)$$

$$Zn - 2e^- + 4OH^- \rightarrow ZnO + H_2O \quad (3)$$

The Zn corrosion in alkaline electrolyte has also been regarded as Zn electrode dissolution, as the metallic Zn is oxidized by generating $Zn(OH)_4^{2-}$ or ZnO by-products with the reduction of active material. Similarly, the Zn corrosion in mild electrolyte would inevitably occur due to its thermodynamic instability in such electrolytes. Unlike the by-products $Zn(OH)_4^{2-}$ or ZnO in alkaline media, the precipitates during the Zn corrosion in mild electrolyte are mainly formed as a result of zincates in the electrolyte, such as the $Zn_4SO_4(OH)_6{\cdot}xH_2O$ by-product in $ZnSO_4$ electrolyte.[9] In a sealed system with mild electrolyte, Zn corrosion is probably accompanied by the H_2 evolution reaction due to the high concentration of H^+ and limited O_2 content, which also differs from the Zn corrosion in an open Zn-air system.

2.1.2 Zn passivation

Passivation of Zn electrode in alkaline electrolyte, which leads to a low utilization rate of Zn, is one of the main challenges for the development of high-performance rechargeable Zn–air batteries.[10] Zn passivation is the formation of an thick insulating ZnO layer on its surface, which inactivates the metallic Zn surface by blocking the migration of electrons/ions at the interphase.[11] Concretely, when a Zn electrode is discharged and the $Zn(OH)_4^{2-}$ discharge product has reached its solubility limit, ZnO product is precipitated and generates a dense film that covers the Zn electrode surface.

This passivating ZnO film serves as a diffusion barrier against the electrons and OH^- ions, with the result that the discharge capacity and power capability of the Zn anode are seriously decreased.

Over the years, several investigations have been conducted to analyze the properties of the passive film and the passivation mechanism in alkaline electrolyte.[10, 12] According to Powers and Breiter,[4] there are two different types of layers generated on the surface of Zn electrode: A loose and porous layer (the so-called type I layer) forms first on the electrode surface in the absence of convection. When the conditions for supersaturation are removed, a compact film (denoted as type II) appears to form directly on the surface of the Zn electrode rather than by precipitation. Interestingly, the formation of a type I film could be effectively avoided in flowing electrolyte, but not that of a type II film. With the help of optical microscopy, Marina Bockelmann et al.[13] observed the appearance of both kinds of the passive films (type II and type II) *in-situ* on Zn electrode (Figure 2.1). After 40 min of discharge at a current density of 70 mA cm^{-2}, the type I passive film becomes visible above the Zn surface. With further discharging, the rupture of the type I passive film can be seen.

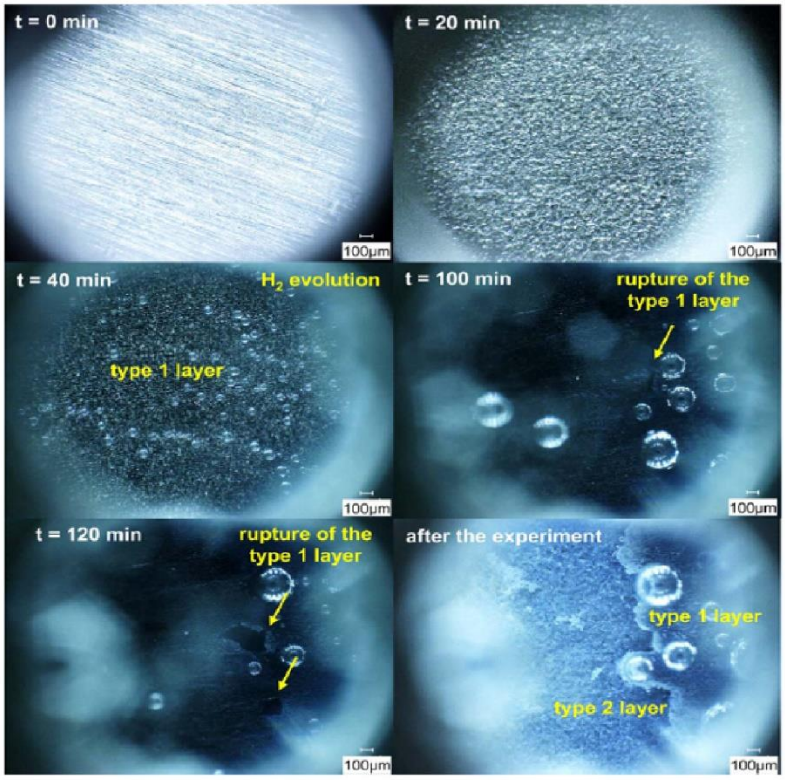

Figure 2.1 *In-situ* microscopic observation of Zn electrode passivation under the current density of 70 mA cm^{-2}. After 40 min, the loose and porous type I layer was generated on the surface. After 100 min, rupturing of this dark passive layer can be recognized. (Reprinted with permission from ref. 13. Copyright 2018, Electrochemical Society, Inc.).

Overall, the passivation of Zn electrode in alkaline systems that is caused by the insulating ZnO discharge product is an important reason for the fast capacity degradation and the battery failure. This negative phenomenon would not exist in mild systems, however, due to the different Zn plating/stripping mechanism without ZnO formation. To date, different strategies have been proposed to diminish the effects of the passivation in alkaline media.

2.1.3 Shape change

Shape change in the alkaline systems refers to the reduction of the electrochemically

active surface area of Zn electrode during battery operation.[14] To be specific, the active material moves away from the edges of the Zn electrode and piles up towards the plate bottom and centre during cycling. The transport of Zn material severely reduces the reversible capacity and shortens the battery's lifespan. Usually, densification and loss of electrode porosity, as well as passivation of the Zn electrode, are often observed where the electrode has undergone such a shape change.

Studies on the shape change of Zn electrode in alkaline electrolyte have been conducted for decades, and the results revealed that the battery and electrode geometry, type of separator, additives, and battery electrolyte are probably the most important factors that influence the extent and rate of shape change.[15] Investigations of the shape change could only be established in an actual battery configuration, and hence, the design of the battery is of crucial importance. Two classical models for the shape change of Zn electrode have been proposed: the concentration-cell model and the membrane-pumping model.[16] As the shape change of Zn electrode proceeds dynamically during cycling, it causes electrode composition changes.[17] To visually investigate the change in the Zn electrode morphology during cycling, synchrotron X–ray diffraction (XRD) mapping analysis of Zn/ZnO electrode has been conducted.[18] During cycling, the dissolved $Zn(OH)_4^{2-}$ species would diffuse from the edge to the ZnO hill (the center of the electrode) due to their concentration gradient, and thus, the transportation of dissolved $Zn(OH)_4^{2-}$ species plays an important role in the shape change of Zn electrode.

It is widely accepted that the shape change of Zn electrode during cycling seriously affects the CE and cycling life of the alkaline Zn–based batteries. At present, however, there are no relevant reports about the shape change of metallic Zn electrode in ZIBs with mild electrolyte. In the future, this fundamental research should be conducted to deeply understand the behaviour of metallic Zn electrode in the mild electrolyte.

2.1.4 Zn dendrite growth

Another major problem in developing alkaline rechargeable batteries is the formation and growth of Zn dendrites during battery operation. It is well known that Zn dendrites form and grow under certain conditions during cycling (Figure 2.2), which severely affects the performance and lifetime of Zn–based batteries.[19, 20] "Dead" Zn easily forms due to Zn dendrites that are shed from the electrodes in alkaline media, causing rapid decay of the CE and reversible capacity of batteries. Also, the continuous growth of Zn dendrites finally leads to direct contact between the anode and cathode, causing a short circuit and the eventual failure of the battery. The formation and growth of Zn dendrites is especially serious in alkaline electrolytes compared to mild electrolyte. This is mainly because Zn metal has high electrochemical activity in alkaline media.

The formation mechanism of Zn dendrites has been extensively studied in alkaline system.[21] The charging-discharging process of Zn electrode is mainly influenced by the "liquid-phase mass transfer" in which the concentration polarization appears near the surface of Zn electrode due to the concentration gradient of the active $Zn(OH)_4^{2-}$ charge carriers. $Zn(OH)_4^{2-}$ ions in the electrolyte are more likely to diffuse to protrusions on the surface of Zn electrode where the local current density is higher than in other places, leading to an uneven current distribution on the electrode. Ultimately, Zn deposition speeds up on the tip of Zn electrode, which further attracts more $Zn(OH)_4^{2-}$ ions to accumulate and gradually form the dendrites during repeated charge/discharge. According to Diggle et al.[22], Zn dendrite growth shows a pyramid-like form, because the effective radius of curvature of the protrusion decreases until it reaches a critical radius, which is the condition for dendrite initiation. Diggel et al. suggested that dendrites may be formed at the tips of pyramids. Mansfeld and Gilman[23], however, who worked on single crystals using *in-situ* light microscopy and scanning electron

microscopy (SEM), found that the dendrites were more frequently initiated at the feet of the pyramids. They further suggest that it is unlikely that a dendrite will form at the tip if a pyramid has reached the necessarily small radius and that the pyramids and dendrites grow independently, with the dendrites being nucleated at macroscopic defects or impurity centers.

Nowadays, it has become widely accepted that the morphology of the Zn dendrites is affected by the over-potential and surface roughness. To date, various morphologies of Zn deposits: mossy, boulder, layered, dendrite, and leaf-like, have also been reported.[24] Electrodeposition at a lower over-potential tends to produce epitaxial, boulder, or sponge morphologies of Zn dendrites. It is important to note, however, given a relatively long time for initiation, that dendrites can also form and grow at an even lower deposition over-potential (Figure 2.2c).[25] Thus, long-term dissolution and deposition cycles can trigger the progressive amplification of surface heterogeneities on Zn electrodes, eventually resulting in dendrite growth, even under relatively low over-potentials.

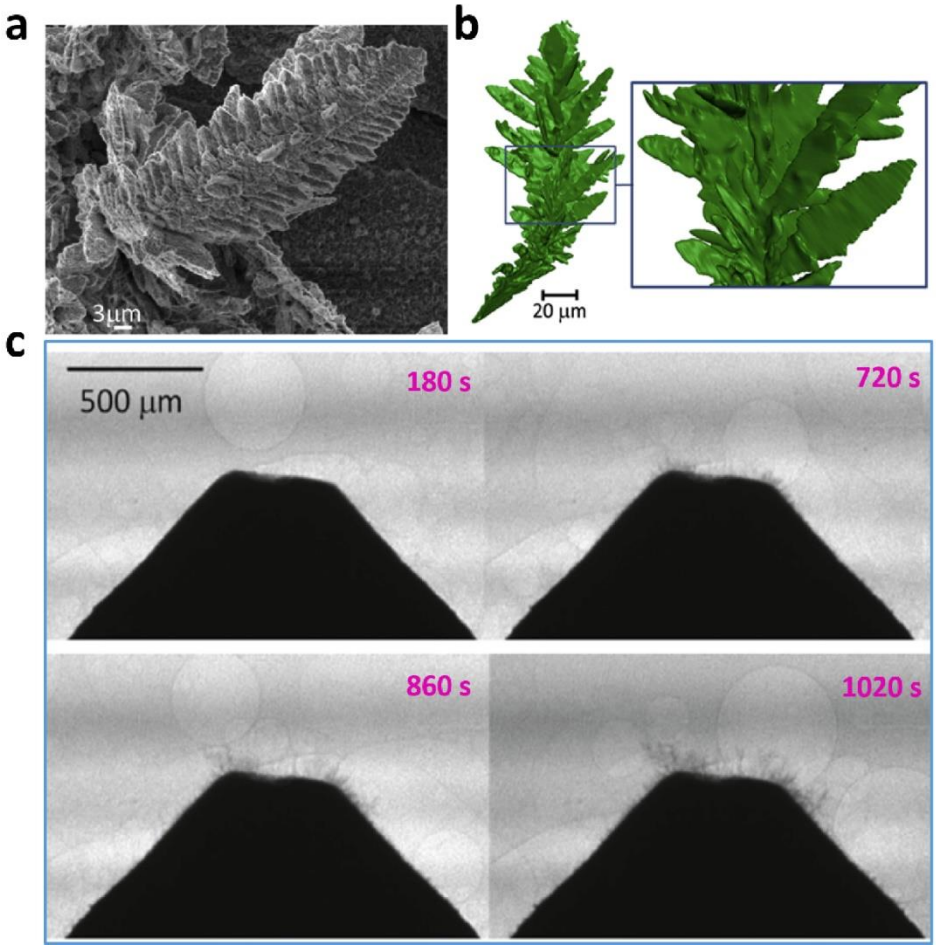

Figure 2.2 (a) SEM image of Zn dendrite. (b) Reconstructed 3D image of Zn dendrite obtained using focused ion beam (FIB)-SEM tomography. (Reprinted with permission from ref. 20. Copyright 2017, Elsevier) (c) Radiographic images of Zn dendritic growth under the current density of 15 mA cm^{-2} after 180 s, 720 s, 860 s, and 1020 s, respectively. (Reprinted with permission from ref. 25. Copyright 2018, Elsevier)

2.1.5 H_2 evolution

The H_2 evolution reaction is a competitive reaction with ZnO reduction during Zn deposition in alkaline electrolyte, which causes CE loss during both charging and discharging processes by promoting water electrolysis.[26] In alkaline electrolyte, the H_2 evolution reaction is affected by both thermodynamic and kinetic factors.

Based on the thermodynamic principle, the standard reduction potential of Zn/ZnO is –

1.22 V *vs.* SHE when the pH value of the electrolyte is 14, lower than that of the H_2 evolution reaction (–0.83 V *vs.* SHE) under the same conditions,[26] indicating thermodynamic favourability for the HER rather than Zn deposition. Nevertheless, the actual H_2 evolution reaction in the alkaline system during battery operation is also suppressed due to the kinetic over-potential, and it can be defined by the over-potential of Zn electrode. The H_2 evolution over-potential (η) on Zn electrode can be expressed as follows:

$$\eta = const. + \frac{RT}{F} ln\alpha_{H_2O}\alpha_{OH^-} - \frac{2RT}{F} lnI \qquad (4)$$

where α denotes the activity, I is the current density, and the other symbols have their usual meaning. At constant temperature and a definite KOH concentration, the above equation can be expressed as the Tafel equation.

$$\eta = A + BlogI \qquad (5)$$

where A and B are constants. Thus, the current density has a significant impact on the actual H_2 evolution reaction. In addition, according to Lee.[27], for the same KOH concentration, the numerical values of the over-potential are higher (less negative) at a higher temperature. This also shows that, at the same temperature, the numerical values of the over-potential are higher (less negative) in a lower KOH concentration. Moreover, the exchange current density and Tafel slope on a Zn electrode surface in 6 m KOH electrolyte were measured to be 8.5×10^{-10} A cm^{-2} and 0.124 V, respectively. The H_2 evolution over-potential in case of the pure Zn electrode is –1.76 V *vs.* Hg/HgO.[28] However, the H_2 evolution over-potential of ZnO is only –1.399 V *vs.* Hg/HgO, which is significantly reduced on a ZnO surface. In other words, the H_2 evolution reaction will be enhanced when the Zn electrode is covered by ZnO product.

2.2 Strategies in alkaline electrolyte

Considerable research efforts have been spent on eliminating, or at least minimizing, the effects of the Zn electrode issues in the alkaline electrolytes, and some effective strategies have been proposed to enhance the performance of Zn electrode, in terms of cycling stability, reversible capacity, and lifespan. Accordingly, these strategies could be divided into four distinct categories: (i) Zn electrode modification; (ii) Electrolyte optimization; (iii) Separator selection; (vi) Other methods. This section represents an attempt to summarize these methods and discuss the electrochemistry and theory behind certain methods.

2.2.1 Zn electrode modification

2.2.1.1 Electrode additive

The incorporation of an additive into the active material of Zn electrode during its fabrication is an extensively used method to improve the performance of Zn electrode in alkaline systems. Different types of electrode additives have been reported in the previous literatures, including heavy metals/metal oxides, alkaline-earth-metal oxides/hydroxides, and organic additives.[29, 30] Heavy metal/metal oxide additives are the most commonly used additives due to their high H_2 evolution over-potential and high stability in alkaline electrolyte.[30] For inhibiting the H_2 evolution and mitigating the corrosion of Zn electrode, mercury has been reported to be extremely effective. It has been found, however, that Zn electrode is more likely to incur the above-mentioned shape change with the incorporation of this additive, which is detrimental to the cycling stability of Zn electrode. Other different heavy metal/metal oxide additives in pasted Zn electrode have been investigated by McBreen et al.[31], and the results show that Pb, Cd, Tl, and In-containing additives have positive effects towards diminishing shape change. This is because these additives can increase the polarization of Zn electrode, which, in turn, enhances the current distribution. Subsequently, the impacts of additive

combinations were also studied, indicating that the shape change of Zn electrode was considerably decreased by using such mixtures of additives, due to the synergistic relationship occurring with these binary compounds.[32] In addition, other metals such as Bi, Sr, and Ni have been used as additives in alkaline systems as well.[33] These metals can serve as substrates for Zn deposition during battery operation. This kind of substrate can improve the conductivity of the electrodes and result in a substrate effect or matrix effect, promoting the even deposition of Zn on the current collector and suppressing the Zn dendrite formation by optimizing the current distribution.

Another class of commonly used additives is the alkaline-earth-metal oxides/hydroxides, in which the most promising candidate is calcium hydroxide ($Ca(OH)_2$).[34, 35] The $Ca(OH)_2$ forms an insoluble solid compound with $Zn(OH)_4^{2-}$, the formula of which can be written as $Ca(OH)_2 \cdot 2Zn(OH)_2 \cdot 2H_2O$.[36] In KOH electrolyte, the solubility of this insoluble solid is lower than that of ZnO by a factor of 1.5 to 2.5, depending on the KOH concentration. In this case, the migration of $Zn(OH)_4^{2-}$ in the electrolyte would be minimized. Therefore, the capacity losses due to shape change would be minimized through the addition of $Ca(OH)_2$ to the Zn electrodes. Moreover, this also minimizes the concentration gradient of $Zn(OH)_4^{2-}$ ions that would normally be established during charging, and hence can create another benefit, a reduced likelihood of dendrite formation. According to Gagnon et al.[37], the effective molar ratio of $Ca(OH)_2$ to ZnO must be greater than 0.5 to 1.0. In addition, magnesium and aluminum hydroxides have been also reported to function in a similar manner by forming an insoluble species that prevents the migration of the $Zn(OH)_4^{2-}$ species.[34]

Organic additives have also received considerable attention in recent years due to their main advantages of low cost and environmental benignity. The most extensively used organic addition is polytetrafluoroethylene binder due to its relatively low cost, ease of

dispersion, and good chemical compatibility with alkaline electrolytes.[38] Small additions of this polymer have been shown to engender a high degree of mechanical stability whilst still maintaining an open network, contributing to reducing the deformation and prolonging the cycling stability of Zn electrode. Furthermore, other similar organic additives, such as carboxymethyl cellulose, agar, poly(ethylene) and poly(vinylidene fluoride), have also been employed in alkaline systems to increase the mechanical strength of Zn electrode. In addition, these polymer binders can also improve the dispersion of Zn/ZnO powders in the electrode, which increases the effective surface area and reduces the shape change during cycling.

In general, introducing electrode additives is an easy option for enhancing the performance of Zn electrode in an alkaline system by inhibiting H_2 evolution, preventing Zn corrosion, reducing the Zn passivation, and mitigating the shape change. Various types of electrode additives have been claimed to effectively address certain issues for Zn electrode in alkaline electrolyte. Nevertheless, each kind of additive suffers from its own limitations and disadvantages. Although most heavy metal/metal oxide additives feature high chemical stability and high H_2 evolution over-potential, they not only enhance the price of electrode fabrication, but also introduce big environmental concerns due to their high cost, high toxicity, and environmental unfriendliness. Despite the advantages of organic additives, they usually act as insulators and impurities in the modified Zn electrode, which increases the internal resistance of the Zn electrode and may affect the battery performance.

2.2.1.2 Anion-exchange films coating

According to our foregoing discussion, the $Zn(OH)_4^{2-}$ product is produced near the Zn surface and likely to move into the bulk electrolyte during discharging. This does not always happen at the same position during the battery cycling, however, and probably

leads to shape change and loss of the active Zn material (Figure 2.3a).[39] Thus, keeping $Zn(OH)_4^{2-}$ near the Zn electrode surface during battery operation will be a promising approach to overcome the Zn electrode issues. One effective strategy to keep $Zn(OH)_4^{2-}$ near the surface of Zn electrode is coating an anion-exchange ionomer layer on the Zn electrode surface (Figure 2.3b). Ionomers are ion-containing polymers that typically contain hydrocarbon backbones and a relatively small number of acid groups.[40] These acid groups are incorporated into the main chain or present as pendant groups, giving the ionomers have the selective capability to conduct typical ions such as OH^- but not $Zn(OH)_4^{2-}$. The strategy of coating an ionomer film on Zn electrode in alkaline system was first introduced in 1998.[41] The ionomer coatings allow the smaller ions relating to the reactions of Zn electrode to pass through, but prevent the migration of the larger $Zn(OH)_4^{2-}$ ions during battery operation. Therefore, the reduced $Zn(OH)_4^{2-}$ migration helps to alleviate the shape change of Zn electrode and reduce concentration gradients during cycling, which further reduces the driving force for Zn dendrite formation and growth. Soon afterwards, Miyazaki et al.[42] incorporated an OH^- conductive binder consisting of a polymer backbone and positively charged head groups into a slurry-based Zn electrode, which resulted in high cycling stability with suppressed dendrite growth in the battery.

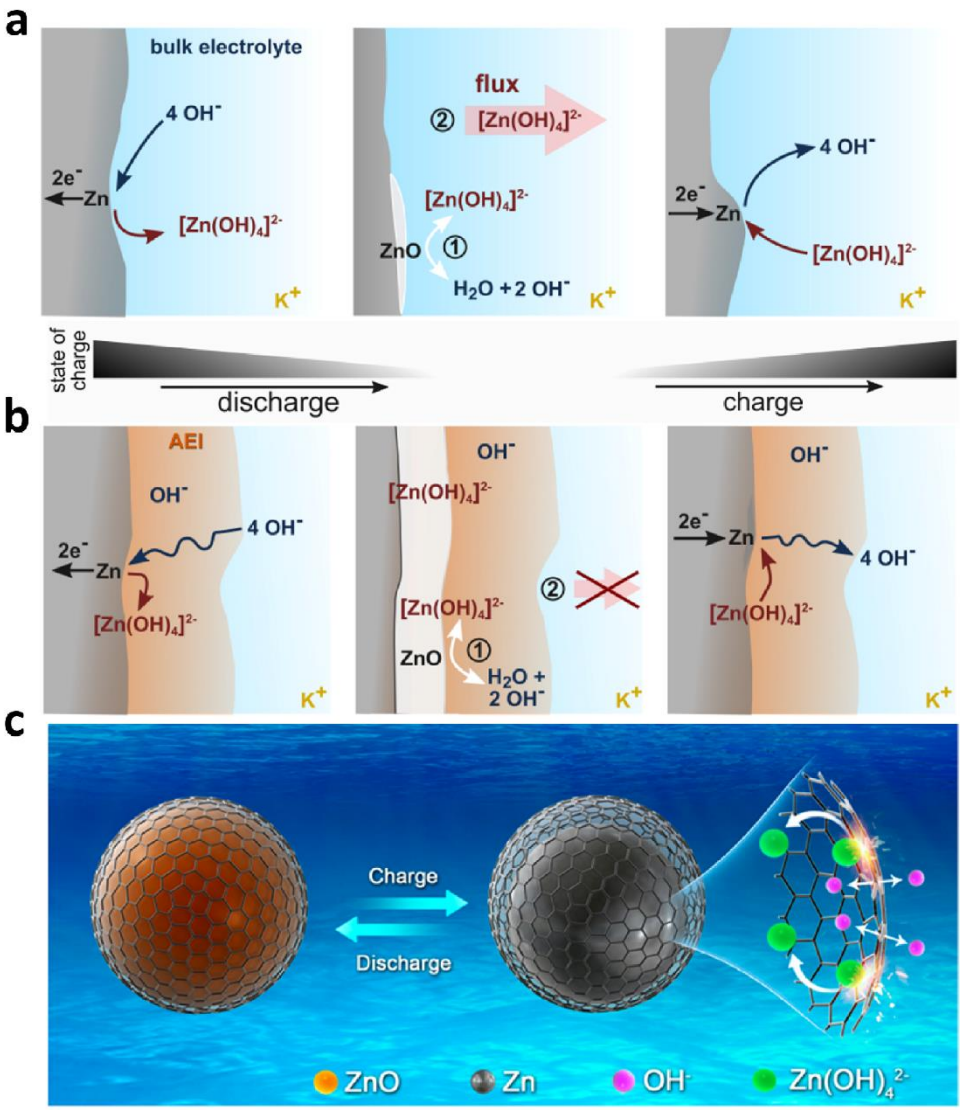

Figure 2.3 Schematic illustration of the working principle of Zn electrode in an alkaline electrolyte: (a) bare Zn electrode. Each Zn atom might not be deposited at the same location on the Zn electrode during cycling, leading to severe changes in the electrode shape/structure and even dendrite growth. (b) Zn electrode homogeneously coated with an anion-exchange ionomer (AEI). The shape change and dendrite growth are suppressed by keeping the $[Zn(OH)_4]^{2-}$ ion near its place of origin. (Reprinted with permission from ref. 39. Copyright 2018, American Chemical Society) (c) Schematic illustration of the ion-sieving nano-shell design for the Zn electrode. (Reprinted with permission from ref. 79. Copyright 2019, American Chemical Society)

Apart from the ionomer films, the carbon-based coating technique has also been widely applied to enhance the Zn electrode performance by solving the problems of Zn passivation, corrosion, and shape change simultaneously.[43-45] Yan and co-workers reported a lasagna-inspired Zn anode,[46] where ZnO nanoparticles are encapsulated by graphene oxide to form a free-standing electrode. Similar to the anion-exchange ionomers, this graphene oxide layer allows the permeation of water and smaller OH^- ions, and prevents the loss of Zn active material through blocking transport of the bigger $Zn(OH)_4^{2-}$ ions (Figure 2.3c). The graphene oxide layer can also be partially reduced after soaking in the alkaline electrolyte, which facilitates electron transfer inside the Zn electrode. Moreover, the fabrication of the ZnO lasagna electrode, starting from the commercially available ZnO nanoparticles ~100 nm in size (smaller than the critical size of passivation), is compatible with the roll-to-roll process, which is ideal for large-scale manufacturing. In addition to graphene oxide, a variety of carbon-based membranes with a controllable pore size and permeability have been demonstrated as well due to their ion-sieving capabilities.[47, 48] According to Wu and co-workers, carbon shells with controllable thickness were obtained on ZnO nanoparticles through carbonization of a uniform polydopamine coating.[49] The scalable synthesized carbon shell with controllable shell thickness was an effective strategy to solve the problems of passivation and corrosion simultaneously. The nanosized ZnO prevents passivation, while the microporous carbon shell slows down the corrosion of Zn species. Under extremely harsh testing conditions (closed cell, lean electrolyte, no ZnO saturation), this Zn anode shows significantly improved performance compared to Zn foil and bare ZnO nanoparticles. In addition, other similar functional coating layers, such as graphene,[50] TiO_2,[51] and TiN_xO_y,[47] have been also proposed to improve the Zn electrode performance in alkaline systems.

Overall, these anion-exchange coating films enable fast OH^- ion and water diffusion as well as preventing the large $Zn(OH)_4^{2-}$ ion from escaping during cycling, thus effectively also preventing Zn corrosion and shape change. Additionally, the limited $Zn(OH)_4^{2-}$ migration also reduces the concentration gradient near the Zn electrode during battery operation, which decreases the driving force to form the Zn dendrites. Although the Zn electrode performance was effectively enhanced under the assistance of the anion-exchange coatings, the inert components were incorporated into the Zn electrode. In this case, the capacity based on the overall Zn electrode as well as the volumetric energy density based on the whole battery would likely be affected, however, these negative effects might be mitigated in future coating designs.

2.2.1.3 Developing 3D electrode

Designing a 3D porous architecture to enhance the surface area of Zn electrode is another generally adopted method to mitigate the Zn electrode issues in alkaline systems.[52-54] Obviously, the high surface area decreases the local current density on the 3D Zn architecture electrode, resulting in a low over-potential and slow Zn deposition process. As a result, even and compact Zn deposition without Zn dendrites could be realized, which obviously enhances the durability of the battery (Figure 2.4a).[55] In addition, other advantages could be achieved when the Zn electrode was transformed into a 3D architecture. First, the metallic 3D Zn electrode features interconnected pathways, which maintains good electronic conductivity during charge and discharge process. Second, the 3D structure of Zn electrode makes the current distribution more uniform throughout the electrode structure. Third, the 3D design also helps to restrain the shape change of Zn electrode in alkaline electrolytes. This is because the porous structure accelerates the saturation/dehydration of $Zn(OH)_4^{2-}$ to ZnO within confined void-volume elements in the interior of the porous electrode. Based on these valuable

features, a Zn electrode with a porous, monolithic, 3D aperiodic architecture was capable of up to ~90% Zn utilization and over 80 charge-discharge cycles at high currents without visible dendrite growth.[56] Subsequently, a $Ca(OH)_2$–infused Zn sponge electrode in the Zn–Ni alkaline system was studied, in which the $Ca(OH)_2$ worked as an additive, the function of which has been discussed above.[55] This Ni–Zn battery maintained 100% of the required discharge capacity for 85 and 65 cycles, respectively, with an average energy efficiency of 84% before capacity fading, which is comparable to the 85% energy efficiency found in Li–ion batteries. Nevertheless, the 3D Zn sponge may affect the volumetric capacity and energy density of the battery due to its porous structure. By increasing the solid volume fraction of Zn sponge from ~20% (Zn_{20}) to 30% (Zn_{30}), the alkaline Zn_{30}–Ag battery demonstrated superior performance with 50% improvement in its Zn-normalized volumetric capacity (up to ~1.6 Ah L_{Zn}^{-1}) as well as supercapacitor-like specific power (up to ~6 kW kg_{Zn}^{-1}) (Figure 2.4b).[57]

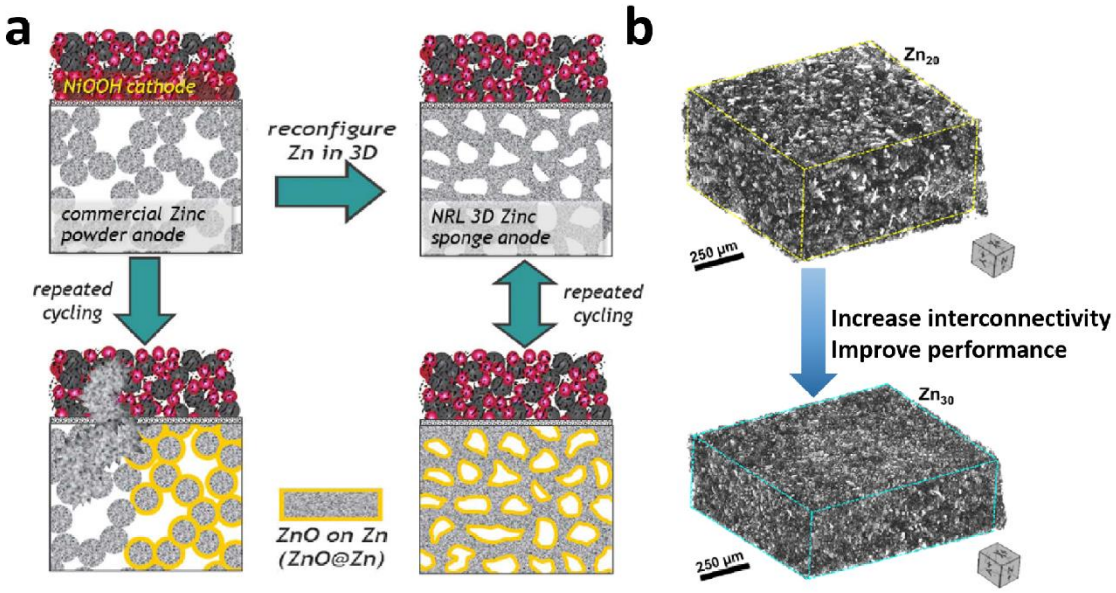

Figure 2.4 (a) Schematic illustration of the effect of recharging a Ni–Zn (using commercial Zn powder electrode) *vs.* a Ni–3D Zn cell, where the anode is redesigned as a monolithic aperiodic sponge, ensuring persistent 3D wiring of the metallic Zn core. Zn dendrites would pierce the separator after a certain number of cycles. (Reprinted with permission from ref. 55. Copyright 2017, AAAS). (b) Three-dimensional volume-rendered X-ray tomograms of Zn_{20} and Zn_{30} sponges. (Reprinted with permission from ref. 57. Copyright 2018, American Chemical Society)

In addition to the above advantages, one should keep in mind that the 3D porous Zn electrode has a higher active surface area compared to a commonly-used Zn electrode. This indicates that more active material of the electrode is in contact with the alkaline electrolyte in 3D Zn electrode. As mentioned above, Zn electrode is thermodynamically unstable in strong alkaline electrolyte. In this case, the Zn corrosion in the 3D Zn electrode has likely caused deterioration, which gravely consumes the active Zn electrode and electrolyte, and degrades the performance. Therefore, this negative effect brought by the 3D Zn design should be considered in later work.

2.2.2 Electrolyte optimization

The performance of Zn–based batteries is not only dependent on the performance of Zn electrode, but also strongly depends on the interaction between the electrode and electrolyte. Therefore, the composition and concentration as well as the format of the electrolyte seriously affects the solubility of $Zn(OH)_4^{2-}$ and the formation process of ZnO, which has further impacts on the reversible capacity as well as the battery rechargeability. To improve the performance of Zn–based batteries, great efforts have been spent on the electrolyte optimization, including introducing electrolyte additives and developing different electrolyte forms. To date, numerous electrolyte additives and gel electrolytes have been proposed to optimize the Zn electrochemical performance by suppressing the Zn corrosion, mitigating the Zn passivation, reducing the shape change, and inhibiting the Zn dendrite growth, which has been summarized below. The underlying reasons are discussed in the following section.

2.2.2.1 Electrolyte additive

Incorporating additives into the electrolyte is an alternative way of improving the reversibility and cycling stability of Zn electrode in alkaline media. Based on their chemical constitution, the frequently used electrolyte additives in alkaline batteries can be divided into two main categories: inorganic and organic additives.[58-60] Among the inorganic additives, ZnO powder has been continuously used to prepare ZnO-saturated KOH solution, which functions as the high-performance electrolyte in alkaline systems.[61] This electrolyte is pre-saturated with $Zn(OH)_4^{2-}$ ions, which helps to suppress the corrosion and mitigate the shape change of Zn electrode, further enhancing the Zn reversibility and lifespan. The addition of lead ions into the electrolyte has long been used to improve the electrochemical behavior of Zn. According to Mansfield et al.[62], lead ions could block the sites that should be active for Zn corrosion and deposition, and hence inhibit the formation and growth of Zn dendrites. The

morphology of the Zn deposition with the lead additive was found to be smooth, as opposed to the classical side-branched monocrystal dendrites obtained in the lead-free electrolyte. Moreover, tin salts as additives have been also been studied in a similar way and have been found to exhibit properties favorable for enhancement of the Zn deposition morphology.[63] Investigations revealed that the tin salts function in a similar way to lead, so as to block the active sites. In addition, various other inorganic electrolyte additives, including silicate, ferricyanide, phosphate, arsenate, borate, and fluoride, have been proposed for addition to alkaline electrolytes to overcome the Zn electrode limitations.[32]

Besides inorganic electrolyte additives, numerous organic additives have also been investigated, in which the surfactants have frequently been reported to significantly suppress the Zn passivation and Zn corrosion, and influence the Zn deposition morphology.[59, 64-66] Based on their structures, the surfactants could be divided into three types: (i) anionic surfactants such as sodium dodecyl sulfate (SDS)[67], dodecyl benzenesulfonate (SDBS)[67], and natrium 1,4-bis(2-ethylhexyl) sulphosuccinate (AOT)[68]; (ii) cationic surfactants such as dodecyltrimethylammonium bromide (DTAB)[69], trimethyloctadecylammonium chloride (STAC)[70], and cetyltrimethylammonium bromide (CTAB)[71]; and (iii) nonionic surfactants, such as Pluronic F-127 (P127)[72] and polyoxyethylene nonylphenyl ether[73]. On the one hand, these surfactants could effectively mitigate the Zn corrosion and passivation, as the surfactant molecules are adsorbed on the Zn electrode surface, which prevents contact between the electrolyte and the Zn electrode. On the other hand, the surfactant additives also help to inhibit the continuous Zn dendrite formation and growth. This is because the adsorption of surfactants on Zn electrode could regulate the local current distribution more uniformly, resulting in an even and smooth Zn deposition.[59] To

visually observe the effects of surfactant on the Zn dendrite growth, *in-situ* optical microscopy was employed to monitor the Zn deposit morphology in the electrolyte with polyethylenimine (PEI) additive (Figure 2.5a,b).[58] The results show that the PEI additive suppresses Zn dendrite growth by lowering the plating exchange current density. A higher PEI concentration leads to a lower exchange current density, and thus, the higher the dendrite suppression efficacy will be (Figure 2.5c,d). The effects of Zn dendrite inhibition were also confirmed by the high-resolution SEM images of Zn deposition (Figure 2.5e,f). Furthermore, the impacts of different surfactants on the Zn electrode performance were also compared, suggesting that Zn electrodes with anionic surfactants (*e.g.,* SDBS) as electrolyte additives displayed an enhanced cycle life compared to those using cationic surfactants (*e.g.,* CTAB).[74] The main reason could be that the negatively charged polar group of SDBS coordinates to Zn^{2+} ions at the Zn electrode surface, leading to the generation of small ZnO particles. The positively charged polar groups of CTAB show weak interactions with Zn^{2+} ions, however, leading to the generation of larger ZnO particles.

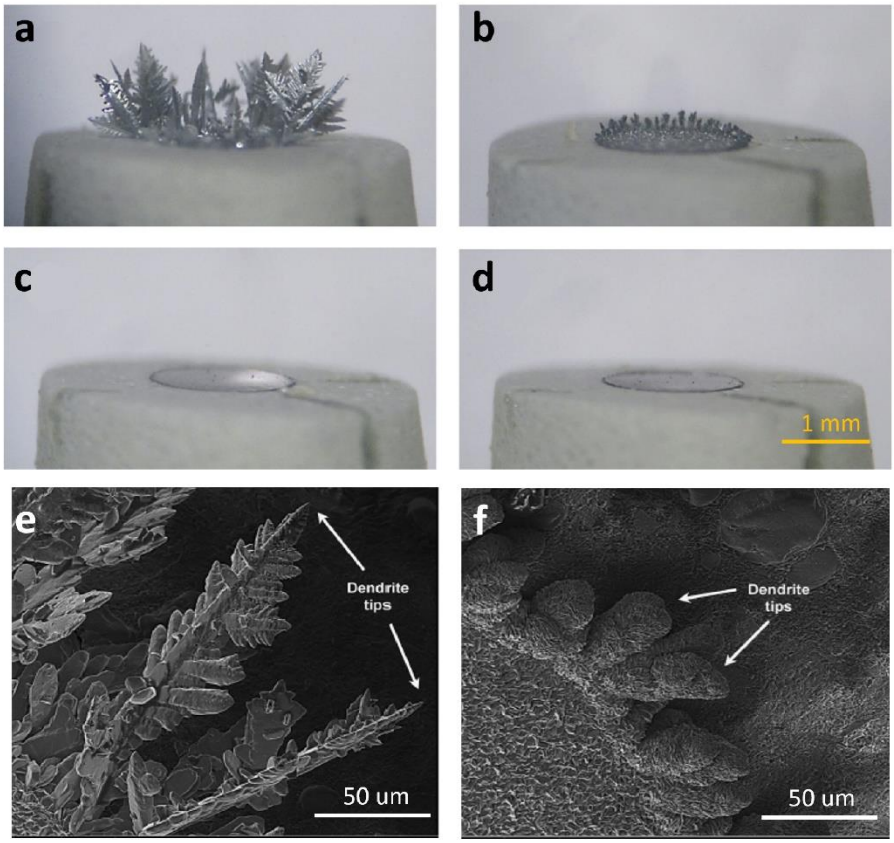

Figure 2.5 *In-situ* optical microscope images of Zn electrode after Zn deposition for 30 min. The electrolyte contains 0.1 M ZnO + 4.0 M KOH with various concentrations of PEI: (a) 0 ppm, (b) 10 ppm, (c) 50 ppm, and (d) 100 ppm. SEM images of Zn deposition morphology: (e) in the additive-free electrolyte, (f) in the electrolyte containing 10 ppm PEI additive. (Reprinted with permission from ref. 58. Copyright 2015, Elsevier).

Although the various electrolyte additives have been proposed to solve the Zn electrode issues to enhance the battery performance, one should be kept in mind that, similar to the electrode additives, the use of electrolyte additives may increase the cost of battery fabrication, reduce the initial content of Zn active material, and lower the specific or volume energy density of the battery. Thus, in order to optimize the battery performance to satisfy market demands, it is necessary to use a combination of different strategies to effectively mitigate any of these detrimental problems for Zn.

2.2.2.2 Gel electrolyte

As previously mentioned, the aqueous electrolyte features low cost, high ionic conductivity, and environmental benignity. Achieving high reversibility and long cycle life for the Zn electrode, however, still faces huge challenges in alkaline electrolyte due to the inevitable Zn corrosion and shape change as well as dendrite growth. Developing solid state electrolytes, without liquid solvents, provides a promising opportunity to address these Zn issues.[75] Furthermore, they also serve as not only electrolytes, but also separators in the battery, which contributes to the simplification of battery assembly. The reported solid state electrolytes mostly suffer, however, from low ionic conductivity and high interfacial resistance between the Zn electrode and the solid electrolyte, leading to poor reversibility and deterioration in the lifespan of the battery.[76] To this end, by combining the advantages of both the liquid and solid electrolytes, Zn–based gel polymer electrolytes have attracted increasing attention for the alkaline system.[54] Due to the workability of polymers, the gel polymer electrolytes can endow energy storage devices with adjustable shapes and high flexibility, which is promising for the burgeoning portable and wearable electronics market. In addition, the flexibility and elasticity of gel electrolyte also enable it to tolerate the volume changes and the dendrites of Zn metal during charge and discharge processes. Many studies on the polymer-based electrolytes in Zn–air batteries have been conducted, and electrolytes such as hydroponics gel[77], epichlorohydrin-ethylene oxide [P(ECHco-EO)][78], and polyvinyl alcohol-polyethylene oxide-glass-fibre-mat doped with KOH solution[79] have been used as the electrolyte component in a Zn–air battery.

The effects of the gel electrolyte on the Zn electrode have been investigated in a Zn–air battery,[80] in which the gel electrolyte was prepared by mixing hydroponics gel with a 6 M KOH aqueous solution. The surface of Zn metal was transformed to a rough surface

by the formation of white ZnO after the discharge. The shape of the circular Zn plate did not show any change after the discharge, suggesting that the gel electrolyte did not cause any change in the shape of the Zn electrode. Furthermore, the impacts of the gel electrolyte on the Zn dendrite growth were also studied in a Zn–air battery,[81] where the gel electrolyte comprises sodium polyacrylate (PANa) hydrogel (Figure 2.6a). As confirmed by the SEM and TEM images, the authors claimed that a quasi-solid-electrolyte interphase (SEI) layer is formed on the Zn electrode surface thanks to the electrostatic interaction between the negatively charged acrylate groups along the sodium polyacrylate hydrogel gel electrolyte chain and the positively charged Zn^{2+} ions. This homogeneous quasi-SEI layer facilitates the ion transport throughout the whole Zn electrode surface and prevents localized Zn metal nucleation and growth, thus further eliminating the Zn dendrite formation (Figure 2.6b). Nonetheless, most gel electrolytes still suffer from limited ionic conductivity and poor electrolyte retention, which impacts on the cycling stability of the battery. Very recently, a porous-structured poly(vinyl alcohol) (PVA)-based nanocomposite gel polymer electrolyte with silica (SiO_2) additive was synthesized in a bendable Zn–air battery (Figure 2.6c).[82] Due to the superior water retention of SiO_2 additive and its porous structure, this PVA-based gel electrolyte exhibited excellent water retention capability, high ionic conductivity (57.3 mS cm^{-1}), and improved mechanical properties, which enabled the battery to display an excellent cycle stability.

Although the interest in developing flexible Zn–based batteries has been increasing in recent years, further improvements in the ionic conductivity, interfacial properties, and mechanical robustness of gel polymer electrolytes are still highly desirable for wide-scale integration of high-performance rechargeable batteries.

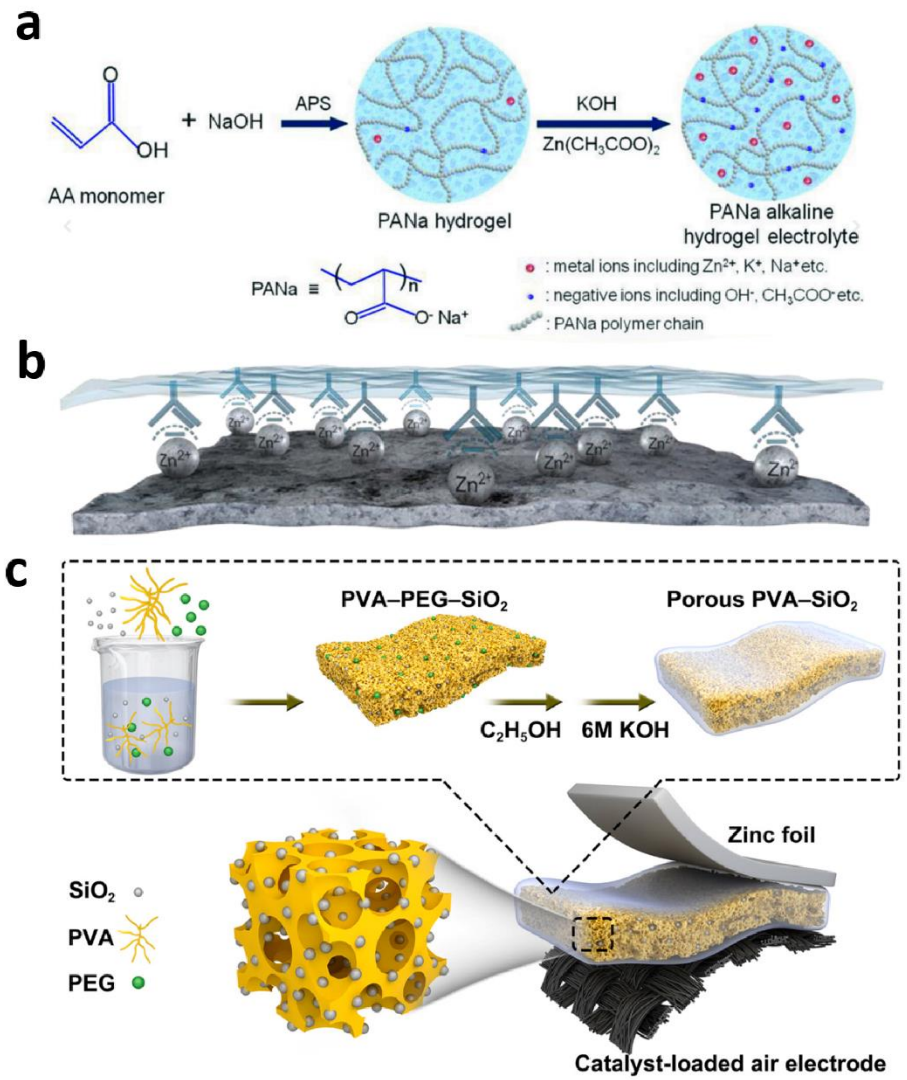

Figure 2.6 (a) Synthesis of the PANa gel electrolyte, which consists of acrylic acid (AA) monomer, NaOH, ammonium persulfate, $Zn(CH_3COO)_2$, and KOH (water and ion content regulator). (b) Schematic illustration of the quasi-SEI formation between Zn anode and PANa electrolyte. (Reprinted with permission from ref. 81. Copyright 2018, John Wiley and Sons). (c) Schematic illustration of the preparation process for the porous PVA-based gel electrolyte along with its inner structure for the Zn–air battery. (Reprinted with permission from ref. 82. Copyright 2019, Elsevier)

2.2.2.3 Flowing electrolyte

The electrolyte plays an essential role in alkaline Zn–based batteries by affecting the

transport properties of the active species between the Zn anode and the cathode. An enormous research effort has been made to enhance the battery performance by developing advanced electrolytes, since this approach is very simple, effective, and cost-efficient. Designing a flowing electrolyte is an effective approach for Zn–based batteries to extend their cycle life by minimizing dendritic growth, shape change, and passivation of the Zn electrodes.[83, 84] For the static Zn–air batteries, when the concentration of $Zn(OH)_4^{2-}$ is high or even saturated, the formation rate of ZnO increases sharply during the discharge process, easily leading to Zn passivation. In addition, the sluggish reaction kinetics of the O_2 reduction reaction on the cathode accompanied by the high species transport resistance has a great impact on the electrochemical performance of the Zn–air battery. For the flow system, however, the generated $Zn(OH)_4^{2-}$ ions could be brought to the outside of the battery by the flowing electrolyte, together with the ZnO product (if any). In this case, the Zn passivation could be effectively suppressed.[85] Moreover, the species transport is accelerated, which helps to reduce the concentration polarization. During the charge process, driven by the pump, the electrolyte containing $Zn(OH)_4^{2-}$ ions would be sent back to the battery to participate in the reaction. Unlike the situation in static Zn–air batteries where the formation of Zn dendrites may occur, the flow of the electrolyte could affect the morphology of the deposited Zn to inhibit dendrite formation.[86] Nevertheless, under prolonged charging, the Zn dendrite growth may still take place eventually and may not be completely suppressed by the flowing electrolyte, especially if high current densities and random cycling conditions are applied.

2.2.3 Separator

A separator is used in virtually all Zn–based batteries, where it acts as a physical barrier to keep the Zn electrode and the counter electrode physically apart, but allows the ions

to flow between both electrodes. In these systems with alkaline electrolytes, the separator should be easily wettable in aqueous media, stable in strong alkaline solution, electrochemically unreactive within a wide operating voltage window, and preferably relatively inexpensive. More importantly, it also should feature high ionic conductivity and low electrical resistance. Currently, polypropylene membranes, such as the Celgard films with porosity of 10–20 mm (e.g., Celgard 5550 and Celgard 4560) for commercial LIBs, are typically employed as separators in most studies of Zn–air batteries, resulting from their superior mechanical strength, which can retard Zn dendritic penetration, and their broad electrochemical stability window.[87] Nevertheless, their pore size is too large to limit the crossover of $Zn(OH)_4^{2-}$ ions, thus leading to increased polarization and decreased long-term durability of the battery. Therefore, selecting a suitable separator is of great importance for the successful operation of the Zn–based systems with alkaline electrolyte.[88] Ideally, an ideal separator should have a specific porous structure allowing smaller OH^- ions to pass while blocking the larger $Zn(OH)_4^{2-}$ ions, which could help to prevent common Zn problems. For instance, an ion selective cationic polysulfonium membrane was developed as a separator for Zn–air batteries.[89] This separator with high anion selectivity due to the high diffusion coefficient of the anion displayed a similar function to the anion-exchange coating layer discussed above. Under basic conditions, the self-discharging of the Zn electrode through the permeation of the $Zn(OH)_4^{2-}$ ions was effectively prevented by the polysulfonium separator, which enabled the battery to have an increased capacity almost six-fold higher than that of a battery using the commercial Celgard separator. In addition, this polysulfonium has a thickness almost 75% less than those of commercial separators, possibly helping to reduce the thickness and further enhance the volumetric energy density of the battery.

Other functional separators have also been developed to suppress the Zn dendrite

growth in alkaline systems. For example, a self-made, cost-effective polybenzimidazole (PBI) membrane (Figure 2.7a) was proposed to alter the morphology of Zn deposition.[90] In order to better understand the role of a PBI separator, the performance of a battery assembled with a Nafion 115 membrane was measured for comparison. The results showed that the battery assembled with a Nafion 115 membrane delivered a CE of 99.20% at 80 mA cm^{-2}, much lower than that (nearly 100%) delivered by the battery with a home-made PBI membrane. Furthermore, the PBI membrane could also deliver high OH^- ion conductivity (Figure 2.7b), which reduces the concentration polarization and suppresses the Zn dendrite growth. A similar separator was also studied in alkaline electrolyte to inhibit Zn dendrite formation and improve battery stability.[91] A 900 mm elastomer porous polyolefin membrane coated with a 4 mm carbon layer was employed (Figure 2.7c). The battery with this functional separator exhibited very stable performance without the formation of Zn dendrites even after hundreds of cycles. Benefiting from the porous structure of the membrane, which eliminates Zn dendrite formation, the battery can self-heal, even if micro-short circuiting occurs after overcharging (Figure 2.7d).

Even though the separator is of vital importance to enhance battery durability, investigations of the advanced separators still have not received their deserved attention compared research on other components, such as with electrode modification and electrolyte optimization. At present, only some functional membranes have been studied as high-performance separators in alkaline batteries and some promising results have been achieved. More attention should be attracted to developing advanced separators to solve the Zn electrode issues. One has to keep in mind, however, that the new functional separators would likely introduce higher costs for battery manufacturing, so it is necessary to find the right balance between achieving low cost and advanced

electrochemical performance.

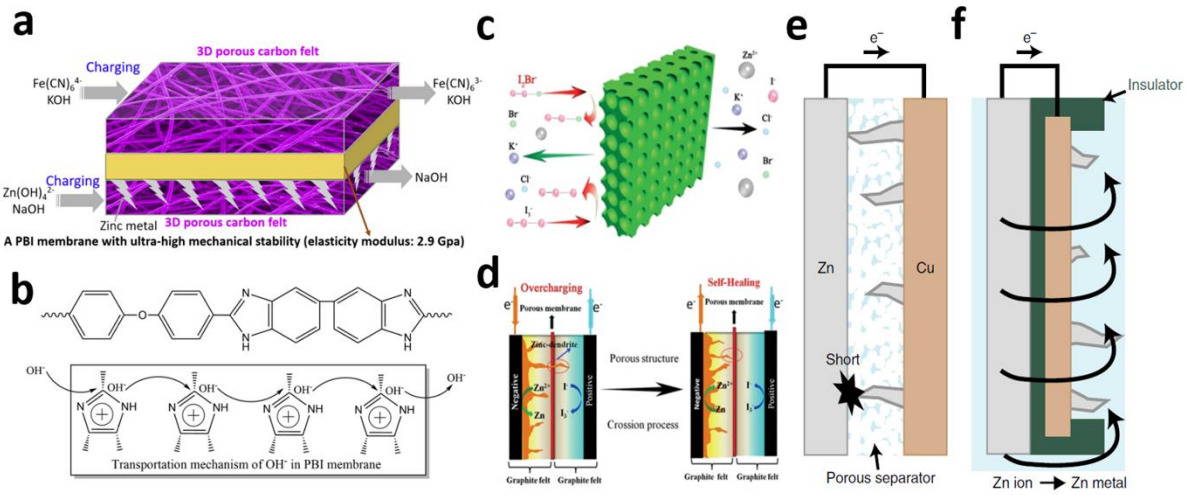

Figure 2.7 (a) Schematic diagram of charging behaviour of a PBI membrane with the ultra-high mechanical stability and a 3D porous carbon felt coating for the alkaline Zn battery. (b) The transportation mechanism of OH^- ions in a PBI membrane. (Reprinted with permission from ref. 90. Copyright 2018, Elsevier). (c) Operating principle of the porous polyolefin membrane for the alkaline Zn battery. (d) Schematic illustration of the self-healing process. (Reprinted with permission from ref. 91. Copyright 2018, John Wiley and Sons). (e) Schematic diagram of a cell with the conventional frontside-plating configuration. (f) Schematic representation of a cell with the backside-plating configuration for avoiding internal short circuits. (Reprinted with permission from ref. 96. Copyright 2016, Springer Nature)

2.2.4 Other methods

Besides the above methods, there are still some other types of methods that have been explored. One of them is modifying the charging current profile, which has received the increasing attentions in recent years. In the late 1980s and early 1990s, there were several studies on mitigating the shape change and dendrite growth of Zn electrodes by applying direct current (DC) pulses or alternating current (AC) charging protocols.[92]

The working mechanisms behind the DC or AC charging strategies for enhancing Zn performance have been summarized and discussed by Bennion.[93] Overall, these methods aim to introduce a relaxation time after a short $Zn(OH)_4^{2-}$ reduction period to re-establish the concentration of $Zn(OH)_4^{2-}$ at the surface of Zn electrode. By doing this, the neighboring sites do not compete for the limited amount of $Zn(OH)_4^{2-}$ under diffusional mass transport and hence enable homogeneous growth over the entire Zn electrode surface without dendrite formation. Recently, the influence of pulsed electroplating protocols on the formation of Zn dendrites was systematically studied by Grecia et al.[94]The study demonstrated that the introduction of a nucleation pulse appears to be more important than the length of the plating and resting pulses for achieving a high initial coverage of Zn nuclei. Furthermore, the combination of an optimal nucleation step and the pulsed DC charging protocol results in smooth Zn films and complete prevention of dendrites.

In addition to modifying the charging current profile, introducing a magnetic field also impacts on the Zn dendrite growth. According to Chiba et al,[95] the growth of Zn dendrites in alkaline electrolyte was inhibited by an external magnetic field to a remarkable extent at high KOH concentrations. There was only a weak dependence on the type of cathode metal and the direction of the lines of magnetic force. The inhibition effect was greatly promoted by magnetic flux densities above 0.11 T.

Recently, the concept of a backside metal plating technique to address the issue of Zn dendrite-induced shorting was proposed by Higashi et al.[96] Cu foil directly serves as the working electrode for Zn plating. In the conventional configuration, Zn plating with subsequent dendrite growth was performed on the “front” surface of the Cu substrate, causing battery shorting when the dendrites reached the counter electrode (Figure 2.7e). In this work, however, the edges and the front surface of the Cu foil facing the counter

electrode were coated by an insulating layer to prevent the Zn from plating on these sites (Figure 2.7f). In this case, the Zn cations in the electrolyte travel over the edge and front, and are deposited on the open back surface of the Cu foil. Thus, even if Zn dendrites form, they grow away from the counter electrode and do not short the battery. Therefore, this backside-plating configuration could enable long-term cycling of Zn metal batteries without short circuits. Nevertheless, this backside metal plating technique does not fundamentally solve the problem of Zn dendrite formation and growth in alkaline systems. Although no battery shorting occurs when using the strategy of Zn backside plating, the issues of poor Zn reversibility as well as low CE caused by the dendrite growth would decrease the capacity and cycling life of the battery.

2.2.5 Discussion

Overall, various effective strategies have been proposed to enhance the performance of alkaline Zn–based batteries by dealing with the Zn anode, which mainly include Zn electrode modification, electrolyte optimization, and separator selection as well as other methods, as summarized in Figure 2.8. These methods were only claimed, however, to mainly address the two or three issues of corrosion, H_2 evolution, shape change or dendrite growth, as discussed above. For example, the problems of Zn corrosion and H_2 evolution were effectively solved by adding Zn electrode additives, whereas the problems of Zn dendrite growth and Zn electrode passivation could still exist. Another example is the 3D Zn electrode design, which inhibits the dendrite formation and growth to some extent, but this design inevitably aggravates the Zn electrode corrosion due to the increase in the contact area of the Zn electrode with the electrolyte. Although it is a huge challenge to completely solve all the issues for Zn electrode through a single approach, engineering the electrode with a combination of different strategies might create a synergy in mitigating these detrimental problems for Zn, and lead to

competitive performance in terms of capacity, reversibility, and cycling stability for commercial success. In addition, the knowledge accumulated in the long history of research on Zn electrode in alkaline systems could provide guidance for the study of fresh Zn metal in the mild systems.

Figure 2.8 Summary of the strategies for addressing the problematic issues for Zn electrode in alkaline electrolyte.

2.3 Issues for Zn electrode in mild electrolyte

ZIBs with mild electrolytes have been the subject of aggressive research efforts in the past five years, with most of them spent on the exploration of cathode candidates as well as their Zn^{2+} storage mechanisms. In contrast, Zn metal anode has so far attracted much less attention than the cathode. This situation may be changed, since the Zn anode is also critical to achieve high performance ZIBs. Compared to the alkaline systems, the Zn electrode could minimize those issues to some extent in nearly neutral media, but it still suffers from low plating/stripping CE due to the Zn dendrite growth and side

reactions (including H_2 evolution and Zn electrode corrosion). Unlike the alkaline media, the main issues for Zn metal in mild electrolyte are Zn dendrite, H_2 evolution, and Zn metal corrosion (as shown in Table 2.1), which are analyzed in more detail as follows.

Table 2.1 Summary of the challenges of Zn in alkaline electrolyte and mild electrolyte.

Electrolyte	Dendrite	Shape change	Corrosion	H_2 evolution	Passivation
Alkaline electrolyte	√	√	√	√	√
Mild electrolyte	√		√	√	

2.3.1 Zn dendrite growth

Zn dendrite growth has been regarded as the main challenge for developing high-performance Zn electrodes in mild electrolyte, and accordingly, most research efforts on the optimization of Zn metal in mild electrolytes have been spent on suppressing Zn dendrite growth.[97] Similar to the alkaline systems, Zn dendrite formation in neutral electrolytes is also triggered by the concentration gradient of Zn^{2+} ions near the electrode surface. Concretely, the Zn electrode normally features an uneven surface morphology, which leads to the inhomogeneous distribution of Zn^{2+} ions. During the plating process, the Zn^{2+} ions near the surface of Zn electrode are initially reduced to metallic Zn, resulting in striking Zn^{2+} concentration polarization in the electrolyte. Furthermore, the protrusions on the Zn electrode surface have higher curvature than other places, leading to a considerably higher electric field at the tips. As a result, more Zn^{2+} ions are accumulated on the tips, leading to further growth of the protrusions by forming Zn nuclei, which eventually evolve into Zn dendrites during long-term cycling.

Based on its formation mechanism described above, Zn dendrite growth is a complex process and would be affected by numerous factors, such as, over-potential (η), Zn^{2+} concentration, temperature, the surface roughness of Zn electrode, the pH value, *etc*. These parameters are discussed in detail as follows, which might be beneficial for the design of controllable strategies to diminish or avoid Zn dendrite growth. It is well known that a higher over-potential tends to augment the Zn^{2+} concentration polarization and aggravate inhomogeneous Zn deposition, resulting in serious Zn dendrite growth. In addition, the concentration of Zn^{2+} ions in the bulk electrolyte is another important factor for Zn dendrite growth. According to Pavlovic et al.[98], the minimum over-potential (η_i) that induces the dendritic growth can be expressed as:

$$\eta_i = \eta_0 \ln k \frac{\eta_L}{\eta_0}, \qquad (6)$$

in which $k \geq 1$ and the value of η_i only depends on the η_L/η_0 ratio. It is well known that, in general, under the same hydrodynamic regime, $\eta_L \propto C_0$ (where C_0 is the bulk concentration of Zn^{2+}), and $\eta_0 \propto C_0^n$ (where $0 < n < 1$). Therefore, η_i has a positive dependence on C_0. In other words, a higher bulk concentration of Zn^{2+} has a positive impact on the Zn dendrite growth, which also has been proved by the experimental results. Recently, different high concentration electrolytes have been studied, where the CE of Zn electrode was effectively enhanced by suppressing the dendrite growth.

The operating temperature also affects the morphology of Zn deposition.[99] A higher working temperature facilitates rapid Zn^{2+} diffusion in the electrolyte, thus inducing a reduced Zn^{2+} concentration polarization near the Zn electrode surface, which mitigates the Zn dendrite formation. Furthermore, the surface roughness of Zn electrode has a severe impact on the formation of nuclei in Zn plating.[99, 100] In the case of a rough Zn electrode, more protrusions exist on its uneven surface. During Zn plating, a mass of

Zn^{2+} ions would likely be attracted near to these protrusions. When the reduction of Zn^{2+} is conducted, plenty of nuclei would be formed on the protrusions and ultimately be converted into Zn dendrites. Thus, a rough surface on the Zn electrode is more likely to trigger dendrite formation and growth. In addition to the factors summarized above, the pH value in the mild electrolyte was also found to influence the formation and growth of Zn dendrites.[101] The relevant investigation was conducted in $ZnSO_4$ solution by adding H_2SO_4 to vary the pH value. At low pH, the Zn plating is more homogeneous with a morphology that reflects the hexagonal structure of the metallic Zn. In contrast, Zn dendrites are easily formed from the inclined crystals (pyramidal) at high pH values.

2.3.2 H_2 evolution

Side reactions between the Zn electrode and mild electrolytes have seriously hindered the practical application of ZIBs, because they not only constantly consume the Zn electrode and electrolyte, leading to a limited shelf life of the battery, but also produce H_2 gas, resulting in poor CE and internal swelling of the battery. Compared to the Zn dendrite research, study of this topic is still in its infancy. Only a few works have been conducted to understand these side reactions of Zn electrode with mild electrolytes.

The H_2 evolution reaction is a crucial part of the side reactions in sealed systems with mild electrolyte. On the one hand, it reduces the reversibility of Zn electrode and results in poor CE and shortened cycling life. On the other hand, the generated H_2 gas in the sealed batteries severely increases the internal pressure, easily leading to battery swelling or even battery explosion.[102] Based on the Pourbaix diagram for water, the H_2 evolution potential in neutral electrolyte is about –0.41 V *vs.* SHE ($E_{H_2} = 0.059 \times \text{pH}$), higher than the standard reduction potential of Zn/Zn^{2+} (–0.76 V *vs.* SHE), indicating that the H_2 evolution is thermodynamically preferred in mild electrolyte (similar to the alkaline system).[103] As discussed above, however, Zn metal features a high H_2 evolution

over-potential according to the Tafel equation, theoretically inhibiting the H_2 evolution reaction, as confirmed by the Pourbaix diagram for Zn in aqueous solution. The actual H_2 evolution reaction in ZIBs is a complicated process, however, affected by many factors, such as the roughness of the Zn electrode surface, electrolyte concentration, operating temperature, *etc*. To detect H_2 evolution in ZIBs *in-situ*, differential electrochemical mass spectrometry (DEMS) was employed.[104] It is worth noting that the chemical H_2 evolution spontaneously occurs once the metallic Zn is in contact with mild aqueous electrolyte, indicating that the H_2 evolution occurs during battery rest (Figure 2.9a). The amount of H_2 gas generated during battery rest was investigated using a Zn symmetric cell with a pouch cell configuration,[105] indicating that ~6.7 mL of H_2 gas was produced with the Zn metal size of 4×4 cm^2 after a dwell time of 4 weeks. Accordingly, ~19.8 μL of aqueous electrolyte was consumed and ~15.9 mA h of active Zn metal was oxidized/deactivated (Figure 2.9b). As a result, the battery performance would be degraded, or even fail, after a long rest time. The main reason for H_2 evolution during battery rest has been thoroughly discussed in the following section (*5.3 Zn metal corrosion)*. In addition, the H_2 evolution during the Zn plating was also observed by *in-situ* optical microscopy in a home-made cell, suggesting that Zn deposition is ineluctably impacted by the competitive H_2 evolution (Figure 2.9c), which seriously reduces the CE of Zn stripping and plating. In summary, the H_2 evolution in mild ZIBs probably occurs in different battery states, during both battery rest and battery cycling.

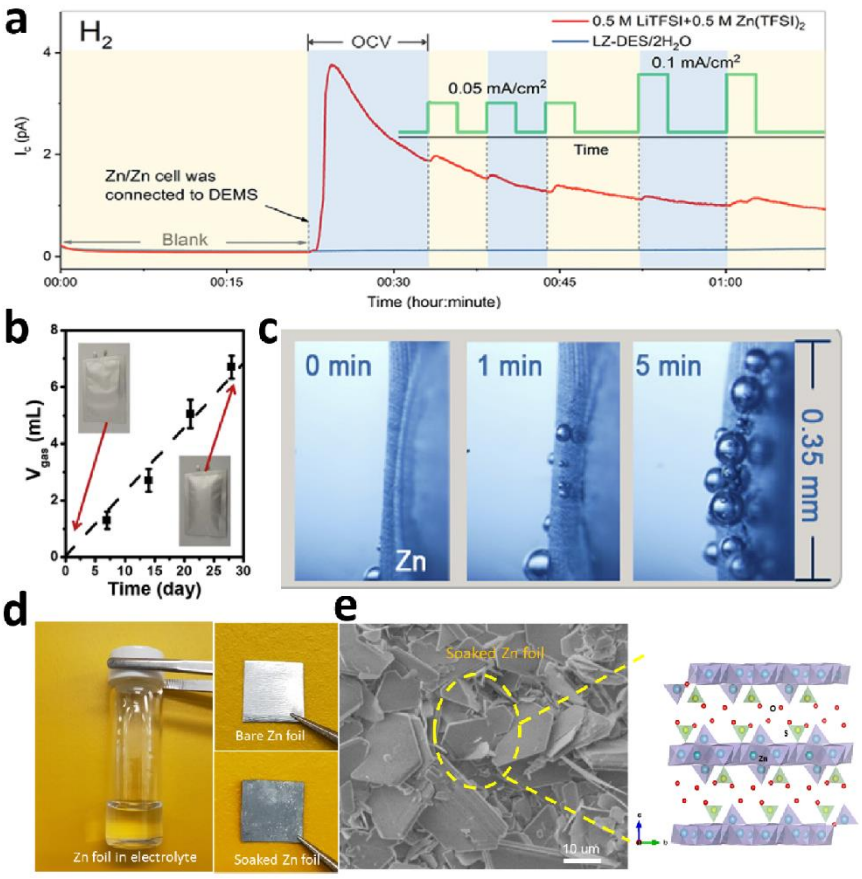

Figure 2.9 (a) DEMS tests on the symmetrical Zn cells to monitor the electrochemical H_2 evolution. (Reprinted with permission from ref. 104. Copyright 2019, Elsevier) (b) H_2 gas evolution accompanied by the chemical corrosion of Zn electrode in 3 M $ZnSO_4$ electrolyte (Reprinted with permission from ref. 105. Copyright 2020, Elsevier). (c) *In-situ* optical microscope images of H_2 gas evolution during the Zn electrodeposition process at 0.2 mA cm^{-2}. (d) Zn foil soaked in 1 M $ZnSO_4$ electrolyte and photographic comparison of Zn foil before/after soaking in electrolyte for 7 days. (e) SEM image of $Zn_4SO_4(OH)_6{\cdot}xH_2O$ by-product on Zn foil and its crystal structure. (Reprinted with permission from ref. 112. Copyright 2020, John Wiley and Sons).

2.3.3 Zn metal corrosion

It should be noted that the H_2 evolution during battery rest was simultaneously accompanied by electrochemical corrosion of the Zn metal. The corrosion of the Zn

metal electrode continually destroys the electrode surface and consumes the Zn electrode after soaking in mild electrolyte (Figure 2.9d), causing enhanced interphase resistance and limited cycle life.[102, 106] Less attention has been spent, however, on thoroughly understanding the fundamental Zn corrosion mechanisms in ZIBs. To the best of our knowledge, Zn metal is thermodynamically unstable in mild electrolyte, especially when the Zn metal contains some impurities. The Zn metal corrosion is mainly attributed to the electrochemical corrosion by the H_2 evolution because of the limited O_2 content in the sealed ZIBs, which is likely to differ from the situation in the Zn–air battery with an open working system. To be specific, numerous microscale primary batteries would be formed in a single Zn electrode when it contacts with the electrolyte, in which the metallic Zn works as anode and the impurities (mainly carbon) work as cathode. The electrochemical corrosion reaction could be expressed as:

Cathode: $2H_2O + 2e^- \leftrightarrow H_2 \uparrow + 2OH^-$ (7)

Anode: Zn $\leftrightarrow Zn^{2+} + 2e^-$ (8)

Thus, H_2 evolution corrosion involves in the Zn corrosion in ZIBs, which leads to local pH fluctuations due to the enhancement of the OH^- concentration. Insoluble by-products will be generated on the surface of the Zn electrode as the local OH^- concentration increases. Currently, the by-products formed during Zn corrosion in the mild system are still inconclusive. On the one hand, $Zn(OH)_2$ and ZnO were claimed to be the by-products generated during the Zn corrosion due to increases in the local OH^- concentration.[107, 108] On the other hand, some new reports gave that the zinc salt would be involved in the Zn corrosion reaction by generating Zn-based basic salts.[109-111] According to our recent studies, a hexagonal $Zn_4SO_4(OH)_6{\cdot}xH_2O$ by-product layer is generated on the Zn metal surface without obvious ZnO or $Zn(OH)_2$ in the 1 M $ZnSO_4$ electrolyte (Figure 2.9e),[112, 113] which can be expressed as follows.

$$4Zn^{2+} + 6OH^- + SO_4^{2-} + xH_2O \leftrightarrow Zn_4SO_4(OH)_6 \cdot xH_2O \qquad (9)$$

Unlike the tight SEI layer on Li metal, this interphase layer on Zn metal is loose and cannot effectively block the electrolyte from reaching the fresh Zn surface (Figure 2.9e), so it cannot terminate the corrosion reactions by passivating the Zn electrode.[105, 114, 115] The unceasing reaction between the electrolyte and Zn metal severely decreases the performance of Zn batteries. Similarly, a loose by-product layer due to Zn corrosion was also found in other mild electrolytes after reaction with zinc salts. In the case of $Zn(TFSI)_2$ electrolyte, $TFSI^-$ ions were involved in the Zn corrosion, leading to a loose by-product of TFSI-based complexes.[104] Similar to the $Zn_4SO_4(OH)_6{\cdot}xH_2O$ by-product layer, this loose layer of TFSI-based complexes cannot stop the Zn corrosion by blocking the electrolyte either, which makes Zn corrosion a huge issue for the real application of ZIBs. The Zn anode will react with $ZnSO_4$ or $Zn(TFSI)_2$ electrolyte during both transport and shelf time after the battery assembly but before customer use. Hence, deeply understanding the mechanisms as well as solving the Zn corrosion problem may be the first step towards achieving the goal of the industrial application of ZIBs.

2.4 Strategies in mild electrolyte

2.4.1 Electrolyte optimization

As a component in direct contact with the Zn anode and controlling the plating/stripping process of Zn, the electrolyte plays a vital role in the electrochemical reversibility and stability of Zn metal anode in the mild system. Similar to the alkaline system, great efforts have been spent on optimizing the mild electrolyte to further enhance the battery performance by solving the Zn metal issues. Current methods of electrolyte optimization mainly include electrolyte additives, developing different electrolyte salts, and designing super-concentrated electrolytes and hydrogel electrolytes.

2.4.1.1 Electrolyte additives

Introducing some additives into electrolytes can regulate the local current distribution, guide uniform Zn deposition, and suppress dendrite growth.[116] Similar to the alkaline electrolytes, the additives applied in a mild aqueous electrolyte can also be classified into organic additives and inorganic additives. The effects of a variety of organic additives on the Zn deposition behaviour, such as polymers, organic molecules, and surfactants, have been thoroughly investigated. The surface texture and crystallographic orientation of the deposited Zn can be manipulated by using different additives, including sodium dodecyl sulfate (SDS), thiourea (TU), cetyltrimethylammonium bromide (CTAB), and polyethylene-glycol (PEG-8000).[117] The prepared Zn anode with these additives exhibits a 6-30 times lower corrosion rate than that of commercial Zn electrode (Figure 2.10a), and the float current in hybrid aqueous batteries assembled from Zn−SDS anode is weakened by as much as 2.5 times. Moreover, the dominant Zn (002) and (103) surface facets of Zn that have been electroplated with SDS and PEG are more likely to restrain dendrite formation compared with the (100) and (110) planes. The tip effect during Zn deposition process is the main dendrite growth mechanism, where the higher electric field strength at the tips attracts more Zn^{2+} ion deposition. This effect can be impaired through the adsorption of some highly polarized organic molecules on the tips. Diethyl ether (Et_2O), a highly polarized organic additive, is prone to adsorb on the high-potential surfaces of Zn tips and obstruct further Zn deposition on the tips, thus reducing the dendrite growth rate and significantly improving the battery performance.[118] It is worth noting that the concentration of organic additives in electrolytes is a significant parameter. Chen et al. has proved that the corrosion current density decreases with an increase in the PEG-200 concentration from 0.1 to 1 vol.%.[119] A further increase of the PEG-200 concentration up to 2 vol.%, however, leads to

excessive surface polarization on the Zn anode, and consequently, the corrosion current density shows a remarkable enhancement. On the other hand, excessive organic additives in the electrolyte would induce large electrode polarization and impede the diffusion kinetics and reduction rate of Zn^{2+}, limiting the high-rate performance of ZIBs. In addition to organic additives, inorganic additives in electrolyte have also been shown to generate distinct crystallographic orientations and morphology. The use of indium sulfate, tin oxide, or boric acid for Zn deposition, in each case, presents an 11 times smaller corrosion current for the electroplated Zn than for the commercial Zn. In particular, the Zn deposited with the aid of boric acid changes the preferred Zn orientation to the (002) plane to constrain the formation of dendrites.[120] Based on the electrostatic shield machanism, the addition of low-cost $NaSO_4$ electrolyte additive has been proved to produce uniform Zn deposition, because the reduction potential of Na^+ is lower than that of Zn^{2+}.[121]

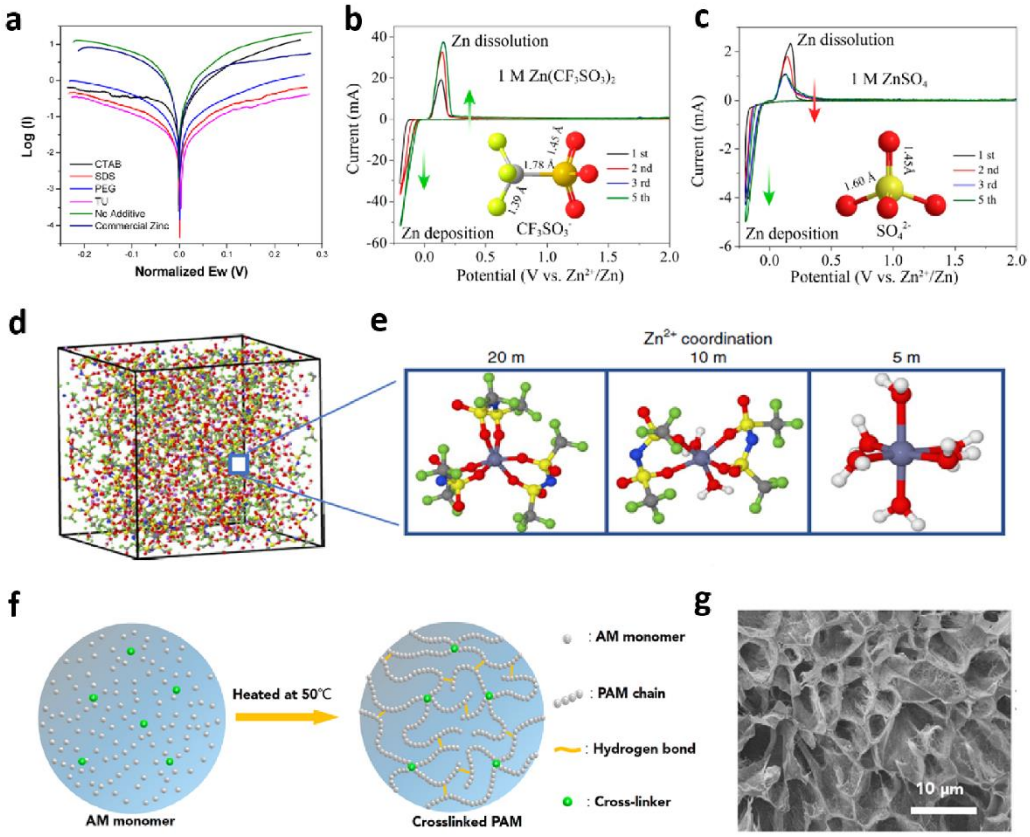

Figure 2.10 (a) Linear polarization curves of the synthesized zinc with and without organic additives and commercial zinc foil when in contact with the battery's electrolyte. (Reprinted with permission from ref. 117. Copyright 2017, American Chemical Society) Cyclic voltammograms of Zn electrode in aqueous electrolyte containing (b) 1 M $Zn(CF_3SO_3)_2$ and (c) 1 M $ZnSO_4$ at the scan rate of 0.5 mV s^{-1} between –0.2 and 2.0 V. (Reprinted with permission from ref. 69. Copyright 2016, American Chemical Society) (d) Snapshot of the molecular dynamics (MD) simulation cell for highly-concentrated electrolyte (HCZE) (1 m $Zn(TFSI)_2$ + 20 m LiTFSI) at 363 K. (e) Representative Zn^{2+}-solvation structures in the electrolytes with 1 m $Zn(TFSI)_2$ and three concentrations of LiTFSI (5 m, 10 m and 20 m). (Reprinted with permission from ref. 54. Copyright 2018, Springer Nature) (f) Schematic diagram for the fabrication of the cross-linked polyacrylamide (PAM)-based electrolyte. (g) SEM image of the free-standing PAM. (Reprinted with permission from ref. 146. Copyright 2018, American Chemical Society)

2.4.1.2 Electrolyte salts

The electrochemical performance of Zn electrode strongly depends on the species of salt in the electrolyte. In mild ZIB systems, the choice of electrolyte salts has a direct influence on the pH, ionic conductivity, and (electro-)chemical stability of the electrolyte, as well as the reaction kinetics and reversibility of the Zn anode.[122] Therefore, manipulating the electrolyte salt chemistry, especially the anion chemistry, is a effective way to address the issues of inferior stability and reversibility of the Zn anode. To date, various electrolyte salts have been systematic investigated, such as $ZnSO_4$, $ZnCl_2$, $ZnNO_3$, ZnF_2, $Zn(CH_3COO)_2$, $Zn(TFSI)_2$, and $Zn(CF_3SO_3)_2$, which show different electrochemical properties in mild ZIBs.[9]

At the early stage of using mild aqueous electrolytes, $Zn(NO_3)_2$ and $Zn(ClO_4)_2$ were introduced into the electrolyte, which led to serious corrosion and degradation of the Zn anode, due to the strong oxidizing property of NO_3^- and ClO_4^- anions.[123] Compared with these oxidative salts, the electrolytes containing ZnF_2 and $ZnCl_2$ showed satisfactory compatibility with Zn anode and could alleviate side reactions.[124] The low solubility of ZnF_2 (~88 mmol in water) and the narrow anodic potential window (~0.75 V) of dilute $ZnCl_2$, however, limit their application in high-performance ZIBs. In contrast, $ZnSO_4$ and $Zn(CF_3SO_3)_2$ electrolytes have been widely used for ZIBs recently, because of their good compatibility, excellent stability and wide electrochemical windows.[24, 63] The price of $ZnSO_4$ is much cheaper than that of the latter, which improves the feasibility of $ZnSO_4$ electrolyte for practical application. As mentioned above, however, the formation of the $Zn_4(OH)_6SO_4{\cdot}xH_2O$ by-product reduces the utilization of Zn^{2+} in $ZnSO_4$ electrolyte. Similarly, in the $Zn(CF_3SO_3)_2$ electrolyte, the formation of zincate by-product, $Zn(CF_3SO_3)_a(OH)_b{\cdot}xH_2O$, after long-term cycling, has also been proved recently, due to the competitive parasitic reaction of H_2 evolution.[125]

In addition, as shown in Figure 2.10b, $Zn(CF_3SO_3)_2$ electrolyte has a much smaller potential separation between Zn deposition and dissolution, and a higher current response than those in $ZnSO_4$ (Figure 2.10c), indicating faster reaction kinetics and better reversibility of the Zn plating/stripping. The bulky $CF_3SO_3^-$ anions can moderate the solvation effect and facilitate Zn^{2+} migration by reducing the number of H_2O molecules surrounding a Zn^{2+} ion. As a result, the CE of Zn plating/stripping in $Zn(CF_3SO_3)_2$ electrolyte reaches as high as 100% after the initial cycles. $Zn(TFSI)_2$, another Zn salt with bulky anions, has also been developed in mild ZIBs, which relieves the solvation effect and enables high reversibility of the Zn, which is attributed to a similar mechanism to that in $Zn(CF_3SO_3)_2$.[126] In consideration of the high price of bulky anion salts, more attention should be paid to exploring low-cost and compatible electrolyte salts for the development of ZIBs as they approach the requirements for grid-scale energy storage.

2.4.1.3 Super-concentrated electrolyte

The low cycling reversibility of Zn anode is closely related to the solvation-sheath structure of Zn^{2+} ions. In mild electrolyte, Zn^{2+} interacts strongly with water molecules to form hydrated Zn^{2+}, which leads to a high energy barrier for desolvation of hydrated Zn^{2+} during Zn plating.[127] Increasing the salt concentration of electrolyte is an essential way to alleviate the solvation effect by reducing the number of H_2O molecules around Zn^{2+}. In addition, the primary reason behind the side reactions at the Zn anode is the presence of free water molecules in electrolyte. As discussed above, the decomposition of water molecules during the Zn plating process is an inevitable parasitic reaction, and the generated H_2 and OH^- would bring safety risks and induce an electrochemically inactive by-product layer, respectively. In this case, the concept of “water-in-salt” or super-concentrated electrolyte has been introduced into mild ZIBs to improve the CE

and the utilization of Zn anode, following similar developments in the field of LIBs.[128, 129]

The breakthrough on super-concentrated electrolyte for mild ZIBs was first achieved in an electrolyte consisting of 1 m $Zn(TFSI)_2$ and 20 m LiTFSI.[54] Molecular dynamics (MD) studies have proved that such a highly concentrated electrolyte can change the solvation sheath structure of Zn^{2+}, as shown in Figure 2.10d. Zn^{2+} is coordinated with six water molecules and has no interaction with $TFSI^-$ in the dilute electrolyte with only 5 m LiTFSI. With increasing LiTFSI concentration, the solvation sheath contributes more from $TFSI^-$ ions, which occupy the whole solvation sheath structure of Zn^{2+} in the electrolyte with 20 m LiTFSI (Figure 2.10e). The unique solvation structure, where Zn^{2+} interacts with $TFSI^-$ instead of H_2O effectively avoids water-induced side reactions and ensures a dendrite-free Zn anode with nearly 100% plating/stripping CE. Benefiting from these properties, the highly concentrated electrolyte (pH ≈ 7) results in excellent cycling performance in different battery systems, which has accelerated the development of mild ZIBs for commercial applications. Moreover, a "water-in-salt" electrolyte with 30 m $ZnCl_2$ has been investigated for mild ZIBs, due to the intrinsically high solubility of $ZnCl_2$.[129] The highly concentrated $ZnCl_2$ electrolyte gives rise to a stable Zn anode with an average CE as high as 95.4%, as well as improved capacity retention with the existence of $[ZnCl_4]_2^-$.[130, 131]

Although the high concentration of electrolyte effectively improves the reversibility of Zn electrode by reducing the free water, it would inevitably raise the cost and viscosity of the electrolyte and reduce the ionic conductivity, so it is suggested that a balance must be found between the salt concentration, manufacturing cost, and battery performance. In addition, the number of super-concentrated electrolyte systems is restricted by the relatively low solubility of most salts. To expand the possible selection,

the introduction of inert anions/cations or other possible salt mixtures into electrolytes for mild ZIBs may offer a promising way to improve the salt concentration, as investigated in other aqueous battery systems.[132, 133]

2.4.1.4 Gel electrolyte

Although neutral electrolytes are widely used due to their high ionic conductivity, low cost, and mild nature, the problematic issues for Zn metal electrode, including Zn dendrites, H_2 evolution, and Zn electrode corrosion cannot be completely eliminated in ZIBs. Moreover, the problems also exist of possible leakage of electrolyte and undesireable dislocation under strain of ZIBs with aqueous electrolytes.[134, 135] To aviod these issues, different gel electrolytes have been employed, which were created by adding some hydrophilic polymers or inorganic components into the aqueous solutions of Zn salts.[110] The gel electrolytes may solve the intrinsic problems of ZIBs arising from mild electrolytes, because they stabilize the electrolyte/electrode interface with less active water, minimize water-induced side reactions, and inhibit dendrite growth.[136] In addition, the gel electrolytes feature desirable electrochemical properties and excellent mechanical integrity for flexible ZIBs, which have shown great potential for application in portable and wearable electronics.[137, 138]

Gel electrolytes with chemical cross-linking possess better thermal stability and mechanical properties compared with those electrolytes without cross-linking and with only physical cross-linking.[139] As one of the most promising electrolytes, polyacrylamide (PAM)-based electrolyte contains strong covalent cross-links and hydrogen bonds among the chain segments, as shown in Figure 2.10f, where hydrophilic groups such as $–CONH_2$ can trap water molecules through hydrogen bonds. Freeze-dried PAM presents a highly porous framework structure, as shown in Figure 2.10g, which is favourable for the solution diffusion and fast transport of Zn^{2+}.[140]

Therefore, the PAM-based gel electrolyte with neutral solution of $ZnSO_4$ and $MnSO_4$ rendered a tensile strength as high as 273 kPa, an ability to withstand stretching strain of 3000%, and high Zn^{2+} conductivity (17.3 mS cm^{-1}). To further improve the electrochemical performance of gel electrolytes, some functional groups could be modified by polymer additives. For instance, nanofibrillated cellulose (NFC), a typical reinforcing agent, has been introduced into PAM-based gel electrolyte, which involves abundant hydroxyl groups and could stabilize the channels for ionic transportation and enhance the water contention. The designed NFC/PAM gel possessed a high ionic conductivity of 22.8 mS cm^{-1}, high stretchability, so as to tolerate 1400% strain, and high adhesion for Zn–MnO_2 batteries.[141] In addition, a hierarchical 3D architecture of gelatin and PAM-based electrolyte showed significantly enhanced the mechanical strength, flexibility, and ionic conductivity. More importantly, the ZIBs with the hierarchical electrolyte demonstrated outstanding electrochemical performance even under various severe conditions, such as being greatly cut, bent, hammered, punctured, sewed, washed in water, or even put on fire.[142]

Similar to the alkaline system, the gel electrolyte in the mild system significantly increases the reversibility of Zn metal electrode by suppressing the Zn dendrite growth as well as the water-induced Zn electrode corrosion and H_2 evolution. One of the main challenges for gel electrolyte, however, is its relatively low Zn^{2+} conductivity, since enhancement of the mechanical capacity of gel electrolyte always sacrifices ionic conductivity, resulting in a inferior rate performance and an unsatisfactory power density. In addition, similar to conventional aqueous electrolytes, the operating potential for gel electrolytes is also limited by a narrow electrochemically stable window. Thus, the selection of a polymer component with novel functional groups and Zn salts with high compatibility could be further studied for gel electrolytes, as well as

the development of flexible and wearable ZIBs.

2.4.2 Artificial SEI layer

Motivated by the quest to suppress Li dendrite growth *via* membranes or interfacial engineering, constructing stable artificial SEI layers on Zn anode in mild electrolyte serves to prevent direct contact between the Zn metal and the electrolyte, constraining the growth of dendrites and alleviating side reactions.[143] Generally, an effective SEI layer as such a coating should not only feature fine (electro-)chemical compatibility with Zn metal and aqueous electrolytes and sufficiently good mechanical properties to inhibit dendrite growth, but also realize fast Zn^{2+} diffusion at the interface. According to the different protective mechanisms, artificial SEI-coating strategies on Zn anode include carbon-based coatings, inorganic passivation layers, and polymer membranes.[144]

Carbon-based materials, such as reduced graphene oxide (rGO) and carbon nanotube, have been employed as protective layers on the surface of Zn metal anode, which provide a flexible matrix to reduce the volume changes during Zn plating/stripping and a large specific surface area to regulate uniform Zn deposition.[145, 146] Due to its large electroactive area and even surface current distribution, a layer-by-layer rGO film on Zn foil could significantly mitigate Zn dendritic growth and demonstrated superior cycling reversibility.[147] Additionally, an inorganic passivation layer with high porosity could usually act as a buffer layer to guide a homogeneous electrolyte flux as well as accelerating the kinetics of Zn diffusion and deposition.[148] Notably, density functional theory (DFT) calculations of the 3D nanoporous ZnO layer have proven that the geometrically optimized oxygen element facilitates extra charge density distribution on the surface (Figure 2.11a), and the Zn^{2+} insertion energy barrier for Zn with the ZnO coating layer is eight times lower than that for bare Zn.[149] As a consequence, the ZnO

layer contributes to electrostatic attraction towards Zn^{2+} rather than the solvated Zn^{2+} in the compact layer of the electric double layers, and thus ensures faster kinetics of Zn^{2+} deposition and effectively prevents the H_2 evolution, as illustrated in Figure 2.11b. This new class of Zn anode modified with 3D nanoporous ZnO exhibited 99.55% Zn utilization and long-term cycling stability. In addition, the atomic layer deposition of the TiO_2 coating and the ZrO_2 protection layer was intended to achieve uniform Zn plating and suppression of Zn dendrites through controlling nucleation sites and enhancing Zn^{2+} transportation.[150, 151] Moreover, a polymer membrane coating is also an attractive and rational alternative, given its inherent water/O_2 resistant capabilities, decent flexibility, and high viscoelasticity.[152] With intrinsic amide groups to coordinate with Zn^{2+}, polyamide (PA) has been designed as a interfacial layer to refine the nucleation grains through overcoming the nucleation barrier and restricting the two-dimensional (2D) diffusion of Zn^{2+}, leading to a dense and dendrite-free Zn anode.[102] As shown in Figure 2.11c, some obvious protuberances of deposited Zn appears from 15 minutes on bare Zn plate in the *in-situ* optical microscope image, and the coated Zn shows a dense and smooth morphology during the whole deposition process (Figure 2.11d). Benefiting from the regulated Zn deposition behaviour and suppressed corrosion in the PA-modified Zn anode, the cycling performance of the Zn–MnO_2 battery was remarkably improved from 450 cycles with a low capacity of 30 mA h g^{-1} to 1000 cycles with a high capacity of 155.4 mA h g^{-1}. Most recently, a coating layer of metal-organic frameworks (MOFs) has offered a super-saturated front surface and realized ultralong lifespan for Zn electrodes, through blocking large-size solvated ion-complexes in the MOF channels.

As discussed in relation to the alkaline system, it has a working mechanism that is different from the artificial SEI layer built on the Zn metal in the mild system. Because

of their ability to block the electrolyte from reaching the Zn electrode and to provide high conductivity of Zn^{2+}, various artificial SEI layers have been applied to restrain Zn dendrites, restrain gas evolution and its by-products, and eventually improve the lifespan of ZIBs. Given the complex synthesis and limited scalability, however, few methods are consistent with the original nature of ZIBs, including low cost, interior safety, and large-scale application prospects. Namely, the evaluation criteria for interfacial engineering of Zn electrode should rely more on practical applications. Compared with artificial interface protection, reports on *in-situ* SEI engineering in ZIBs are almost non-existent, but it deserves more attention.

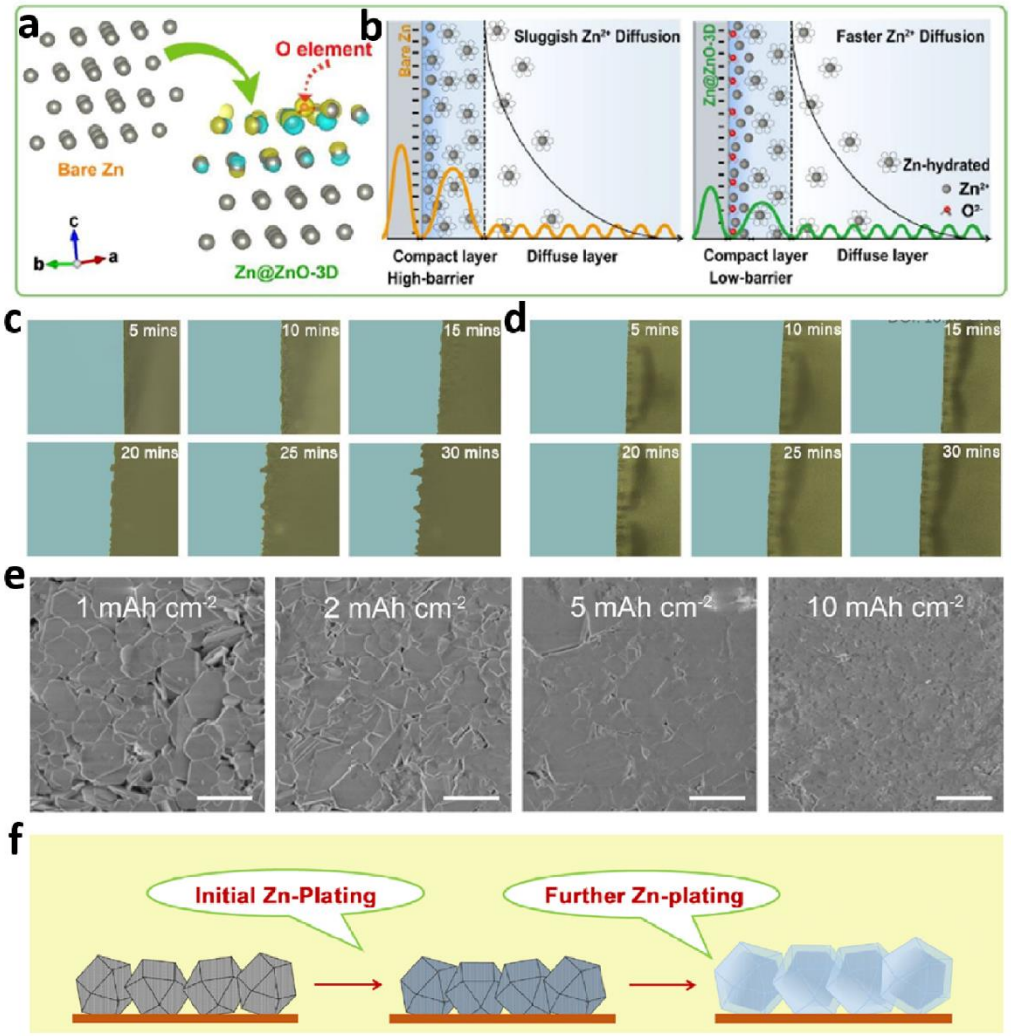

Figure 2.11 (a) Differential charge density distribution of Zn@ZnO-3D from first-principles calculations. (b) Electric double layer structure in the vicinity of the anode and the corresponding energy barriers. (Reprinted with permission from ref. 149. Copyright 2020, Royal Society of Chemistry) *In-situ* optical microscope images of cross-sectional Zn deposition morphology on (c) bare Zn plate and (d) PA-coated Zn plate in a symmetrical Zn cell at a current density of 10 mA cm^{-2}. (Reprinted with permission from ref. 102. Copyright 2019, Royal Society of Chemistry) (e) SEM images of Zn deposits on ZIF-8-500 electrode at a current density of 1.0 mA cm^{-2} for different capacities. Scale bars, 2 mm. (f) Schematic illustration of the Zn plating. (Reprinted with permission from ref. 157. Copyright 2019, Elsevier.)

2.4.3 Modification of current collectors

Although commercial Zn foil with excess Zn has been widely adopted as anode and directly adopted as current collector in most ZIBs, some deposited Zn electrodes have been reported in certain mild ZIBs. The selection of the current collector is of great significance for the deposited Zn electrode, given the importance of gravimetric energy density in practical application of ZIBs. Carbon-based, copper-based, and MOF-based current collectors have been widely used to support Zn, due to their great chemical and electrochemical stability in various electrolytes, robust mechanical strength to accommodate deposition, high electrical conductivity, and fine affinity for Zn.[108]

3D porous substrates with high surface area and an even electrical distribution, such as carbon fibre,[153] carbon cloth,[154] and copper foam,[155] could inhibit the growth of dendrites in continuous Zn plating/stripping processes. Lu et al.[156] designed a flexible 3D carbon nanotube (CNT) architecture for Zn deposition, and the dendrite-free Zn/CNT anode afforded low voltage hysteresis (27 mV) and outstanding cycling stability with a high average CE of 97.9%, which was attributable to the low Zn nucleation over-potential and the homogeneously distributed electric field. Notably, the metal-organic framework zeolitic imidazolate framework-8 (ZIF-8) with large cages has been demonstrated as a host material for highly reversible and highly stable Zn deposition and dissolution.[157] The trace amount of Zn^0 in the annealed ZIF-8 provides uniform nuclei for Zn plating, and the high over-potential for H_2 evolution constrains the consumption of water during cycling. Even at a high areal capacity, the Zn deposition morphology on the host is consistently smooth and dense, as shown in Figure 2.11e. The Zn plating mechanism is illustrated in Figure 2.11f, where initial Zn deposition occurs in and/or on the particles of the host and the homogeneous Zn-nuclei lead to subsequent dendrite-free plating. Moreover, based on an epitaxial

electrodeposition mechanism to regulate the nucleation and growth of Zn, graphene, with a low lattice mismatch for Zn, can work as a substrate, achieving the electrodeposition of Zn with a locked and correlated crystallographic orientation, and exceptional reversibility and rate capability.[158] Recently, a Zn-Al lamellar alloy with eutectic structure was proposed to guide uniform Zn deposition.[159] Compared to the Zn^{2+}/Zn, the Al^{3+}/Al couple features a much lower redox potential (–1.66 V *vs.* SHE), which causes the initial formation of an insulating Al_2O_3 shell on Al lamellas. Thus, a positive electrostatic shield forms around the Al lamellas due to the insulating shell, which guides dendite-free Zn deposition that avoids the Al surface.

It should be noted that high-cost 3D substrates are likely to be impaired under external stress, and the complex synthesis method for some substrates may reduce manufacturing productivity. Considering that a substrate with high surface area may accelerate gas evolution, combining a modified current collector with an optimized electrolyte should be a promising strategy for superior stability and reversibility of Zn anode.

2.4.4 Discussion

Compared to the alkaline electrolyte, the nearly neutral electrolyte provides a mild working environment for the Zn electrode, which helps to alleviate the Zn issues to some extent. Nevertheless, the Zn dendrite growth, gas evolution, and Zn metal corrosion still limit the reversibility of Zn electrode in mild systems. With the aim of addressing these issues, various strategies, including electrolyte optimization, building artificial SEI, and current collector modification have been proposed in recent decades, as summarized in Figure 2.12. Manipulating the anion salt chemistry (normally bulky anion salts) and constructing “water-in-salt” electrolytes are effective methods to relieve the solvation effect, enhancing the stability and reversibility of Zn electrode.

The high cost of these electrolytes, however, may restrict their practical application on a large scale. To keep the low-cost nature of ZIBs, more attention should be paid to exploring economical and compatible electrolyte salts. Considering that water molecules in electrolytes are the essential reason for corrosion and H_2 evolution, gel electrolytes have been introduced into flexible and wearable ZIBs. Poor Zn-ion migration and unsatisfactory power density are the main bottlenecks for gel electrolytes. In addition, artificial SEI layers on the surfaces of Zn electrodes include carbon-based materials, inorganic passivation layer, and polymer films, which block direct contact of the Zn metal with the electrolyte and restrain Zn dendrites and side reactions. Based on the industrial principle of ZIBs, *in-situ* SEI engineering is much more attractive than a complex artificial coating. Reports on *in-situ* SEI layers in ZIBs, however, are almost non-existent. Carbon-based, copper-based and MOF-based current collectors have been utilized in ZIBs for uniform nucleation and growth of Zn deposits. Simplified synthesis methods and affordable raw materials for those substrates, especially 3D substrates, should be exploited to improve their scalability and manufacturing productivity.

Figure 2.12 Summary of the strategies for addressing the problematic issues for Zn electrode in mild electrolyte.

2.5 References

1. P. Tan, B. Chen, H. Xu, W. Cai, W. He and M. Ni, *Appl. Catal. B*, 2019, **241**, 104-112.
2. C.-X. Zu and H. Li, *Energy Environ. Sci.*, 2011, **4**, 2614-2624.
3. S. Siahrostami, V. Tripković, K. T. Lundgaard, K. E. Jensen, H. A. Hansen, J. S. Hummelshøj, J. S. Mýrdal, T. Vegge, J. K. Nørskov and J. Rossmeisl, *Phys. Chem. Chem. Phys.*, 2013, **15**, 6416-6421.
4. R. W. Powers and M. W. Breiter, *J. Electrochem. Soc.*, 1969, **116**, 719-729.
5. C. Cachet, B. Saidani and R. Wiart, *J. Electrochem. Soc.*, 1992, **139**, 644-654.
6. C. Cachet, U. Ströder and R. Wiart, *Electrochim. Acta*, 1982, **27**, 903-908.

7. J. Hendrikx, A. van der Putten, W. Visscher and E. Barendrecht, *Electrochim. Acta*, 1984, **29**, 81-89.
8. Y. C. Chang and G. Prentice, *J. Electrochem. Soc.*, 1984, **131**, 1465.
9. S. Huang, J. Zhu, J. Tian and Z. Niu, *Chem. Eur. J.*, 2019, **25**, 14480-14494.
10. M. B. Liu, G. Cook and N. Yao, *J. Electrochem. Soc.*, 1981, **128**, 1663-1668.
11. M. Breiter, *Electrochim. Acta*, 1970, **15**, 1297-1304.
12. L. Baugh and A. Higginson, *Electrochim. Acta*, 1985, **30**, 1163-1172.
13. M. Bockelmann, M. Becker, L. Reining, U. Kunz and T. Turek, *J. Electrochem. Soc.*, 2018, **165**, A3048-A3055.
14. V. Caldeira, R. Rouget, F. Fourgeot, J. Thiel, F. Lacoste, L. Dubau and M. Chatenet, *J. Power Sources*, 2017, **350**, 109-116.
15. J. McBreen, *J. Electrochem. Soc.*, 1972, **119**, 1620.
16. R. Einerhand, W. Visscher, J. De Goeij and E. Barendrecht, *J. Electrochem. Soc.*, 1991, **138**, 7.
17. J. Yi, P. Liang, X. Liu, K. Wu, Y. Liu, Y. Wang, Y. Xia and J. Zhang, *Energy Environ. Sci.*, 2018, **11**, 3075-3095.
18. H. A. Akiyoshi Nakata, H. Murayama, K. Fukuda, T. Yamane, T. Hirai, Y. Uchimoto, J. Yamaki, Z. Ogumi, *Apl Mater.*, 2018, **6**, 047703.
19. M. Liu, X. Pu, Z. Cong, Z. Liu, T. Liu, Y. Chen, J. Fu, W. Hu and Z. L. Wang, *ACS Appl. Mater. Interfaces*, 2019, **11**, 5095-5106.
20. M. Biton, F. Tariq, V. Yufit, Z. Chen and N. Brandon, *Acta Mater.*, 2017, **141**, 39-46.
21. J. Diggle, A. Despic and J. M. Bockris, *J. Electrochem. Soc.*, 1969, **116**, 1503-1514.
22. J. W. D. A. Damjanovic, *J. Electrochem. Soc.*, 1970, **117** 65.

23. F. Mansfeld and S. Gilman, *J. Electrochem. Soc.*, 1970, **117**, 1521.

24. M. Audero and H. Biloni, *J. Cryst. Growth*, 1972, **12**, 297-308.

25. V. Yufit, F. Tariq, D. S. Eastwood, M. Biton, B. Wu, P. D. Lee and N. P. Brandon, *Joule*, 2019, **3**, 485-502.

26. S. M. Lee, Y. J. Kim, S. W. Eom, N. S. Choi, K. W. Kim and S. B. Cho, *J. Power Sources*, 2013, **227**, 177-184.

27. T. Lee, *J. Electrochem. Soc.*, 1971, **118**, 1278-1282.

28. C. W. Lee, S. W. Eom, K. Sathiyanarayanan and M. S. Yun, *Electrochim. Acta*, 2006, **52**, 1588-1591.

29. R. Shivkumar, G. P. Kalaignan and T. Vasudevan, *J. Power Sources*, 1995, **55**, 53-62.

30. R. Shivkumar, G. P. Kalaignan and T. Vasudevan, *J. Power Sources*, 1998, **75**, 90-100.

31. J. McBreen and E. Gannon, *Electrochim. Acta*, 1981, **26**, 1439-1446.

32. P. J. M. a. G. D. W. K. Bass, *J. Power Sources*, 1991, **35**, 333-351.

33. R. Renuka, L. Srinivasan, S. Ramamurthy, A. Veluchamy and N. Venkatakrishnan, *J. Appl. Electrochem.*, 2001, **31**, 655-661.

34. S. Hosseini, A. Abbasi, L. O. Uginet, N. Haustraete, S. Praserthdam, T. Yonezawa and S. Kheawhom, *Sci. Rep.*, 2019, **9**, 1-12.

35. Y. Yuan, J. Tu, H. Wu, Y. Li, D. Shi and X. Zhao, *J. Power Sources*, 2006, **159**, 357-360.

36. D. E. Turney, J. W. Gallaway, G. G. Yadav, R. Ramirez, M. Nyce, S. Banerjee, Y. K. Chen-Wiegart, J. Wang, M. J. D'Ambrose and S. Kolhekar, *Chem. Mater.*, 2017, **29**, 4819-4832.

37. E. G. G. Y. M. Wang, *J. Electrochem. Soc.*, 1987, **134**, 2091-2096.

38. B. Kavitha, P. Santhosh, M. Renukadevi, A. Kalpana, P. Shakkthivel and T. Vasudevan, *Surf. Coat. Technol.*, 2006, **201**, 3438-3442.

39. D. Stock, S. Dongmo, F. Walther, J. Sann, J. Janek and D. Schroder, *ACS Appl. Mater. Interfaces*, 2018, **10**, 8640-8648.

40. W. MacKnight and T. R. Earnest Jr, *J. Polym. Sci. Macromol. Rev.*, 1981, **16**, 41-122.

41. Y. Z. Jiling Zhu, *J. Power Sources*, 1998, **73**, 266-270.

42. K. Miyazaki, Y. S. Lee, T. Fukutsuka and T. Abe, *Electrochem.*, 2012, **80**, 725-727.

43. J. Huang, Z. Yang, X. Xie, Z. Feng and Z. Zhang, *J. Power Sources*, 2015, **289**, 8-16.

44. X. Zeng, Z. Yang, J. Long, L. Chen, H. Qin and M. Fan, *Ionics*, 2019, **25**, 1223-1233.

45. Z. Zhou, Y. Zhang, P. Chen, Y. Wu, H. Yang, H. Ding, Y. Zhang, Z. Wang, X. Du and N. Liu, *Chem. Eng. Sci.*, 2019, **194**, 142-147.

46. Y. Yan, Y. Zhang, Y. Wu, Z. Wang, A. Mathur, H. Yang, P. Chen, S. Nair and N. Liu, *ACS Appl. Energy Mater.*, 2018, **1**, 6345-6351.

47. Y. Zhang, Y. Wu, H. Ding, Y. Yan, Z. Zhou, Y. Ding and N. Liu, *Nano Energy*, 2018, **53**, 666-674.

48. P. Chen, Y. Wu, Y. Zhang, T.-H. Wu, Y. Ma, C. Pelkowski, H. Yang, Y. Zhang, X. Hu and N. Liu, *J. Mater. Chem. A*, 2018, **6**, 21933-21940.

49. Y. Wu, Y. Zhang, Y. Ma, J. D. Howe, H. Yang, P. Chen, S. Aluri and N. Liu, *Adv. Energy Mater.*, 2018, **8**, 1802470.

50. L. Sun, Z. Yi, J. Lin, F. Liang, Y. Wu, Z. Cao and L. Wang, *J. Phys. Chem. C.*, 2016, **120**, 12337-12343.

51. S. H. Lee, C.-W. Yi and K. Kim, *J. Phys. Chem. C*, 2011, **115**, 2572-2577.

52. J. F. Parker, E. S. Nelson, M. D. Wattendorf, C. N. Chervin, J. W. Long and D. R. Rolison, *ACS Appl. Mater. Interfaces*, 2014, **6**, 19471-19476.

53. P. Liu, X. Ling, C. Zhong, Y. Deng, X. Han and W. Hu, *Front. Chem.*, 2019, **7**, 656.

54. J. Liu, C. Guan, C. Zhou, Z. Fan, Q. Ke, G. Zhang, C. Liu and J. Wang, *Adv. Mater.*, 2016, **28**, 8732-8739.

55. J. F. Parker, C. N. Chervin, I. R. Pala, M. Machler, M. F. Burz, J. W. Long and D. R. Rolison, *Science*, 2017, **356**, 415-418.

56. J. F. Parker, C. N. Chervin, E. S. Nelson, D. R. Rolison and J. W. Long, *Energy Environ. Sci.*, 2014, **7**, 1117-1124.

57. J. S. Ko, A. B. Geltmacher, B. J. Hopkins, D. R. Rolison, J. W. Long and J. F. Parker, *ACS Appl. Energy Mater.*, 2018, **2**, 212-216.

58. S. J. Banik and R. Akolkar, *Electrochim. Acta*, 2015, **179**, 475-481.

59. A. B. Hashemi, G. Kasiri and F. La Mantia, *Electrochim. Acta*, 2017, **258**, 703-708.

60. S. Hosseini, S. J. Han, A. Arponwichanop, T. Yonezawa and S. Kheawhom, *Sci. Rep.*, 2018, **8**, 1-11.

61. H. I. Kim, E. J. Kim, S. J. Kim and H. C. Shin, *J. Appl. Electrochem.*, 2015, **45**, 335-342.

62. F. Mansfeld and S. Gilman, *J. Electrochem. Soc.*, 1970, **117**, 588-592.

63. F. Mansfeld and S. Gilman, *J. Electrochem. Soc.*, 1970, **117**, 1154-1155.

64. B. Szcześniak, M. Cyrankowska and A. Nowacki, *J. Power Sources*, 1998, **75**, 130-138.

65. J. Zhu, Y. Zhou and C. Gao, *J. Power Sources*, 1998, **72**, 231-235.

66. J. Dobryszycki and S. Biallozor, *Corros. Sci.*, 2001, **43**, 1309-1319.

67. R. K. Ghavami and Z. Rafiei, *J. Power Sources*, 2006, **162**, 893-899.

68. V. Branzoi, A. Pruna and F. Branzoi, *Rev. Roum. Chim.*, 2007, **52**, 587-595.

69. K. Liu, P. He, H. Bai, J. Chen, F. Dong, S. Wang, M. He and S. Yuan, *Mater. Chem. Phys.*, 2017, **199**, 73-78.

70. M. Shimizu, K. Hirahara and S. Arai, *Phys. Chem. Chem. Phys.*, 2019, **21**, 7045-7052.

71. D. P. Trudgeon, K. Qiu, X. Li, T. Mallick, O. O. Taiwo, B. Chakrabarti, V. Yufit, N. P. Brandon, D. Crevillen-Garcia and A. Shah, *J. Power Sources*, 2019, **412**, 44-54.

72. S. Hosseini, W. Lao-Atiman, S. J. Han, A. Arpornwichanop, T. Yonezawa and S. Kheawhom, *Sci. Rep.*, 2018, **8**, 14909.

73. M. Deyab, *J. Power Sources*, 2015, **292**, 66-71.

74. R. K. Ghavami, Z. Rafiei and S. M. Tabatabaei, *J. Power Sources*, 2007, **164**, 934-946.

75. A. Sumboja, M. Lübke, Y. Wang, T. An, Y. Zong and Z. Liu, *Adv. Energy Mater.*, 2017, **7**, 1700927.

76. S. Clark, A. R. Mainar, E. Iruin, L. C. Colmenares, J. A. Blázquez, J. R. Tolchard, A. Latz and B. Horstmann, *J. Mater. Chem. A*, 2019, **7**, 11387-11399.

77. R. Othman, W. Basirun, A. Yahaya and A. Arof, *J. Power Sources*, 2001, **103**, 34-41.

78. N. Vassal, E. Salmon and J. F. Fauvarque, *Electrochim. Acta*, 2000, **45**, 1527-1532.

79. C. C. Yang and S. J. Lin, *J. Power Sources*, 2002, **112**, 497-503.

80. A. A. Mohamad, *J. Power Sources*, 2006, **159**, 752-757.

81. Y. Huang, Z. Li, Z. Pei, Z. Liu, H. Li, M. Zhu, J. Fan, Q. Dai, M. Zhang, L. Dai and C. Zhi, *Adv. Energy Mater.*, 2018, **8**, 1802288.

82. X. Fan, J. Liu, Z. Song, X. Han, Y. Deng, C. Zhong and W. Hu, *Nano Energy*, 2019, **56**, 454-462.

83. Q. Lai, H. Zhang, X. Li, L. Zhang and Y. Cheng, *J. Power Sources*, 2013, **235**, 1-4.

84. Z. Yuan, Y. Yin, C. Xie, H. Zhang, Y. Yao and X. Li, *Adv. Mater.*, 2019, **31**, 1902025.

85. A. Gavrilović-Wohlmuther, A. Laskos, C. Zelger, B. Gollas and A. H. Whitehead, *J. Energy Power Eng.*, 2015, **9**, 1019-1028.

86. J. Jorne, Y. J. Lii and K. E. Yee, *J. Electrochem. Soc.*, 1987, **134**, 1399.

87. H. Lin, D. Chen, C. Lu, C. Zhang, F. Qiu, S. Han and X. Zhuang, *Electrochim. Acta*, 2018, **266**, 17-26.

88. Z. Wang, Z. Wu, N. Bramnik and S. Mitra, *Adv. Mater.*, 2014, **26**, 970-976.

89. E. L. Dewi, K. Oyaizu, H. Nishide and E. Tsuchida, *J. Power Sources*, 2003, **115**, 149-152.

90. Z. Yuan, Y. Duan, T. Liu, H. Zhang and X. Li, *iScience*, 2018, **3**, 40-49.

91. C. Xie, H. Zhang, W. Xu, W. Wang and X. Li, *Angew. Chem. Int. Ed.*, 2018, **57**, 11171-11176.

92. K. Bass, P. Mitchell, G. Wilcox and J. Smith, *J. Power Sources*, 1991, **35**, 333-351.

93. D. Bennion, Brigham Young Univ., Provo, UT (USA). *Dept. of Chemical Engineering*, 1980, D.E. 83011663..

94. G. Garcia, E. Ventosa and W. Schuhmann, *ACS Appl. Mater. Interfaces*, 2017, **9**, 18691-18698.

95. T. N. A.Chiba, H. Kitayama and T. Ogawa, *Surf. Coat. Technol.*, 1986, **29**, 347-355.

96. S. Higashi, S. W. Lee, J. S. Lee, K. Takechi and Y. Cui, *Nat. Commun.*, 2016, **7**, 11801.

97. Z. Liu, T. Cui, G. Pulletikurthi, A. Lahiri, T. Carstens, M. Olschewski and F. Endres, *Angew. Chem. Int. Ed.*, 2016, **55**, 2889-2893.

98. M. Pavlović, Š. Kindlova and I. Roušar, *Electrochim. Acta*, 1992, **37**, 23-27.

99. L. N. Bengoa, S. Bruno, H. A. Lazzarino, P. R. Seré and W. A. Egli, *J. Appl. Electrochem.*, 2014, **44**, 1261-1269.

100. K. Popov, M. Pavlović and M. Maksimović, *J. Appl. Electrochem.*, 1982, **12**, 525-531.

101. L. N. Bengoa, P. Pary, P. R. Seré, M. S. Conconi and W. A. Egli, *J. Mater. Eng. Perform.*, 2018, **27**, 1103-1108.

102. Z. Zhao, J. Zhao, Z. Hu, J. Li, J. Li, Y. Zhang, C. Wang and G. Cui, *Energy Environ. Sci.*, 2019, **12**, 1938-1949.

103. R. Woods, R. Yoon and C. Young, *Int. J. Miner. Process.*, 1987, **20**, 109-120.

104. J. Zhao, J. Zhang, W. Yang, B. Chen, Z. Zhao, H. Qiu, S. Dong, X. Zhou, G. Cui and L. Chen, *Nano Energy*, 2019, **57**, 625-634.

105. Z. Cai, Y. Ou, J. Wang, R. Xiao, L. Fu, Z. Yuan, R. Zhan and Y. Sun, *Energy Storage Mater.*, 2020, **27**, 205-211.

106. P. Liang, J. Yi, X. Liu, K. Wu, Z. Wang, J. Cui, Y. Liu, Y. Wang, Y. Xia and J. Zhang, *Adv. Funct. Mater.*, 2020, **30,** 1908528.

107. H. Jia, Z. Wang, B. Tawiah, Y. Wang, C. Y. Chan, B. Fei and F. Pan, *Nano Energy*, 2020, **70**, 104523.

108. H. Yang, Z. Chang, Y. Qiao, H. Deng, X. Mu, P. He and H. Zhou, *Angew. Chem. Int. Ed.*, 2020, **59**, 9377-9381.

109. Z. Hong, Z. Ahmad and V. Viswanathan, *ACS Energy Lett.*, 2020, **5**, 2466-2474.

110. Y. Tang, C. Liu, H. Zhu, X. Xie, J. Gao, C. Deng, M. Han, S. Liang and J. Zhou, *Energy Storage Mater.*, 2020, **27**, 109-116.

111. C. Deng, X. Xie, J. Han, Y. Tang, J. Gao, C. Liu, X. Shi, J. Zhou and S. Liang, *Adv. Funct. Mater.*, 2020, **30**, 2000599.

112. J. Hao, B. Li, X. Li, X. Zeng, S. Zhang, F. Yang, S. Liu, D. Li, C. Wu and Z. Guo, *Adv. Mater.*, 2020, **32,** 2003021.

113. J. Hao, X. Li, S. Zhang, F. Yang, X. Zeng, S. Zhang, G. Bo, C. Wang and Z. Guo, *Adv. Funct. Mater.*, 2020, **30**, 2001263.

114. H. Li, L. Ma, C. Han, Z. Wang, Z. Liu, Z. Tang and C. Zhi, *Nano Energy*, 2019, **62**, 550-587.

115. J. Hao, J. Zhang, G. Xia, Y. Liu, Y. Zheng, W. Zhang, Y. Tang, W. K. Pang and Z. Guo, *ACS Nano*, 2018, **12**, 10430-10438.

116. J. Hao, J. Long, B. Li, X. Li, S. Zhang, F. Yang, X. Zeng, Z. Yang, W. K. Pang and Z. Guo, *Adv. Funct. Mater.*, 2019, **29**, 1903605.

117. K. E. Sun, T. K. Hoang, T. N. L. Doan, Y. Yu, X. Zhu, Y. Tian and P. Chen, *ACS Appl. Mater. Interfaces*, 2017, **9**, 9681-9687.

118. W. Xu, K. Zhao, W. Huo, Y. Wang, G. Yao, X. Gu, H. Cheng, L. Mai, C. Hu and X. Wang, *Nano Energy*, 2019, **62**, 275-281.

119. A. Mitha, A. Z. Yazdi, M. Ahmed and P. Chen, *ChemElectroChem*, 2018, **5**, 2409-2418.

120. K. E. Sun, T. K. Hoang, T. N. L. Doan, Y. Yu and P. Chen, *Chem. Eur. J.*, 2018, **24**, 1667-1673.

121. F. Wan, L. Zhang, X. Dai, X. Wang, Z. Niu and J. Chen, *Nat. Commun.*, 2018, **9**, 1-11.

122. L. Wang, Y. Zhang, H. Hu, H. Y. Shi, Y. Song, D. Guo, X. X. Liu and X. Sun, *ACS Appl. Mater. Interfaces*, 2019, **11**, 42000-42005.

123. M. S. Chae, J. W. Heo, H. H. Kwak, H. Lee and S. T. Hong, *J. Power Sources*, 2017, **337**, 204-211.

124. G. Kasiri, R. Trócoli, A. B. Hashemi and F. La Mantia, *Electrochim. Acta*, 2016, **222**, 74-83.

125. X. Zeng, J. Liu, J. Mao, J. Hao, Z. Wang, S. Zhou, C. D. Ling and Z. Guo, *Adv. Energy Mater.*, 2020, 1904163. https://doi.org/10.1002/aenm.201904163.

126. Z. Peng, Q. Wei, S. Tan, P. He, W. Luo, Q. An and L. Mai, *Chem. Commun.*, 2018, **54**, 4041-4044.

127. Z. Hou, M. Dong, Y. Xiong, X. Zhang, H. Ao, M. Liu, Y. Zhu and Y. Qian, *Small*, 2020, **16**, 2001228.

128. L. Suo, O. Borodin, T. Gao, M. Olguin, J. Ho, X. Fan, C. Luo, C. Wang and K. Xu, *Science*, 2015, **350**, 938-943.

129. X. Wu, Y. Xu, C. Zhang, D. P. Leonard, A. Markir, J. Lu and X. Ji, *J. Am. Chem. Soc.*, 2019, **141**, 6338-6344.

130. C. Zhang, J. Holoubek, X. Wu, A. Daniyar, L. Zhu, C. Chen, D. P. Leonard, I. A. Rodríguez-Pérez, J. X. Jiang and C. Fang, *Chem. Commun.*, 2018, **54**, 14097-14099.

131. L. Zhang, I. A. Rodríguez-Pérez, H. Jiang, C. Zhang, D. P. Leonard, Q. Guo, W. Wang, S. Han, L. Wang and X. Ji, *Adv. Funct. Mater.*, 2019, **29**, 1902653.

132. L. Jiang, L. Liu, J. Yue, Q. Zhang, A. Zhou, O. Borodin, L. Suo, H. Li, L. Chen and K. Xu, *Adv. Mater.*, 2019, **32**, 1904427.

133. L. Suo, O. Borodin, W. Sun, X. Fan, C. Yang, F. Wang, T. Gao, Z. Ma, M. Schroeder and A. von Cresce, *Angew. Chem. Int. Ed.*, 2016, **55**, 7136-7141.

134. L. Ma, S. Chen, D. Wang, Q. Yang, F. Mo, G. Liang, N. Li, H. Zhang, J. A. Zapien and C. Zhi, *Adv. Energy Mater.*, 2019, **9**, 1803046.

135. X. Li, Y. Tang, H. Lv, W. Wang, F. Mo, G. Liang, C. Zhi and H. Li, *Nanoscale*, 2019, **11**, 17992-18008.

136. X. Li, J. Hao, R. Liu, H. He, Y. Wang, G. Liang, Y. Liu, G. Yuan and Z. Guo, *Energy Storage Mater.*, 2020, **33**, 62-70.

137. X. Zhang, Y. He, M. L. Sushko, J. Liu, L. Luo, J. J. De Yoreo, S. X. Mao, C. Wang and K. M. Rosso, *Science*, 2017, **356**, 434-437.

138. D. Chao, C. Zhu, M. Song, P. Liang, X. Zhang, N. H. Tiep, H. Zhao, J. Wang, R. Wang and H. Zhang, *Adv. Mater.*, 2018, **30**, 1803181.

139. C. Liu, A. Gao, F. Yi, D. Shu, H. Yi, X. Zhou, J. Hao, C. He and Z. Zhu, *Electrochim. Acta*, 2019, **326**, 134965.

140. H. Li, Z. Liu, G. Liang, Y. Huang, Y. Huang, M. Zhu, Z. Pei, Q. Xue, Z. Tang and Y. Wang, *ACS Nano*, 2018, **12**, 3140-3148.

141. D. Wang, H. Li, Z. Liu, Z. Tang, G. Liang, F. Mo, Q. Yang, L. Ma and C. Zhi, *Small*, 2018, **14**, 1803978.

142. H. Li, C. Han, Y. Huang, Y. Huang, M. Zhu, Z. Pei, Q. Xue, Z. Wang, Z. Liu and Z. Tang, *Energy Environ. Sci.*, 2018, **11**, 941-951.

143. F. Liu, R. Xu, Z. Hu, S. Ye, S. Zeng, Y. Yao, S. Li and Y. Yu, *Small*, 2019, **15**, 1803734.

144. P. He, Q. Chen, M. Yan, X. Xu, L. Zhou, L. Mai and C.-W. Nan, *EnergyChem*, 2019, **1**, 100022.

145. C. Shen, X. Li, N. Li, K. Xie, J.-g. Wang, X. Liu and B. Wei, *ACS Appl. Mater. Interfaces*, 2018, **10**, 25446-25453.

146. W. Li, K. Wang, M. Zhou, H. Zhan, S. Cheng and K. Jiang, *ACS Appl. Mater. Interfaces*, 2018, **10**, 22059-22066.

147. A. Xia, X. Pu, Y. Tao, H. Liu and Y. Wang, *Appl. Surf. Sci.*, 2019, **481**, 852-859.

148. L. Kang, M. Cui, F. Jiang, Y. Gao, H. Luo, J. Liu, W. Liang and C. Zhi, *Adv. Energy Mater.*, 2018, **8**, 1801090.

149. X. Xie, S. Liang, J. Gao, S. Guo, J. Guo, C. Wang, G. Xu, X. Wu, G. Chen and J. Zhou, *Energy Environ. Sci.*, 2020, **13**, 503-510.

150. K. Zhao, C. Wang, Y. Yu, M. Yan, Q. Wei, P. He, Y. Dong, Z. Zhang, X. Wang and L. Mai, *Adv. Mater. Interfaces*, 2018, **5**, 1800848.

151. P. Liang, J. Yi, X. Liu, K. Wu, Z. Wang, J. Cui, Y. Liu, Y. Wang, Y. Xia and J. Zhang, *Adv. Funct. Mater.*, 2020, **30**, 1908528.

152. B. S. Lee, S. Cui, X. Xing, H. Liu, X. Yue, V. Petrova, H.-D. Lim, R. Chen and P. Liu, *ACS Appl. Mater. Interfaces*, 2018, **10**, 38928-38935.

153. W. Dong, J. L. Shi, T. S. Wang, Y. X. Yin, C. R. Wang and Y. G. Guo, *RSC Adv.*, 2018, **8**, 19157-19163.

154. Y. Zeng, X. Zhang, Y. Meng, M. Yu, J. Yi, Y. Wu, X. Lu and Y. Tong, *Adv. Mater.*, 2017, **29**, 1700274.

155. C. Li, X. Shi, S. Liang, X. Ma, M. Han, X. Wu and J. Zhou, *Chem. Eng. J.*, 2020, **379**, 122248.

156. Y. Zeng, X. Zhang, R. Qin, X. Liu, P. Fang, D. Zheng, Y. Tong and X. Lu, *Adv. Mater.*, 2019, **31**, 1903675.

157. Z. Wang, J. Huang, Z. Guo, X. Dong, Y. Liu, Y. Wang and Y. Xia, *Joule*, 2019, **3**, 1289-1300.

158. J. Zheng, Q. Zhao, T. Tang, J. Yin, C. D. Quilty, G. D. Renderos, X. Liu, Y. Deng, L. Wang and D. C. Bock, *Science*, 2019, **366**, 645-648.

159. S. B. Wang, Q. Ran, R. Q. Yao, H. Shi, Z. Wen, M. Zhao, X. Y. Lang and Q. Jiang, *Nat. Commun.*, 2020, **11**, 1634.

Chapter 3

Experimental Section

3.1 Chemicals and materials

Table 3.1 The chemicals and materials applied in the research.

Chemicals	Formula	Purity	Supplier
Zinc triflate	$Zn(CF_3SO_3)_2$	> 98%	Sigma-Aldrich
Zinc sulfate	$ZnSO_4 \cdot 7H_2O$	99%	Sigma-Aldrich
Zinc acetate dihydrate	$(Zn(CH_3COO)_2 \cdot 2H_2O$	99%	Sigma-Aldrich
Zinc dihydrogen phosphate	$Zn(H_2PO_4)_2 \cdot 2H_2O$	99%	American Elements
Zinc phosphate tetrahydrate	$Zn_3(PO_4)_2 \cdot 4H_2O$	99.9%	American Elements
Manganese triflate	$Mn(CF_3SO_3)_2$	99%	Sigma-Aldrich
Manganese (II) sulfate	$MnSO_4 \cdot H_2O$	99%	Sigma-Aldrich
Manganese acetate tetrahydrate	$(Mn(CH_3COO)_2 \cdot 4H_2O$	99%	Sigma-Aldrich
Zinc foil	Zn	N/A	Kejing Star Technology
Titanium foil	Ti	N/A	Kejing Star Technology
Copper foil	Cu	N/A	Kejing Star Technology
Acetylene black	C	N/A	Timcal, Belgium
dopamine hydrochloride	DA·HCl	99%	Sigma-Aldrich
Sulfuric acid	H_2SO_4	95.0-98.0%	Sigma-Aldrich
Phosphoric acid	H_3PO_4	85wt%	Sigma-Aldrich
Potassium permanganate	$KMnO_4$	99%	Sigma-Aldrich
Carbon cloth	C	N/A	CeTech

3.2 Preparation of electrolytes and electrodes

The functional electrolytes designed in this doctoral thesis were prepared by dissolving

electrolyte salts, such as $Zn(CF_3SO_3)_2$ or $Zn(CH_3COO)_2$, and electrolyte additives, such as $Zn(H_2PO_4)_2 \cdot 2H_2O$ or DA in deionized water at room temperature. Zn foil was punched into discs, which were directly used as Zn electrodes. The V_2O_5 electrodes were prepared by a slurry coating method, where commercial V_2O_5 powder, Super P, and polyvinylidene fluoride (PVDF) in a mass ratio of 7: 2:1 were mixed in N-methyl-2-pyrrolidine (NMP). Then, the slurry was pasted onto a Ti current collector and vacuum-dried at 120 ºC overnight. Ultrathin Zn electrodes (10 μm, 5.85 mA h cm^{-2}) were used for the full cell tests, and Zn electrodes 60 μm in thickness were used in the symmetric Zn/Zn and asymmetrical Cu/Zn cells. The amount of electrolyte used in the symmetric Zn/Zn and asymmetrical Zn/Cu cells was controlled at 100 μL. For the fabrication of Zn/MnO_2 coin cells and Swagelok cells in this thesis, 2032-type coin cells were assembled with carbon cloth (0.8 mm diameter disc) as the cathode-less current collector, Zn foil (0.1 mm thick) as the anode, and glass fibre as the separator. The edge of the positive case was covered with electrically insulating Kapton tape to avoid the deposition of MnO_2 on the positive case. The standard two-electrode Swagelok cell was constructed by using carbon felt as the cathode-less current collector instead and high-purity Ti foil was also used to avoid any possible contamination. The carbon cloth and carbon felt were immersed in a 5wt % aqueous solution of $KMnO_4$ for 0.5 h at room temperature, followed by thorough ultrasonic washing in deionized water and ethanol, before they were used as current collectors.

3.3 Characterization analysis

3.3.1 X-ray powder diffraction (XRD)

XRD was employed to characterize the crystalline part of the materials. A monochromate beam of X-ray is obtained by bombarding a piece of targe materials, in our case a copper target, emitting a characteristic wavelength equivalent to the energy

between two atomic states, in our case between n = 1 and n = 2 (n is the main quantum number). This wavelength, 1.5406 Å, called Kα, is the strongest of a series of emission lines called K lines which are close in energy to each other. To filter out the Kα line, a nickel foil is placed right after the emission. The absorption edge of nickel is just higher than Kα line and lower than all other K lines in terms of energy. The above process of emission and absorption take place in a vacuum sealed tube and a proper cooling system as the anode emission process generates more heat than useful X-ray photons. A more advanced way of filtering is to use a dedicated monochromator which is usually a piece of silicon or graphite crystal, using exact the same principle of diffraction to get a sharp energy profile. This monochromate X-ray then runs pass a collimator and a slit before diffracts on our sample which is mounted on a flat plate. The sample itself is also a flat piece of electrode. The detector is always placed at an angle to the normal direction of the sample stage equivalent to the angle between the incoming X-ray and the normal direction of the sample stage. An XRD pattern is collected for the range of angle of interest which is realized by moving the detector and the light source simultaneously in an arc of a fixed radius distance. This mode of measurement is called Bragg-Brentano, or reflection geometry, which suits our purpose of measuring the materials grown on a substrate. The other common type of measurement is Debye-Scherrer, or transmission geometry which requires a curved focusing mirror, often a monochromator at the same time. In contrast, the reflection geometry only requires a slit to realize the focusing purpose if a dedicated monochromator is not available. In terms of data resolution, both geometries are of no difference.

3.3.2 Transmission electron microscopy (TEM)

In this thesis, TEM was used to characterize the microstructure of electrode materials. The high-resolution image obtained by TEM is in essence phase contrast image which

is the inverse Fourier transformation of the Fourier transformation of the sample by the objective lens (OL). This requires the high angle scattered beam from the sample, i.e. a large OL aperture. The astigmatism and spherical aberrations of the OL itself should also be properly addressed. If the OL spherical aberration is not available, a smaller OL aperture can be used to balance between the spherical aberration and resolution. The spherical aberration and the focusing length, or defocus to be more precise, together determine the contrast transformation function (CTF) of the objective lens which in turn determines to what extent the phase contrast image is related to the actual atomic configuration. A properly chosen OL aperture could also maximize the "good" part of CTF, resulting in more realistic high-resolution image. The aberration corrections of the condenser lens above OL and the projector lens below the OL are not strictly required in high resolution mode since electron beam as parallel as possible is used to maximize coherency before the interaction with sample and the projector lens does the job of magnification not focus, but their astigmatisms have to be minimized. Finally, the magnified, high resolution and high contrast image is projected onto a scintillating screen or a densely patterned optical fibre transforming the electronic signal to light signal which subsequently are read-out by a camera made up of charge-coupled device (CCD) or complementary metal oxide semiconductor (CMOS).

In scanning TEM (STEM) mode where the resolution is determined by the size and the quality of the probe, the aberration of condenser lens must be minimized either by means of using a smaller aperture or hexapole correctors. The detector is no longer a camera as the signals are recorded in annular shaped scintillators connected to photomultipliers. These detectors are placed around the beam axis and collect those scattered electrons at a desired angle from the beam axis, giving information on the atomic number of the sample, or Z-contrast, of course on condition that the sample is

thin enough such that the multi-scattering events are neglected. In STEM mode, the objective lens and projector lens are not in use at all.

3.3.3 Scanning electron microscopy (SEM)

SEM was applied to obtain the microscopic information of electrode materials. The most prominent signal of SEM is the secondary electron (SE) generation due to the inelastic scattering of the electron beam by the sample and coming out of the surface of the sample. SEs, with a typical energy around 50 eV, are firstly attracted to a high voltage grid close to the sample and then collected by a scintillator before amplified to digital signal. The sample chamber is kept at a high vacuum because of the low energy of SEs which also gives its high sensitivity to the surface roughness of the sample. The lower the voltage of the electron beam, the smaller the interaction volume, hence the higher the spatial resolution of a SE image. By using small aperture, the beam size can be kept at a great length in the z direction, giving a depth of the viewing field of hundreds of nano-meters, revealing the morphology of the sample in three dimensions.

Another significant signal is the collection of back-scattered electrons (BSE) that comes from the elastic or quasi-elastic scattering of the sample with the coming electron beam in a larger volume than the secondary electron. The annular detector is placed above the sample and concentric to the beam axis, similar to those used in STEM signal collection. BSE signal also gives Z-contrast information as the back scattering cross-sections are proportional to the atomic number. It should be noted that the morphology factor should be decoupled before getting trustworthy Z-contrast image, i.e. the sample must be made as flat as possible. The elastic nature of BSEs can also give crystallography orientation information by forming the Kikuchi patterns, pairs of bright and dark lines following the projection of crystal planes on an areal detector. The generation of Kikuchi pattern is similar to that of powder diffraction, except that in the former the light source is

randomly distributed while in the latter the randomness comes from the crystals. Both lead to diffraction cones. The third most proliferate signal is the characteristic X-ray emission from even larger volume of the sample, also called energy dispersive spectroscopy (EDS). These X-rays are collected from a limited solid angle and their energies are then transformed into electric signals by photo-voltaic effect on a Si (Li) detector. EDS can give half quantitative elemental distribution information.

3.3.4 Atomic force microscopy (AFM)

AFM can obtain atomic resolved images for flat sample cross-section at ambient pressure and humidity. This is achieved by scanning the surface of the sample with a finely fabricated tip of the size of a few nanometres mounted on a cantilever. The distance of this tip is kept at a distance of a few to tens of nanometres to the sample, at which range the Van de Waals force dominates. This distance is maintained by an electronic feed loop and a piezoelectric system to monitor the position of the cantilever and move the sample to and from the cantilever. The position of the cantilever is monitored by its reflecting a beam of laser onto a position-sensitive detector. At ambient pressure and humidity, the cantilever is usually operated in a “tapping” mode, i.e. oscillating with a defined frequency and amplitude, to minimize the dragging of the capillary force from a thin layer of water prevalently found on the sample surface. That said, it is also possible to operate an AFM in a vacuum system. Though the interaction of the probe, a tip usually made of silicon nitride, and the sample is almost perfectly non-destructive and the microscopy is truly free from aberration and diffraction limit, AFM images must be interpreted with care since they can contain artifact from the shape of the probe. The tip can be modified to enable AFM measuring the force of interest, e.g. chemical bonding, surface tension, magnetism.

3.3.5 Raman spectroscopy

The vibrational modes of molecules, or phonons of solid, can be characterized by Raman spectroscopy. Raman spectroscopy is obtained from the interaction of photons with the sample. The sample transits between vibrational states due to the polarization effect of the electro-magnetic field of the laser. Hence only those vibrations that change the polarizability are Raman-active. All relevant vibration modes can be counted using the character table for the specific point group of the material. Each element in the character table reflects whether an irreproducible representation (row) equals to itself under a class of symmetry operation (column). Raman active modes corresponds to those rows denoted with quadratic functions. These rules apply to molecules as well as solids in which only point group symmetry operations are concerned since only Gamma point phonons are detected in Raman spectroscopy. In a spectrometer, a monochromat laser is directed to the sample through a split-mirror. The reflected beam from the sample and from the mirror is then filtered out the original frequency. The Raman shift signals are scanned by a grating and recorded onto a charge coupled device (CCD) due to its weak intensity. The CCD for Raman purpose is often so sensitive that it occasionally records glitches, e.g., cosmic rays.

3.3.6 Fourier transform infrared (FTIR) spectroscopy

FTIR spectroscopy is a type of absorption spectroscopy that is the result of the sample absorbing the energy quanta of the probe photon and transiting to another vibrational state. Unlike in Raman measurement where the energy of the photon is much higher, the energy of the photon is equivalent to energy difference between vibrational states. Further the photon frequency matches that corresponding to the ground state vibration according quantum mechanics. This requires the infrared active vibration having a non-zero electric dipole to enable the energy transfer. This selection rule results in the major absorption peaks able to be assigned unambiguously based on the index database.

Sometimes the photon frequency matches twice that corresponding to the ground state vibration, violating the selection rule which in consequence leads to peaks that are rare and weak. For some materials it is possible to observe frequencies corresponding to vibration-rotation coupling or vibration-electronic coupling due to the fact that infrared signal is intensive. Using the selection rule, it is easy to work out the number of infrared active vibrational modes with the help of character table in the same way as their Raman counterparts except looking for the denotations with dipole functions. A modern infrared spectrometer measures in Fourier transfer mode where a source provides a wide spectrum beam which passes an interferometer before through the sample and run into a pyroelectric detector. The interferometer Fourier transformed the absorption-frequency spectrum into an absorption-time spectrum, which is Fourier transformed back to the absorption-frequency spectrum by the computer.

3.3.7 X-ray photoelectron spectroscopy (XPS)

XPS is a type of secondary electron resulted from photo-electron effect. Different from those generated by an electron beam in a SEM, these electrons are generated by a monochromatic X-ray radiation, e.g. Al Kα (1486.7 eV), and range from zero to the energy of the source. By retarding and focusing these photoelectrons to a slit using a series of voltage bias and electromagnetic lens, the counts of the electrons of a specific kinetic energy can be recorded by a hemisphere analyzer. By scanning the retarding voltage bias and using a single channeltron or by using a micro-channel plate and a proper calibration of the hemisphere analyzer, an energy spectrum (XPS) can be obtained in a scan-mode or a snapshot-mode. The difference between the X-ray radiation and the recorded energies gives directly the binding energies of electrons at certain atomic levels within the material. The spectrum are made of three key components: valence band region that starts from zero binding energy to tens of eV;

peaks that could either be photoelectrons or Auger electrons (a two electron process involves one electron fill in the core-level hole created by the X-ray photon and the other knocked out of its energy level at the same time); background that stands up immediately after a peak along the binding energy increase direction and that are resulted from the inelastic scattering of the photo electrons corresponding to that peak. Depending on the chemical environment (the coordination and oxidation state) and the final after the photo-electron event, the peaks can vary position, shape and can have satellite peaks.

3.4 Theoretical calculations

The theoretical calculations in this thesis were performed through the density functional theory (DFT) using the projector augmented plane-wave method, as implemented in the Vienna Ab initio Simulation Package (VASP). The generalized gradient approximation proposed by Perdew, Burke, and Ernzerhof (GGA-PBE) was utilized for the exchange-correlation functional. The plane-wave energy cut-off was set to 400 eV, and the Brillouin zone calculations were carried out on a k-point mesh of 2×1×2. During the optimization, the total energy convergence was set to 10^{-5} eV in an iterative solution of the Kohn-Sham equation, and the structures were relaxed until the residual forces on the atoms were smaller than 0.03 eV/Å. The Brillouin-zone integration was sampled by the single Γ point. The DFT-D3 mode was employed to simulate the van der Waals interaction.

3.5 Electrochemical measurements

3.5.1 Cyclic voltammetry (CV)

CV is an important potentiodynamic technique to evaluate the redox reactions of the battery system. In a typical test, a cyclic potential is applied with a constant scanning

rate, and oxidation/reduction peaks can be verified. Repeated cycles are normally conducted during the test to illustrate the change or reversibility of the peaks. This method is a very useful way to investigate redox reactions in battery system, the electron stoichiometry, and polarization and electrochemical behaviors. In this thesis, the CV curves were obtained by a two-electrode coin cell model, where Zn foil was applied as both the counter electrode and reference electrode. All the CV measurements were conducted on a Biologic VMP-3 electrochemical workstation.

3.5.2 Galvanostatic charge and discharge

Galvanostatic charge/discharge tests are applied to investigate the electrochemical performance of the battery system in this thesis. Generally, this measurement technique is conducted at a constant current density and a specified voltage window. It is widely used to evaluate the charge/discharge capacity, cycling stability, as well as rate performance of the battery system. The charge/discharge capacity is estimated via the applied current and the accumulated time during electrochemical process. Galvanostatic charge/discharge characterizations in this thesis were performed on a NEWARE battery tester.

3.5.3 Electrochemical impedance spectroscopy (EIS)

EIS technique is an effective characterization to illustrate the electrochemical resistance of the battery system. Through data fitting, the ohmic resistance and the charge transfer resistance could be estimated. The typical impedance spectrum normally displays a high-frequency semicircle and a low-frequency linear tail. The semicircle gives information about the kinetic process, which indicates the impedance of charge transfer. The linear diagram reflects the diffusion of ions migrating from the electrolyte into the bulk electrode. Moreover, it is a meaningful method to estimate activation energies of

electrodes via Arrhenius curves fitted at different temperatures. In this thesis, EIS was implemented using a Biologic VMP-3 electrochemical workstation.

Chapter 4

Electrolyte design for *in-situ* construction of highly Zn^{2+}-conductive solid electrolyte interphase to enable high-performance aqueous Zn-ion batteries under practical conditions

4.1 Introduction

Along with the rapidly increasing demands of sustainable and clean energy applications, tremendous efforts have been devoted to developing battery systems beyond Li-based batteries because of the rare and expensive nature of Li resources.[1, 2] Among them, aqueous Zn-ion batteries (AZIBs) have emerged as one of the most promising alternatives for economical and large-format energy deployment due to their intrinsic properties of low cost, environmental friendliness, and non-flammability.[3-5] The Zn metal anode for AZIBs possesses particularly significant advantages due to the high abundance, low toxicity, and high theoretical capacity of zinc (820 mA h g^{-1} and 5855 Ah L^{-1}).[6-8] Its notorious dendrite formation and side reactions (e.g. corrosion, passivation, and H_2 evolution), however, induce inferior Zn plating/stripping Coulombic efficiency (CE), low utilization of Zn electrodes, and short lifespans.[9-12]

Several strategies have been proposed to improve the reversibility and durability of Zn electrodes, including optimization of the Zn electrode structure,[9, 13-15] introduction of artificial protective layers,[16, 17] and electrolyte formulation.[18-20] Constructing nanostructured Zn electrodes has been proved to be an effective strategy to alleviate the dendrite growth. The complex fabrication process, low density, decreased capacity, and surface-dependent side reactions (e.g. corrosion, hydrogen evolution), however, make these approaches questionable for practical applications. Building an artificial solid electrolyte interface (SEI) could restrain the side reactions by blocking the electrolyte

from the Zn electrode surface. Such unstable SEI layers, however, are inclined to be damaged and detached from the Zn surface during electrochemical cycling, due to the repeated large volume changes of Zn metal.[21] Furthermore, due to their low ionic conductivities, low Zn-ion transference numbers ($t_{Zn^{2+}}$), and poor interfacial contact with Zn, the artificial SEI layers have only a limited effect on dendrite suppression, inevitably causing an unsatisfactory CE. Although various electrolytes and additives have also been employed to improve the CEs and cycle life, the lack of a stable and effective SEI protective layer has hindered their success. On the other hand, highly concentrated ("water-in-salt") electrolytes were introduced to reduce the water-induced side reactions and enhance the reversibility of Zn plating/stripping by significantly reducing the H_2O activity in solution.[18, 22] Nonetheless, the high cost, high viscosity, and poor wettability of the highly concentrated electrolytes are preventing their practical application.[15]

The critical issue rooted in Zn metal in aqueous electrolytes is the lack of an appropriate SEI protective layer. As is well-known in the case of organic-electrolyte batteries, the *in-situ* formation of an SEI layer in the first few cycles is crucial to suppress the further consumption of electrolyte, stabilize the metal anode, and maintain high CEs.[23, 24] Nevertheless, building an SEI layer *in situ* on Zn electrode in water-based electrolyte is highly challenging. It is well established that the *in-situ* formation of an SEI layer at the electrode surface may be derived from the decomposition of electrolyte components and/or salt anions. In aqueous electrolytes, however, the water decomposition generates detrimental gases instead of precipitates, and the salt anions are difficult to decompose due to the relatively high reduction potential of Zn deposition (-0.76 V vs. the standard hydrogen electrode (SHE)) and restricted voltage windows of water.[25, 26] Although the parasitic H_2 evolution during Zn deposition increases the local pH value and triggers

the formation of passivation layers (e.g. ZnO), the thus-formed passivation layers are insulating and loose, and cannot be used as the functional SEI layer.[27, 28] In contrast, *in-situ* SEI layers have been demonstrated in Zn-based batteries with organic-aqueous hybrid electrolytes,[21] deep eutectic electrolytes,[26] and organic electrolytes.[29] The introduction of organic species into the electrolytes, however, increases the de-solvation barriers for Zn deposition, and to some extent, abandons the original advantages of conventional water-based electrolytes, including high safety, low price, and environmental compatibility. To date, *in-situ* SEI engineering for Zn electrodes in aqueous electrolytes remains a huge challenge, and a feasible design principle for achieving *in-situ* SEI layers is in great demand for aqueous Zn chemistry.

Another critical issue for the practical application of AZIBs is the lack of testing protocols regarding the current density, plating/stripping capacity, electrolyte amount, and areal capacity of the cathode, when evaluating the performance of viable Zn electrodes and AZIBs.[30] Specifically, two significant indicators, the electrolyte-to-capacity ratio (E/C) and the capacity ratio of the negative electrode to the positive electrode (N/P) have not been taken into consideration for most reported AZIBs. It is well known that the testing conditions have a significant effect on the Zn anode performance.[31, 32] Under long-term cycling, the unfavourable Zn dendrites, dead Zn, and side reactions proliferate at the electrode-electrolyte interface, leading to continuous consumption of the active Zn and electrolyte.[33] In most previous reports on AZIBs, however, greatly excessive Zn anode and flooded electrolyte were used to expand their cycle life, which not only mask the problem of low Zn utilization and electrolyte-induced side reactions, but also make the results difficult to compare and interpret. Attaining long-term cyclability of AZIBs under practical conditions is urgently needed for the development of rechargeable AZIBs for real applications.

Herein, unlike the traditional wisdom involved in designing *in-situ* SEI layers via the decomposition of solvent and/or salt anions, we report a novel electrolyte design principle to enable an *in-situ* SEI protective layer on aqueous Zn electrode for the first time. As aforementioned, the Zn electrode surface experiences a local pH increase, stemming from H_2 side reactions during cycling. By turning this disadvantage into an advantage, we demonstrate the *in-situ* formation of a dense and uniform SEI layer of hopeite ($Zn_3(PO_4)_2 \cdot 4H_2O$) on the Zn surface by the simple addition of a small amount of $Zn(H_2PO_4)_2$ salt to the conventional aqueous electrolyte (1 M $Zn(CF_3SO_3)_2$). The *in-situ* formed hopeite SEI (thickness: ~ 140 nm) possesses high interfacial stability, a high Zn-ion transference number, and high Zn-ion conductivity, which not only restrains the side reactions via isolating the active Zn from the bulk electrolyte, but also ensures uniform and rapid Zn-ion transport kinetics for dendrite-free Zn deposition. As a result, the Zn electrodes in the designed electrolyte (DE) (1 M Zn $(CF_3SO_3)_2$ + 25 mM $Zn(H_2PO_4)_2$), exhibit significantly enhanced CE and cycling stability compared to those in the baseline electrolyte (BE) (1 M Zn $(CF_3SO_3)_2$), due to the side reaction-free and dendrite-free plating/stripping behaviour of the *in-situ* SEI protected Zn (denoted as SEI-Zn). Moreover, the proposed electrolyte design strategy is also feasible in the electrolyte for the $ZnSO_4$ system, suggesting the universality of this method to enable an *in-situ* SEI layer for a stable Zn electrode. More importantly, under practical testing conditions with ultrathin Zn anode (10 μm), low E/C (9 μL mAh^{-1}), and low N/P (2.3), the Zn/V_2O_5 full cell delivered high capacity retention of 94.4 % over 500 cycles. To the best of our knowledge, this work is not only the first success in building *in-situ* SEI layers in aqueous Zn chemistry, but also the first successful attempt to obtain high-performance AZIBs under practical conditions, opening up a new avenue towards advanced aqueous energy-storage applications.

4.2 Experimental section

4.2.1 Materials characterization

The crystalline structure of the electrodes was characterized by X-ray diffraction (XRD, PANalytical Empyrean, Cu Kα radiation). The morphologies of the electrodes were investigated using field emission scanning electron microscopy (FESEM, JEOL JSM-7500FA) along with energy dispersive X-ray spectroscopy (EDX) mapping. XPS measurements were conducted on an X-ray photoelectron spectrometer (Thermo Fisher K-Alpha system) under a vacuum of 2×10^{-6} Pa. All of the binding energies were referenced to the C 1s peak at 284.6 eV. Raman spectra were obtained through a Raman JY HR800 Spectrometer. Fourier transform infrared (FTIR) mapping was performed with a Spotlight 400 FTIR Imaging System (PerkinElmer). Cross-sectional focused ion beam (FIB)-SEM measurements were conducted on a FEI Helios Nanolab with a Ga^+ ion beam. *In-situ* observation of Zn plating was carried out using an ECC-Opto-Std test cell with an optical window. Atomic force microscopy (AFM) images were acquired in tapping mode using a Cypher ES AFM (Asylum Research, US). The ionic conductivity of the hopeite ($Zn_3(PO_4)_2 \cdot 4H_2O$) was measured by electrochemical impedance spectroscopy (EIS). Typically, commercial hopeite powder was pressed into a pellet with a diameter of 6 mm by a hydraulic press for approximately 10 min at ambient temperature. The thickness of the pellet was determined by calipers with multiple measurements. Gold was coated on both faces of the pellet using a sputter coater. The impedance spectrum of the pellet was obtained at 25 ℃ in the frequency range from 1 MHz to 10 mHz. The ionic conductivity of the hopeite was calculated based on the following equation:

$$\sigma = \frac{L}{R_b \cdot S} \qquad (1)$$

where L represents the thickness of the hopeite pellet, R_b represents the bulk resistance

obtained by EIS measurements, and *S* is the area. For the electronic conductivity measurement, the current response of the hopeite pellet under an applied voltage of 3 V was measured. The electronic resistivity of the hopeite was estimated according to the following equation:

$$\rho = \frac{R \cdot S}{L} = \frac{U \cdot S}{I \cdot L} \qquad (2)$$

Where *U* is the applied voltage, *S* is the area, *I* is the average current response, and *L* is the thickness of the hopeite pellet.

4.2.2 Electrochemical measurements

The electrochemical performance of the batteries in this work was evaluated using CR2032 coin-type cells on a Land BT2000 battery test system. The Zn stripping/plating test was implemented by using Zn/Zn symmetrical cells in the electrolytes with and without $Zn(H_2PO_4)_2$. Coulombic efficiency (CE) measurements were conducted on asymmetrical Zn/Cu cells. Electrochemical impedance spectroscopy (EIS) was performed using a Biologic VMP-3 electrochemical workstation within the frequency range from 10^5 to 10^{-2} Hz. Linear polarization measurements were carried out using a three-electrode system with bare Zn and SEI-Zn as the working electrode, Pt plate as the counter electrode, and Ag/AgCl as the reference electrode, respectively. The Zn/V_2O_5 full cells were galvanostatically cycled between 0.2 and 1.6 V vs. Zn/Zn^{2+} at different current densities, and the specific capacities were calculated based on the active mass of V_2O_5. Hydrophilic mixed cellulose membrane was used as the separator in the Zn/V_2O_5 full cells with controlled electrolyte volume. Cyclic voltammetry (CV) of the Zn/V_2O_5 cells was recorded on a Biologic VMP-3 electrochemical workstation between 0.2 and 1.6 V.

4.2.3 Computational methods

The theoretical calculations in this work were performed through the density functional theory using the projector augmented plane-wave method, as implemented in the Vienna Ab initio Simulation Package (VASP).[1] The generalized gradient approximation proposed by Perdew, Burke, and Ernzerhof (GGA-PBE) was utilized for the exchange-correlation functional.[2] The energy barriers for Zn ion diffusion in the hopeite were computed by the nudged elastic band method with 5 images. The plane-wave energy cut-off was set to 400 eV, and the Brillouin zone calculations were carried out on a k-point mesh of 2×1×2. During the optimization, the total energy convergence was set to 10^{-5} eV in an iterative solution of the Kohn-Sham equation, and the structures were relaxed until the residual forces on the atoms were smaller than 0.03 eV/Å.

4.3 Results and discussion

4.3.1 Electrolyte design and hopeite SEI formation

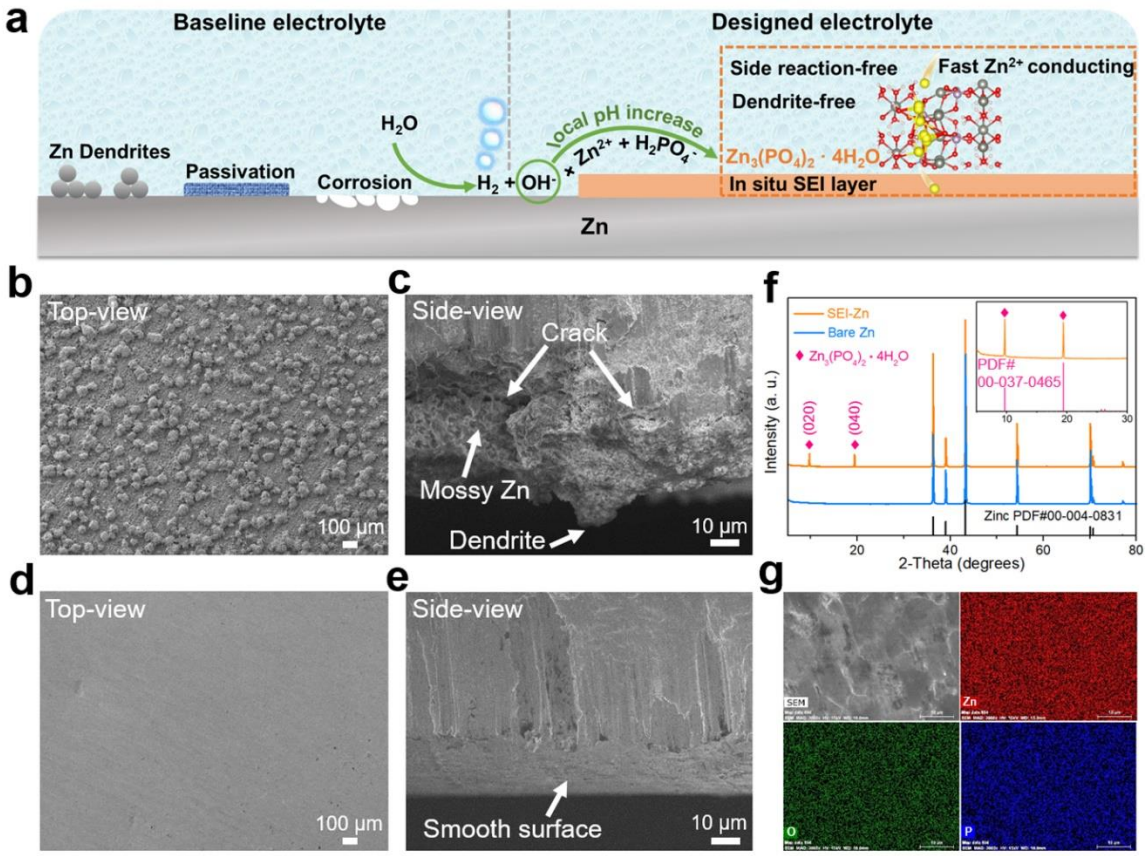

Figure 4.1 Schematic illustration of the Zn surface evolution and characterization of Zn electrodes in the baseline and designed electrolytes. (a) Schematic illustration of Zn surface evolution and the SEI formation mechanism. SEM images of Zn electrodes after 20 cycles in (b, c) the baseline electrolyte and (d, e) the designed electrolyte. The Zn electrodes were stripped out of their symmetrical cells after 20 cycles in 1 M $Zn(CF_3SO_3)_2$ with/without 25 mM $Zn(H_2PO_4)_2$ as electrolyte, respectively. The applied current density was 1 mA cm^{-2}, and the areal capacity was 1 mA h cm^{-2}. (f) XRD patterns of Zn electrode before and after 20 cycles in the designed electrolyte, with enlargement in the inset. (g) EDX mapping of the SEI-Zn electrode in the designed electrolyte.

In conventional aqueous electrolytes for AZIBs, the major impediment facing Zn electrodes is the tip-effect-derived dendrite growth during cycling, which contributes to the accumulation of dead Zn and possible internal short circuits, as illustrated in Figure

4.1a. In addition, due to the poor thermodynamic stability of Zn metal in aqueous environments, the Zn corrosion reaction and competitive H_2 evolution are inevitable.[16] The H_2 generation leads to a local pH increase and continuous Zn consumption by generating a detrimental Zn^{2+} insulating passivation layer (e.g. ZnO). By utilizing the local pH change derived from H_2 evolution, however, a dense and Zn^{2+} conductive hopeite ($Zn_3(PO_4)_2 \cdot 4H_2O$) film can be formed and coated on the Zn surface in the designed electrolyte with $Zn(H_2PO_4)_2$. The *in-situ* formation mechanism of the SEI film can be described as follows:

$$2H_2O + 2e^- \rightarrow H_2\uparrow + 2OH^- \quad (3)$$

$$2H_2PO_4^- + 4OH^- + 3Zn^{2+} \rightarrow Zn_3(PO_4)_2 \cdot 4H_2O\downarrow \quad (4)$$

Specifically, the electrochemical parasitic reaction (3) of H_2 evolution during Zn deposition increases the concentration of OH^- at the electrode-electrolyte interface. In the electrolyte with $Zn(H_2PO_4)_2$ addition, the increased OH^- concentration causes chemical reaction (4), leading to precipitation of a $Zn_3(PO_4)_2 \cdot 4H_2O$ film.

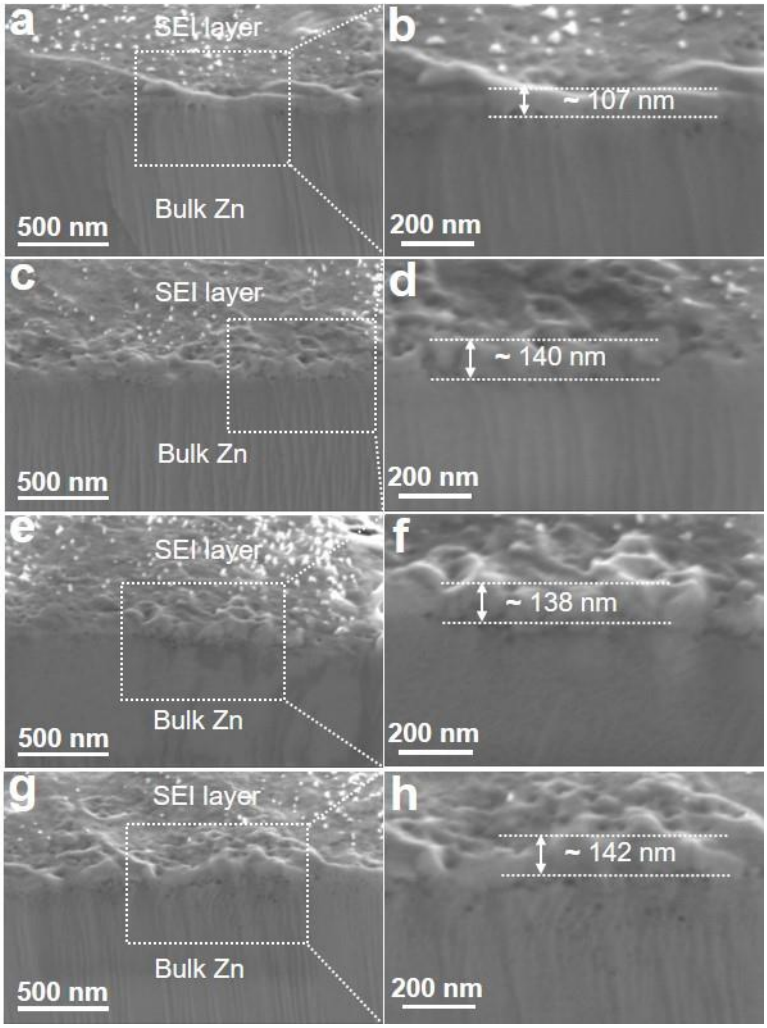

Figure 4.2 Cross-sectional focused ion beam (FIB)-SEM images of the SEI-Zn electrode after (a, b) 10 cycles, (c, d) 20 cycles, (e, f) 30 cycles, and (g, h) 50 cycles. The Zn electrodes were stripped out of symmetrical cells after specific cycles (1 mA cm^{-2}, 1 mA h cm^{-2}) in the designed electrolyte.

The morphology of Zn electrodes after cycling in the baseline and designed electrolytes is shown in both top-view and side-view scanning electron microscope (SEM) images. The cycled Zn electrodes in the baseline electrolyte (Figure 4.1b, c) present obvious cracks and a rough surface with mossy and dendritic Zn. In contrast, in the designed electrolyte, a smooth Zn electrode surface with a dense SEI layer can be observed (Figure 4.1d, e). The SEI-Zn electrode was characterized by X-ray diffraction (XRD)

(Figure 4.1f), which clearly shows the emerging characteristic peaks of hopeite (PDF no. 00-037-0465) at 9.7° and 19.4°, corresponding to the (020) and (040) planes, respectively. The thickness of the hopeite SEI layer formed *in situ* on the Zn surface was maintained at around 140 nm after 20 cycles, as measured by cross-sectional focused ion beam (FIB)-SEM (Figure 4.2). The composition of the SEI layer was further probed by Raman analysis (Figure 4.3), and Fourier transform infrared (FTIR) micro-spectroscopy (Figure 4.4). The Raman spectrum in Figure 4.3 shows the typical orthophosphate bands at 583, 934, 986, 1065, and 1146 cm^{-1}, which are ascribed to lattice vibrations of P-O and P=O in the hopeite structure. The FTIR mapping in Figure 4.4 displays an even surface absorbance distribution of the SEI-Zn electrode, indicating homogenous coating of the *in-situ* SEI layer on the Zn surface. The corresponding FTIR spectrum shows strong characteristic absorption peaks of the PO_4^{3-} group from 900 to 1200 cm^{-1}. The broad adsorption peaks at ~3250 and ~1600 cm^{-1} can be attributed to O-H stretching vibrations and H_2O molecule bending vibrations from the adsorption of water and crystal water in the hopeite structure.[34]

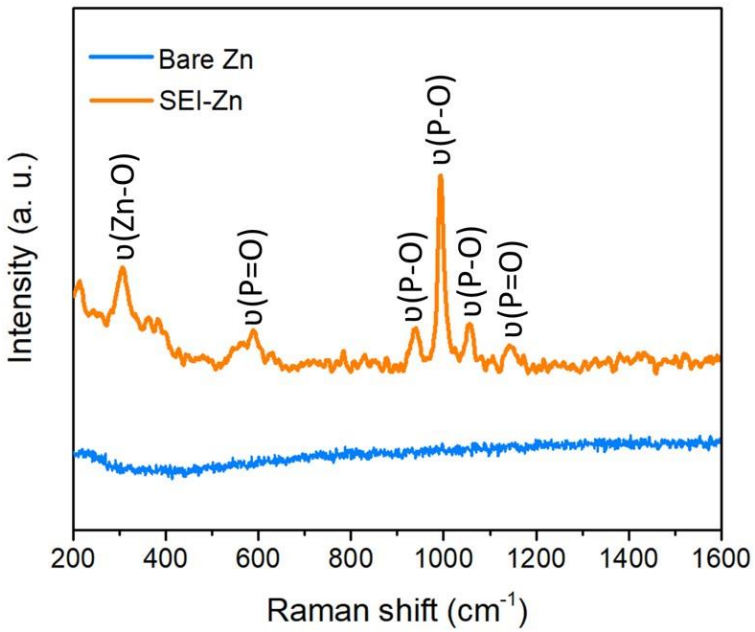

Figure 4.3 Raman spectra of the SEI-Zn electrode and bare Zn. The Zn electrode was stripped out of its symmetrical cell (1 mA cm^{-2}, 1 mA h cm^{-2}) after 20 cycles in the designed electrolyte.

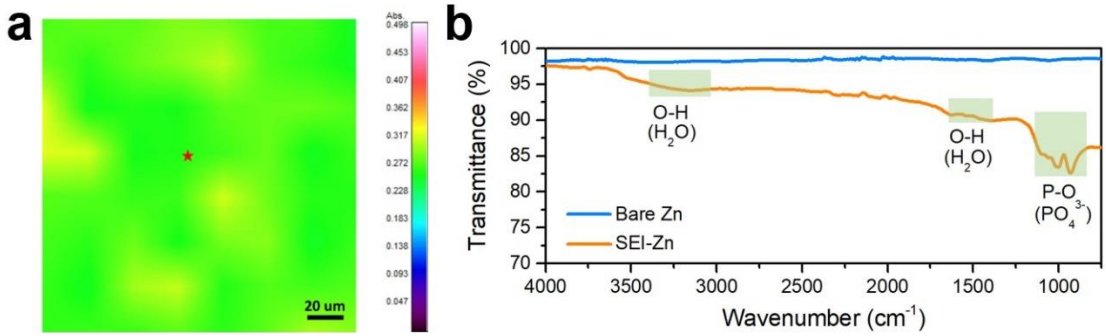

Figure 4.4 FTIR characterization of the SEI-Zn electrode. (a) FTIR mapping of the SEI-Zn electrode, (b) FTIR spectra of a bare Zn electrode and the SEI-Zn electrode for the marked point in A. The Zn electrode was stripped out of its symmetrical cell after 20 cycles (1 mA cm^{-2}, 1 mA h cm^{-2}) in the designed electrolyte.

The energy dispersive X-ray spectroscopy (EDX) mapping of the SEI-Zn electrode in Figure 1g indicates uniform distributions of Zn, P, and O on the Zn surface. The concentration of $Zn(H_2PO_4)_2$ in the designed electrolyte was fixed at the optimized

molarity of 25 mM in this work, based on the integrity and uniformity of the *in-situ* SEI film (Figure 4.5), as well as the Zn plating/stripping stability (Figure 4.6). With a low concentration of 10 mM $Zn(H_2PO_4)_2$, the Zn electrode possessed an incomplete SEI coating layer. On increasing the concentration to 100 mM, the SEI layer was inclined to be broken. A relatively dense and intact SEI layer was detected for 25 and 50 mM $Zn(H_2PO_4)_2$ additions. The electrolytes with $Zn(H_2PO_4)_2$ additive displayed a slightly lower pH than the baseline electrolyte as shown in Table 4.1, although the formation of the *in-situ* SEI layer ($Zn_3(PO_4)_2 \cdot 4H_2O$) on the surface of Zn electrode can block the mild acidic electrolyte from reaching the Zn anode, which restrains the side reactions of H_2 evolution and corrosion.

Table 4.1 The pH of electrolytes with different $Zn(H_2PO_4)_2$ concentrations.

Electrolyte	pH
1 M $Zn(CF_3SO_3)_2$	4.2
1 M $Zn(CF_3SO_3)_2$ + 10 mM $Zn(H_2PO_4)_2$	3.3
1 M $Zn(CF_3SO_3)_2$ + 25 mM $Zn(H_2PO_4)_2$	3.1
1 M $Zn(CF_3SO_3)_2$ + 50 mM $Zn(H_2PO_4)_2$	3.0

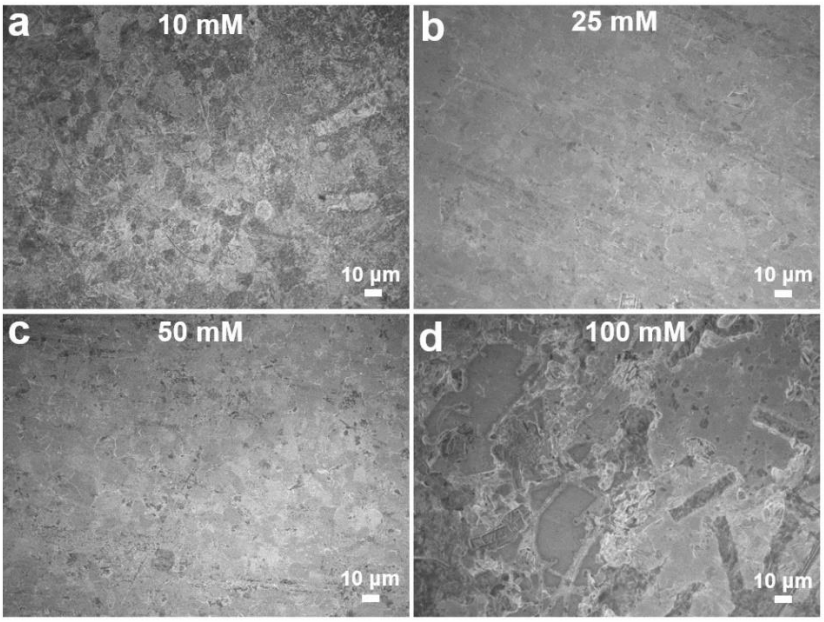

Figure 4.5 SEM images of cycled Zn electrodes in electrolytes consisting of 1 M $Zn(CF_3SO_3)_2$ with different $Zn(H_2PO_4)_2$ concentrations. (a) 10 mM, (b) 25 mM, (c) 50 mM, and (d) 100 mM. The Zn electrodes were stripped out of the symmetrical cells after 20 cycles at 1 mA cm^{-2} with areal capacity of 1 mA h cm^{-2}.

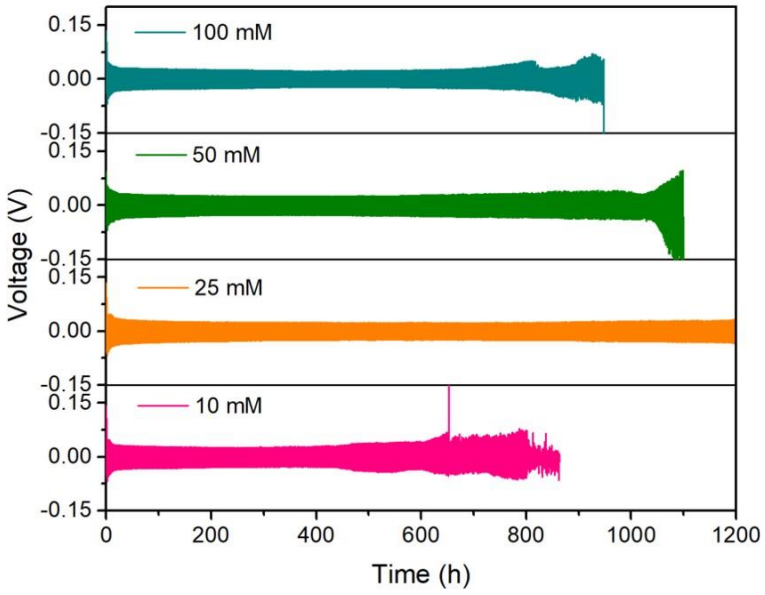

Figure 4.6 Comparison of the cycling stability of Zn electrodes in 1 M $Zn(CF_3SO_3)_2$ with different concentrations of $Zn(H_2PO_4)_2$. The Zn symmetric cells were cycled at 1 mA cm^{-2} with the areal capacity of 1 mA h cm^{-2}.

4.3.2 High interfacial stability and fast Zn-ion transport property

Zn corrosion reactions, including H_2 evolution and dissolved O_2-induced passivation reactions, are regarded as an important degradation mechanism of Zn electrode.[14, 18] The effect of the *in-situ* SEI layer on Zn corrosion was confirmed by linear polarization measurements (Figure 4.7a). Compared to the bare Zn, the corrosion potential of the SEI-Zn increased from -0.949 V to -0.945 V, reflecting less tendency towards corrosion reactions. Remarkably, the SEI layer reduced the corrosion current by 372.63 μA cm^{-2}, indicating a lower corrosion rate. The results agree well with the fact that hopeite is the main component of the industrial phosphating coating technique for metal surface treatment to prevent its corrosion.[35]

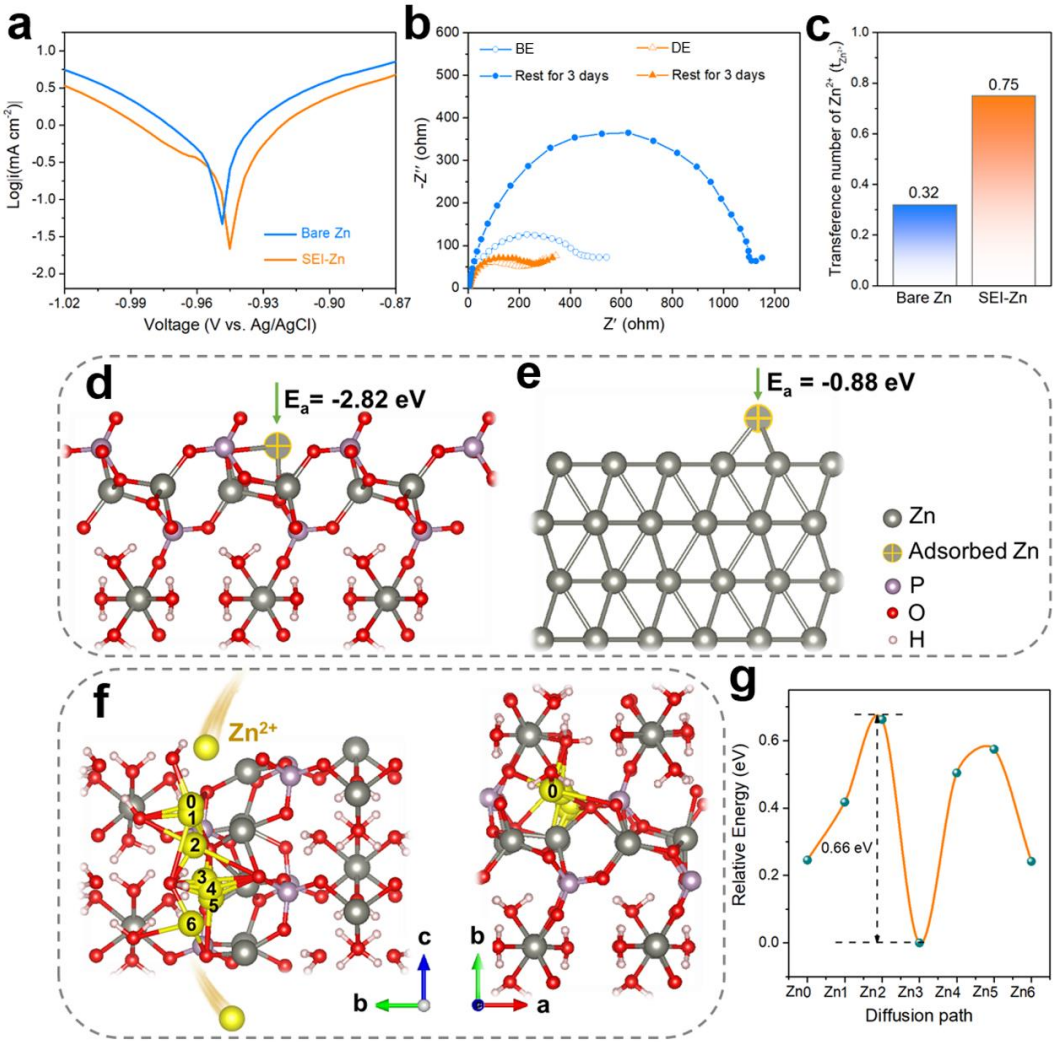

Figure 4.7 Interfacial stability and Zn-ion transport property of the *in-situ* SEI layer. (a) Linear polarization curves showing the corrosion on bare Zn and SEI-Zn electrodes. The SEI-Zn electrode was stripped out of its symmetrical cell after 20 cycles in the designed electrolyte. (b) EIS spectra of the Zn symmetric cells (cycled for 20 cycles at 1 mA cm^{-2}) in the baseline and designed electrolytes before and after rest for 3 days. (c) Comparison of the Zn-ion transference number of a bare Zn electrode and a SEI-Zn electrode. Calculated models of the interaction between a foreign zinc ion and the surfaces of (d) the SEI layer and (e) the bare Zn electrode. First-principles calculations of (f) the optimum Zn-ion diffusion pathway in the SEI layer and (g) the corresponding migration energy barrier.

Moreover, the validity of the hopeite SEI layer for improving the stability of Zn electrode was also evaluated by electrochemical impedance spectroscopy (EIS) (Figure 4.7b). After rest for three days, the impedance of the Zn symmetric cell in the baseline electrolyte was almost triple the initial value. In the designed electrolyte, however, the SEI-Zn symmetric cell exhibited a steady charge-transfer resistance of ~ 230 Ω. This result indicates that the SEI layer formed in the designed electrolyte acts as a barrier, which effectively alleviates unfavourable (electro-)chemical side reactions between the aqueous electrolyte and the Zn metal electrode, and consequently ensures superior interfacial stability. The hydrophilicity of the SEI layer on Zn was evaluated by contact angle tests at ambient temperature (Figure 4.8). Compared with bare Zn electrode, the SEI-Zn electrode exhibited significantly enhanced hydrophilicity, which was favourable for homogeneous Zn deposition by reducing the interfacial free energy between the Zn electrode and the electrolyte.[33]

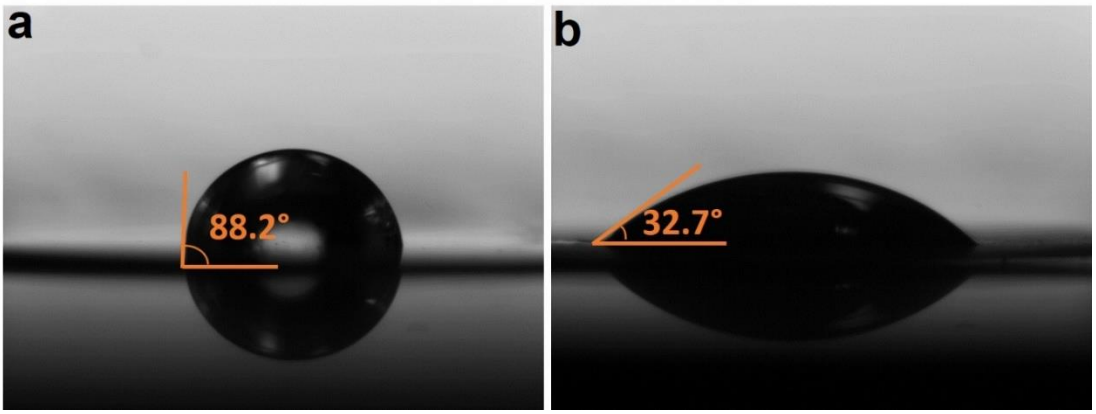

Figure 4.8 Contact angle measurements of the electrolyte on (a) bare Zn foil and (b) SEI-Zn foil.

The ion-transport property of SEI is a critical parameter for effective metal anode protection.[36,37] A Zn-ion transference number ($t_{Zn^{2+}}$) measurement was first conducted to describe the Zn^{2+}-conduction in the SEI layer. Generally, a low $t_{Zn^{2+}}$ is

likely to give rise to a large Zn^{2+} concentration gradient near the Zn electrode surface, thus leading to a strong interfacial electric field and detrimental dendrite propagation.[37] This becomes even more severe as the current density increases. Due to the slower migration rate of solvated Zn^{2+} than that of the counter-ions, the $t_{Zn^{2+}}$ of a bare Zn symmetrical cell was evaluated to be as low as 0.32, which is consistent with previous reports.[17] Notably, as shown in Figure 4.7c, in the case of the SEI-Zn electrode, the $t_{Zn^{2+}}$ was dramatically improved to 0.75. A detailed data analysis of the $t_{Zn^{2+}}$ results is provided in the Figure 4.9 and Table 4.2. The significant improvement of $t_{Zn^{2+}}$ suggests that the protective SEI layer on Zn electrode can effectively retard detrimental ions and suppress the formation of Zn dendrites.

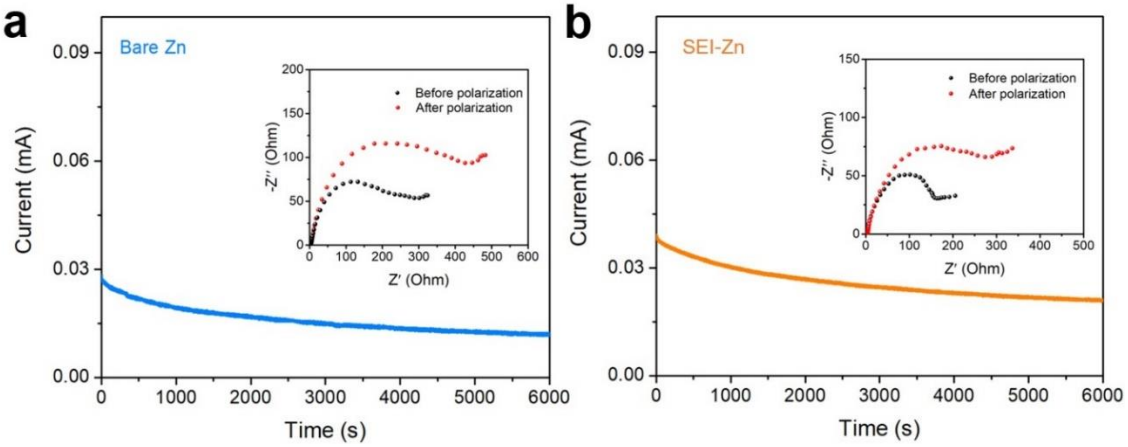

Figure 4.9 Measurements of Zn^{2+} transference number. Current-time plots of Zn symmetric cells with (a) bare Zn and (b) SEI-Zn after polarization at a constant potential (10 mV) for 6000 s. The insets are the impedance spectra before and after polarization.

The transference number of Zn^{2+} ($t_{Zn^{2+}}$) was evaluated by the following equation:

$$t_{Zn^{2+}} = \frac{I_s(\Delta V - I_0 R_0)}{I_0(\Delta V - I_s R_s)} \qquad (5)$$

where ΔV is the constant polarization voltage applied (10 mV here), I_0 and R_0 are the initial current and resistance, and I_s and R_s are the steady-state current and resistance,

respectively.

Table 4.2 The currents and resistances obtained before/after polarization for the calculation of the Zn-ion transference number.

	I_0 (mA)	I_s (mA)	R_0 (Ω)	R_s (Ω)	$t_{Zn^{2+}}$
Bare Zn	0.026	0.012	281	509	0.32
SEI-coated Zn	0.039	0.022	165	332	0.75

Additionally, the ionic conductivity of the hopeite was evaluated by electrochemical impedance spectroscopy at room temperature (Figure 4.10). Commercial hopeite powder was pressed into a pellet (6 mm diameter) and coated with gold on both faces using a sputter coater. The ionic conductivity of the hopeite can be calculated based on the following equation:

$$\sigma = \frac{L}{R_b \cdot S} \qquad (6)$$

where L is the thickness of the hopeite pellet (0.55 mm in this work), S is the area (0.28 cm^2 in this work), and R_b is the bulk resistance (2690 Ω, as fitted in Supplementary Figure 11). A high value of 7.2×10^{-5} S cm^{-1} was evaluated, in line with previous reports that hopeite is an ambient-temperature high Zn^{2+}-conductive solid electrolyte.[38]

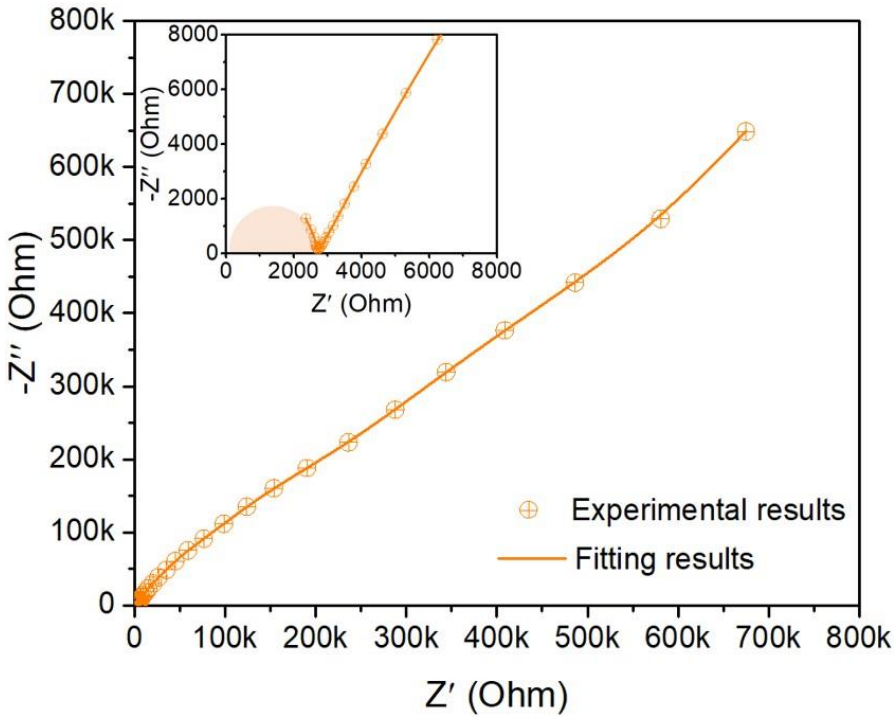

Figure 4.10 Ionic conductivity test of the hopeite. A Nyquist plot of the hopeite was obtained to determine the ionic conductivity, and the inset is the corresponding enlargement of the indicated range.

Moreover, the activation energies for the de-solvation of Zn^{2+} in the process of Zn plating were simulated by Nyquist plots of symmetric cells at different temperatures (Figure 4.11). The SEI-Zn exhibited lower activation energy (33.4 kJ mol^{-1}) than that of bare Zn (41.7 kJ mol^{-1}), indicating fast de-solvation of Zn^{2+} enabled by the SEI layer on the Zn surface.[14, 39] Accordingly, the SEI layer on the Zn electrode can offer rapid Zn^{2+} transport highways and enable fast reaction kinetics.

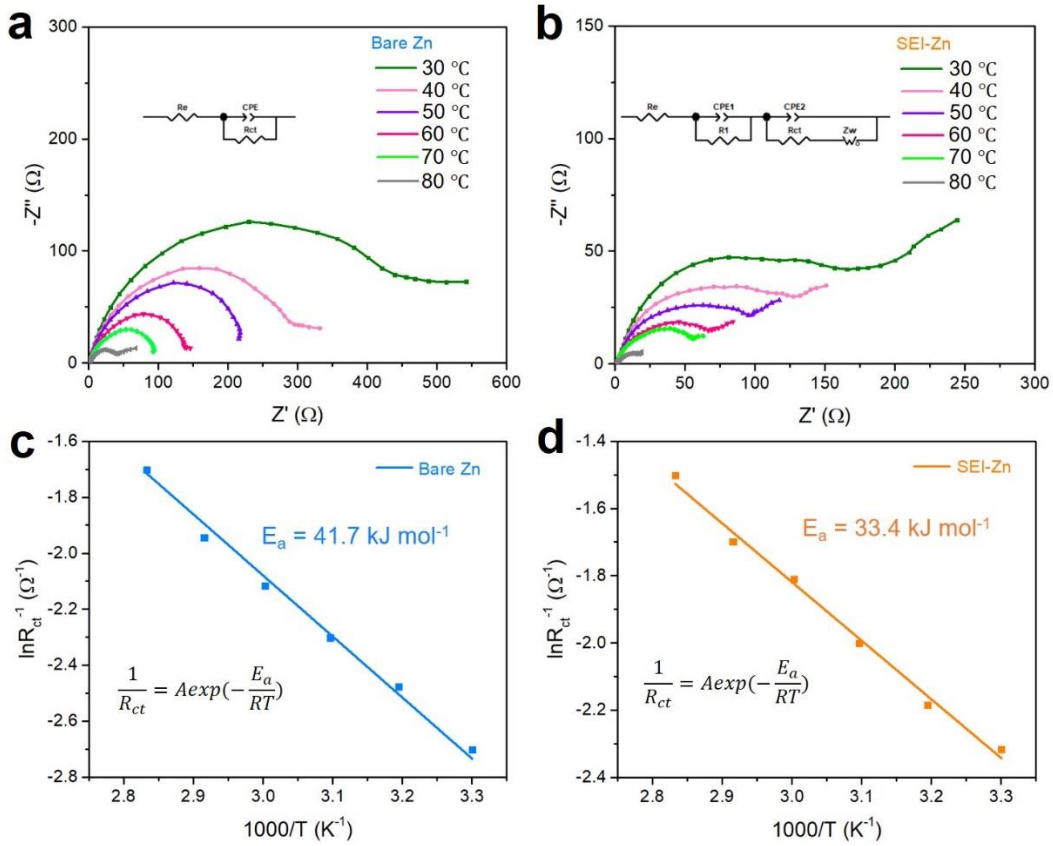

Figure 4.11 Nyquist plots and corresponding Arrhenius curves of Zn symmetric cells at different temperatures. (a, c) bare Zn, (b, d) SEI-Zn.

The electronic resistivity of hopeite was measured to be 9.4×10^7 Ω cm (that is, the electronic conductivity $\sigma = 1.1 \times 10^{-8}$ S cm^{-1}) (Figure 4.12), indicating its electronically insulating nature.

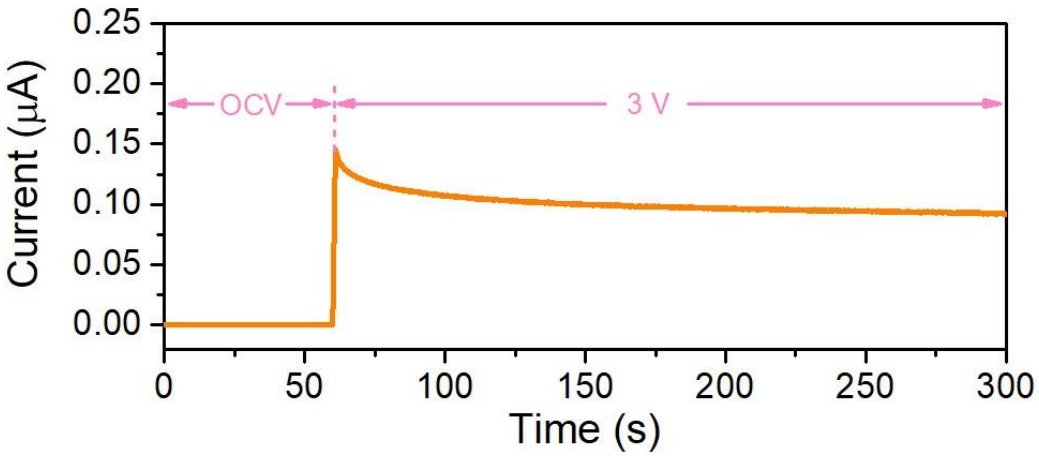

Figure 4.12 Electronic conductivity test of the hopeite.

For the electronic conductivity measurement, the current response of the hopeite under an applied voltage of 3 V was measured (Figure S20). The electronic resistivity of the hopeite was estimated according to the following equation:

$$\rho = \frac{R \cdot S}{L} = \frac{U \cdot S}{I \cdot L} \quad (7)$$

Where U is the applied voltage (3 V in this work), S is the area (0.28 cm^2 in this work), I is the average current response (0.12 μA, as measured in Supplementary Figure 12), and L is the thickness of the hopeite pellet (0.74 mm in this work). The calculated value of the electronic resistivity for the hopeite is 9.4×10^7 Ω cm (that is, the electronic conductivity $\sigma = 1.1 \times 10^{-8}$ S cm^{-1}). The electronically-insulating property of the hopeite SEI layer is significant for forming the necessary potential gradient across the SEI to drive Zn^{2+} transfer through the layer.[40, 41]

To gain insight into the role of the hopeite SEI layer in Zn transport and deposition processes at the electrolyte-electrode interface, density functional theory (DFT) calculations were performed. Figure 4.7d shows the calculated models of the interaction between a foreign zinc ion and the (010) surface of the SEI layer. The SEI layer manifested a strong adsorption capability towards Zn^{2+} with a considerable binding energy of -2.82 eV, much higher than that of the bare Zn electrode (-0.88 eV) (Figure 4.7e). The weak interaction between a foreign Zn^{2+} ion and the bare Zn surface is prone to cause the formation of Zn dendrites.[42] In contrast, the favorable adsorption of Zn^{2+} on the SEI surface could effectively regulate a uniform Zn^{2+} flux towards the surface of the Zn electrode and hence facilitate homogeneous Zn deposition.[43] In addition to the strong interaction between Zn^{2+} and the SEI structure, a fast Zn^{2+} transport pathway in the SEI layer is also essential to ensure a dendrite-free Zn electrode. Figure 4.7f displays a facile Zn^{2+} diffusion channel in the SEI along the *c*-axis, with seven zinc migration sites tagged from Zn0 to Zn6. The corresponding Zn^{2+} diffusion energy barrier for this

pathway was calculated to be 0.66 eV (Figure 4.7g), which is a relatively low value considering the generally high energy barriers for multivalent-cation migration, such as 1.15 eV for Mg^{2+} diffusion in the olivine $FePO_4$ framework,[44] 1.1 eV for Mg^{2+} in V_2O_5,[45] and 1.4 eV for Al^{3+} in spinel Mn_2O_4.[46] After comprehensive consideration of the physicochemical properties and computational analysis discussed above, it is clear that the *in-situ* hopeite SEI on Zn electrode could ensure homogeneous and highly efficient Zn^{2+} diffusion behaviour, suppression of electrolyte-induced side reactions, and a dendrite-free Zn deposition pattern, resulting in enhanced stability and reversibility of the Zn electrode.

4.3.3 Electrochemical stability of Zn electrode

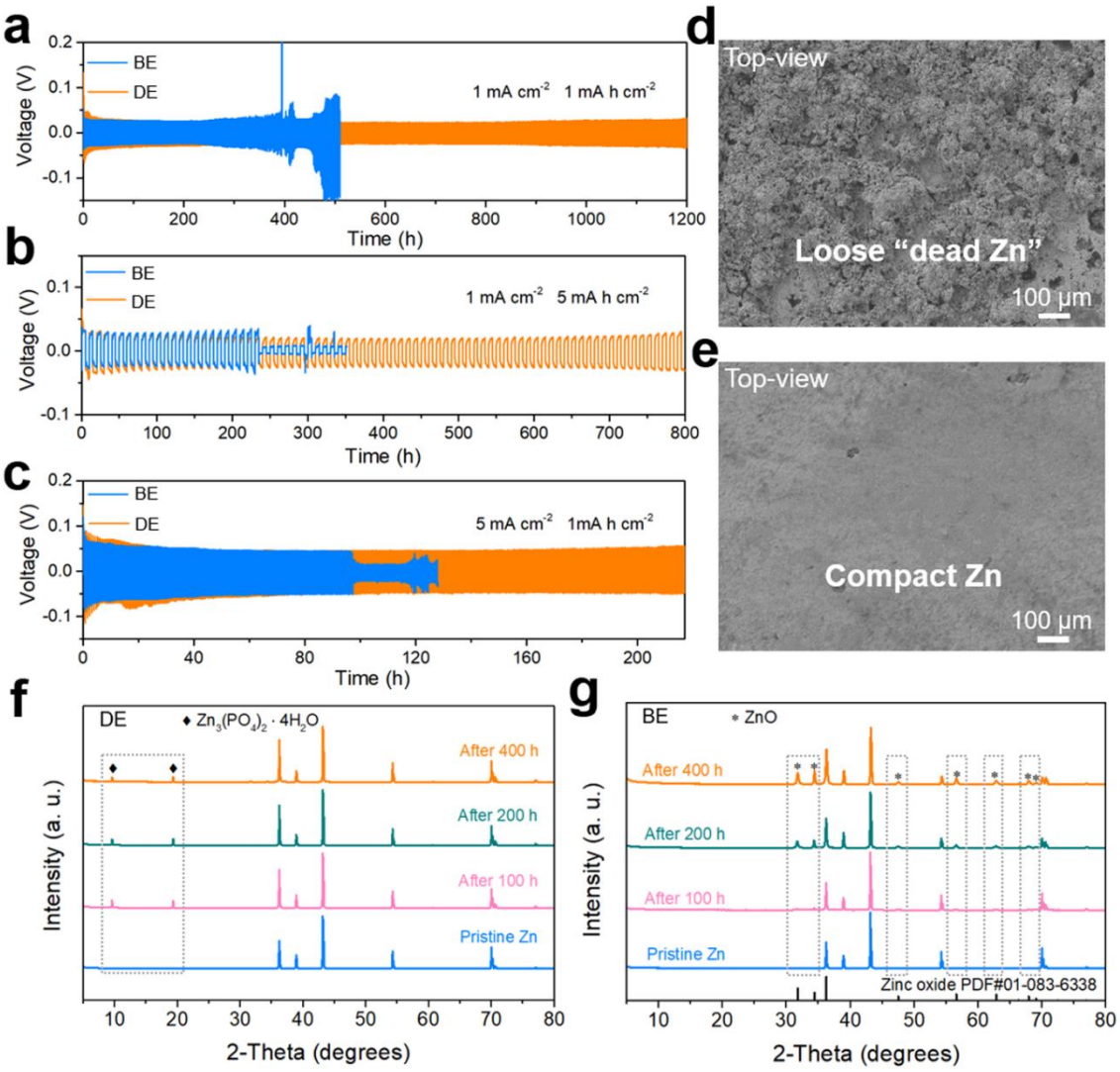

Figure 4.13 Plating/stripping cycling stability of Zn symmetric cells. Long-term galvanostatic cycling performance of symmetrical cells in the baseline and designed electrolytes at (a) 1 mA cm^{-2} and an areal capacity of 1 mA h cm^{-2}, (b) 1 mA cm^{-2} and an areal capacity of 5 mA h cm^{-2}, (c) 5 mA cm^{-2} and an areal capacity of 1 mA h cm^{-2}. SEM images of Zn electrodes after cycling for 400 hours in (d) the baseline electrolyte and (e) the designed electrolyte at 1 mA cm^{-2} with an areal capacity of 1 mA h cm^{-2}. XRD spectra of Zn electrodes in (f) the designed electrolyte and (g) the baseline electrolyte after specific cycling hours.

The efficacy of the hopeite SEI in the designed electrolyte towards improving the

electrochemical stability of Zn was first evaluated by long-term galvanostatic cycling of Zn/Zn symmetric cells. Under typical current density and areal capacity conditions (1 mA cm^{-2}, 1 mA h cm^{-2}), the overpotential of Zn plating/stripping in the designed electrolyte was slightly higher than that in the baseline electrolyte (about 80 mV versus Zn^{2+}/Zn) during the initial cycles (Figure 4.13a). The symmetric cell in the baseline electrolyte exhibited an irregularly fluctuating voltage profile after 400 h, however, and failed at 510 h, which is ascribed to the accumulation of "dead" Zn and detrimental side reactions. In contrast, benefiting from the hopeite SEI layer, the symmetric cell in the designed electrolyte showed highly reversible and stable cycling for 1200 h. To meet practical application requirements and further verify the effects of the SEI layer, increasing the plating/stripping capacity to 5 mA h cm^{-2} was also evaluated. As shown in Figure 4.13b, stable voltage polarization for 800 h was observed in the designed electrolyte, but a dendrite-induced short circuit occurred after approximately 240 h in the baseline electrolyte at a current density of 1 mA cm^{-2}. With an increase in the current density to 5 mA cm^{-2} (Figure 4.13c), the symmetrical cell in the designed electrolyte also remarkably outperformed the baseline electrolyte with long-term cycling for more than 200 h. The difference in cycling stability became increasingly prominent under more rigorous testing parameters (5 mA cm^{-2}, 5 mA h cm^{-2}). In addition, the rate performances of the symmetrical cells were investigated at different current densities from 0.5 to 10 mA cm^{-2} (Figure 4.14). For the symmetrical cell in the baseline electrolyte, unstable polarization and an adjacent short circuit occurred after cycling at high current densities, which are prone to accelerate the formation of Zn dendrites. Comparatively, the cell with the *in-situ* SEI protective layer in the designed electrolyte displayed a stable voltage profile, even with a high current density and areal capacity (10 mA cm^{-2}, 10 mA h cm^{-2}). These results further verified that the robust SEI layer

with a fast Zn^{2+} diffusion pathway formed in the designed electrolyte could offer homogeneous Zn deposition and ensure stable Zn plating/stripping.

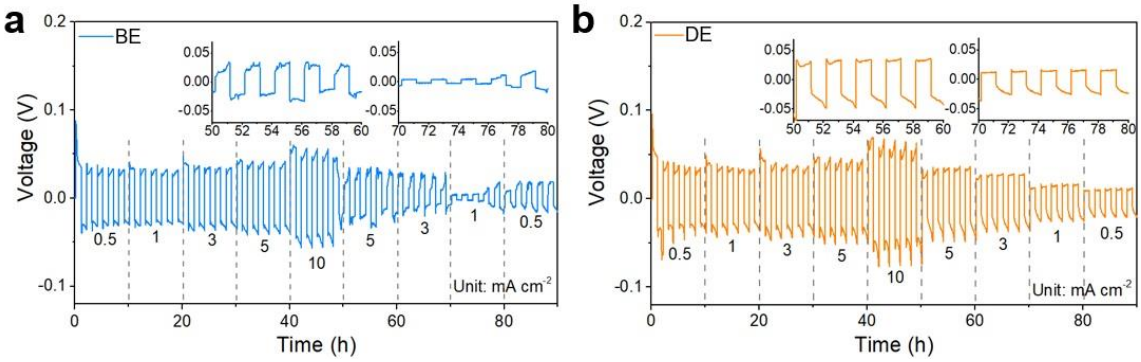

Figure 4.14 Rate performances of Zn symmetric cells. (a) The baseline electrolyte, (b) the designed electrolyte. The insets in (a) and (b) are the high-resolution voltage profiles at specific times.

The morphology evolution of the Zn electrode during long cycling provides strong evidence for the protective mechanism of the SEI film. The top-view SEM images (Figure 4.13d and Figure 4.15) and side-view SEM images (Figure 4.16) of the cycled Zn electrode in the baseline electrolyte display loose structures with massive amounts of dendritic Zn and thick "dead" Zn, in accordance with the polarization fluctuation mentioned above. In contrast, the Zn electrode in the designed electrolyte presented an ultra-flat and compact surface without any dendrites, even after long-term cycling for 400 h at 1 mA cm^{-2} (Figure 4.13e, Figures 4.15-16). This reveals that the uniform and Zn^{2+}-conductive SEI layer is stable enough to maintain its protective function during extended cycling.

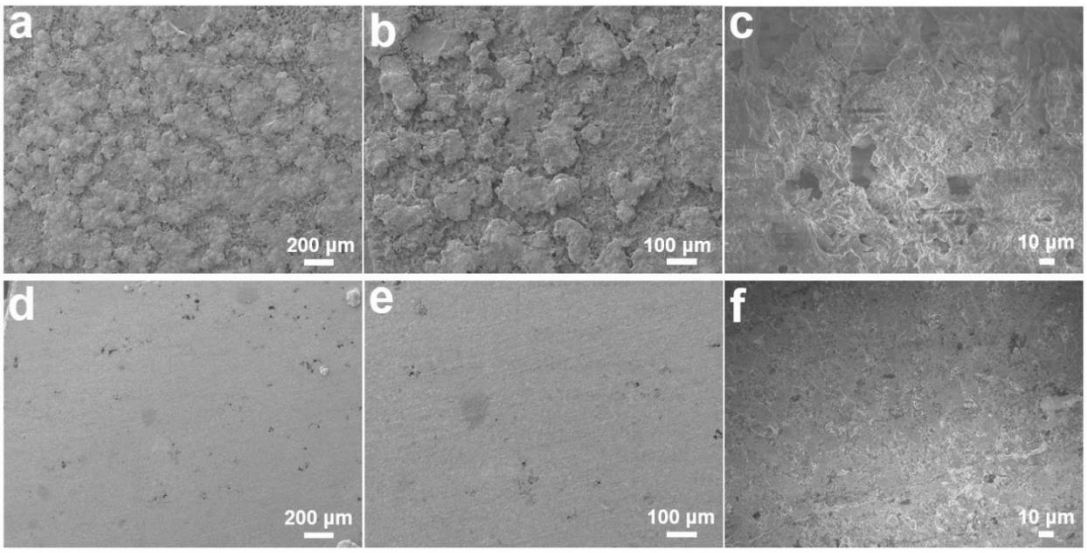

Figure 4.15 SEM images of Zn electrodes after cycling for 200 hours. (a-c) The baseline electrolyte, (d-f) the designed electrolyte. The applied current density was 1 mA cm^{-2}, and the areal capacity was 1 mA h cm^{-2}.

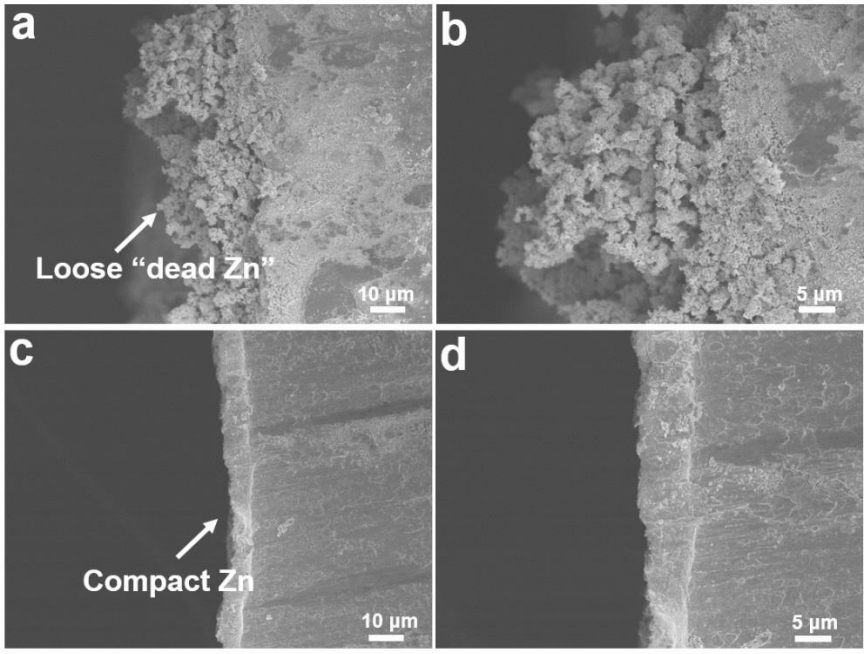

Figure 4.16 Cross-sectional SEM images of Zn electrodes after cycling for 400 hours. (a, b) The baseline electrolyte, (c, d) the designed electrolyte. The applied current density was 1 mA cm^{-2}, and the areal capacity was 1 mA h cm^{-2}.

Optical images of the cycled Zn electrodes in Figure 4.17 demonstrate that the surface of the Zn electrode gradually dimmed with cycling in the baseline electrolyte, and an obvious pulverization phenomenon could be observed, while the Zn electrode in the designed electrolyte still displayed a relatively smooth surface with metallic lustre, even after long cycling. In addition, electrochemical impedance spectroscopy (EIS) was performed on the Zn symmetrical cells at different stages, as shown in Figure 4.18. The smaller overall impedance of the Zn electrode in the designed electrolyte compared to that in the baseline electrolyte could be ascribed to the superior stability and interfacial compatibility of the SEI layer, which facilitated high-efficiency Zn^{2+} transport and minimized side reactions (e.g. gas evolution, passivating by-products) on the interface between the electrolyte and the Zn electrode.

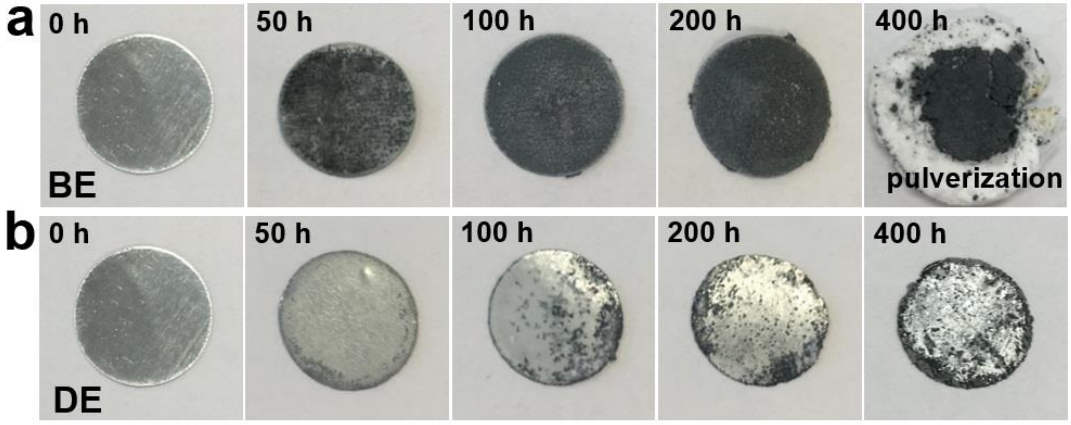

Figure 4.17 Digital images of cycled Zn metal electrodes. The Zn electrodes were stripped out of the symmetrical cells after cycling for different numbers of hours in (a) the baseline electrolyte and (b) the designed electrolyte.

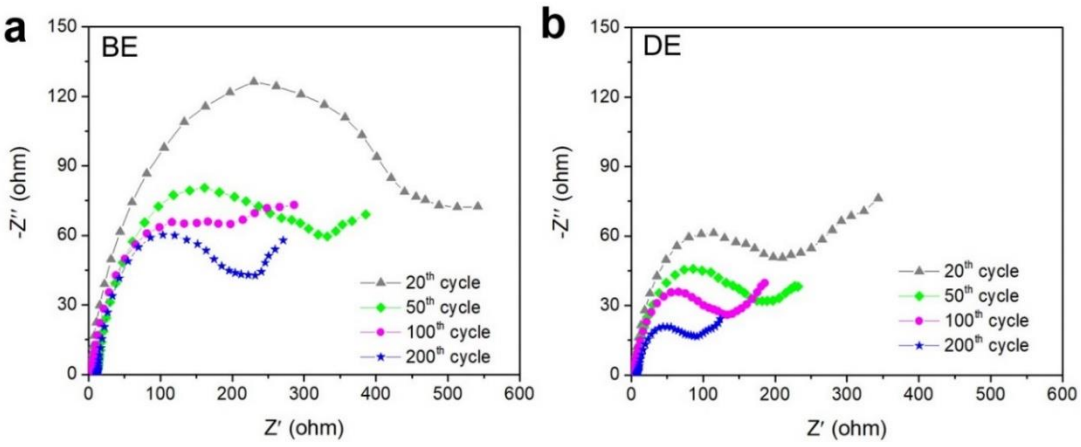

Figure 4.18 EIS spectra for different cycles of the Zn symmetrical cells. (a) In the baseline electrolyte, (b) in the designed electrolyte.

To further confirm the durability of the *in-situ* SEI protective layer, XRD characterization (Figure 4.13f) of the Zn electrode in the designed electrolyte was conducted. The XRD patterns of the Zn electrodes after long cycling in the designed electrolyte exhibited distinct and steady peaks, agreeing well with the patterns of hopeite and Zn metal. In the baseline electrolyte, however, the diffraction peaks of zinc oxide (PDF no. 01-083-6338) gradually appeared and were strengthened due to the continuous corrosion reaction and H_2 evolution along with Zn plating/stripping (Figure 4.13g).[21, 27] It should be noted that the constant consumption of active Zn electrode and the electrolyte would lead to the underutilization of Zn and a limited lifespan. To provide additional insight into the effect of the robust SEI layer, after the *in-situ* formation of the hopeite SEI layer in the designed electrolyte, the Zn electrodes were stripped out and re-cycled in the baseline electrolyte (Figure 4.19). As expected, the reassembled Zn electrodes with the SEI layer possessed durable cycling stability for 1000 h at 1 mA cm^{-2}, which further demonstrated the stability and robustness of the SEI layer.

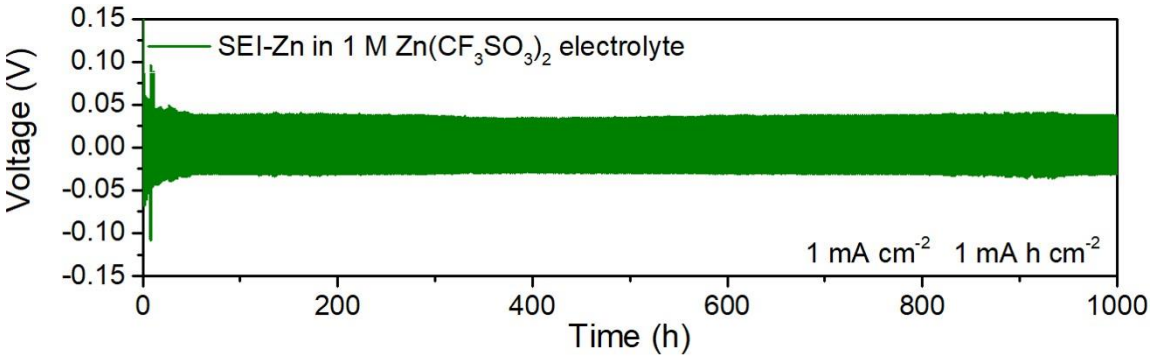

Figure 4.19 Cycling stability of a Zn symmetrical cell with SEI-Zn electrodes in the baseline electrolyte. The SEI-Zn electrodes were stripped from the symmetrical cell in the designed electrolyte after 20 cycles.

4.3.4 Zn deposition behaviour and reversibility

To further reveal the modulated Zn growth behaviour enabled by the SEI layer, optical microscopy was employed to directly visualize the Zn deposition morphology at the electrolyte-electrode interface. A working-principle diagram of the in-situ test cell is provided in Figure 4.20.

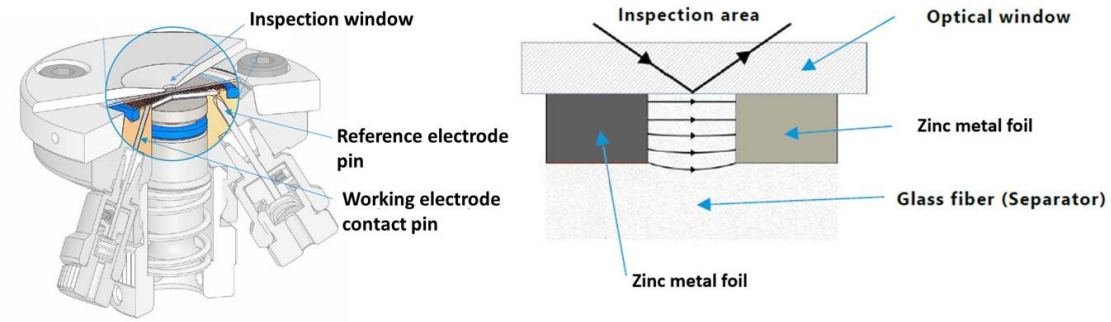

Figure 4.20 Working-principle diagram of the ECC-Opto-Std test cell. The ECC-Opto-Std cell was applied for in-situ observation of Zn deposition.

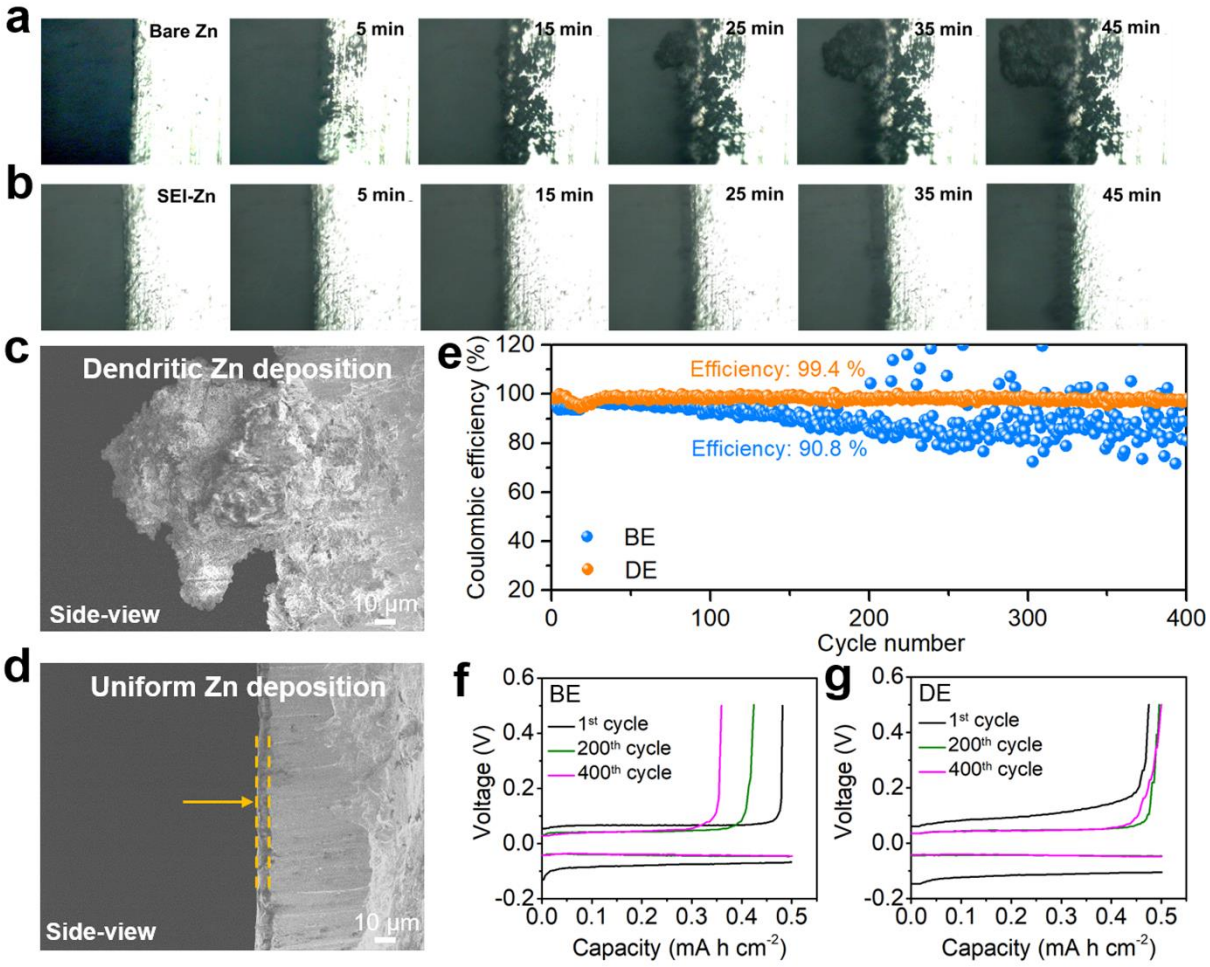

Figure 4.21 Investigations of Zn deposition behaviour and reversibility. *In-situ* optical microscope images of the cross-sectional Zn deposition morphology on (a) a bare Zn electrode and (b) an SEI-Zn electrode in symmetrical cells at a current density of about 10 mA cm^{-2}. The SEI-Zn electrode was stripped out of the symmetrical cell after 20 cycles in the designed electrolyte. Cross-sectional SEM images of Zn deposition on (c) a bare Zn electrode and (d) an SEI-Zn electrode at 1 mA cm^{-2} to an areal capacity of 3 mA h cm^{-2}. (e) Coulombic efficiency of Zn plating/stripping on Cu in the baseline and designed electrolytes. Corresponding voltage profiles of the Cu/Zn cells in (f) the baseline electrolyte and (g) the designed electrolyte at different cycles.

For the Zn electrode in the baseline electrolyte, uneven mossy-like Zn appeared along the edge of the Zn electrode after deposition for 15 minutes (Figure 4.21a). These

protruding Zn deposits continuously grew and aggregated into high-surface-area dendrites, which would result in severe side reactions, poor cycling reversibility, and battery degradation. Apart from the inhomogeneous Zn deposition, a progressive increase in gas bubbles derived from competitive H_2 evolution was also observed during the process of electroplating (Figure 4.22). It is noteworthy that the gas generation could not only reduce the Zn plating/stripping Coulombic efficiency (CE), but also resulted in a potential safety issue.

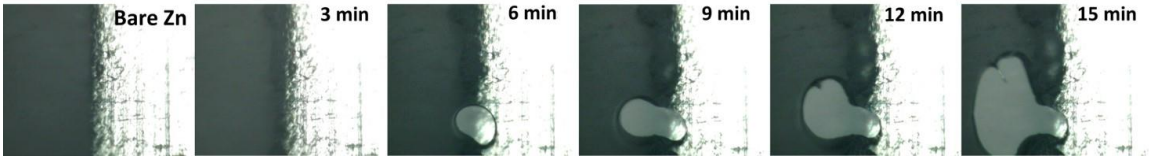

Figure 4.22 *In-situ* optical microscope images of Zn deposition on a bare Zn electrode. Some gas bubbles derived from H_2 evolution were observed during the process of Zn deposition. The applied current density was ~10 mA cm^{-2}.

For the Zn electrode cycled in the designed electrolyte (Figure 4.21b), however, smooth and dense Zn deposits were stacked on the electrode without obvious dendrite or gas formation during the whole electrodeposition process. SEM was further utilized to observe the electrodeposited Zn with/without the SEI film, as shown in Figure 4.21c, d. After plating at 1 mA cm^{-2} to an areal capacity of 3 mA h cm^{-2}, the side-view SEM image of Zn deposition on the Zn electrode in the baseline electrolyte clearly shows its loose and dendritic microstructure with serious agglomeration. In the designed electrolyte, homogeneous and compact Zn deposition was achieved due to the robust and highly Zn^{2+}-conductive SEI layer, and the thickness of the deposited Zn (about 5.8 μm) was in accordance with the expected value (5.1 μm) for the areal capacity of 3 mA h cm^{-2}. Such a dense morphology of the deposited Zn indicates the critical role of the *in-situ* SEI in suppressing Zn dendrite growth and guiding uniform Zn deposition.

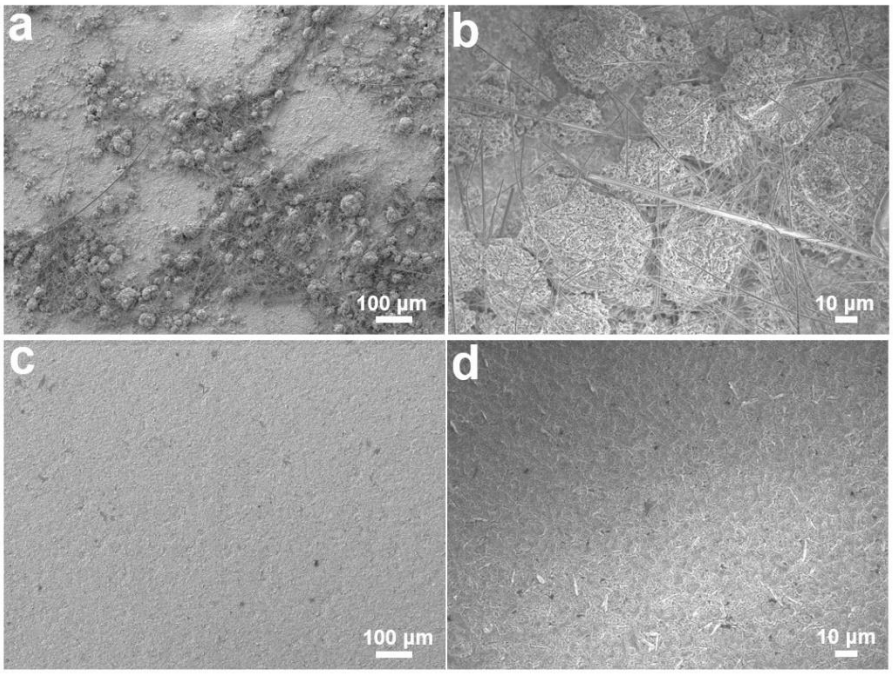

Figure 4.23 SEM images of Zn deposition on Cu foil. (a, b) In the baseline electrolyte, (c, d) in the designed electrolyte. The applied current density was 5 mA cm^{-2}, and the areal capacity was 0.5 mA h cm^{-2}. The Cu foil was pre-cycled in Cu/Zn cells with the respective electrolytes for 10 cycles.

The reversibility of Zn plating/stripping was also evaluated using asymmetrical Cu/Zn cells, where Cu foil and Zn foil were used as the working electrode and counter electrode, respectively. The CEs of Zn plating/stripping were calculated from the ratio of Zn dissolved from the Cu substrate to that deposited during the same cycle.[18] The morphologies of the deposited Zn on the Cu foil in the baseline electrolyte and the designed electrolyte are shown in Figure 4.23, where dendritic and agglomerated Zn protrusions were formed on the former and even Zn deposition on the latter. The CEs of Zn plating/stripping on Cu in the baseline and designed electrolytes, as well as corresponding voltage profiles at specific cycles, are presented in Figure 4.21e-g. The Cu/Zn cell in the baseline electrolyte displayed inferior CEs, with an average CE of only 90.8 %, due to Zn dendrite formation and side reactions. Meanwhile, its CEs

obviously fluctuated after 150 cycles, which was mainly ascribed to competitive H_2 generation during cycling. For the Cu/Zn cell in the designed electrolyte, however, a dramatically improved and stable CE could be detected, with an average CE of 99.4% over 400 cycles, along with stable voltage profiles during cycling. The relatively low CEs in the initial cycles might be derived from the consumption of active Zn^{2+} for the interfacial activation.[16] The significantly enhanced CEs demonstrated that the hopeite SEI layer formed *in situ* could not only promote more homogenous Zn plating/stripping, but could also restrain the side reactions between Zn electrode and the electrolyte, consequently improving the Zn utilization.

4.3.5 Full cell performance with lean electrolyte and low N/P ratio

Electrochemical characterization of Zn/V_2O_5 cells was conducted to explore the potential for practical applications. Micron-sized V_2O_5 powder was directly used as the cathode material, as shown in Figure 4.24.

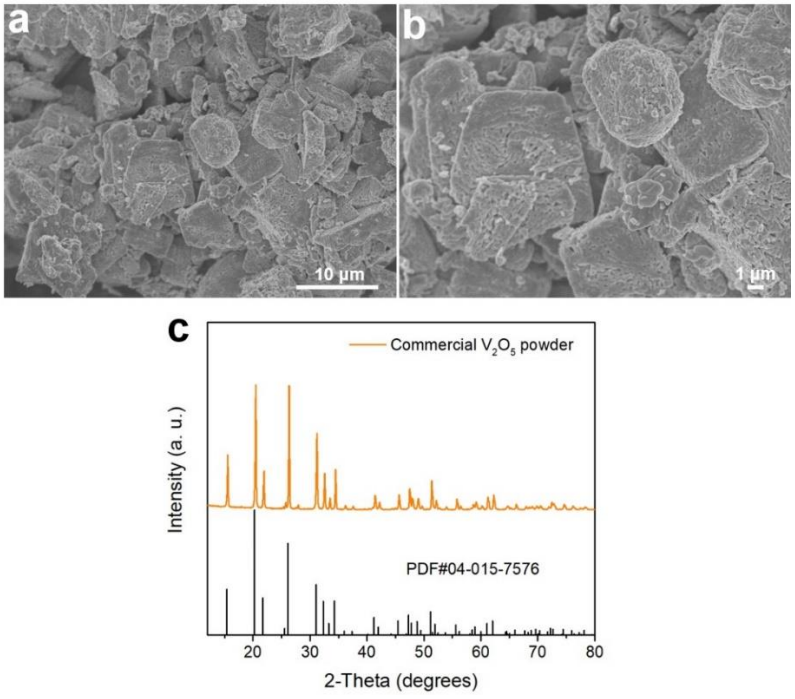

Figure 4.24 SEM images (a, b) and XRD pattern (c) of commercial V_2O_5 cathode.

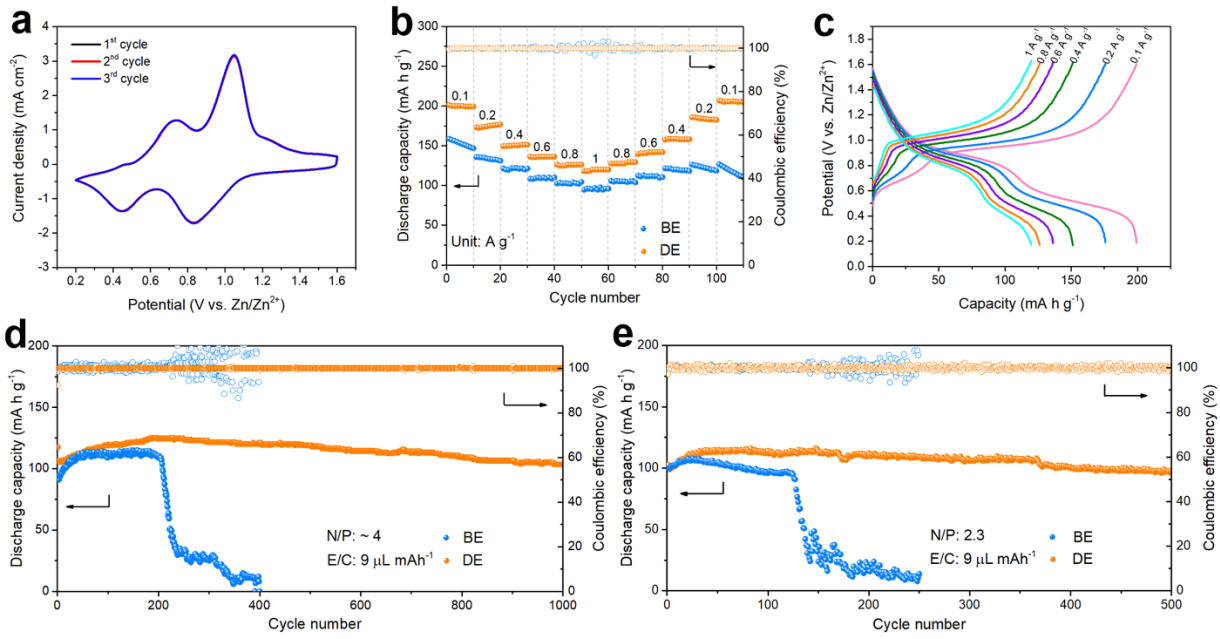

Figure 4.25 Electrochemical behaviour of AZIBs with lean electrolyte and low N/P ratio. (a) Cyclic voltammograms for the Zn/V_2O_5 full cell in the designed electrolyte at a scan rate of 1 mV s^{-1}. (b) Rate capability and (c) the corresponding discharge/charge profiles of Zn/V_2O_5 cells at various current densities. (d, e) Long-term cycling stability and efficiency of Zn/V_2O_5 cells at a current density of 0.8 A g^{-1}. The electrolyte-to-capacity ratio (E/C) used here was controlled at 9 μL mA h^{-1}, and the Zn electrodes were ultrathin (10 μm thickness, ~ 5.85 mA h cm^{-2}). All the Zn/V_2O_5 cells were pre-activated at 0.1 A g^{-1} for 10 cycles.

The cyclic voltammetry (CV) curves of the Zn/V_2O_5 cell in the designed electrolyte are shown in Figure 4.25a. The two pairs of redox peaks can be ascribed to reversible Zn^{2+}/H^+ insertion/extraction reactions on the cathode.[47, 48] The rate performance of the Zn/V_2O_5 cells in the baseline and designed electrolytes was also investigated, as shown in Figure 4.25b. In the designed electrolyte, high capacities of 203, 176, 151, 136, 126, and 120 mA h g^{-1} could be achieved at 0.1, 0.2, 0.4, 0.6, 0.8, and 1 A g^{-1}, respectively. Notably, when the rate shifted gradually back to 0.1 A g^{-1} after such high-rate cycling, the highly reversible capacities recovered to 206 mA h g^{-1}, suggesting the suppression

of side reactions and improved durability of the SEI-Zn anode. In addition, a hopeite layer was also formed *in situ* on the V_2O_5 cathode in the designed electrolyte (Figure 4.26), due to the local pH increase during the process of H^+ insertion into the cathode. The formation process can be expressed as follows:

$$H_2O \rightarrow H^+ + OH^- \quad (8)$$

$$V_2O_5 + xH^+ + xe^- \rightarrow H_xV_2O_5 \quad (9)$$

$$2H_2PO_4^- + 4OH^- + 3Zn^{2+} \rightarrow Zn_3(PO_4)_2 \cdot 4H_2O \downarrow \quad (10)$$

The hopeite layer on the cathode could suppress the detrimental dissolution of V_2O_5 in aqueous electrolyte, and further improve the cycling performance of the Zn/V_2O_5 full cells. The corresponding voltage profiles at different current densities are presented in Figure 4.25c, which manifested an average discharge voltage of 0.78 V. For comparison, the Zn/V_2O_5 cell in the baseline electrolyte showed inferior rate performance with relatively low capacity and rapid performance degradation after high-rate cycling, which was attributed to the poor reversibility and stability of the Zn electrode.

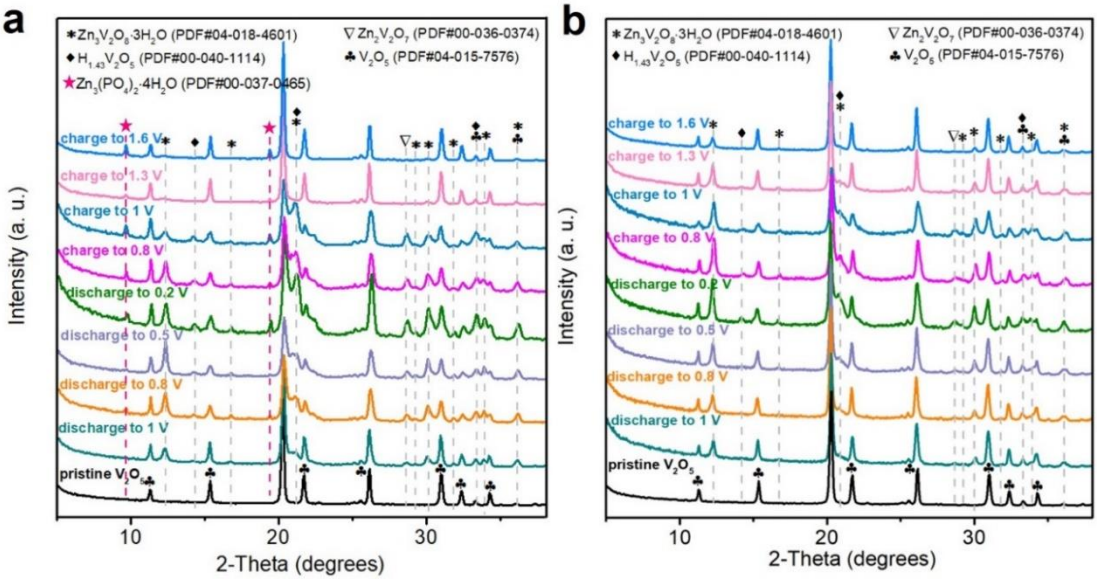

Figure 4.26 Ex-situ XRD patterns of the V_2O_5 cathode at different voltage states during the first cycle in (a) the designed electrolyte and (b) the baseline electrolyte, respectively.

In most previous reports, flooded electrolytes (> 100 μL) and very excessive Zn (> 100 μm) were used to prolong the cycle lifespan of AZIBs, although they mask the problem of low Zn utilization and continuous electrolyte consumption.[30] In contrast, to evaluate the truly competitive AZIBs for industrial applications, characterization under practical conditions is very much needed. Herein, the electrolyte-to-capacity ratio (E/C) used was controlled at 9 μL mA h^{-1} through replacing thick glass fibre with hydrophilic cellulose membrane (30 μm thickness) as the separator. Moreover, the capacity ratio of the negative electrode to the positive electrode (N/P) was set to ~4 and 2.3, achieved by utilizing high V_2O_5 loadings (1.45 and 2.52 mA h cm^{-2}, respectively) and ultrathin Zn anodes (10 μm thickness, ~ 5.85 mA h cm^{-2}).

The long-term cycling stability of the Zn/V_2O_5 cells with lean electrolyte and low N/P ratios is shown in Figure 4.25d, e. Without the protection of a stable SEI layer, the control cell with N/P of 4 exhibited a cliff-style capacity decay after only 202 cycles (Figure 4.25d), which is mainly attributed to the formation of thick dead Zn and the aforementioned side reactions. Notably, the cycling stability of the Zn/V_2O_5 cell in the designed electrolyte was enhanced significantly, and it exhibited nearly 100 % CE and high capacity retention of 88.1 % and 93.6 % at current density of 0.8 A g^{-1} (Figure 4.25d) and 0.4 A g^{-1} (Figure 4.27), respectively, for over 1000 cycles.

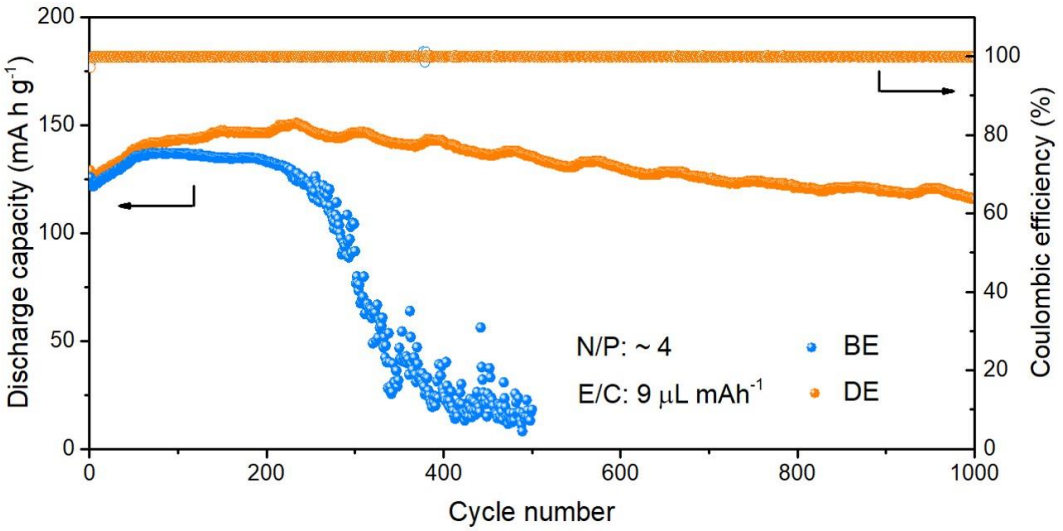

Figure 4.27 Long-term cycling stability and efficiency of Zn/V_2O_5 cells at 0.4 A g^{-1}. The Zn/V_2O_5 cells were assembled with lean electrolyte (9 μL mAh^{-1}) and low N/P (~ 4).

Remarkably, on further reducing the N:P ratio to 2.3, a discharge capacity of 98.4 mA h g^{-1} was retained over 500 cycles with 94.4 % capacity retention (Figure 4.25e). In contrast, the cell in the baseline electrolyte suffered from fast degradation. According to these results, we conclude that the hopeite SEI layer formed *in situ* on Zn anode ensured high Zn utilization, fast ionic transport, and effective suppression of Zn dendrites and side reactions, which enabled a highly improved lifespan for the AZIBs even under such practical testing conditions.

4.4 Conclusion

In this work, a unique electrolyte design strategy for *in-situ* SEI construction is proposed for the first time in aqueous Zn chemistry to address the critical issues for Zn electrodes and promote the development of practical aqueous Zn-ion batteries. A robust and highly Zn^{2+}-conductive hopeite SEI layer is formed *in situ*, by simply introducing $Zn(H_2PO_4)_2$ salt into the aqueous electrolyte and taking advantage of the local pH increase originating from the competitive side reaction of water decomposition. Based

on a combination of experimental results and computational analysis, we have demonstrated that the hopeite SEI layer stabilizes the Zn-electrolyte interface through guiding dendrite-free Zn plating/stripping and inhibiting continuous consumption of both Zn and aqueous electrolyte during cycling. Apart from the realization of high Zn reversibility and utilization, the exploitation of the *in-situ* SEI design also enables significantly enhanced cyclability of Zn/V_2O_5 full cells under practical conditions, including lean electrolyte (9 μL mAh^{-1}), limited Zn excess, and a high-capacity cathode (2.52 mA h cm^{-2}). Thus, the new *in-situ* interfacial design in this work offers a promising strategy towards practical high-performance AZIBs. We believe that this strategy can also be extended to other aqueous battery systems facing the same issues, providing a brand-new route for the development of aqueous rechargeable energy-storage applications.

4.5 References

[1] W. Chen, G. Li, A. Pei, Y. Li, L. Liao, H. Wang, J. Wan, Z. Liang, G. Chen, H. Zhang, J. Wang, Y. Cui, *Nat. Energy* **2018**, 3, 428.

[2] D. Chao, W. Zhou, F. Xie, C. Ye, H. Li, M. Jaroniec, S. Zhang, *Sci. Adv.* **2020**, 6, eaba4098.

[3] X. Ji, *Energy Environ. Sci.* **2019**, 12, 3203.

[4] Y. Zhang, F. Wan, S. Huang, S. Wang, Z. Niu, J. Chen, *Nat. Commun.* **2020**, 11, 1.

[5] L. Wang, K.-W. Huang, J. Chen, J. Zheng, *Sci. Adv.* **2019**, 5, eaax4279.

[6] T. Zhang, Y. Tang, G. Fang, C. Zhang, H. Zhang, X. Guo, X. Cao, J. Zhou, A. Pan, S. Liang, *Adv. Funct. Mater.* **2020**, 30, 2002711.

[7] M. Yu, N. Chandrasekhar, R. K. M. Raghupathy, K. H. Ly, H. Zhang, E. Dmitrieva, C. Liang, X. Lu, T. D. Kuhne, H. Mirhosseini, I. M. Weidinger, X. Feng, *J. Am. Chem. Soc.* **2020**, 142, 19570.

[8] H. Liang, Z. Cao, F. Ming, W. Zhang, D. H. Anjum, Y. Cui, L. Cavallo, H. N. Alshareef, *Nano Lett.* **2019**, 19, 3199.

[9] J. Zheng, Q. Zhao, T. Tang, J. Yin, C. D. Quilty, G. D. Renderos, X. Liu, Y. Deng, L. Wang, D. C. Bock, C. Jaye, D. Zhang, E. S. Takeuchi, K. J. Takeuchi, A. C. Marschilok, L. A. Archer, *Science* **2019**, 366, 645.

[10] D. Kundu, B. D. Adams, V. Duffort, S. H. Vajargah, L. F. Nazar, *Nat. Energy* **2016**, 1, 1.

[11] H. Pan, Y. Shao, P. Yan, Y. Cheng, K. S. Han, Z. Nie, C. Wang, J. Yang, X. Li, P. Bhattacharya, K. T. Mueller, J. Liu, *Nat. Energy* **2016**, 1, 16039.

[12] M. Song, H. Tan, D. Chao, H. J. Fan, *Adv. Funct. Mater.* **2018**, 28, 1802564.

[13] S.-B. Wang, Q. Ran, R.-Q. Yao, H. Shi, Z. Wen, M. Zhao, X.-Y. Lang, Q. Jiang, *Nat. Commun.* **2020**, 11, 1.

[14] X. Xie, S. Liang, J. Gao, S. Guo, J. Guo, C. Wang, G. Xu, X. Wu, G. Chen, J. Zhou, *Energy Environ. Sci.* **2020**, 13, 503.

[15] Z. Wang, J. Huang, Z. Guo, X. Dong, Y. Liu, Y. Wang, Y. Xia, *Joule* **2019**, 3, 1289.

[16] Z. Zhao, J. Zhao, Z. Hu, J. Li, J. Li, Y. Zhang, C. Wang, G. Cui, *Energy Environ. Sci.* **2019**, 12, 1938.

[17] J. Hao, B. Li, X. Li, X. Zeng, S. Zhang, F. Yang, S. Liu, D. Li, C. Wu, Z. Guo, *Adv. Mater.* **2020**, 2003021.

[18] F. Wang, O. Borodin, T. Gao, X. Fan, W. Sun, F. Han, A. Faraone, J. A. Dura, K. Xu, C. Wang, *Nat. Mater.* **2018**, 17, 543.

[19] N. Zhang, F. Cheng, Y. Liu, Q. Zhao, K. Lei, C. Chen, X. Liu, J. Chen, *J. Am. Chem. Soc.* **2016**, 138, 12894.

[20] X. Zeng, J. Liu, J. Mao, J. Hao, Z. Wang, S. Zhou, C. D. Ling, Z. Guo, *Adv. Energy Mater.* **2020**, 1904163.

[21] L. Cao, D. Li, T. Deng, Q. Li, C. Wang, *Angew. Chem. Int. Ed.* **2020**, 59, 19292.

[22] X. Wu, Y. Xu, C. Zhang, D. P. Leonard, A. Markir, J. Lu, X. Ji, *J. Am. Chem. Soc.* **2019**, 141, 6338.

[23] X. Cao, X. Ren, L. Zou, M. H. Engelhard, W. Huang, H. Wang, B. E. Matthews, H. Lee, C. Niu, B. W. Arey, Y. Cui, C. Wang, J. Xiao, J. Liu, W. Xu, J.-G. Zhang, *Nat. Energy* **2019**, 4, 796.

[24] H. Yuan, J. Nai, H. Tian, Z. Ju, W. Zhang, Y. Liu, X. Tao, X. W. Lou, *Sci. Adv.* **2020**, 6, eaaz3112.

[25] X. Zeng, J. Hao, Z. Wang, J. Mao, Z. Guo, *Energy Storage Mater.* **2019**, 20, 410.

[26] H. Qiu, X. Du, J. Zhao, Y. Wang, J. Ju, Z. Chen, Z. Hu, D. Yan, X. Zhou, G. Cui, *Nat. Commun.* **2019**, 10, 1.

[27] H. Yang, Z. Chang, Y. Qiao, H. Deng, X. Mu, P. He, H. Zhou, *Angew. Chem. Int. Ed.* **2020**, 59, 9377.

[28] Z. Liu, Y. Huang, Y. Huang, Q. Yang, X. Li, Z. Huang, C. Zhi, *Chem. Soc. Rev.* **2020**, 49, 180.

[29] A. Naveed, H. Yang, J. Yang, Y. Nuli, J. Wang, *Angew. Chem. Int. Ed.* **2019**, 58, 2760-2764.

[30] L. E. Blanc, D. Kundu, L. F. Nazar, *Joule* **2020**, 4, 771.

[31] L. Ma, M. A. Schroeder, O. Borodin, T. P. Pollard, M. S. Ding, C. Wang, K. Xu, *Nat. Energy* **2020**, 5, 743.

[32] J. Zhi, S. Li, M. Han, P. Chen, *Sci. Adv.* **2020**, 6, eabb1342.

[33] S. Guo, L. Qin, T. Zhang, M. Zhou, J. Zhou, G. Fang, S. Liang, *Energy Storage Mater.* **2021**, 34, 545.

[34] B. Zhang, P. Li, H. Zhang, L. Fan, H. Wang, X. Li, L. Tian, N. Ali, Z. Ali, Q. Zhang, *RSC Adv.* **2016**, 6, 46702.

[35] L. Kouisni, M. Azzi, M. Zertoubi, F. Dalard, S. Maximovitch, *Surf. Coat. Technol.* **2004**, 185, 58.

[36] Z. Tu, S. Choudhury, M. J. Zachman, S. Wei, K. Zhang, L. F. Kourkoutis, L. A. Archer, *Nat. Energy* **2018**, 3, 310.

[37] R. Xu, Y. Xiao, R. Zhang, X.-B. Cheng, C.-Z. Zhao, X.-Q. Zhang, C. Yan, Q. Zhang, J.-Q. Huang, *Adv. Mater.* **2019**, 31, 1808392.

[38] W. Shin, J. Lee, Y. Kim, H. Steinfink, A. Heller, *J. Am. Chem. Soc.* **2005**, 127, 14590.

[39] H. Zhang, W. Wu, Q. Liu, F. Yang, X. Shi, X. Liu, M. Yu, X. Lu, *Angew. Chem. Int. Ed.* **2020**, 59, 2.

[40] X. Liang, Q. Pang, I. R. Kochetkov, M. S. Sempere, H. Huang, X. Sun, L. F. Nazar, *Nat. Energy* **2017**, 2, 17119.

[41] T. Zhang, Y. Tang, S. Guo, X. Cao, A. Pan, G. Fang, J. Zhou, S. Liang, *Energy Environ. Sci.* **2020**. DOI: 10.1039/d0ee02620d

[42] Q. Zhang, J. Luan, L. Fu, S. Wu, Y. Tang, X. Ji, H. Wang, *Angew. Chem. Int. Ed.* **2019**, 58, 15841.

[43] Z. Wang, Y. Wang, Z. Zhang, X. Chen, W. Lie, Y.-B. He, Z. Zhou, G. Xia, Z. Guo, *Adv. Funct. Mater.* **2020**, 30, 2002414.

[44] Z. Rong, R. Malik, P. Canepa, G. S. Gautam, M. Liu, A. Jain, K. Persson, G. Ceder, *Chem. Mater.* **2015**, 27, 6016.

[45] V. V. Kulish, S. Manzhos, *RSC Adv.* **2017**, 7, 18643.

[46] M. Liu, Z. Rong, R. Malik, P. Canepa, A. Jain, G. Ceder, K. A. Persson, *Energy Environ. Sci.* **2015**, 8, 964.

[47] G. Yang, Q. Li, K. Ma, C. Hong, C. Wang, *J. Mater. Chem. A* **2020**, 8, 8084.

[48] F. Wan, L. Zhang, X. Dai, X. Wang, Z. Liu, J. Chen, *Nat. Commun.* **2018**, 9, 1656.

Chapter 5

Bio-inspired design of an *in-situ* multifunctional polymeric solid-electrolyte interphase for Zn metal anode cycling at 30 mA cm^{-2} and 30 mA h cm^{-2}

5.1 Introduction

Large-scale storage of renewable energy from such sources as solar and wind plays a key role in decarbonizing our economy in a more clean and sustainable way. Lithium-ion batteries (LIBs) are the dominant energy storage system nowadays, but known safety issues, high costs, and potential resource concerns arise due to the expensive and flammable nature of organic electrolytes and the rarity of lithium and cobalt resources[1,2]. The development of alternative energy storage solutions for safe, economical, and large-scale energy storage has become increasingly urgent. Rechargeable aqueous zinc-ion batteries (RAZBs) have been revived as complementary to LIBs as a result of the intrinsic safety of aqueous electrolytes and the attractive properties of Zn metal anode, including high theoretical capacity (820 mA h g^{-1} and 5855 mA h cm^{-3}), low redox potential, and abundant resources[3-5]. Despite these unique advantages, their practical application is largely impeded by their inferior cycling stability and their low Zn plating/stripping Coulombic efficiency (CE) surrounding the Zn electrode[6]. Zn metal is thermodynamically unstable in conventional aqueous electrolytes, and consequently, side reactions (*e.g.*, H_2 evolution and Zn corrosion) occur at the electrode-electrolyte interface[7-9]. In addition, the initial Zn nucleation is normally localized during the process of Zn deposition, leading to an uneven interfacial electric field and tip-effect-derived dendrite formation. These notorious issues of dendrite growth and side reactions are even more critical under practical conditions such as high plating/stripping current density, lean electrolyte, and limited excess Zn[10,11].

The issues of the dendrites and the side reactions stem directly or indirectly from the interaction between the Zn metal and the electrolyte. Hence, extensive efforts have been focused on improvement of the Zn host structure[12,13], electrolyte optimization[3,14-16], and interfacial engineering[17-19]. Nanostructured Zn electrodes were introduced to suppress the growth of Zn dendrites, but they require complex fabrication processes and undergo high-potential surface-dependent side reactions. Among the various optimization strategies for aqueous electrolytes, super-concentrated electrolytes have been proved to reduce the activity of H_2O molecules and alleviate H_2O-induced side reactions, consequently improving the CEs of Zn, although the high cost and unsatisfactory viscosity of super-concentrated electrolytes make this approach questionable for practical applications[3,12]. In contrast, building a suitable solid-electrolyte interphase (SEI) is well known as a promising solution to stabilizing the metal anode[20,21]. An artificial interface layer could isolate the Zn anode from the electrolyte and thus inhibit the side reactions and dendrite formation, but such layers are prone to be detached and cannot easily tolerate the dynamic Zn plating/stripping process, due to their poor adhesion with Zn[8,22]. Constructing an *in-situ* SEI layer that has a strong interaction with Zn is a major goal in the quest for high-performance Zn metal anodes. It is highly challenging, however, to design a stable *in-situ* SEI on Zn in aqueous electrolytes, and until now, there have only been a few successful attempts[11,23]. The main reason is the relatively high reduction potential of Zn plating (-0.76 V vs. standard hydrogen electrode (SHE)). At this potential, the salt anion is difficult to decompose, while the water decomposition generates detrimental gases instead of an effective interphase. To ensure durable protective effects towards hindering Zn dendrites and side reactions, an ideal SEI layer should be robust against repeated volume changes of Zn, electronically insulating, have high Zn-ion conductivity, and exhibit self-passivating growth[10,24]. Such

an effective interphase for the Zn metal anode has not yet been well developed or understood.

For the design of interfacial materials, nature is undoubtedly our best mentor. A good example is phenolics or phenolic-like molecules such as dopamine (DA). DA is a bio-inspired adhesive molecule that mimics the critical bio-adhesive moieties of marine mussels, and it can be readily deposited as polydopamine (PDA) on virtually all types of substrates via self-oxidation in air or electrochemical polymerization in aqueous solution[25,26]. Due to its universal adhesion properties, PDA has moved into the spotlight and been recognized as a novel coating material for decades. When used in batteries, it is anticipated that the robust and strong adhesion between PDA and substrates, electrodes in this case, can stabilize the electrode-electrolyte interface by suppressing interfacial side reactions. Moreover, the excellent hydrophilicity of PDA endows the substrate with drastically reduced surface energy in aqueous electrolytes, contributing to uniform metal deposition[27]. In addition, it was reported that the functional groups in PDA have strong interactions with multivalent metal ions, which is favourable for uniform ion interaction and diffusion[28,29]. Inspired by these multifunctional features of PDA, we constructed PDA layers *in situ* on Zn metal anode by introducing DA into the aqueous electrolyte, which could serve as a highly efficient SEI to create a stable Zn electrode through suppressing side reactions and ensuring uniform Zn deposition.

As proof of concept, in this work, a multifunctional polymeric SEI layer of PDA was established on Zn metal anode, via the *in-situ* polymerization of DA during the charge-discharge process. The successful construction of a PDA layer on Zn electrode was confirmed by *in-situ* Raman spectroscopy, cryogenic electron microscopy (cryo-EM), Fourier transform infrared spectroscopy (FTIR), *etc*. It was found that the PDA SEI

layer acts as a protective layer at the electrode-electrolyte interface, effectively suppressing corrosion reactions and electrolyte decomposition, hence ensuring high interfacial stability. Meanwhile, the SEI layer favorably interacts with Zn^{2+} via the functional catechol groups in the PDA chains, which regulates the homogeneous distribution of Zn^{2+} flux and harmonizes ion migration, hence facilitating uniform Zn nucleation and evolution. As a result, a highly stable and dendrite-free Zn electrode has been attained in conventional aqueous electrolytes with DA additive, as demonstrated by *in-situ* Zn deposition observations and electrochemical characterizations. The Zn electrode in the prepared electrolyte delivers stable cycling performance, even under harsh plating/stripping conditions (30 mA cm^{-2}, 30 mA h cm^{-2}), and high plating/stripping reversibility, with a high average CE of 99.5 % for over 1000 cycles, which is ascribed to the superiority of the multifunctional SEI on Zn. Notably, with practical testing parameters of lean electrolyte and low ratio of the negative capacity to the positive capacity (N/P), the Zn/V_2O_5 full cell in the prepared electrolyte still displayed a high capacity of 141.8 mA h g^{-1} and high capacity retention of 94.3 % after 1000 cycles. This bio-inspired *in-situ* polymerization strategy provides a brand-new method for SEI design in aqueous battery chemistry and boosts the practical application of RAZBs.

5.2 Experimental section

5.2.1 Materials characterization

The morphologies of the electrodes were characterized by field emission scanning electron microscopy (FESEM, JEOL JSM-7500FA) along with energy dispersive X-ray spectroscopy (EDX) mapping. *In-situ* Raman spectroscopy (JY HR800 Spectrometer) was conducted on a sealed cell (ECC-Opto-Std) with an optical window. The laser light was focused onto the sample using a 100× objective with a long working distance. The

laser power was 1 mW, and the accumulation time for each spectrum was set at about 10 s to avoid laser induced degradation. Atomic force microscopy (AFM) images were acquired in tapping mode using a Cypher ES AFM (Asylum Research, US). The specimen of cycled Zn electrode for cryogenic electron microscopy (cryo-EM) was prepared by focused ion beam (FIB) milling on a FEI Helios Nanolab with a Ga^+ ion beam. The surface of the specimen was coated with a Pt/C protective layer. Cryo-EM images were acquired on a JEOL JEM-ARM200F at liquid N_2 temperature to eliminate contamination and reduce beam damage to the SEI layer. X-ray photoelectron spectroscopy (XPS) testing was performed on an X-ray photoelectron spectrometer (Thermo Fisher K-Alpha system). The XPS depth profiles were acquired by applying an Ar^+ beam with a scanning region of 200 × 200 μm and a sputtering rate of 2 kV. Fourier transform infrared (FTIR) mapping was performed on a Bruker Vertex 80v spectrometer coupled with a Hyperion 3000 FT-IR microscope. *In-situ* observations of Zn plating were carried out using an ECC-Opto-Std test cell.

5.2.2 Electrochemical measurements

The electrochemical performance of the batteries in this work was evaluated by using CR2032 coin-type cells on a Land BT2000 battery test system. The Zn plating/stripping tests were performed on Zn symmetrical cells in the electrolytes with and without DA. Coulombic efficiency (CE) measurements were carried out on asymmetrical Zn/Cu cells. Linear polarization analyses were conducted using a three-electrode device with Zn foil (working electrode), Ag/AgCl (reference electrode), and Pt (counter electrode). Electrochemical impedance spectroscopy (EIS) was implemented using a Biologic VMP-3 electrochemical workstation within the range of 10^5 to 10^{-2} Hz. The Zn/V_2O_5 cells were cycled between 0.2 and 1.6 V vs. Zn/Zn^{2+}, and the specific capacities were evaluated according to the active mass of V_2O_5. Hydrophilic mixed cellulose

membranes were applied as the separator in Zn/V_2O_5 full cells with controlled electrolyte volume. Cyclic voltammetry (CV) of the Zn/V_2O_5 cells was carried out on a Biologic VMP-3 electrochemical workstation.

5.2.3 Calculation methods

The first-principles density functional theory (DFT) calculations in this work were conducted by using the Vienna Ab initio Simulation Package (VASP) with the projector augmented wave (PAW) method[1,2]. The generalized gradient approximation (GGA) with the Perdew-Burke-Ernzerhof (PBE) functional was used to describe the exchange-correlation interaction[3]. The energy cut-off was set at 450 eV. For geometry relaxation, the convergence criterion was set at 0.03 eV/Å for force, and 10^{-4} eV for energy. The Brillouin-zone integration was sampled by the single Γ point. The DFT-D3 mode was employed to simulate the van der Waals interaction[4]. Transition state searching was performed using the climbing-image nudged elastic band (CI-NEB) method[5]. The adsorption energy was calculated according to

$$E_{ads} = E_{total} - E_{Poly} - E_{Zn} \qquad (1)$$

where E_{total} is the total energy of the Zn adsorbed system, and E_{Poly} and E_{Zn} are the energies of the PDA structure and the adsorption of a Zn atom, respectively.

5.3 Results and discussion

5.3.1 Formation of the polymeric SEI and enhanced electrochemical stability.

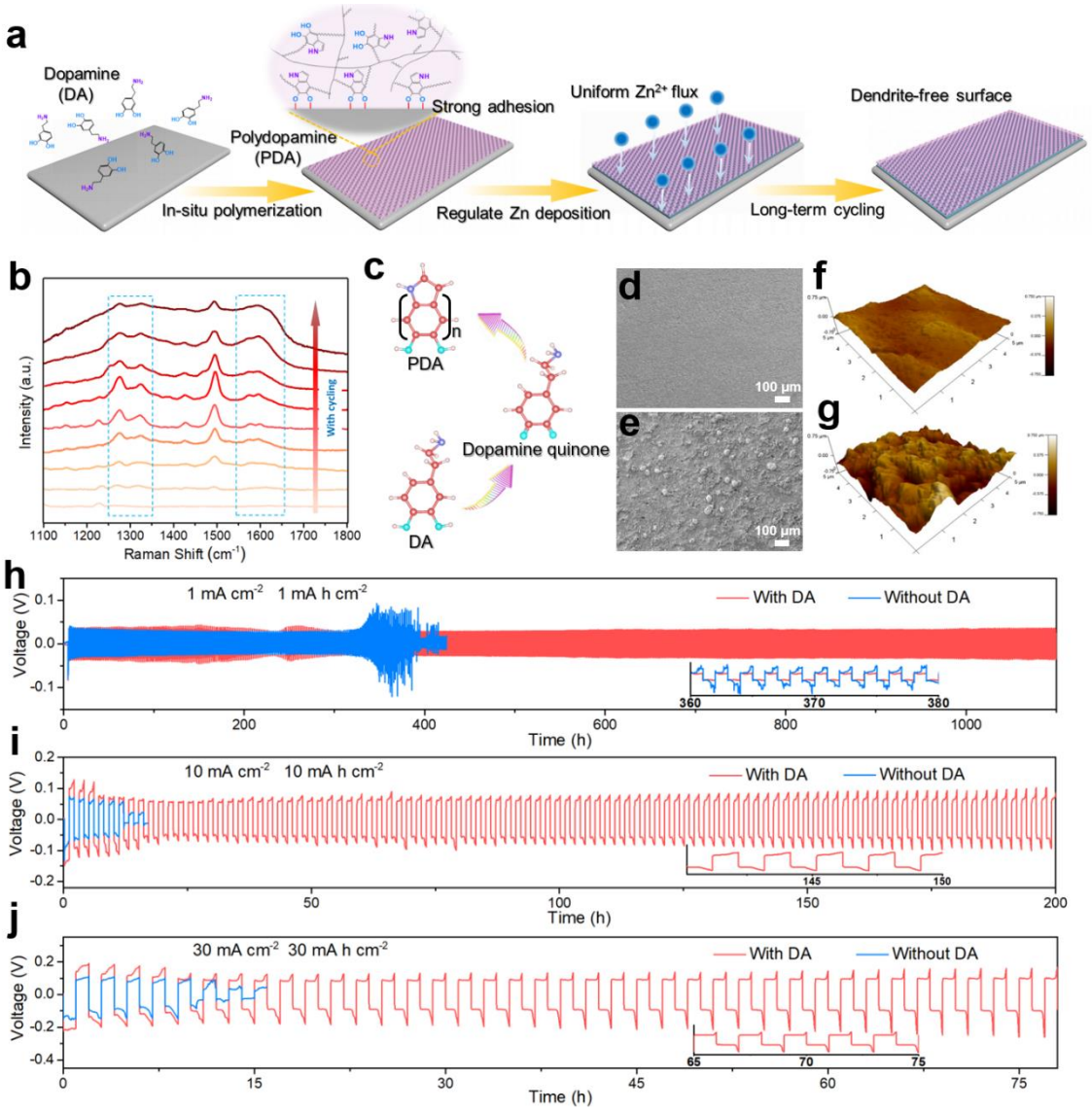

Figure 5.1 Schematic illustration of the polymeric SEI formation and characterization of Zn electrodes. (a) Schematic illustration of the *in-situ* formation of the multifunctional PDA SEI and its effective mechanism for dendrite-free Zn anode. (b) *In-situ* Raman spectra of the Zn electrode during cycling in the electrolyte (1 M $Zn(CF_3SO_3)_2$) with DA additive. (c) Representative polymerization procedure for PDA. SEM images and three-dimensional AFM images of Zn electrodes after 10 cycles in the electrolyte (d, f) with DA and (e, g) without DA. Comparison of galvanostatic cycling properties of Zn symmetrical cells in the electrolytes with and without DA at (h) 1 mA cm^{-2}, 1 mA h cm^{-2}; (i) 10 mA cm^{-2}, 10 mA h cm^{-2}; and (j) 30 mA cm^{-2}, 30 mA h cm^{-2}.

Figure 5.1a illustrates the formation of PDA as well as its function as SEI for regulating Zn deposition. The DA molecules in the aqueous electrolyte (1 M $Zn(CF_3SO_3)_2$) are electrochemically polymerized during the initial cycling process, causing the *in-situ* formation of a thin PDA layer on the surface of the Zn. The *in-situ* polymerization process for DA during electrochemical processes was investigated by *in-situ* Raman spectroscopy, as shown in Figure 5.1b. During cycling, peaks at 1280, 1330, 1500, and 1580 cm^{-1} emerged, which can be attributed to dopamine quinone, a typical polymerization intermediate[30]. The peaks at around 1300 and 1600 cm^{-1} (highlighted in the blue rectangle) became broader and were strengthened with further cycling. Such broad peaks are typical stretching and deformation features of aromatic rings in PDA[31], indicating the successful deposition process of a PDA layer on Zn electrode. Accordingly, an abbreviated schematic illustration of the polymerization mechanism of PDA is presented in Figure 5.1c, although it has long been the topic of scientific debate due to the complex intermediates[25]. The PDA exhibits a strong interaction with Zn metal, as verified by the theoretical calculation that the binding energy of PDA on the Zn surface is as high as -2.08 eV (Figure 5.2).

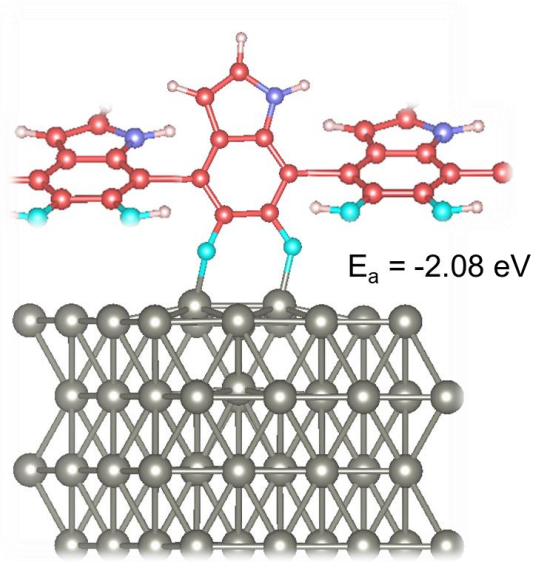

Figure 5.2 Geometrical configuration and adsorption energy of polydopamine (PDA) on the Zn (002) plane.

In addition, the robust PDA layer with abundant functional groups promotes a homogeneous Zn^{2+} flux at the electrode-electrolyte interface, and hence guides dendrite-free Zn deposition. As demonstrated by scanning electron microscopy (SEM) and atomic force microscopy (AFM), after the formation of PDA, the cycled Zn electrode presents a smooth and dendrite-free surface topology (surface roughness: 0.11 μm) in the electrolyte with DA (Figure 5.1d and f). In contrast, the cycled Zn electrode in the electrolyte without DA exhibited a rough surface (surface roughness: 0.56 μm) with obvious dendrites (Figure 5.1e and g).

As shown in Figure 5.3, the Coulombic efficiency of Zn plating/stripping in electrolytes with a molarity of 50 mM DA additive shows the optimal electrochemical performance. When the concentration of DA additive in the electrolyte is too low, the PDA layer formed on Cu foil will be scattered and loose. This imperfect PDA layer is unable to suppress dendrite formation and parasitic reactions at the electrode/electrolyte interface, and consequently leads to unsatisfactory Coulombic efficiency of Zn plating/stripping

on Cu. On the other hand, with excessive DA additive in the electrolyte, this polymeric layer would be very thick and not favorable for the ion-transference kinetics during Zn plating/stripping processes.

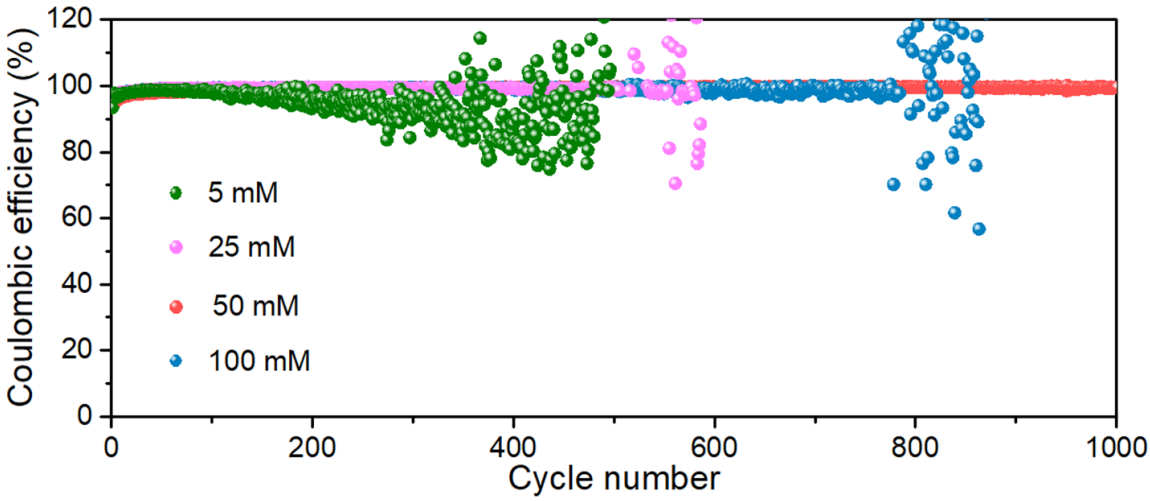

Figure 5.3 Comparison of the Coulombic efficiency of Zn plating/stripping on Cu in electrolytes consisting of 1 M $Zn(CF_3SO_3)_2$ with different DA concentrations. The applied current density was 1 mA cm^{-2}, and the areal capacity was 1 mA h cm^{-2}.

Due to the effectiveness of the polymeric SEI, the Zn electrodes exhibited significantly enhanced electrochemical stability. Under the optimized electrolyte of 1 M $Zn(CF_3SO_3)_2$ with a molarity of 50 mM DA additive, the Zn symmetrical cell displayed highly stable cycling performance for over 1100 h at a current density of 1 mA cm^{-2} and an areal capacity of 1 mA h cm^{-2} (Figure 5.1h). Conversely, the voltage profiles of Zn plating/stripping in the blank electrolyte presented obvious fluctuations after only 340 h, and a short-circuit occurred subsequently. It is evident that high current density and high plating/stripping capacity are prone to accelerate the growth of dendritic Zn and lead to an extremely short battery lifespan[11,32]. As shown in Figure 5.1i and j, the Zn electrode in the blank electrolyte showed a short-circuit in less than 15 h at higher current densities and areal capacity (≥ 10 mA cm^{-2}, 10 mA h cm^{-2}), although the Zn

electrode in the electrolyte with DA featured a much prolonged cycle life at higher current densities and areal capacities of 10 mA cm^{-2}, 10 mA h cm^{-2} (Figure 5.1i), which represented an almost tenfold enhancement compared with the lifespan of Zn electrodes in the blank electrolyte. Remarkably, on further increasing the testing parameters to 30 mA cm^{-2} and 30 mA h cm^{-2} (Figure 5.1j), the Zn electrode in the symmetrical cell with the optimized electrolyte delivered stable voltage oscillations and stable cycling for more than 75 h, which outperformed all the reported Zn metal anodes working at high current densities and areal capacities (Table 5.1). The highly stable Zn electrode under these rigorous testing parameters confirmed the efficacy of the robust PDA layer derived from the *in-situ* polymerization process.

Table 5.1 Comparison of the electrochemical stability of state-of-the-art Zn metal electrodes at high current densities and areal capacities.

Electrode	Current density and areal capacity	Lifespan	Reference
***In situ* PDA-Zn**	**10 mA cm^{-2}, 10 mA h cm^{-2}** **20 mA cm^{-2}, 20 mA h cm^{-2}** **30 mA cm^{-2}, 30 mA h cm^{-2}**	**200 h** **120 h** **78 h**	**This work**
Interdigitated Zn/IHS	20 mA cm^{-2}, 20 mA h cm^{-2}	80 h	*J. Am. Chem. Soc.* 2021, 143, 3143-3152
Zn/CNT	5 mA cm^{-2}, 2.5 mA h cm^{-2} 2 mA cm^{-2}, 2 mA h cm^{-2}	110 h 200 h	*Adv. Mater.* 2019, 31, 1903675
PA-coated Zn	10 mA cm^{-2}, 10 mA h cm^{-2}	75 h	*Energy Environ. Sci.* 2019, 12,1938-1949
Zn in $Zn(OTF)_2$-$Zn(NO_3)_2$	10 mA cm^{-2}, 10 mA h cm^{-2}	90 h	*Angew. Chem. Int. Ed.* 2021, 60, 13035-13041
Zn(002)	10 mA cm^{-2}, 2 mA h cm^{-2}	200 h	*Angew. Chem.* 2021, 133, 7289-7295
Zn@ZnO HPA	5 mA cm^{-2}, 2.5 mA h cm^{-2}	100 h	*Adv. Funct. Mater.* 2020, 30, 2004210
CM@CuO@Zn	2 mA cm^{-2}, 2 mA h cm^{-2}	200 h	*Small* 2020, 16, 2000929
Zn@C	10 mA cm^{-2}, 1 mA h cm^{-2}	100 h	*ACS Appl. Mater. Interfaces* 2018, 10, 22059-22066

3D-Zn in TBA electrolyte	5 mA cm^{-2}, 5 mA h cm^{-2}	160 h	*ACS Energy Lett.* 2020, 5, 3012-3020
DCP-Zn-30	5 mA cm^{-2}, 10 mA h cm^{-2}	200 h	*Energy Storage Mater.* 2020, 30, 104-112
Zn in $ZnSO_4$ + LiCl	5 mA cm^{-2}, 1 mA h cm^{-2}	170 h	*ACS Energy Lett.* 2021, 6, 395-403
$CaCO_3$-coated Zn	3 mA cm^{-2}, 0.1 mA h cm^{-2}	80 h	*Adv. Energy Mater.* 2018, 8, 1801090
Zn foam in 1 M $ZnSO_4$ + 1 M $MnSO_4$ + 0.1 M H_2SO_4	20 mA cm^{-2}, 2 mA h cm^{-2}	100 h	*Angew. Chem. Int. Ed.* 2019, 58, 7823-7828
Zn/SS mesh	2 mA cm^{-2}, 1 mA h cm^{-2}	300 h	*Nano Energy* 2019, 62, 94-102
Zn with 3D VG	5 mA cm^{-2}, 5 mA h cm^{-2}	75 h	*Adv. Mater.* 2020, 2003425
Zn@F-TiO_2	2 mA cm^{-2}, 2 mA h cm^{-2}	280 h	*Nat. Commun.* 2019, 11, 3961
Sc_2O_3-coated Zn	2 mA cm^{-2}, 2 mA h cm^{-2}	240 h	*J. Energy Chem.* 2021, 55, 549-556
Alg-Zn	8.8 mA cm^{-2}, 2.2 mA h cm^{-2}	200 h	*Energy Storage Mater.* 2020, 27, 109-116
Zn in PAM added electrolyte	20 mA cm^{-2}, 1 mA h cm^{-2}	105 h	*Angew.Chem. Int.Ed.* 2019, 58,15841-15847
MOF-PVDF coated Zn	3 mA cm^{-2}, 3 mA h cm^{-2}	100 h	*ACS Appl. Mater. Interfaces* 2019, 11, 32046-32051
Zn/CNT foam	3 mA cm^{-2}, 0.5 mA h cm^{-2}	167 h	*J. Mater. Chem. A,* 2020, 8, 11719-11727
Cu foam @Zn	2 mA cm^{-2}, 1 mA h cm^{-2}	150 h	*Chem. Eng. J.* 2020, 379, 1222482

5.3.2 Characterization of the polymeric SEI

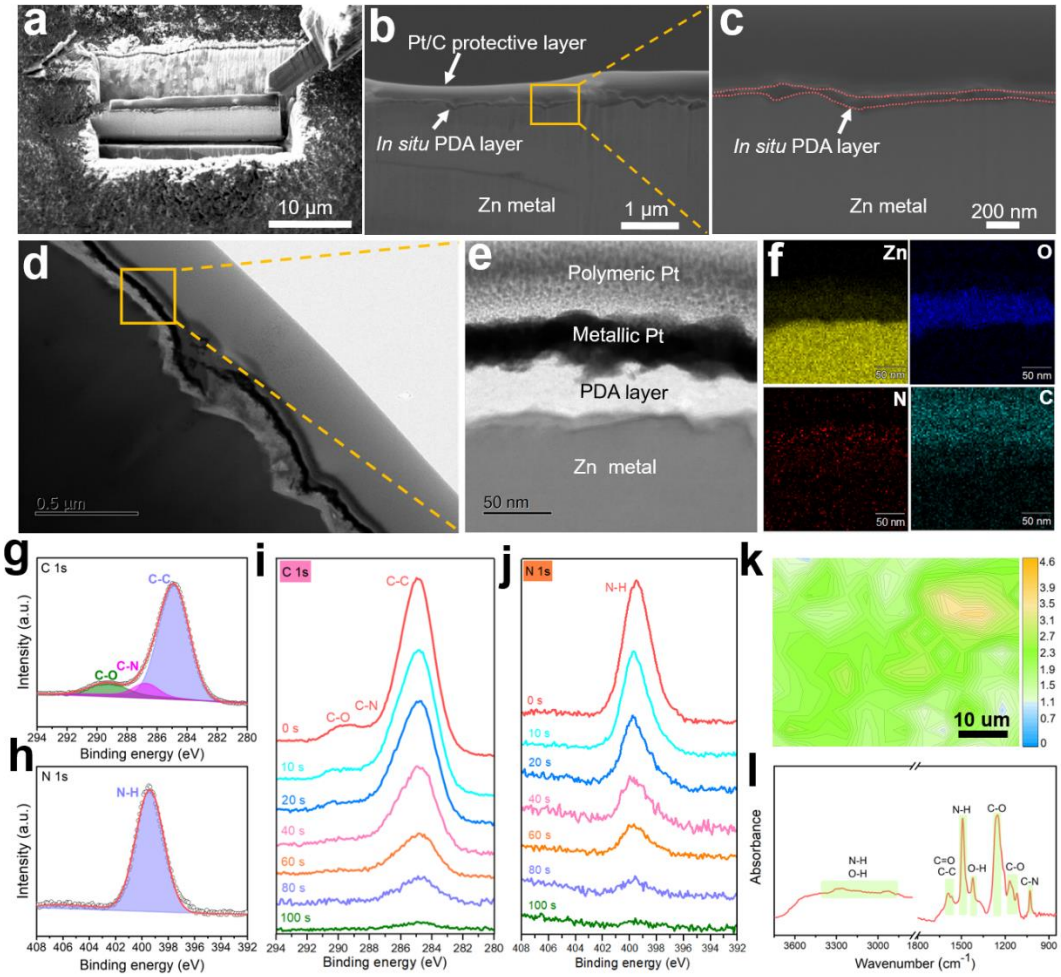

Figure 5.4 Characterization of the *in situ* polymeric SEI layer on Zn electrode. (a) Top-view and (b, c) side-view focused ion beam (FIB)-SEM images of the Zn electrode after 10 cycles in the electrolyte with DA. To protect the *in-situ* PDA layer from incurring electron/ion beam induced damage, the Zn electrode was coated with a Pt/C protective layer. (d) Low-resolution and (e) high-resolution cryo-EM images of Zn electrode with the PDA layer (the PDA-Zn electrode). (f) Corresponding elemental mapping images. High-resolution X-ray photoelectron spectroscopy (XPS) spectra of (g) C 1s and (h) N 1s orbitals for the PDA-Zn electrode. XPS depth profiles of (i) C 1s and (j) N 1s for the PDA-Zn electrode with various Ar sputtering times. (k) FTIR mapping and (l) the corresponding spectrum of the PDA-Zn electrode. The PDA-Zn electrodes were stripped out of the Zn symmetrical cells after 10 cycles in the electrolyte consisting of 1 M $Zn(CF_3SO_3)_2$ with DA additive.

The *in-situ* formation of a PDA layer on Zn was confirmed by focused ion beam (FIB)-SEM and cryogenic electron microscopy (cryo-EM). As shown in Figure 5.4a, the cycled Zn electrode in the electrolyte with DA was first milled into a lamella by FIB. Then, a thin layer could be observed between the bulk Zn and the Pt/C protective layer in the side-view SEM images of the lamella (Figure 5.4b and c). Cryo-EM was applied to reveal the thin layer more clearly (Figure 5.4d-f). In particular, the high resolution cryo-EM image (Figure 5.4e) clearly displays a homogeneous polymeric interphase layer on the Zn metal with a thickness of ~ 40 nm. The corresponding elemental mapping images (Figure 5.4f) demonstrate the uniform elemental distribution of C, N, and O at the interphase.

To identify the chemical environment and composition of the polymeric SEI layer, the Zn electrode was evaluated by X-ray photoelectron spectroscopy (XPS) after the 10^{th} stripping/plating process in the electrolyte with DA. The high-resolution XPS C 1s (Figure 5.4g) and N 1s (Figure 5.4h) spectra show strong C-C (284.8 eV), C-N (286.7 eV), C-O (289.4 eV), and N-H (399.5 eV) bonds, providing additional evidence for the successful *in-situ* polymerization strategy[33]. Furthermore, Ar^+ sputtering was introduced to investigate different depths of the polymeric SEI layer, as shown in the XPS depth profiles (Figure 5.4i and j). With increasing sputtering time, the intensity of the C 1s and N 1s peaks decreased gradually without obvious shifts, indicating the uniformity of the polymeric film on the Zn electrode. Based on the disappearance of C and N signals after sputtering for 100 s, the thickness of the polymeric SEI can be estimated to be about 40-50 nm, which is in consistent with the cryo-EM observations. Notably, the thickness of most of the reported SEI layers for RAZBs is normally in the range from over a hundred nanometers to micrometer size[34]. The *in-situ* polymeric SEI in this work, however, is much thinner, which could significantly minimize the sacrifice

of the volumetric energy density of Zn metal. Additionally, Fourier transform infrared (FTIR) analysis can give insights into the distribution and composition of the SEI layer. A uniform surface absorbance distribution can be detected in the FTIR mapping (Figure 5.4k), demonstrating the even formation of PDA on the Zn electrode during the electrochemical cycling process. The corresponding FTIR spectrum (Figure 5.4l) shows abundant characteristic peaks of organic functional groups in PDA.

5.3.3 Multifunctional features of the polymeric SEI

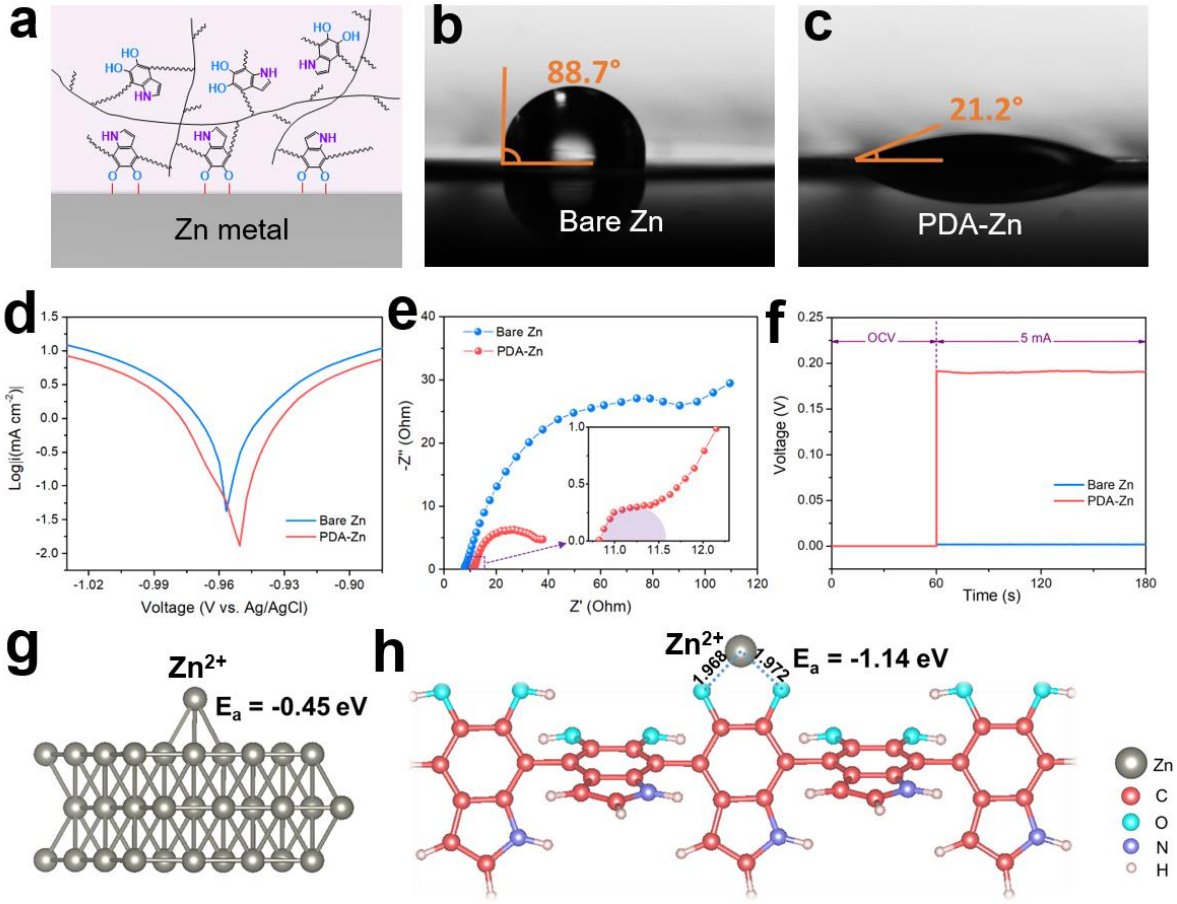

Figure 5.5 Multifunctional features of the polymeric SEI. (a) Schematic illustration of the PDA SEI layer on Zn electrode. Contact angle measurements of the electrolyte on (b) bare Zn electrode and (c) PDA-Zn electrode. (d) Linear polarization curves of bare Zn and PDA-Zn electrodes. (e) EIS spectra of the Zn symmetrical cells. (f) Voltage response of bare Zn and PDA-Zn electrodes. DFT calculation of the interactions of a foreign Zn^{2+} ion on (g) bare Zn electrode and (h) the PDA layer.

The abundant functional groups in PDA, as illustrated in Figure 5.5a, not only induce strong interaction between PDA and Zn, but also endow the robust SEI layer with multifunctional features to promote a highly stable Zn electrode. It is well known that Zn metal has poor wettability in aqueous electrolyte due to its hydrophobic nature. As shown in Figure 5.5b, the contact angle of bare Zn electrode was measured to be high as 88.7°. In contrast, the PDA-Zn electrode exhibits a significantly decreased contact

angle of 21.2° (Figure 5.5c). The outstanding wettability of Zn electrode with the *in-situ* PDA layer is favorable for reducing the interfacial energy barriers and thus producing homogeneous Zn plating[35]. Additionally, Zn corrosion has been evaluated as a crucial failure mechanism of zinc metal anode because of the poor thermodynamic stability of Zn metal in aqueous electrolytes[18,36,37]. As demonstrated in Figure 5.5d, the PDA-Zn electrode exhibited a higher corrosion voltage of -0.949 V than that of bare Zn (-0.957 V), suggesting lower liability towards corrosion side reactions due to the blocking effect of the SEI layer. In particular, the dense polymeric film reduced the corrosion current by 321.46 μA cm^{-2}, reflecting a slower corrosion rate of the PDA-Zn electrode. To further verify that the PDA SEI layer could block direct contact of Zn with the electrolyte and consequently suppress side reactions at the interface, the bare Zn and PDA-Zn electrodes were immersed in aqueous electrolyte for three days. Due to the thermodynamic instability of Zn metal in an aqueous environment, the products of interfacial corrosion reactions, zinc oxide and basic zincate, were detected for the bare Zn electrode after the immersion test (Figure 5.6), while no corrosion by-products were found for the PDA-Zn electrode. The formation mechanism of the basic zincate can be described as follows:

$$2H_2O + 2e^- \rightarrow H_2\uparrow + 2OH^- \quad (2)$$

$$xZn^{2+} + y(CF_3SO_3)^- + (2x-y)OH^- + nH_2O \rightarrow Zn_x(CF_3SO_3)_y(OH)_{2x-y} \cdot nH_2O \downarrow \quad (3)$$

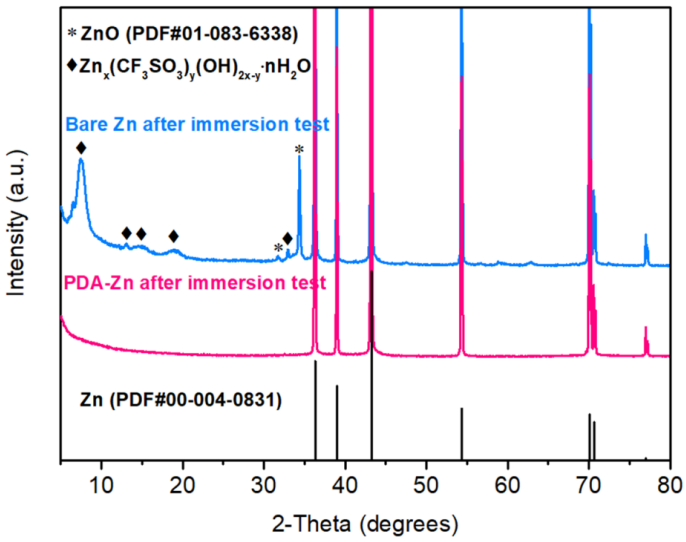

Figure 5.6 XRD patterns of bare Zn electrode and PDA-Zn electrode after immersion in aqueous electrolyte for 3 days.

Moreover, the introduction of DA into the electrolyte significantly restrained the electrochemical water decomposition, as evidenced by the negatively shifted potential and reduced current for H_2 evolution in Figure 5.7. The reduction current of 46 μA cm^{-2} at 0.16 V was reduced to 3 μA cm^{-2} with the addition of DA. These results demonstrate that the PDA layer on Zn could act as a barrier to isolate Zn from the electrolyte, which would impede interfacial side reactions.

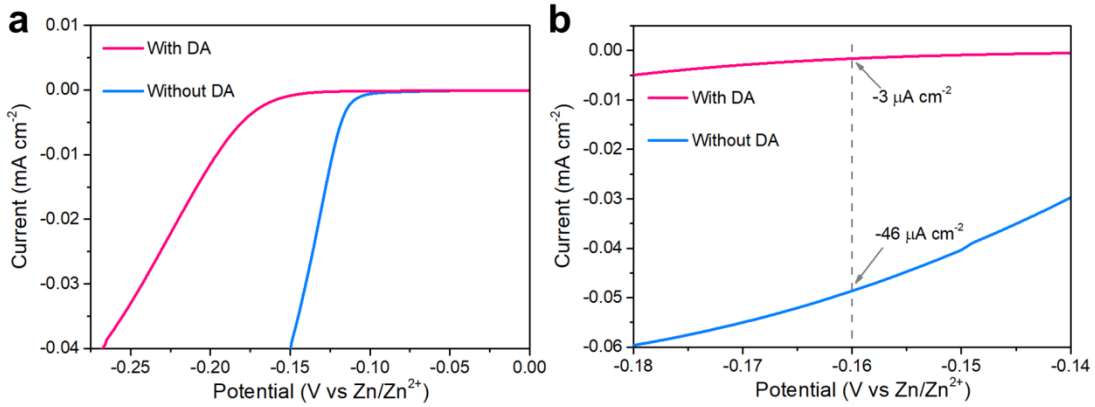

Figure 5.7 Linear sweep voltammograms (LSVs) of 1 M Zn $(CF_3SO_3)_2$ electrolyte with and without DA additive measured in a Zn/Ti half-cell at 0.1 mV s^{-1}.

Electrochemical impedance spectroscopy (EIS) analyses were also applied to validate the improved stability due to the PDA protective layer on Zn electrode. The impedance of the symmetrical cell with the PDA-Zn electrode was much lower than the impedance with the bare Zn electrode, as shown in Figure 5.5e. The high charge-transfer resistance of bare Zn electrode could be ascribed to the competing H_2 evolution and the formation of passivating by-products (such as ZnO and $Zn(OH)_2$) on the Zn electrode surface[8]. In contrast, the polymeric interphase layer on the Zn surface could effectively alleviate the detrimental interfacial side reactions and improve the interfacial stability, via blocking direct contact of the active Zn with the electrolyte. Moreover, the ionic conductivity of the SEI layer was estimated to be as high as 1.1×10^{-5} S cm^{-1} by fitting the impedance spectra at high frequencies (Figure 5.5e). The fast Zn^{2+} transport through the SEI layer could be ascribed to the charge transfer interactions between the abundant catechol functional groups in PDA[38,39], as discussed below. In addition, it has been proven that the energy consumption of the de-solvation at the interface is also the major factor dictating the ion-transfer kinetics[17]. To demonstrate how the PDA layer affects the de-solvation of Zn^{2+}, the Arrhenius curves and the activation energies of the bare Zn and the PDA-Zn are presented in Figure 5.8, which were determined by EIS of symmetric cells at different temperatures. The activation energy of PDA-Zn (23.3 kJ mol^{-1}) was much lower than that of bare Zn (35.4 kJ mol^{-1}). The reduced activation energy of the PDA-Zn suggested that the PDA SEI layer could ensure fast de-solvation of Zn^{2+} and facilitate a fast ion-transference process.

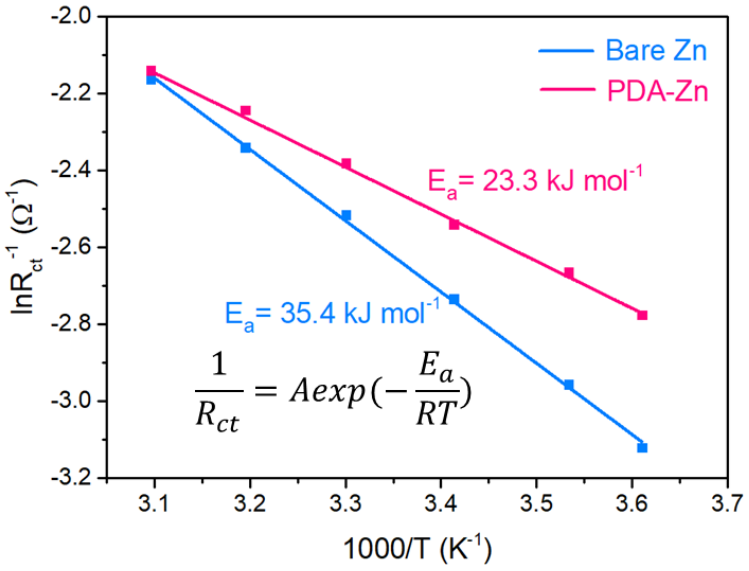

Figure 5.8 Arrhenius curves and activation energies of bare Zn and PDA-Zn, determined by EIS of symmetric cells at different temperatures. The symmetric cells were cycled for 20 cycles in the electrolyte with or without DA additive at room temperature.

The voltage-current response of the PDA-Zn electrode (Figure 5.5f) was employed to determine the electronic resistivity of the SEI, which was measured to be 7.46×10^6 **Ω** cm (that is, the electronic conductivity $\sigma = 1.34 \times 10^{-7}$ S cm^{-1}). The high electronic resistivity of the PDA ensures the necessary potential gradient through the SEI to drive Zn^{2+} diffusion. Therefore, the highly Zn^{2+}-conductive but electronically insulating PDA layer could not only provide effective Zn^{2+} diffusion pathways, but also suppress the electron-dependent interfacial side reactions.

Density functional theory (DFT) calculations were subsequently employed to explore the working mechanism of the SEI layer. Figure 5.5g and h present the calculated models of the interaction between a foreign Zn^{2+} and bulk Zn as well as the polymeric SEI chains, respectively. The binding energy of Zn^{2+} on the polymeric structure could reach -1.14 eV, much higher than that on bare Zn (-0.45 eV). The high binding energy

of the PDA layer directly demonstrates that the polymeric layer retained a strong adsorption capability towards Zn^{2+} at the electrode-electrolyte interphase, which could facilitate a uniform Zn^{2+} flux and hence regulate dendrite-free Zn deposition[40]. In addition, the transport mechanism for Zn^{2+} ions in PDA as investigated by DFT calculations is illustrated in Figure 5.9. The PDA chain could offer a large distribution of binding sites for Zn^{2+} ions, where Zn^{2+} ions coordinate with oxygen atoms in the abundant catechol functional groups. Zn^{2+} ions diffuse along tunnels formed by these consecutive catechol groups. The corresponding Zn^{2+} migration energy barrier is calculated to be 0.40 eV, which is comparable to the Li^{+} migration energy barriers in some fast Li-ion conductors[41,42]. The DFT analysis suggests that PDA offers low barrier diffusion channels for the transport of Zn^{2+} through the consecutive catechol groups in PDA chains.

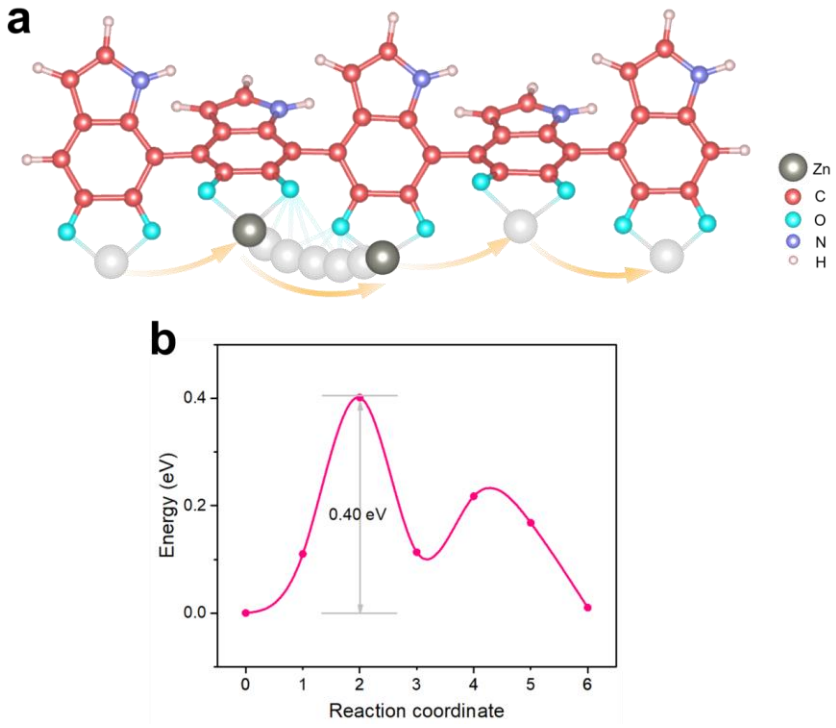

Figure 5.9 First-principles calculations of (a) the Zn-ion migration path in the PDA SEI layer and (b) the corresponding migration energy barrier.

5.3.4 Zn deposition behavior and reversibility

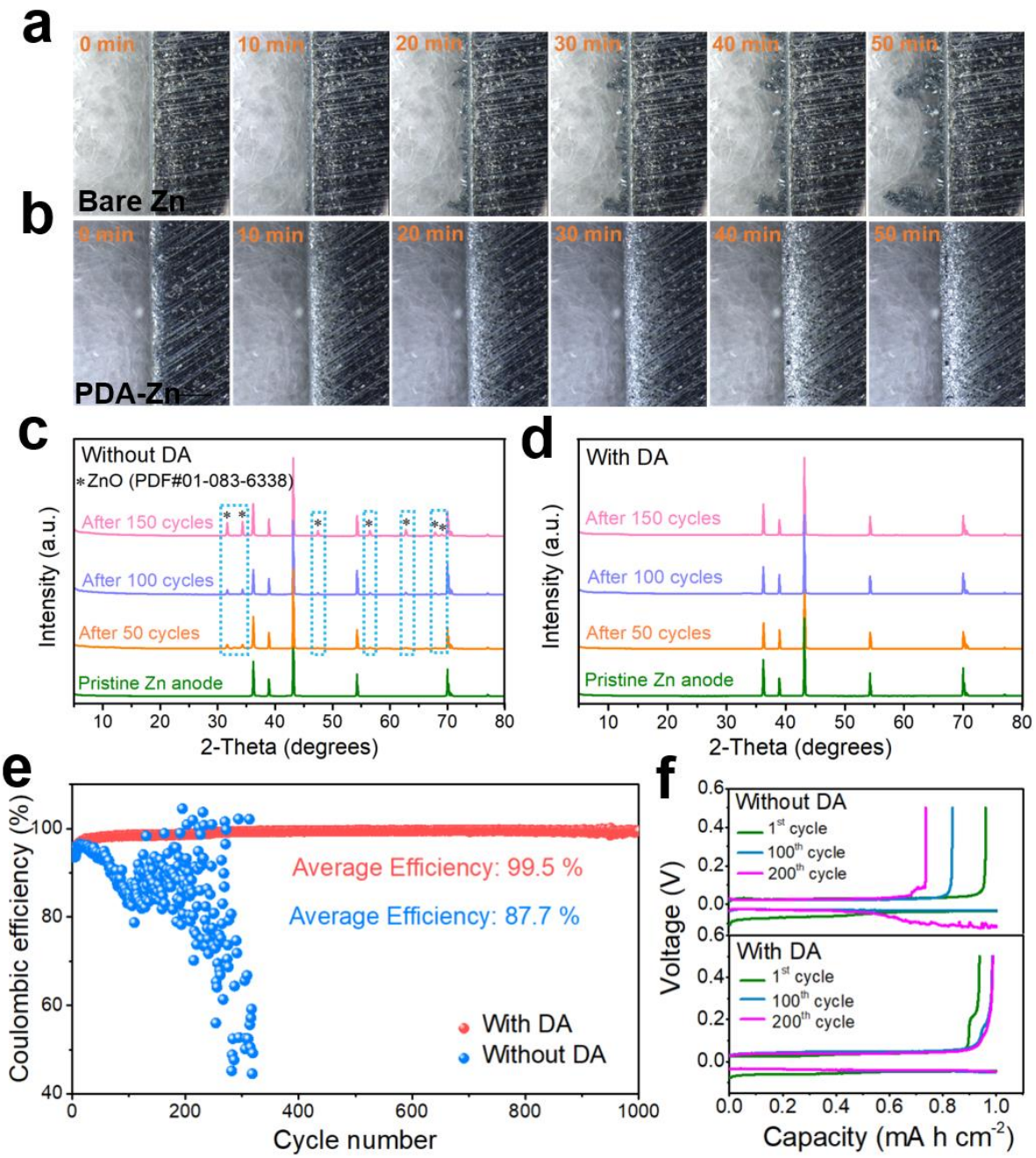

Figure 5.10 Effect of the polymeric SEI layer on Zn plating behavior and reversibility. *In-situ* optical microscope images of Zn plating on (a) bare Zn electrode and (b) PDA-Zn electrode. XRD characterization of Zn electrodes after specific cycles in 1 M $Zn(CF_3SO_3)_2$ (c) without and (d) with DA. (e) Coulombic efficiency (CE) measurements and (f) corresponding voltage profiles of Cu/Zn cells in the electrolytes with and without DA.

To clarify the effect of the SEI on Zn, *in-situ* observations of the Zn plating behavior were conducted by optical microscopy. As shown in Figure 5.10a, uneven moss-like Zn deposition occurred on the bare Zn after electrochemical plating for 20 min. With a continuous plating process, these protuberances developed into obvious dendrites. The formation of dendrites would potentially induce interior short-circuits, a low Zn plating/stripping CE, and battery degradation. In strong contrast, the Zn deposition on the PDA-Zn electrode was dense and homogeneous without dendritic morphology during the whole electrodeposition process, as evidenced in Figure 5.10b.

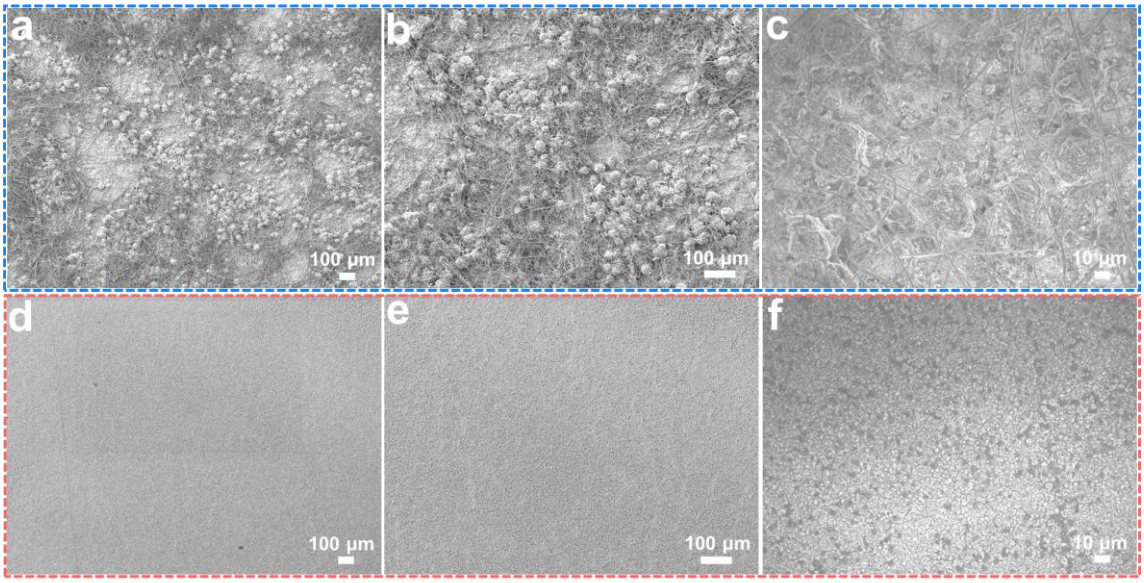

Figure 5.11 SEM images of Zn deposition morphology on Cu foil. (a-c) 1 M $Zn(CF_3SO_3)_2$, (d-f) 1 M $Zn(CF_3SO_3)_2$ with DA as electrolyte. The applied current density was 1 mA cm^{-2}, and the areal capacity was 1 mA h cm^{-2}. The Cu foil was pre-cycled in Cu/Zn cells with the respective electrolytes for 5 cycles.

For further verifying the effectiveness of the PDA SEI for inhibiting the Zn dendrites, the Zn plating morphology on Cu substrate was inspected in the electrolyte with and without the DA (Figure 5.11). The Cu foil was pre-cycled in Cu/Zn cells with the

respective electrolyte for 5 cycles. After plating to 1 mA h cm^{-2} at 1 mA cm^{-2}, the Zn deposits were dendritic and agglomerated in the blank electrolyte. A homogeneous and compact morphology of Zn deposition on Cu, however, was obtained in the electrolyte with DA. This validates the critical effect of the *in-situ* SEI towards dendrite-free Zn plating.

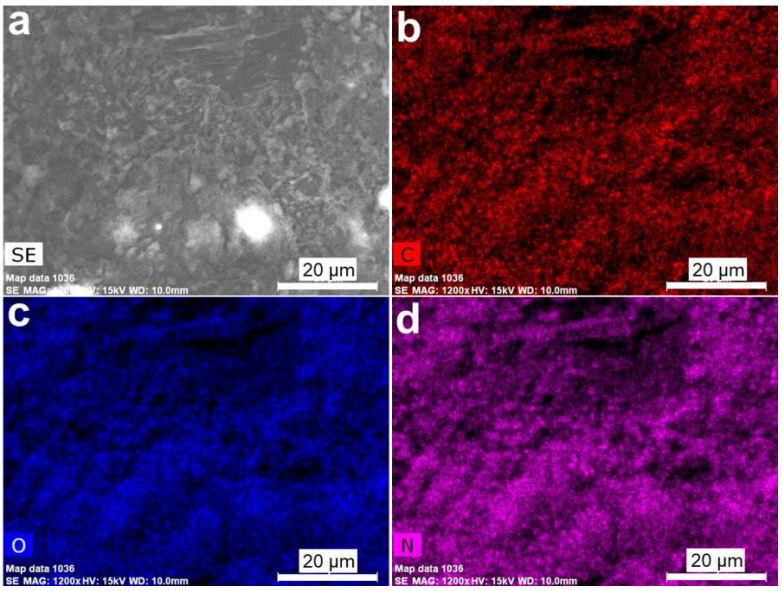

Figure 5.12 (a) SEM image and (b-d) corresponding EDX mapping of the Zn electrode after 400 h of plating/stripping in electrolyte with DA.

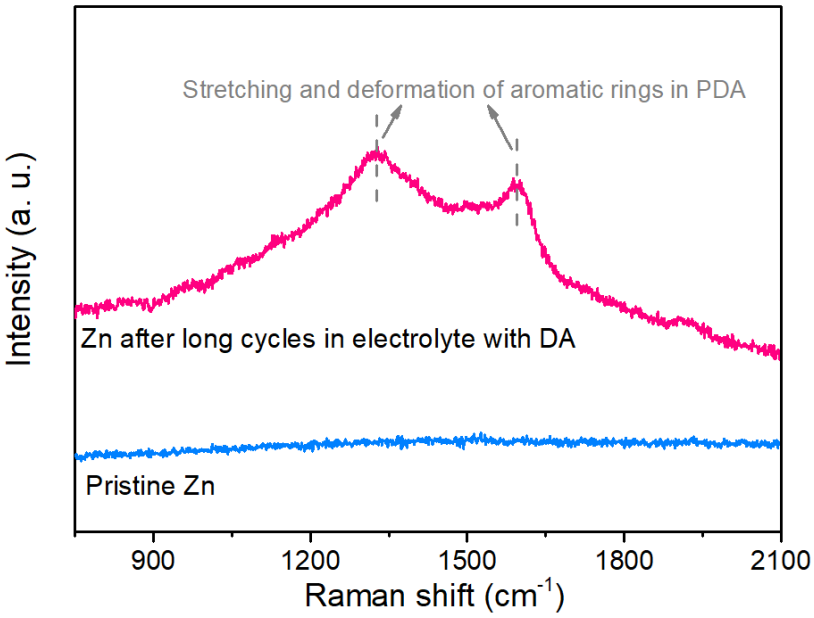

Figure 5.13 Raman spectra of pristine Zn and Zn electrode after long cycling in electrolyte with DA. The cycled Zn electrode was stripped out of its symmetrical cell (1 mA cm^{-2}, 1 mA h cm^{-2}) after 400 h of plating/stripping in electrolyte with DA. The Raman spectrum of long-cycled Zn still shows the typical stretching and deformation peaks of aromatic rings in PDA.

Surface characterization of Zn electrodes after long-term plating/stripping processes was conducted to demonstrate the stability of the SEI layer. As shown in Figure 5.12, the EDX mapping of Zn electrode after 400 h of plating/stripping still displays uniform elemental distributions of C, O, and N, demonstrating the stability and uniformity of the PDA SEI layer on the Zn surface. The Raman spectrum (Figure 5.13) of long-cycled Zn electrode also shows the typical stretching and deformation peaks of aromatic rings in PDA.

Top-view and side-view SEM images of Zn electrodes after plating/stripping for 400 h are presented in Figures 5.14 and 5.15. The Zn cycled in the blank electrolyte exhibited sloppy and dendritic morphology. Moreover, obvious volume expansion and electrode

pulverization could be detected (Figure 5.15), which were responsible for the low Zn utilization and battery degradation. Comparatively, the long-cycled Zn electrode in the electrolyte with DA showed a compact and undamaged surface, demonstrating the durability and robustness of the PDA protective layer on Zn electrode. In addition, digital images (Figure 5.16) of the glass fiber separators and the dimmed Zn electrodes after cycling also indicated the severe dendrite growth and pulverization of Zn electrode in the blank electrolyte. An uncontaminated glass fiber separator and a lustrous Zn electrode, however, were obtained even after 400 h in the electrolyte with DA additive, owing to the stable Zn and suppressed side reactions enabled by the PDA interfacial layer.

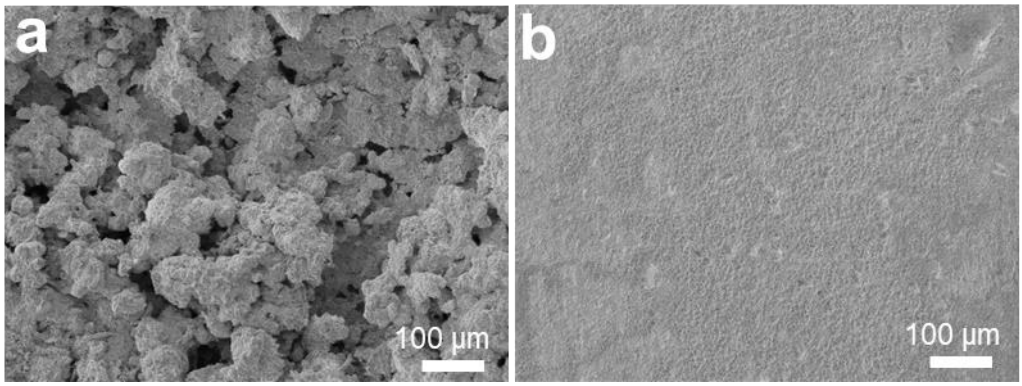

Figure 5.14 Top-view SEM images of Zn electrodes after 400 h of plating/stripping. (a) 1 M $Zn(CF_3SO_3)_2$, (b) 1 M $Zn(CF_3SO_3)_2$ with DA as electrolyte.

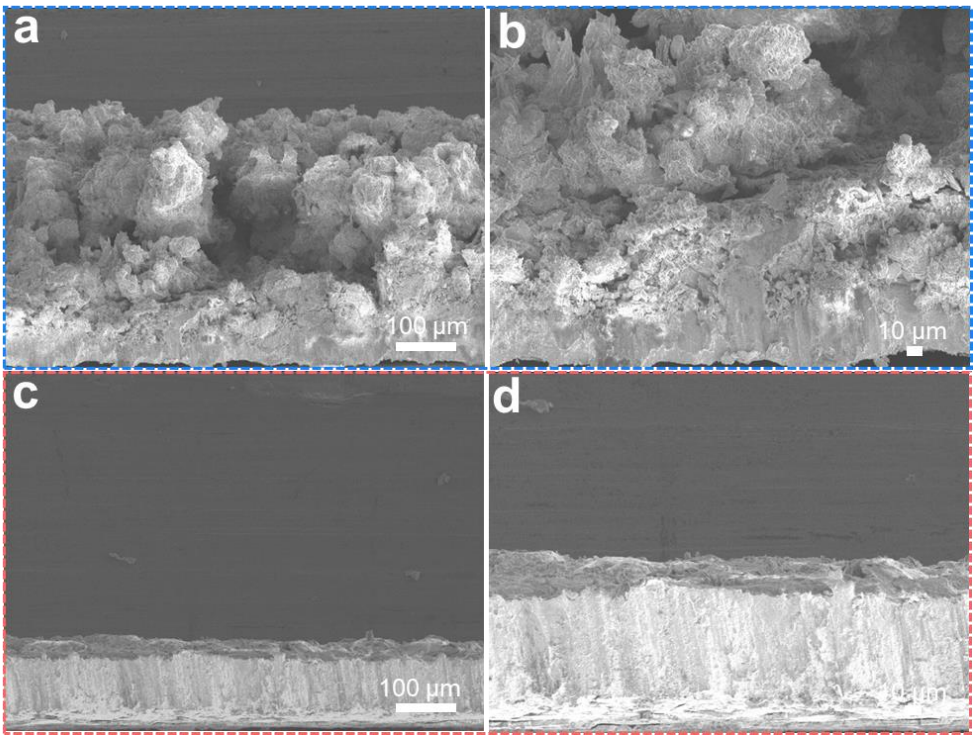

Figure 5.15 Side-view SEM images of Zn electrodes after 400 h of plating/stripping. (a, b) 1 M $Zn(CF_3SO_3)_2$, (c, d) 1 M $Zn(CF_3SO_3)_2$ with DA as electrolyte.

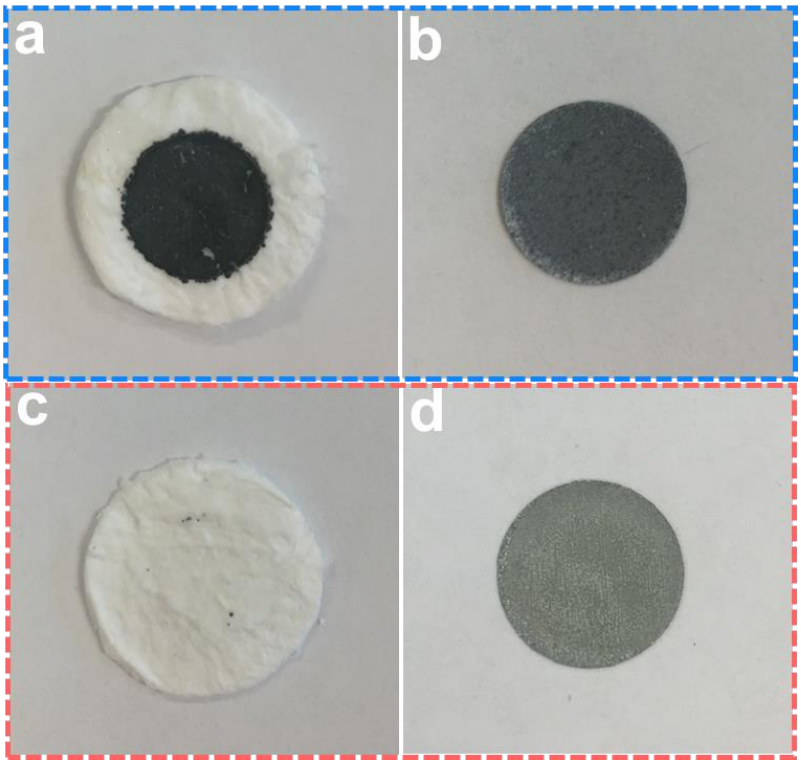

Figure 5.16 Digital images of Zn electrodes and glass fiber separators stripped from symmetrical cells after 400 h. (a) Glass fiber separator and (b) Zn electrode after cycling in the 1 M $Zn(CF_3SO_3)_2$ electrolyte. (c) Glass fiber separator and (d) Zn electrode after cycling in the electrolyte with DA. The applied current density was 1 mA cm^{-2}, and the areal capacity was 1 mA h cm^{-2}. In 1 M $Zn(CF_3SO_3)_2$ without DA, significant pulverization and corrosion of the Zn electrode could be observed after long-term cycling.

X-ray diffraction (XRD) analysis of the cycled Zn electrode could provide further insight into the durability and protective mechanism of the polymeric SEI layer. In the blank electrolyte, the diffraction peaks of the by-products of ZnO gradually emerged and were strengthened, as highlighted in the blue rectangles in Figure 5.10c. The formation of ZnO by-product was derived from competitive H_2 evolution during the process of Zn deposition, and consequently an increase in the local concentration of OH^- at the electrode/electrolyte interface[22]. As evidenced by the steady XRD patterns of Zn in the electrolyte with DA (Figure 5.10d), however, the formation of the PDA layer could impede the parasitic reactions between Zn metal and the electrolyte such as the hydrogen evolution and ZnO formation, and ensure a stable Zn structure during repeated Zn plating/stripping.

The reversibility of the aqueous Zn chemistry was examined by plating/stripping tests in Cu/Zn cells at 1 mA cm^{-2} with an areal capacity of 1 mA h cm^{-2}. Figure 5.10e, f presents the CEs and the corresponding voltage profiles in the electrolyte with and without DA. An inferior average CE of 87.7 % was evaluated in the electrolyte without DA, which was mainly caused by the growth of dendritic Zn and parasitic reactions. Moreover, the CEs and voltage profiles in the blank electrolyte showed obvious

fluctuations after 100 cycles, reflecting the severe competitive reaction of H_2 evolution. The continuous water decomposition could not only lead to a short cycling lifespan, but could also induce a potential safety issue. In the electrolyte with DA, however, stable CEs and voltage profiles for 1000 cycles were revealed with a tremendously improved average CE of 99.5 %. The boosted reversibility of Zn plating/stripping confirmed that the *in-situ* formation of the PDA protective layer could suppress detrimental Zn dendrites and side reactions to promote the utilization of Zn metal anode.

5.3.5 Full cell performance with lean electrolyte and low N/P ratio

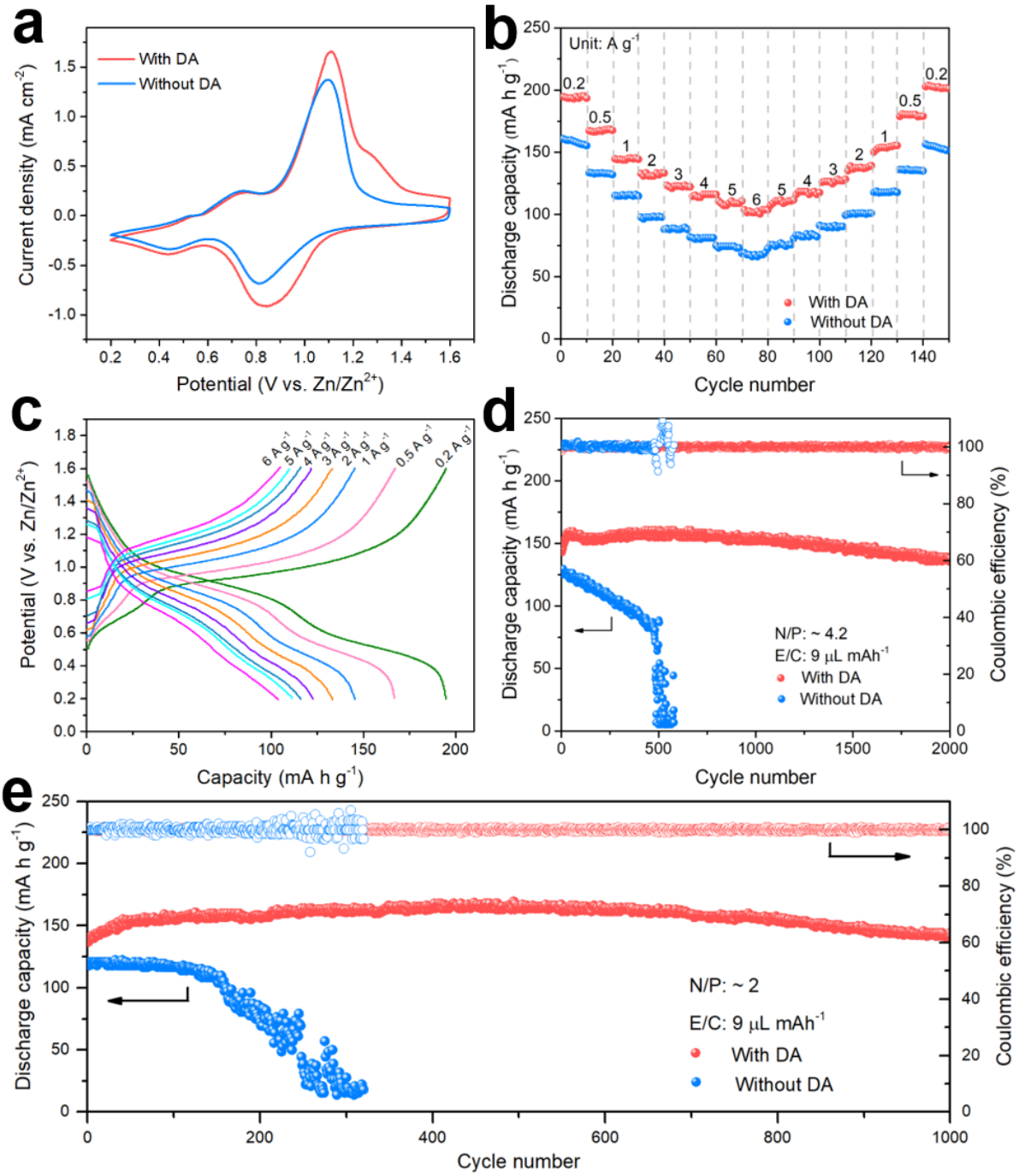

Figure 5.17 Electrochemical performances of RAZBs under practical conditions. (a) CV curves of Zn/V_2O_5 full cells. (b) Comparison of rate performances of Zn/V_2O_5 full cells in the electrolyte with and without DA additive. (c) Corresponding voltage profiles of Zn/V_2O_5 full cells in the electrolyte with DA at different current densities. (d, e) Comparison of the cycling performances of Zn/V_2O_5 full cells at 1 A g^{-1} under lean electrolyte and low N/P ratios.

In order to assess the feasibility of the *in-situ* polymerization strategy in a practical battery system, full cells of Zn/V_2O_5 were assembled to investigate their electrochemical properties. Cyclic voltammetry (CV) tests of Zn/V_2O_5 cells in the two electrolytes were performed. As shown in Figure 5.17a, the V_2O_5 cathode in both electrolytes exhibited similar redox peaks, which were assigned to the Zn^{2+}/H^+ co-insertion mechanism and consistent with previous works[43]. The rate capability and corresponding voltage profiles at various current densities from 0.2 A g^{-1} to 6 A g^{-1} are displayed in Figure 5.17b and c. In the electrolyte with DA additive, the full cell delivered a high specific capacity of 191 mA h g^{-1} at the low rate of 0.2 A g^{-1}, and 104 mA h g^{-1} at the high rate of 6 A g^{-1}, respectively. Moreover, after long-term cycling at different rates, the capacities were recoverable when the rate shifted back towards the low rates, which reflected the restrained side reactions and highly stable Zn anode. On the contrary, the full cell in the blank electrolyte displayed poor rate capability and low capacity, owing to the low CE and stability of the Zn anode. In addition, due to the electrochemical polymerization mechanism of PDA, a PDA layer was also detected on the V_2O_5 cathode after cycling, as demonstrated by XPS and Raman spectroscopy (Figures 5.18 and 5.19).

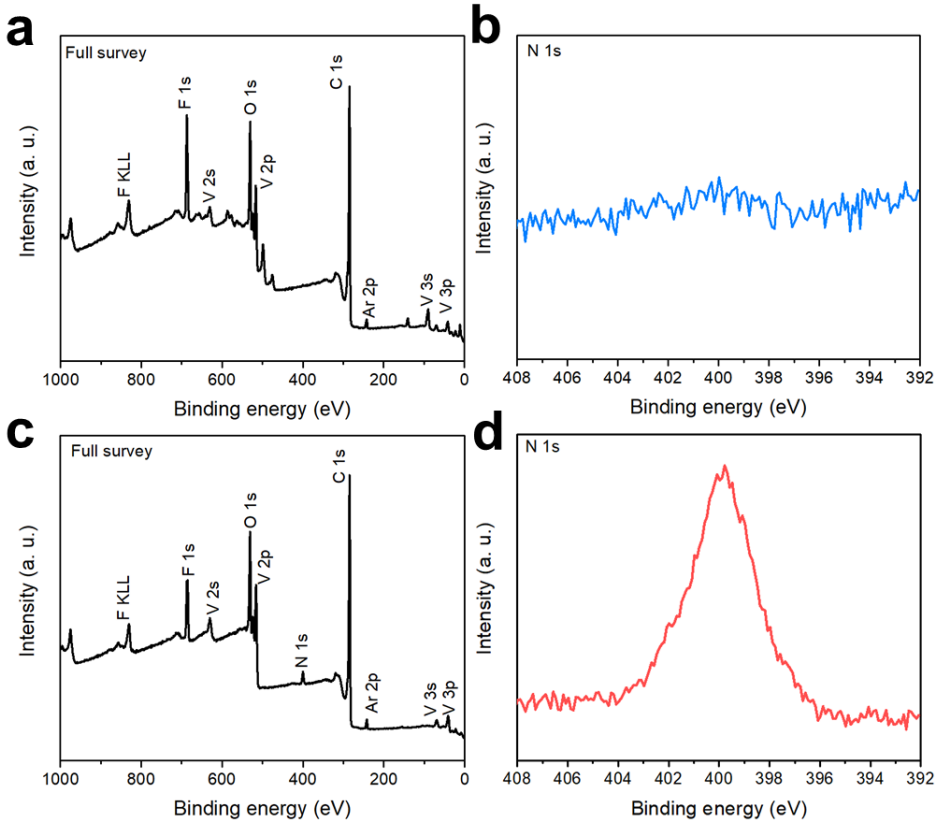

Figure 5.18 XPS characterization of V_2O_5 cathode after cycling. (a, b) 1 M $Zn(CF_3SO_3)_2$, (c, d) 1 M $Zn(CF_3SO_3)_2$ with DA additive as electrolyte**.**

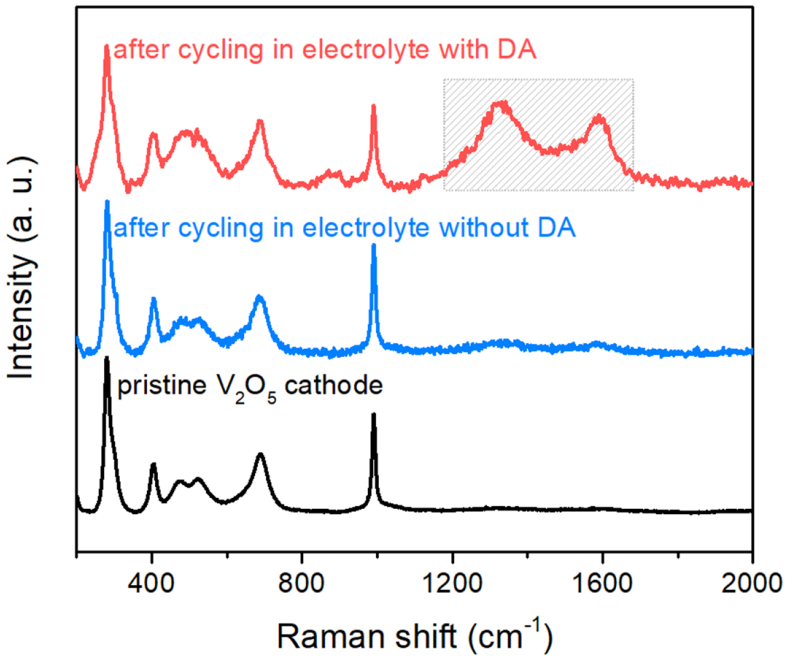

Figure 5.19 Raman spectra of V_2O_5 cathode before and after cycling.

The formation of a uniform PDA layer on the V_2O_5 electrode could significantly relieve the unfavorable issue of V_2O_5 dissolution, further ensuring high capacity and superior cycling capability. As indicated in Figure 5.20, after 200 cycles in the blank electrolyte, massive dissolution of V_2O_5 was discovered; with the introduction of DA, however, dense V_2O_5 cathode could be found without detectable dissolution. Due to the highly stable cathode and metal anode, the Zn/V_2O_5 cell in the electrolyte with DA showed outstanding cycling capability for 4000 cycles (Figure 5.21).

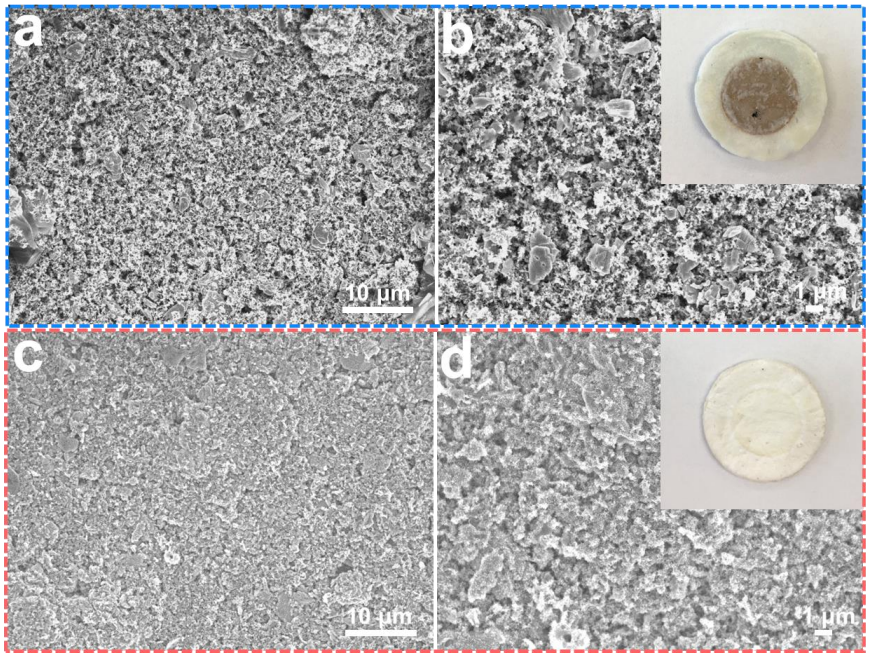

Figure 5.20 SEM images of cycled V_2O_5 cathodes and digital images of glass fiber separators (insets) stripped from Zn/V_2O_5 full cells after cycling at 1 A g^{-1} for 200 cycles. (a, b) Cycling in 1 M $Zn(CF_3SO_3)_2$ electrolyte. (c, d) Cycling in 1 M $Zn(CF_3SO_3)_2$ electrolyte with 50 mM DA.

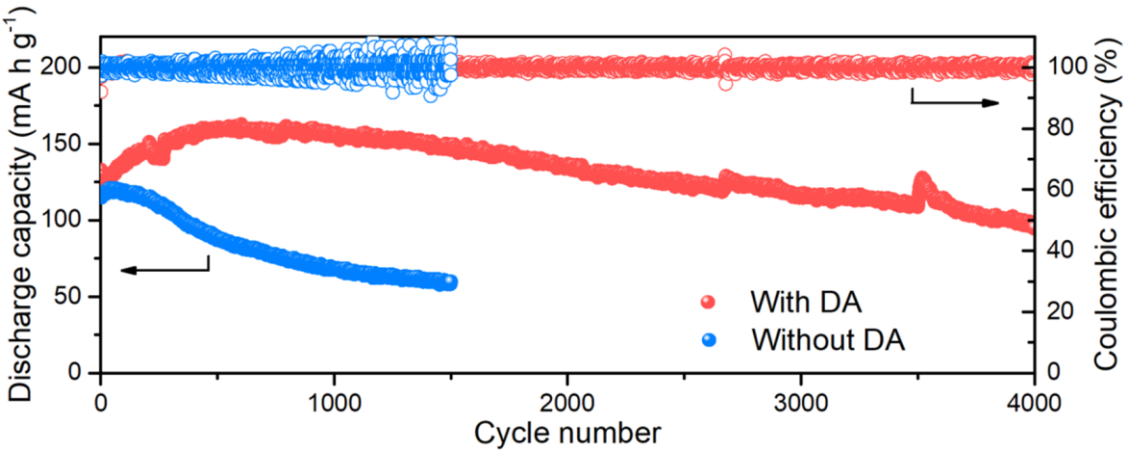

Figure 5.21 Long-term cycling stability of Zn/V_2O_5 full cells with high excess Zn (thickness 60 μm) and electrolyte with and without DA. The applied current density was 1 A g^{-1}.

For real applications, the cycling performance of the full cells was measured under practical conditions, including lean electrolyte and ultrathin Zn anode (thickness: 10 μm). In most previous reports, flooded electrolyte and greatly excessive Zn electrode were used, which not only masked the problem of electrolyte-induced side reactions and low Zn utilization, but also made the results difficult to compare and interpret[10,44,45]. In this work, however, the electrolyte-to-capacity ratio (E/C) was reduced to 9 μL mA h^{-1}, and the ratio of the negative capacity to the positive capacity (N/P) was controlled to ~ 4.2 and 2, respectively. As shown in Figure 5.17d, the full cell in the blank electrolyte with very limited excess Zn suffered from a sharply decreasing capacity and subsequent battery failure after only 500 cycles. The battery degradation of the control cell could be mainly attributed to the growth of Zn dendrites and continuous consumption of active Zn metal, as indicated in Figure 5.22.

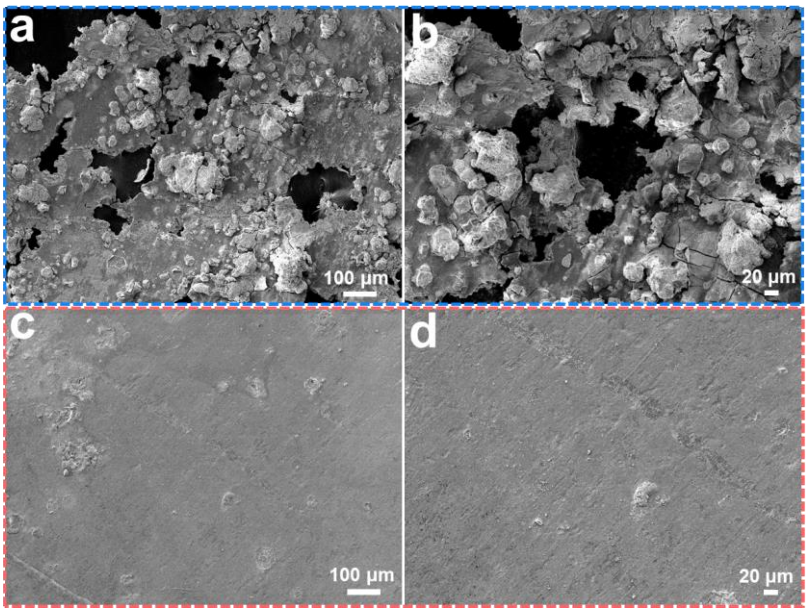

Figure 5.22 SEM images of ultrathin Zn electrodes (10 µm) after cycling for 200 cycles in Zn/V_2O_5 full cells. (a, b) Cycling in 1 M Zn(CF_3SO_3)$_2$ as electrolyte, (c, d) cycling in 1 M Zn(CF_3SO_3)$_2$ with 50 mM DA.

In sharp contrast, with the protection of the polymeric SEI layer, the full cell exhibited significantly enhanced cycling stability, with high capacity retention of 92.8 % for 2000 cycles, confirming the success of the SEI layer for stabilizing Zn electrode and achieving high-performance RAZBs. Notably, on further restricting the N/P ratio to 2, nearly 100 % CE and high discharge capacity of the full cell could still be retained in the electrolyte with DA additive, as shown in Figure 5.17e. For over 1000 cycles, a high discharge capacity of 141.8 mA h g^{-1} was maintained with 94.3 % capacity retention. Conversely, the control cell in the blank electrolyte showed a fast capacity decay and unstable CE after only 120 cycles. These results provide direct evidence that the *in-situ* formation of the PDA film could enable high utilization and stability of the Zn electrode by manipulating dendrite-free plating/stripping and hindering interfacial side reactions, so that it could further attain excellent electrochemical performance in Zn/V_2O_5 full cells under practical conditions.

5.4 Conclusion

In this work, the bio-inspired construction of a PDA SEI layer on Zn anode via an *in-situ* polymerization strategy has been successfully established, by simply introducing dopamine as an electrolyte additive to facilitate a highly stable Zn metal anode. The uniform PDA SEI layer possesses multifunctional features, strong adhesion to the surface of the Zn metal, remarkable hydrophilicity, and high Zn-ion conductivity, due to the abundant functional groups in its molecular chains. Such a robust SEI layer on Zn could alleviate interfacial side reactions via isolating Zn from the electrolyte. The favorable interaction of Zn^{2+} with the polymeric SEI layer was also verified by the combination of experimental characterizations and DFT computations. This SEI layer could promote a homogeneous Zn^{2+} flux at the electrode-electrolyte interface, and hence, effectively guide dendrite-free Zn deposition. Therefore, the Zn electrode in the electrolyte with DA additive exhibited tremendously improved Zn utilization (99.5 %) and stable Zn plating/stripping when cycling at high current densities and high areal capacities up to 30 mA cm^{-2} and 30 mA h cm^{-2}. The as-developed Zn anode further enables Zn/V_2O_5 full cells with high capacity, excellent rate performance, and long-term cycling capability, even with a practically relevant N/P ratio and lean electrolyte. This simple yet effective strategy for *in-situ* construction of a polymeric SEI layer in aqueous chemistry opens up a fresh route towards advanced energy storage systems for practical applications.

5.5 References

1. X. Cao, X. Ren, L. Zou, M. H. Engelhard, W. Huang, H. Wang, B. E. Matthews, H. Lee, C. Niu, B. W. Arey, Y. Cui, C. Wang, J. Xiao, J.Liu, W. Xu and J. Zhang, *Nat. Energy*, 2019, **4**, 796-805.

2. Z. Liu, Y. Huang, Y. Huang, Q. Yang, X. Li, Z. Huang and C. Zhi, *Chem. Soc. Rev.*, 2020, **49**, 180-232.

3. F. Wang, O. Borodin, T. Gao, X. Fan, W. Sun, F. Han, A. Faraone, J. A. Dura, K. Xu and C. Wang, *Nat. Mater.*, 2018, **17**, 543-549.

4. H. Pan, Y. Shao, P. Yan, Y. Cheng, K. S. Han, Z. Nie, C. Wang, J. Yang, X. Li, P. Bhattacharya, K. T. Mueller and J. Liu, *Nat. Energy*, 2016, **1**, 1-7.

5. H. Qiu, X. Du, J. Zhao, Y. Wang, J. Ju, Z. Chen, Z. Hu, D. Yan, X. Zhou and G. Cui, *Nat. Commun.*, 2019, **10**, 1-12.

6. J. Zheng, Q. Zhao, T. Tang, J. Yin, C. D. Quilty, G. D. Renderos, X. Liu, Y. Deng, L. Wang D.C. Bock, C. Jaye, D. Zhang, E. S. Takeuchi, K. J. Takeuchi, A. C. Marschilok and L. A. Archer, *Science*, 2019, **366**, 645-648.

7. H. Yang, Z. Chang, Y. Qiao, H. Deng, X. Mu, P. He and H. Zhou, *Angew. Chem. Int. Ed.*, 2020, **59**, 9377-9381.

8. S. Wang, Q. Ran, R. Yao, H. Shi, Z. Wen, M. Zhao, X. Lang and Q. Jiang, *Nat. Commun.*, 2020, **11**, 1-9.

9. Y. Zhang, F. Wan, S. Huang, S. Wang, Z. Niu and J. Chen, *Nat. Commun.*, 2020, **11**, 1-10.

10. L. W. Blanc, D. Kundu and L. F. Nazar, *Joule*, 2020, **4**, 771-799.

11. X. Zeng, J. Mao, J. Hao, J. Liu, S. Liu, Z. Wang, Y. Wang, S. Zhang, T. Zheng, J. Liu, P. Rao and Z. Guo, *Adv. Mater.*, 2021, **33**, 2007416.

12. Z. Wang, J. Huang, Z. Guo, X. Dong, Y. Liu, Y. Wang and Y. Wang, *Joule*, 2019, **3**, 1289-1300.

13. Q. Zhang, J. Luan, L. Fu, S. Wu, Y. Tang, X. Ji and H. Wang, *Angew. Chem. Int. Ed.*, 2019, **58**, 15841-15847.

14. L. Ma, S. Chen, X. Li, A. Chen, B. Dong and C. Zhi, *Angew. Chem. Int. Ed.*, 2020, **132**, 24044-24052.

15. A. Naveed, H. Yang, J. Yang, Y. Nuli and J. Wang, *Angew. Chem. Int. Ed.*, 2019, **58**, 2760-2764.

16. X. Zeng, J. Liu, J. Mao, J. Hao, Z. Wang, S. Zhou, C. D. Ling and Z. Guo, *Adv. Energy Mater.*, 2020, **10**, 1904163.

17. X. Xie, S. Liang, J. Gao, S. Guo, J. Guo, C. Wang, G. Xu, X. Wu, G. Chen and J. Zhou, *Energy Environ. Sci.*, 2020, **13**, 503-510.

18. Z. Zhao, J. Zhao, Z. Hu, J. Li, J. Li, Y. Zhang, C. Wang and G. Cui, *Energy Environ. Sci.*, 2019, **12**, 1938-1949.

19. Q. Yang, Y. Guo, B. Yan, C. Wang, Z. Liu, Z. Huang, Y. Wang, Y. Li, H. Li, L. Song, J. Fan and C. Zhi, *Adv. Mater.*, 2020, **32**, 2001755.

20. Y. Chu, S. Zhang, S. Wu, Z. Hu, G. Cui and J. Luo, *Energy Environ. Sci.*, 2021,**14**, 3609-3620.

21. J. Hao, B. Li, X. Li, X. Zeng, S. Zhang, F. Yang, S. Liu, D. Li, C. Wu and Z. Guo, *Adv. Mater.*, 2020, **32**, 2003021.

22. L. Cao, D. Li, T. Deng, Q. Li and C. Wang, *Angew. Chem. Int. Ed.*, 2020, **59**, 19292-19296.

23. L. Cao, D. Li, E. Hu, J. Xu, T. Deng, L. Ma, Y. Wang, X. Yang and C. Wang, *J. Am. Chem. Soc.*, 2020, **142**, 21404-21409.

24. X. Zeng, J. Hao, Z. Wang, J. Mao and Z. Guo, *Energy Storage Mater.*, 2019, **20**, 410-437.

25. Y. Liu, K. Ai and L. Lu, *Chem. Rev.*, 2014, **114**, 5057-5115.

26. T. Liu, K. C. Kim, B. Lee, Z. Chen, S. Noda, S. S. Jang and S. W. Lee, *Energy Environ. Sci.*, 2017, **10**, 205-215.

27. W. Zhang, F. K. Yang, Y. Han, R. Gaikwad, Z. Leonenko and B. Zhao, *Biomacromolecules,* 2013, **14**, 394-405.

28. Q. Meng, H. Zhang, Y. Liu, S. Huang, T. Zhou, X. Yang, B. Wang, W. Zhang, H. Ming, Y. Xiang, M. Li, G. Cao, Y. Huang, L. Fan, H. Zhang and Y. Guan, *Nano Res.*, 2019, **12**, 2919-2924.

29. J. Cai, J. Huang, M. Ge, J. Iocozzia, Z. Lin, K. Zhang, Y. Lai, *Small*, 2017, **13**, 1604240.

30. L. Qin, X. Li, S. Kang and J. Mu, *Colloids Surf. B,* 2015, **126**, 210-216.

31. J. Ma, H. Yang, S. Li, R. Ren, J. Li, X. Zhang and J. Ma, *RSC Adv.*, 2015, **5**, 97520-97527.

32. Z. Cai, Y. Ou, B. Zhang, J. Wang, L. Fu, M. Wan, G. Li, W. Wang, L. Wang, J. Jiang, Z. W. She, E. Hu, X. Yang, Y. Cui and Y. Sun, *J. Am. Chem. Soc.*, 2021, **143**, 3143-3152.

33. H. Lee, T. Han, K. Y. Cho, M. H. Ryou and Y. M. Lee, *ACS Appl. Mater. Interfaces*, 2016, **8**, 21366-21372.

34. C. Li, Z. Sun, T. Yang, L. Yu, N. Wei, Z. Tian, J. Cai, J. Lv, Y. Shao, M. H. Rümmeli, J. Sun and Z. Liu, *Adv. Mater.*, 2020, **32**, 2003425.

35. J. Hao, X. Li, S. Zhang, F. Yang, X. Zeng, S. Zhang, G. Bo, C. Wang and Z. Guo, *Adv. Funct. Mater.*, 2020, **30**, 2001263.

36. M. Zhou, S. Guo, J. Li, X. Luo, Z. Liu, T. Zhang, X. Cao, M. Long, B. Lu, A. Pan, G. Fang, J. Zhou, S. Liang, *Adv. Mater.*, 2021, **33**, 2100187.

37. M. Zhou, S. Guo, G. Fang, H. Sun, X. Cao, J. Zhou, A. Pan, S. Liang, *J. Energy Chem.*, 2021, **55**, 549-556.

38. B. Yu, J. Liu, S. Liu and F. Zhou, *Chem. Commun.*, 2010, **46**, 5900-5902.

39. G. Liu, J. Shi, M. Zhu, W. Weng, L. Shen, J. Yang and X. Yao, *Energy Storage Mater.*, 2021, **38**, 249-254.

40. Z. Wang, Y. Wang, Z. Zhang, X. Chen, W. Lie, Y. He, Z. Zhou, G. Xia and Z. Guo, *Adv. Funct. Mater.*, 2020, **30**, 2002414.

41. S. Muy, J. C. Bachman, L. Giordano, H. Chang, D. L. Abernathy, D. Bansal, O. Delaire, S. Hori, R. Kanno, F. Maglia, S. Lupart, P. Lamp and Y. Shao-Horn, *Energy Environ. Sci.*, 2018, **11**, 850-859.

42. H. Buschmann, J. Dölle, S. Berendts, A. Kuhn, P. Bottke, M. Wilkening, P. Heitjans, A. Senyshyn, H. Ehrenberg, A. Lotnyk, V. Duppel, L. Kienle and J. Janek, *Phys. Chem. Chem. Phys.*, 2011, **13**, 19378-19392.

43. F. Wan, L. Zhang, X. Dai, X. Wang, Z. Niu and J. Chen, *Nat. Commun.*, 2018, **9**, 1-11.

44. J. Hao, X. Li, X. Zeng, D. Li, J. Mao and Z. Guo, *Energy Environ. Sci.*, 2020, **13**, 3917-3949.

45. D. Luo, L. Zheng, Z. Zhang, M. Li, Z. Chen, R. Cui, Y. Shen, G. Li, R. Feng, S. Zhang, G. Jiang, L. Chen, A. Yu and X. Wang, *Nat. Commun.*, 2021, **12**, 1-11.

Chapter 6

Towards a Reversible Mn^{4+}/Mn^{2+} Redox Reaction and Dendrite-Free Zn Anode in Near-Neutral Aqueous Zn/MnO_2 Batteries via Salt Anion Chemistry

6.1 Introduction

Large-scale energy storage is critical to ensure the reliability of smart electricity grid systems and the integration of renewable intermittent energy sources such as solar and wind. Rechargeable batteries are one of the most promising methods for energy storage.[1-4] For large-scale energy storage to be feasible, however, the electrodes employed need to be cost-effective, and the systems should be long lasting and safe during operation. Aqueous batteries are favorable candidates owing to their intrinsic safety and environmental friendliness.[5-7] Among them, rechargeable Zn/MnO_2 batteries employing a mild aqueous electrolyte have attracted extensive attention, due to the high abundance and environmental compatibility of manganese dioxide, as well as the low cost, low redox potential (-0.76 V *vs.* standard hydrogen electrode (SHE)), and high capacity (820 mA h g^{-1}) of Zn anode.[8, 9] Several key challenges, however, have limited the practical application of rechargeable aqueous Zn/MnO_2 batteries. These include the structural change and collapse of MnO_2 during repeated Zn^{2+} or H^+ ion insertion/extraction and Mn^{2+} ion dissolution, their low capacity (normally ~300 mA h g^{-1} based on the one-electron reaction *via* Mn^{4+}/Mn^{3+} redox couple), and the unsatisfactory reversibility of Zn metal anode.[9, 10] Accordingly, it is highly desirable to explore new battery chemistries in the Zn/MnO_2 system.

The nature of salt anions in electrolytes plays a critical role in dictating the electrochemical behaviour and performance of batteries.[11, 12] Different anion species

may strongly affect the ion association properties in solution, possible side reactions, and even redox reactions in electrode materials.[13-15] Recently, an electrolyte-dependent reaction mechanism has been identified for the high-rate δ-MnO_2 cathode, where the bulky anion bis(trifluoromethane)sulfonimide ($TFSI^-$) in aqueous electrolytes leads to a joint non-diffusion-controlled Zn^{2+} intercalation and H^+ conversion reaction.[13] It has been shown that the electrolyte media, especially the species of the anion salts, can tailor the reaction mechanism of electrode materials. The reaction mechanisms in aqueous Zn/MnO_2 batteries are complicated and still in dispute, however. The prevailing reaction mechanism includes Zn^{2+} intercalation, H^+ conversion reaction, and Zn^{2+}/H^+ co-insertion, which still follows the one-electron redox reaction of Mn^{4+}/Mn^{3+}. A reversible two-electron Mn^{4+}/Mn^{2+} reaction can be realized by adding H_2SO_4 into the sulfate-based electrolyte.[16, 17] However, the strongly acidic (pH $\approx$ 1) nature of this electrolyte would result in significant safety hazards and zinc corrosion, and consequently lead to limited battery calendar life in the aqueous Zn/MnO_2 batteries. It is therefore very interesting to investigate the reversibility of the two-electron Mn^{4+}/Mn^{2+} redox couple via manipulating the salt anion in different electrolytes, especially in mild aqueous electrolytes. An in-depth understanding of the influence of the electrolyte salt on the charge storage mechanism could provide guidance for the development of high-performance aqueous Zn/MnO_2 batteries.

The stability and reversibility of Zn metal anode in aqueous electrolytes is another crucial parameter for electrochemical performance, especially for long-term cycling durability.[18, 19] Representative electrolytes in aqueous Zn/MnO_2 batteries and their corresponding pH ranges are illustrated in Figure 6.1a. Early attempts at employing strongly alkaline electrolytes, such as KOH solution, are rather impractical, mainly due to the growth of Zn dendrites and the formation of irreversible by-products.[9] At the

opposite extreme, strongly acidic electrolytes are responsible for inherent corrosion issues and low Coulombic efficiency (CE) for Zn plating/stripping, adversely affecting the overall electrochemical performance. Meanwhile, the high proton concentration in the electrolytes may also accelerate vigorous H_2 evolution and the sustained consumption of water. Although mildly acidic electroytes (pH ≈ 4), such as $ZnSO_4$ with $MnSO_4$, $Zn(CF_3SO_3)_2$ with $Mn(CF_3SO_3)_2$, have been intensively investigated, the goal of high stability and CE of Zn electrodes in aqueous Zn/MnO_2 batteries remains a challenge.[20, 21] The main problems are rooted in Zn dendrite formation and the poor thermodynamic and electrochemical stability of Zn anode in aqueous electrolytes.[22-24] The (electro)chemical reactions between Zn metal anodes and electrolytes are regarded as an important mechanism of cell failure for aqueous Zn metal batteries.[23, 25] Neutral or near-neutral aqueous electrolytes, providing a more benign solution environment for Zn metal anode, might address these issues. To date, however, neutral or near-neutral aqueous electrolytes have received little attention for rechargeable Zn/MnO_2 batteries.

Herein, a Zn/MnO_2 battery with extraordinary electrochemical performance is proposed by simply optimizing the salt anions in aqueous electrolytes. Acetate salts, $Zn(CH_3COO)_2$ with $Mn(CH_3COO)_2$, were selected as the electrolyte salt to unlock the two-electron Mn^{4+}/Mn^{2+} redox reaction, considering the adsorption effect of CH_3COO^- ions. The density functional theory (DFT) calculations clarify that the acetate ions modify the surface properties of MnO_2 and reduce the barrier for its dissolution process. X-ray diffraction and transmission electron microscopy (TEM) characterizations show that the MnO_2 cathode in our work is gamma phase. The unique MnO_2/Mn^{2+} cathode reaction almost doubles the capacity compared to conventional Zn/MnO_2 batteries based on the MnO_2/Mn^{3+} redox reaction, and effectively avoids the issue of structural collapse of the MnO_2 cathode due to the nature of its deposition/dissolution reaction,

which significantly enhances the cycling stability. Meanwhile, the near-neutral acetate-based electrolyte (pH ≈ 6) ensures excellent stability and compatibility of the Zn anode, and thus enables a dendrite-free Zn anode with high CE (99.8%). Accordingly, our aqueous Zn/MnO_2 battery chemistry delivers a high practical specific capacity of ~ 556 mA h g^{-1} with a high operating voltage of 1.5 V, a superior rate capability, and a lifetime of 4000 cycles without decay. This work is expected to shed light on the importance of salt anions and provide opportunities to regulate the salt anion chemistry for high-performance rechargeable aqueous Zn/MnO_2 batteries towards large-scale energy storage applications.

6.2 Experimental section

6.2.1 Materials characterization

The crystalline structure of the electrodes was identified by X-ray diffraction (XRD, PANalytical X'Pert PRO) with Cu Kα radiation. The morphologies of the samples were examined by field-emission scanning electron microscopy (FESEM, JEOL JSM-7500FA) and transmission electron microscopy (TEM, JOEL JEM-2200FS). XPS measurements were performed on an X-ray photoelectron spectrometer (Thermo Fisher K-Alpha system). All of the binding energies were referenced to the C 1s peak at 284.6 eV. Raman spectra were collected with a Raman JY HR800 Spectrometer. Thermogravimetric analysis was conducted on a TGA 8000 PerkinElmer from 50 to 950 °C in air atmosphere with a ramp rate of 10 °C min^{-1}. Fourier transform infrared (FT-IR) spectra were collected by FT-IR Spectrometer System (PerkinElmer). N_2 adsorption-desorption isotherms were obtained with TriStar II Micromeritics equipment.

6.2.2 Electrochemical measurements

The electrochemical performance of the Zn/MnO_2 cells was evaluated using both 2032-type coin cells and two-electrode Swagelok cells on a Land BT2000 battery test system. The cells were charged at 1.8 V (*vs.* Zn/Zn^{2+}) to a specified areal capacity, with the chronoamperometry (constant-potential) technique applied to obtain an *in-situ* electrodeposited MnO_2 cathode. Based on the weight difference between the bare carbon current collector and the MnO_2 deposited carbon current collector after charge, the mass loading of MnO_2 on the carbon current collector corresponding to 0.5, 1, and 2 mA h cm^{-2} was about 0.9, 1.8 ,and 3.6 mg cm^{-2}, respectively. The corresponding molar ratio of deposited Mn to that in the electrolyte is approximately 1:8, 1:4, and 1:2, respectively. Galvanostatic currents from 1 mA cm^{-2} to 70 mA cm^{-2} were employed in the process of discharge. The cyclic voltammetry (CV) tests of the Zn/MnO_2 cells using different electrolytes were conducted on a Biologic VPM3 electrochemical workstation at a scanning rate of 0.1 mV s^{-1}. Linear sweep voltammetry was carried out at 1 mV s^{-1} within the voltage range from -1.3 V to 2.1 V (*versus* Ag/AgCl) using a three-electrode system with carbon cloth as the working electrode, Zn foil as counter electrode, and Ag/AgCl as reference electrode, respectively. The galvanostatic Zn stripping/plating test was conducted on a Zn/Zn symmetrical cell at a fixed current density of 1 mA cm^{-2}. CE measurements were implemented by using coin cells with Zn anode (diameter 12 mm) and Ti foil (diameter 14 mm) in the respective electrolytes. The electrodeposition of Zn on Ti foil was conducted at a current density of 5 mA cm^{-2} for 1 h. Electrochemical impedance spectroscopy (EIS) was conducted on a Biologic VPM3 electrochemical workstation within the frequency range from 10^6 to 10^{-2} Hz.

6.2.3 Computational method

Spin-polarized DFT calculations were performed with the Vienna ab initio simulation package (VASP),[1] using the plane wave basis set with energy cut-off of 500 eV,

projector augmented wave (PAW) potentials,[2] and the generalized gradient approximation proposed by Perdew, Burke and Ernzerhof (GGA-PBE) for the exchange-correlation functional.[3] The MnO_2(301) surface of the ramsdellite phase was modelled by a slab consisting of 4 O–Mn–O layers and 2 × 1 unit cells for the lateral dimension. A vacuum region of 16 Å was applied in the direction perpendicular to the MnO_2 surface. To explore the effect of acetate ions on the dissociation process of MnO_2, half of the O atoms on the MnO_2 surface were replaced by acetate groups. The Brillouin zone was sampled by a 6 × 2 × 1 uniform k-point mesh. With a constrained lattice, the model structures were optimized for ionic and electronic degrees of freedom, using thresholds for the total energy of 10^{-4} eV and for force of 0.02 eV/Å. Grimme's semi-empirical DFT-D3 scheme for dispersion correction was adopted for a better description of the interaction between the reaction intermediates and MnO_2.[4]

6.3 Results and discussion

6.3.1 Charge Storage Mechanism of the Zn/MnO_2 Cell

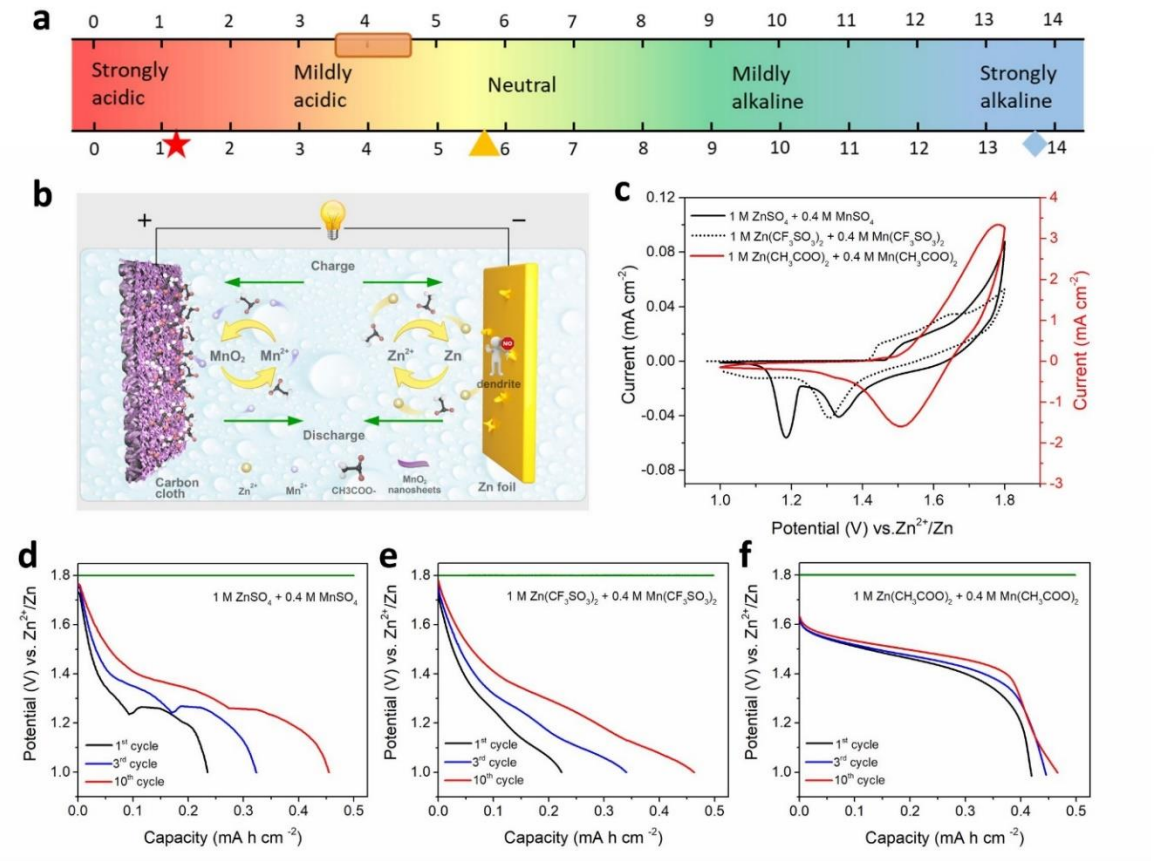

Figure 6.1 Electrochemical behavior of MnO_2 cathode in different aqueous electrolytes. (a) Different pH ranges of representative aqueous electrolytes in reported Zn/MnO_2 batteries. The star represents strongly acidic $ZnSO_4$ + $MnSO_4$ + H_2SO_4 aqueous electrolyte. The rectangle represents mildly acidic $ZnSO_4$, $ZnCl_2$, $Zn(NO_3)_2$, $Zn(TFSI)_2$ + $Mn(TFSI)_2$, $ZnSO_4$ + $MnSO_4$, and $Zn(CF_3SO_3)_2$ + $Mn(CF_3SO_3)_2$ electrolytes. The triangle represents near-neutral $Zn(CH_3COO)_2$ + $Mn(CH_3COO)_2$ electrolyte. The rhombus represents strongly alkaline KOH and NaOH electrolytes. (b) Schematic illustration of the aqueous rechargeable Zn/MnO_2 energy storage system in the acetate-based electrolyte. (c) CV curves in different electrolytes at 0.1 mV s^{-1} from 1.0 V to 1.8 V, and (d-f) galvanostatic discharge curves (5 mA cm^{-2}, charge to 0.5 mA h cm^{-2} at 1.8 V) of the Zn/MnO_2 battery in sulfate-based, sulfonate-based and acetate-based aqueous electrolytes, respectively.

Figure 6.1b shows the cell configuration, which comprises carbon cloth as the cathode current collector, Zn foil as the anode, and near-neutral $Zn(CH_3COO)_2$ with $Mn(CH_3COO)_2$ aqueous solution as the electrolyte. During charging at a constant voltage of 1.8 V, soluble Mn^{2+} in the electrolyte is oxidized to MnO_2 nanosheets deposited evenly on the carbon substrate, while simultaneous electrodeposition of Zn occurs on the anode. The linear sweep voltammogram (Figure 6.2) shows the electrodeposition of MnO_2 cathode and Zn anode, as well as the H_2/O_2 evolution reaction. To eliminate the influence of overlapping MnO_2 deposition and O_2 evolution, $Zn(CH_3COO)_2$ electrolyte without $Mn(CH_3COO)_2$ was also used. The minimum deposition potential for MnO_2 cathode and Zn anode is 1.55 V, and the upper limit of the electrochemical stability window is 2.64 V. A constant-voltage charge at 1.8 V was selected in consideration of both the successful electrodeposition reaction on the electrodes and the need to avoid water splitting.

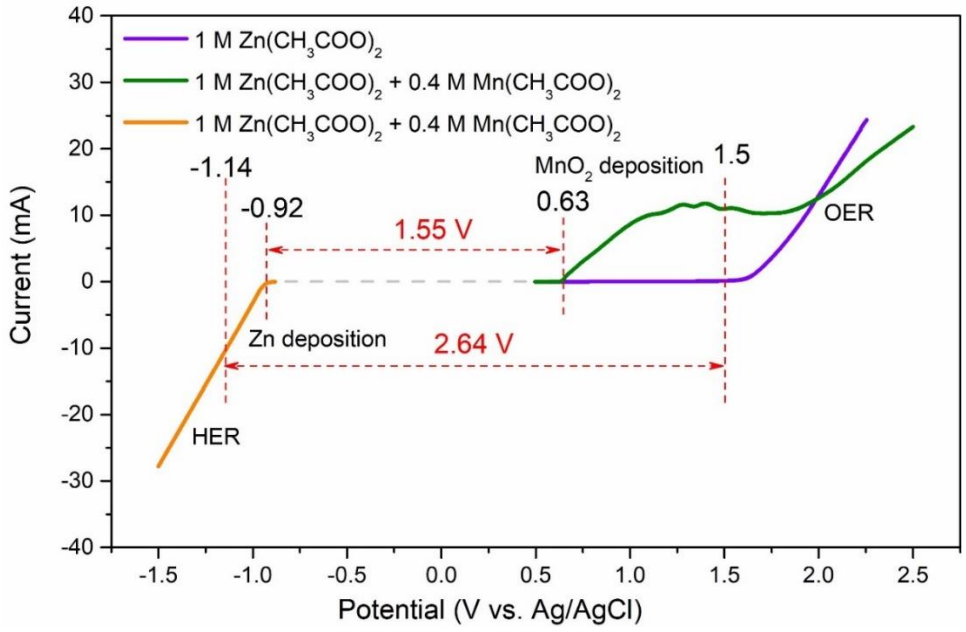

Figure 6.2 Working potential window analysis of the Zn/MnO_2 battery in a three-electrode system.

In the process of galvanostatic discharge, the as-deposited MnO_2 is reduced to Mn^{2+}

and dissolved back into the aqueous electrolyte due to the presence of acetate ions. Thus, the theoretical specific capacity is calculated to be 616 mA h g^{-1} based on the two-electron MnO_2/Mn^{2+} redox reaction on the cathode. The electrodeposited synthetic approach of the MnO_2 cathode could simplify the battery fabrication process without the use of any polymer binder or conductive additives. To compare the effects of different electrolyte salts on the electrochemical behaviors of MnO_2 cathode, Figure 6.1c shows the cyclic voltammetry (CV) curves in the acetate-based electrolyte (1 M $Zn(CH_3COO)_2$ + 0.4 M $Mn(CH_3COO)_2$), the sulfate-based electrolyte (1 M $ZnSO_4$ + 0.4 M $MnSO_4$), and the sulfonate-based electrolyte (1 M $Zn(CF_3SO_3)_2$ + 0.4 M $Mn(CF_3SO_3)_2$). The CV curve in the acetate-based electrolyte exhibits a similar oxidation peak for MnO_2 deposition, but totally different reduction peaks from those in the sulfate-based and sulfonate-based electrolytes, indicating different charge storage mechanisms. The higher reduction potential at 1.5 V in the acetate-based electrolyte suggests the two-electron MnO_2/Mn^{2+} reaction, while the two reduction peaks at 1.35 V and 1.2 V in the sulfate-based and sulfonate-based electrolytes are consistent with the reported insertion mechanism of Zn^{2+} and H^+ ions into the MnO_2 cathode.[21, 26, 27] These results are further confirmed by the galvanostatic discharge behavior shown in Figure 6.1d, f. The discharge profiles of the MnO_2 cathode in the sulfate-based and sulfonate-based electrolytes display at least two distinct discharge plateaus, while only one discharge plateau at higher voltage was observed in the case of the acetate-based electrolyte.

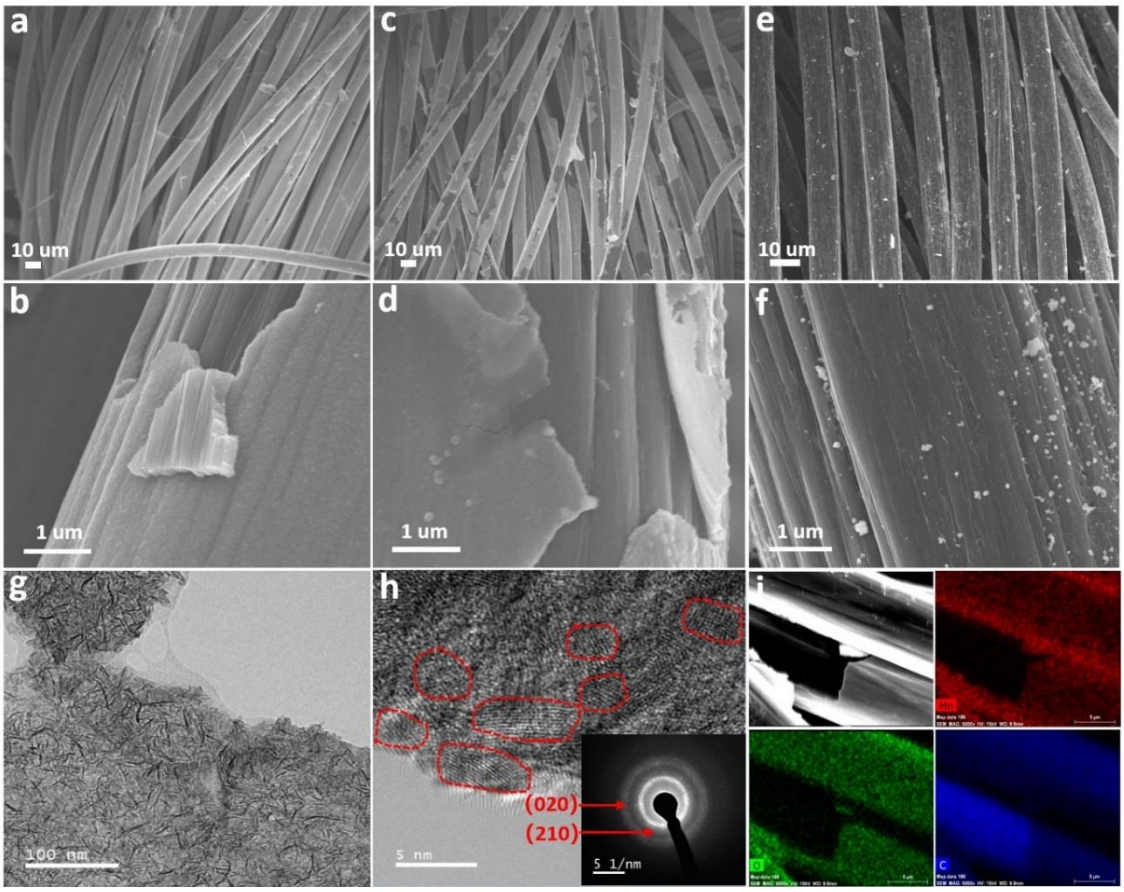

Figure 6.3 Characterization of the cathode in the acetate-based electrolyte. (a, b) SEM images of the cathode after the first charge to 0.5 mA h cm^{-2}. (c, d) SEM images of the cathode after the first discharge to 1.4 V at 5 mA cm^{-2}. (e, f) SEM images of the cathode after the first discharge to 1.0 V. (g, h) TEM images and the corresponding SAED pattern (inset of h) of the MnO_2 cathode after charge. (i) Elemental mapping images of the cathode after charge.

To confirm the charge storage mechanism of the MnO_2 cathode in the acetate-based electrolyte, *ex situ* scnning electron microscope (SEM) characterization was conducted at different charge/discharge states. Figure 6.3a, b shows typical SEM images of the cathode after the first charge, with the electrodeposited MnO_2 coated uniformly on the surface of the carbon cloth. The high-magnification SEM images reveal a highly porous MnO_2 layer with nearly vertically aligned nanosheet structures and a thickness of ~150

nm, which presents a specific surface area of 106.5 m^2 g^{-1} (Figure 6.4).

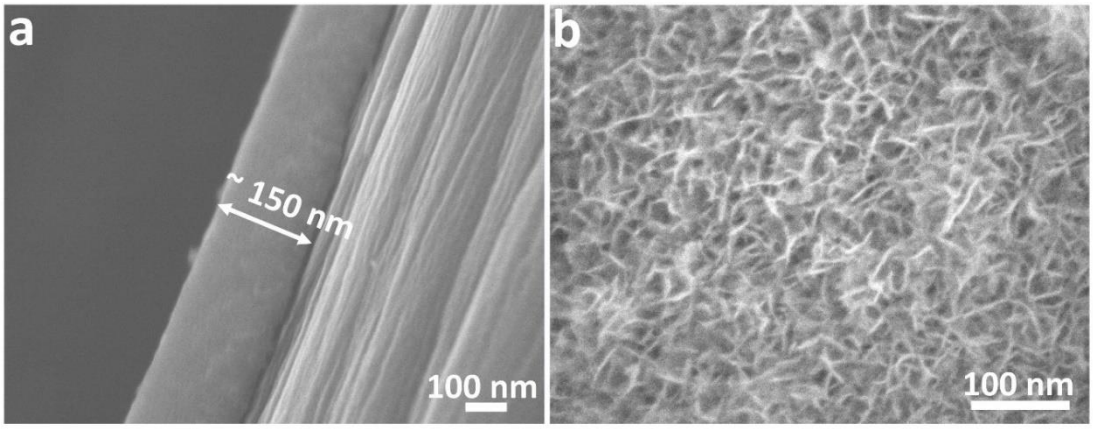

Figure 6.4 SEM images of the electrodeposited MnO_2 cathode in the Zn/MnO_2 cell after the first charge to 0.5 mA h cm^{-2}.

When discharged to 1.4 V, the cathode exhibited the morphology of carbon cloth with a partial coating of MnO_2, while the MnO_2 layer became thinner (Figure 6.3c, d), indicating the gradual dissolution process of MnO_2 during discharging. After full discharge to 1.0 V, the MnO_2 on the cathode disappeared, restoring the pristine morphology of the clean carbon substrate, as shown in Figure 6.3e, f. A very small amount of MnO_2 residue was found, probably due to the incomplete dissolution process in the first cycle. TEM images (Figure 6.3g, h) of the cathode after charging confirm that the MnO_2 nanosheets are formed from nanograins with a typical size in the range of 5 nm and that the particle size of the MnO_2 nanosheets is about 40 nm. The vertical nanosheet structure and nanocrystalline character of the MnO_2 cathode would facilitate mass diffusion and enable fast electrochemical kinetics. The diffraction rings of the selected area electron diffraction (SAED) pattern (inset of Figure 6.3h) can be indexed to the (210) and (020) planes of γ-MnO_2, and the elemental mapping of the cathode in Figure 6.3i reveals the homogeneous distributions of Mn and O elements.

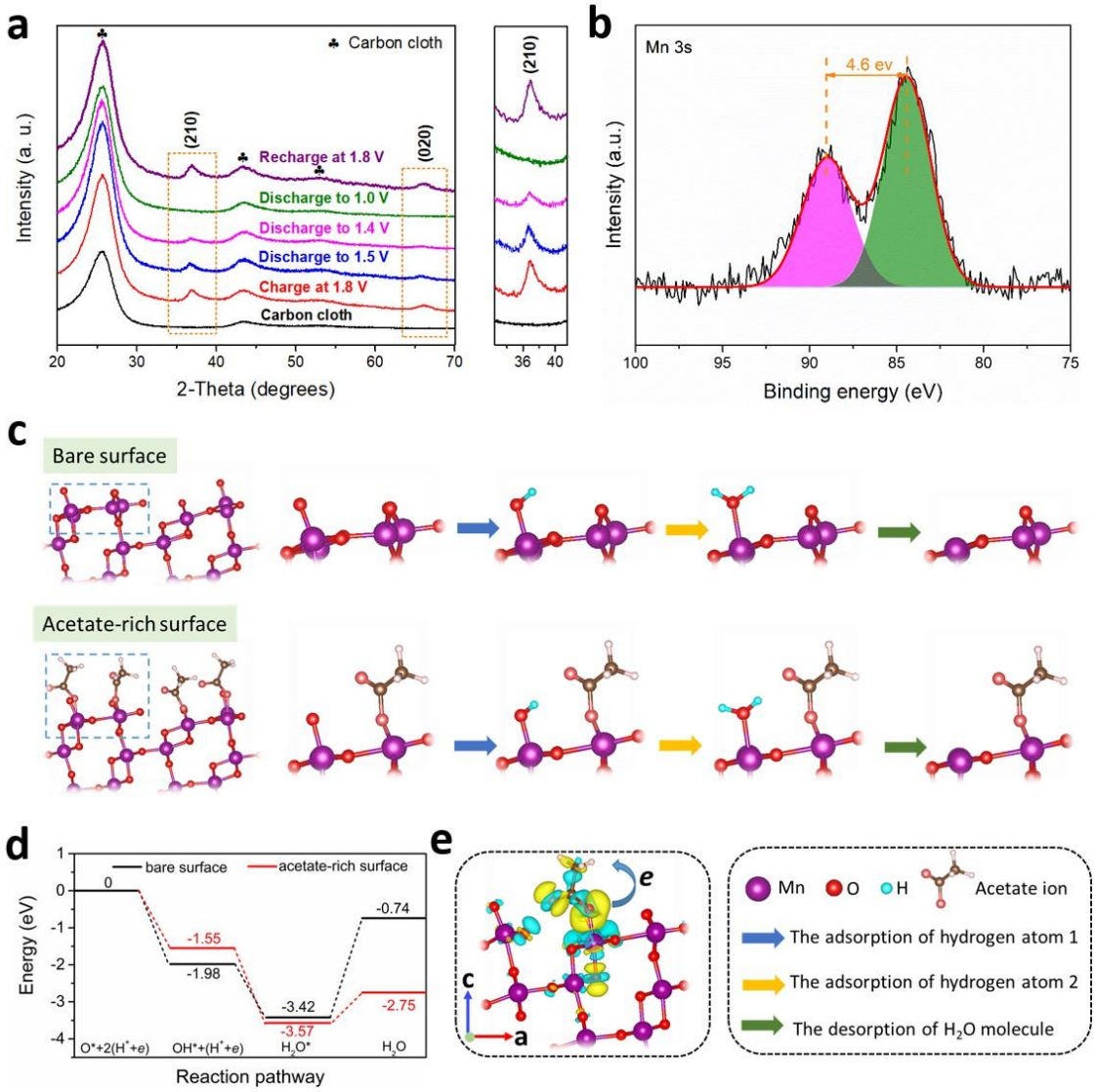

Figure 6.5 Investigation of the reaction mechanism. (a) *Ex situ* XRD patterns of the MnO_2 cathode at different charge/discharge states in the acetate-based electrolyte. (b) Mn 3s XPS spectrum of the MnO_2 cathode in the charged state. (c) Atomic structures for the dissolution reaction on MnO_2 with a bare surface and with an acetate-rich surface. (d) Energy diagram of the dissolution reaction on MnO_2 with a bare surface and with an acetate-rich surface. (e) Differential charge density of an acetate ion adsorbed on MnO_2, with yellow and blue colors representing electron accumulation and depletion regions, respectively, with an isosurface value of 0.002 e/Å^3.

The deposition/dissolution evolution mechanism of the MnO_2 cathode was also clarified through *ex-situ* X-ray diffraction (XRD), Raman scattering spectroscopy, and X-ray photoelectron spectroscopy (XPS). As shown in Figure 6.5a, the emerging diffraction peaks at 37 ° and 66.5 ° upon charging at 1.8 V correspond to the (210) and (020) planes of γ-MnO_2 (JCPDS no. 04-007-8867), respectively, which is consistent with the SAED pattern (Figure 6.3h inset). The characteristic peaks of the MnO_2 cathode were weak and broad, which could be ascribed to the distinct feature of nanocrystalline MnO_2. During the step-by-step process of discharge, the crystalline peaks of MnO_2 gradually weakened until they completely disappeared after full discharge to 1.0 V, as shown magnified on the right-hand plot of Figure 6.5a. Moreover, the MnO_2 cathode after charge showed five Raman bands at 166, 370, 474, 602, and 649 cm^{-1} in Figure 6.6, which were ascribed to the Mn-O lattice vibrations within the MnO_6 octahedral frameworks of deposited MnO_2.[28] In the process of galvanostatic discharge, the peaks were weakened gradually until they almost disappeared, and no new Raman bands or obvious shifts were observed. This indicated the dissolution process of MnO_2 cathode, and no other Mn chemicals were formed during discharging.

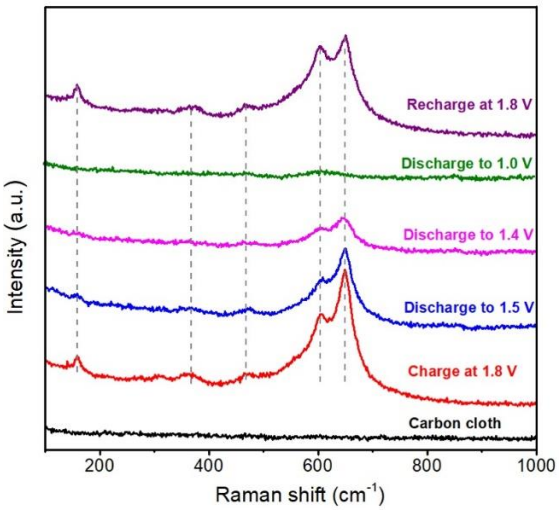

Figure 6.6 Raman spectra of the MnO_2 cathode on carbon cloth at different charge/discharge states.

The XPS analysis of the cathode at different discharge states also followed the same trend as the XRD patterns and Raman spectra. The peak separation energy of Mn 3s and Mn 2p remained constant for all the electrodes, as shown in Figure 6.7. The intensity of the Mn signal gradually became weaker with discharge and recovered after charge, indicating that the abundance of MnO_2 on the carbon cloth decreased steadily with discharge and increased in the process of recharge. The weak XPS signals after full discharge could be attributed to a partially incomplete dissolution process in the initial cycles, as observed in Figure 6.3e, f.

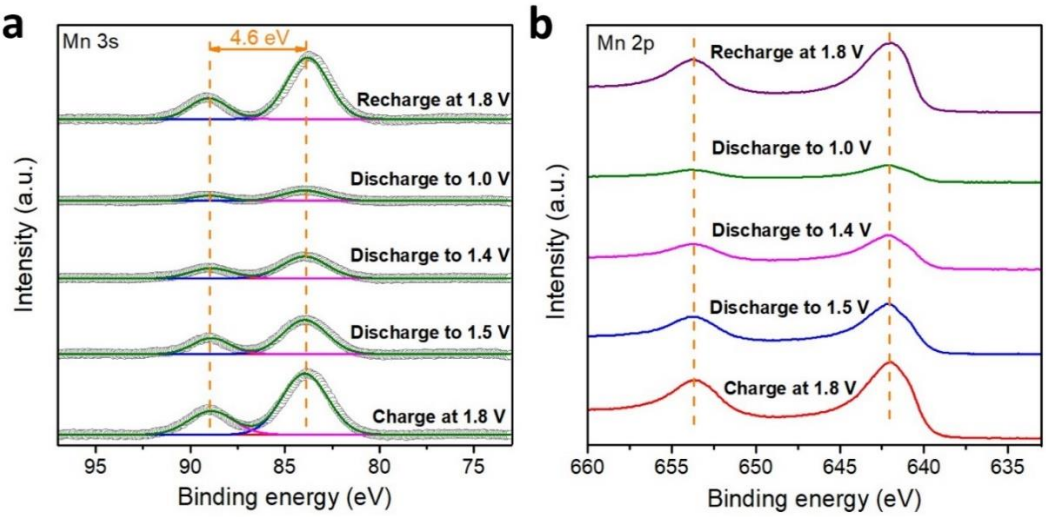

Figure 6.7 XPS spectra of (a) Mn 3s and (b) Mn 2p for the cathode at different charge/discharge states.

The combination of SEM, XRD, Raman and XPS results demonstrated the MnO_2/Mn^{2+} deposition/dissolution redox mechanism. The multiplet splitting of the Mn 3s X-ray photoelectron spectrum is useful for determining the average oxidation state (AOS) of manganese, as there is a linear relationship between the Mn 3s peak splitting energy and the average oxidation state of Mn. The peak separation of electrons in the core level with unpaired electrons in the valence band level is caused by the electron exchange interaction upon photoelectron ejection. Such an exchange between electrons in the 3s-

3d level of Mn occurs as a representative multiplet splitting, and the corresponding separation of peak energies (ΔE) is described in terms of exchange interaction energy. The linear relationship between ΔE and AOS can be expressed as follows: [29]

$$\mathrm{AOS} = 8.95 - 1.13\Delta E \ (\mathrm{eV}) \qquad (1)$$

The peak separation energy of the Mn 3s component was 4.6 eV, as shown in Figure 6.5b, and the average Mn valence state was calculated to be 3.8 in the electrode. Therefore, when the MnO_2 cathode dissolved to free Mn^{2+} ions into the aqueous electrolyte, the actual electron transfer number was 1.8. For comparison, *ex-situ* XRD and SEM measurements of the Zn/MnO_2 battery in the sulfate-based electrolyte were also conducted. In contrast to the acetate-based electrolyte, the cathode in the sulfate-based electrolyte still exhibited the morphology of carbon cloth fully coated with discharge products, which were identified to be Zn_xMnO_2 and MnOOH (Figure 6.8). These are typical discharge products derived from the one-electron conversion reaction of Zn^{2+}/H^+ intercalating into MnO_2 cathode.[16, 21] The flake-like structure observed in Figure 6.9 was a discharge by-product, the osakite salt $ZnSO_4[Zn(OH)_2]_3 \cdot xH_2O$, formed from proton insertion and an increase in the local OH^- concentration.[9]

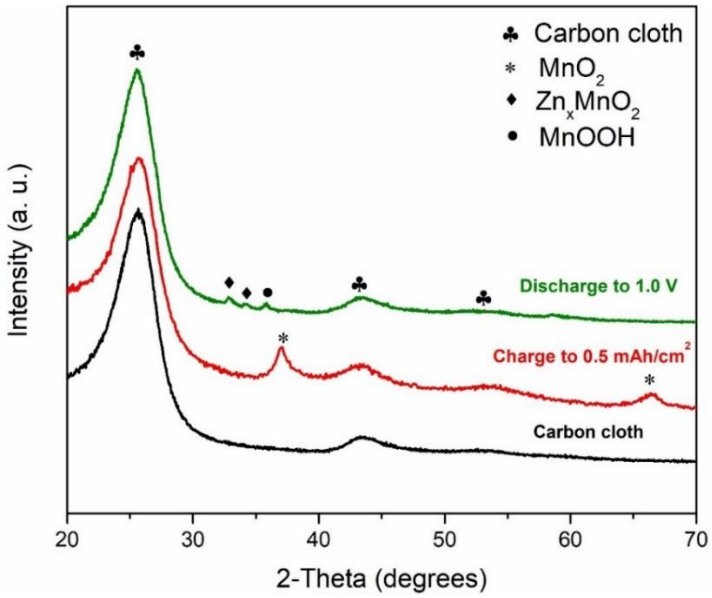

Figure 6.8 *Ex-situ* XRD patterns of MnO_2 cathode in the sulfate-based electrolyte.

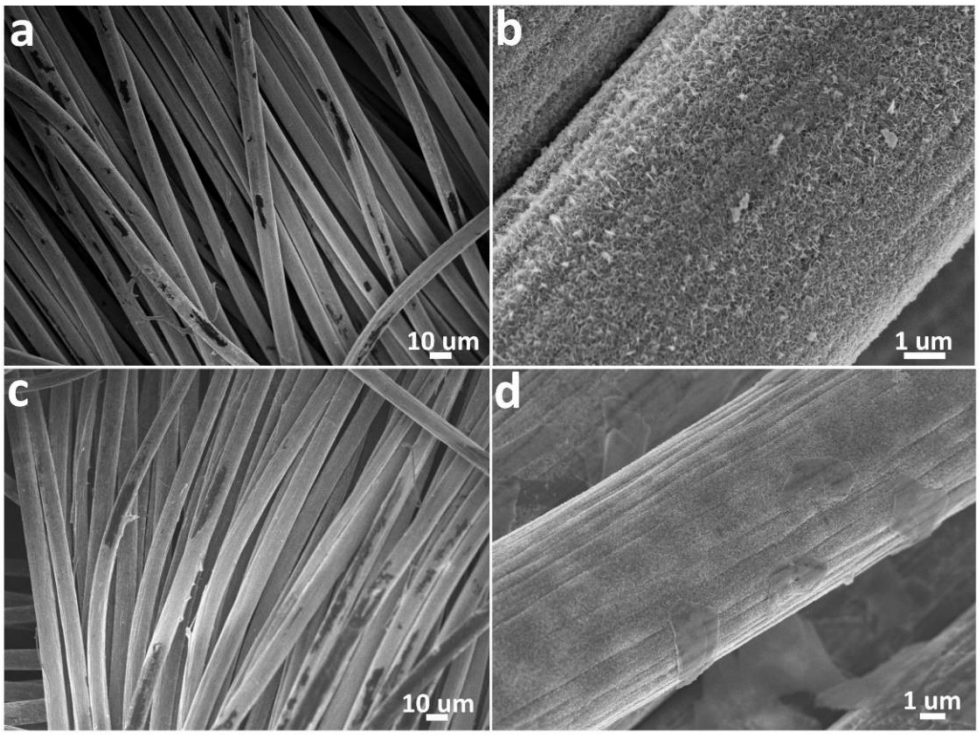

Figure 6.9 SEM images of the MnO_2 cathode in the sulfate-based electrolyte. (a, b) After the first charge to 0.5 mA h cm^{-2}. (c, d) After the first discharge to 1.0 V.

Herein, the reaction mechanism of the Zn/MnO_2 cell in the acetate-based electrolyte can be described by the following equations:

Cathode: $Mn^{2+} + 2H_2O \leftrightarrow MnO_2 + 4H^+ + 2e^-$ (2)

Anode: $Zn^{2+} + 2e^- \leftrightarrow Zn$ (3)

Total reaction: $Mn^{2+} + 2H_2O + Zn^{2+} \leftrightarrow MnO_2 + 4H^+ + Zn$ (4)

To gain atomistic insight into the unique energy storage mechanism induced by the salt anions, we performed density functional theory (DFT) calculations to explore the role of acetates in the discharge process of MnO_2. A slab model of MnO_2(301) in the γ phase was adopted, as shown in Figure 6.10.

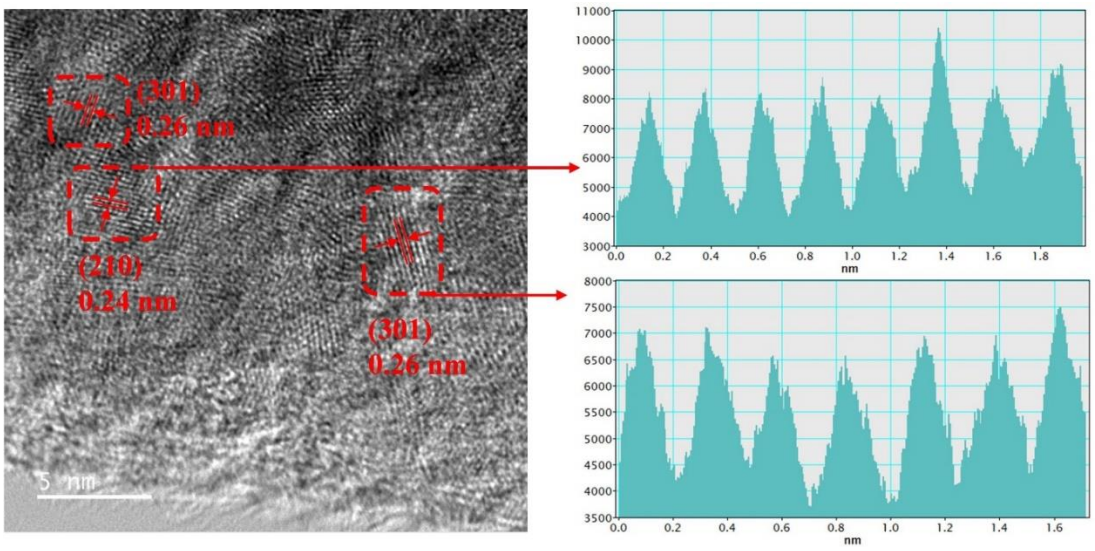

Figure 6.10 High-resolution TEM (HRTEM) image of the electrodeposited MnO_2 cathode.

Figure 6.5c shows that the dissolution of MnO_2 can proceed through the protonation of a surface O atom to form an OH* intermediate. Then, the reaction of the OH* with a second H^+ ion leads to the formation and desorption of H_2O. On the bare MnO_2 surface, the formation of OH* and H_2O is exothermic, as revealed in Figure 6.5d. The produced H_2O binds strongly to the MnO_2, however, with an adsorption energy of 2.68 eV (relative to a free H_2O molecule), which prevents its desorption and hinders the reduction of MnO_2. In comparison, the acetate ion is a typical weak-acid ion with high polarizability and high electronegativity, where the COO^- group is known to strongly adsorb on the surface Mn sites of MnO_2 particles.[30-32] Thus, the acetate ion significantly weakens the binding of H_2O on MnO_2, giving an adsorption energy of only 0.82 eV, which reduces the barrier for dissolution. The modification of the surface properties of MnO_2 upon acetate adsorption can be understood by the differential charge density distributions in Figure 6.5e. Prominent electron transfer occurs from the MnO_2 to the acetate ions, i.e., 0.38 e^- on average to each acetate ion from Bader charge analysis. The surface Mn atoms carry fewer electrons and provide weaker binding with

OH* and H_2O species, facilitating the dissolution process of MnO_2 in our acetate system. Additionally, to eliminate interference from the pH condition in the electrolyte, concentrated H_2SO_4 was added into the acetate-based electrolyte to adjust the pH, until its pH was the same as that of the sulfate-based electrolyte (pH ≈ 3.8). As a result, our Zn/MnO_2 battery in the acetate-based electrolyte with H_2SO_4 still delivered similar galvanostatic discharge profiles as in the acetate-based electrolyte without H_2SO_4 (Figure 6.11). This result further confirms the role of acetate ions in dictating the MnO_2/Mn^{2+} deposition/dissolution reaction mechanism.

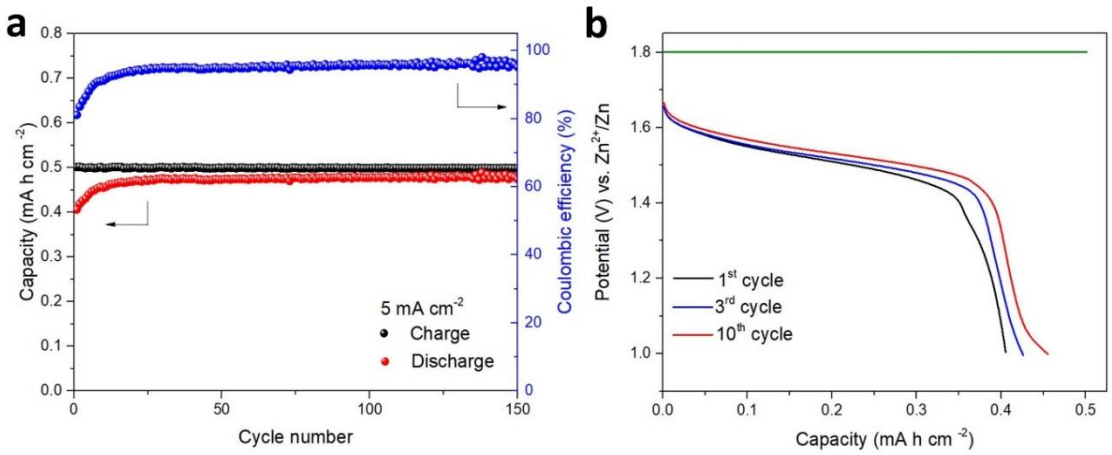

Figure 6.11 Electrochemical behaviour of the Zn/MnO_2 battery in the acetate-based electrolyte with added H_2SO_4 (pH ≈ 3.8). (a) Cycling performance. (b) Corresponding galvanostatic discharge curves.

6.3.2 Electrochemical Stability and Reversibility of Zn Anode

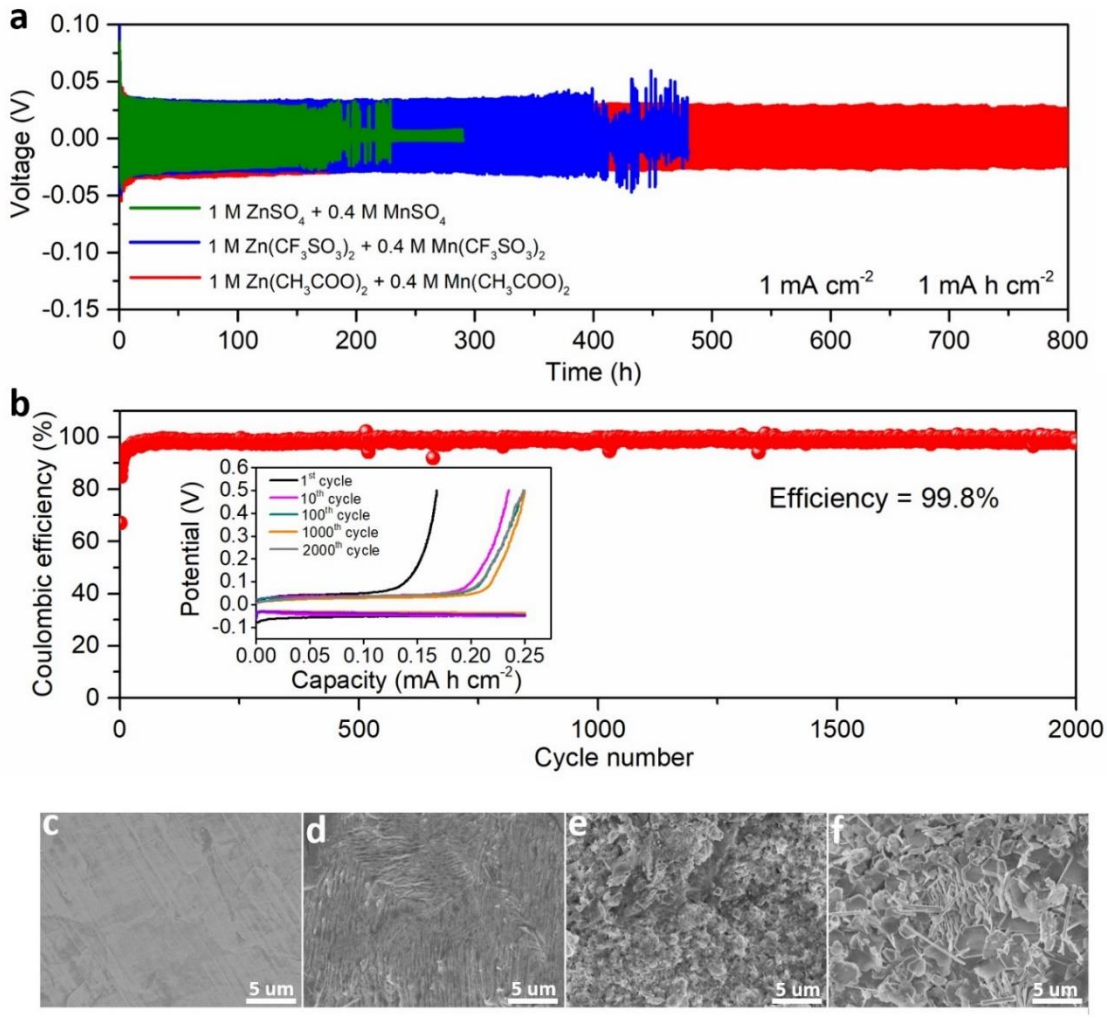

Figure 6.12 Electrochemical stability and reversibility of Zn metal anode. (a) Zn plating/ stripping test of Zn/Zn symmetrical cells at a current density of 1 mA cm^{-2} in the acetate-based electrolyte, the sulfonate-based electrolyte, and the sulfate-based electrolyte. The plating/stripping capacities of the Zn electrodes (0.1 mm) were 1 mA h cm^{-2} in each cycle. (b) Coulombic efficiency of a Zn/Ti cell in the acetate-based electrolyte at 1 mA cm^{-2}. The cut-off potential was 0.5 V, and the inset shows the corresponding voltage profiles. (c-f) SEM images of c the pristine Zn anode and the Zn anodes from the Zn/Zn symmetrical cells after plating/stripping for 100 h in d the acetate-based electrolyte, e the sulfonate-based electrolyte, and f the sulfate-based electrolyte.

The stability and reversibility of Zn anode in the different electrolytes were first investigated using Zn/Zn symmetrical batteries, as displayed in Figure 6.12a. The results demonstrate exceptional Zn plating/stripping behavior with outstanding cycling durability (800 h at 1 mA cm^{-2} with a capacity of 1 mA h cm^{-2}) in the acetate-based electrolyte. In sharp contrast, in mildly/strongly acidic electrolytes, the symmetrical cells showed unstable voltage hysteresis and shorter lifespans, with only 190 h for the $ZnSO_4$ + $MnSO_4$ system and 410 h for the $Zn(CF_3SO_3)_2$ + $Mn(CF_3SO_3)_2$ system, respectively. The unstable voltage hysteresis and limited lifespan in the sulfate and sulfonate electrolytes would be attributed to the intensified formation of Zn dendrites and the poor thermodynamic stability of Zn anode in these acidic electrolytes. The Zn/Zn symmetrical cell in the acetate-based electrolyte also displayed attractive rate performance (from 0.5 to 5 mA cm^{-2}) and long-term cyclability at 0.5 mA cm^{-2} (Figure 6.13).

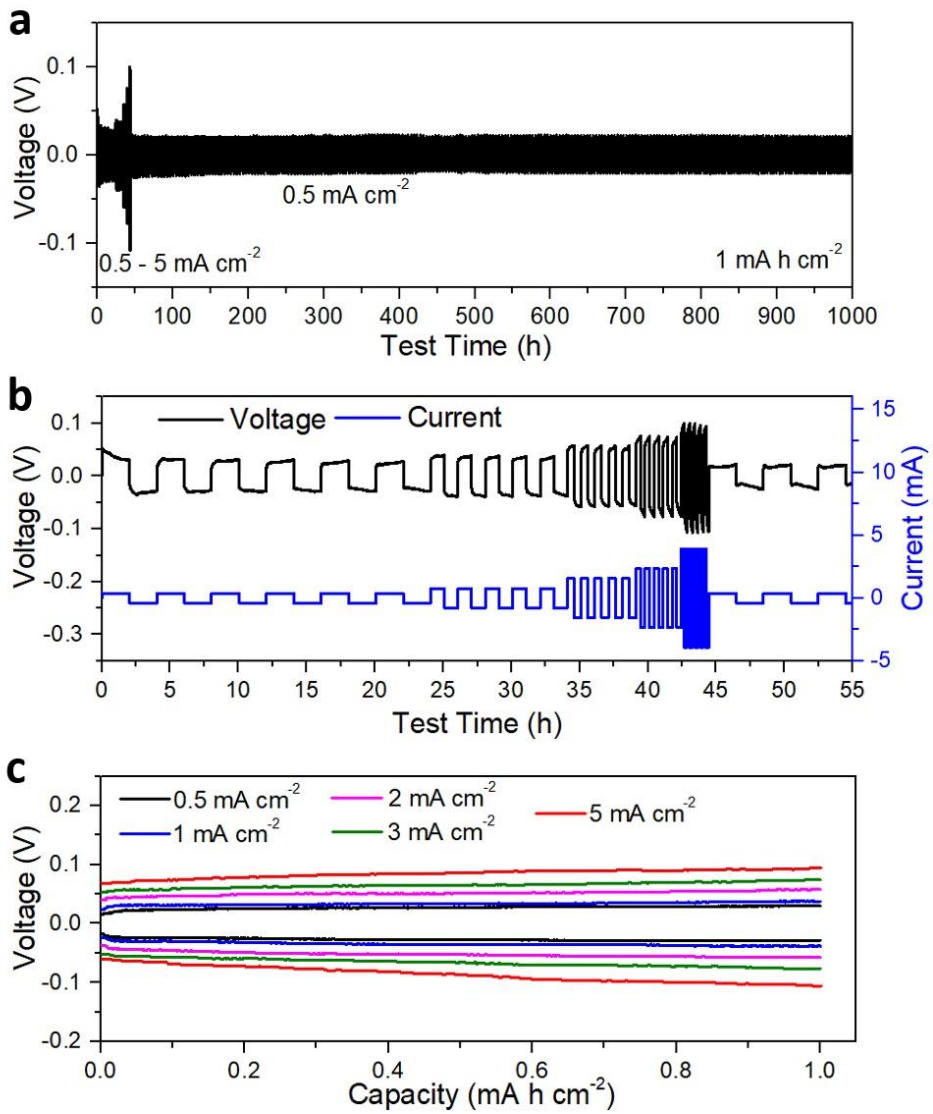

Figure 6.13 Long-term cyclability and rate performance of Zn/Zn symmetric cell in the acetate-based electrolyte. (a) Long-term cyclability at 0.5 mA cm^{-2}. (b) Rate performance at current densities from 0.5 to 5 mA cm^{-2}. (c) Corresponding voltage profiles at each current density. The areal capacity was 1.0 mA h cm^{-2}.

In addition, the reversibility of Zn in different electrolytes was also inspected in asymmetrical Zn/Ti cells, where Zn and Ti were used as the counter electrode and working electrode, respectively. During the galvanostatic discharge process in each cycle, Zn is dissolved from the Zn metal counter electrode and deposited on the surface of Ti foil. The applied current density was 1 mA cm^{-2} and the discharge time was set as

0.25 h. During the subsequent galvanostatic charge process, the deposited Zn on Ti foil is stripped back and returns to the counter electrode with a cut-off potential of 0.5 V. The Coulombic efficiency (CE) of Zn plating/stripping was calculated from the ratio of Zn dissolved from Ti foil to that deposited during the cycle. Figure 6.12b and its inset present high CEs approaching 100% after the first few cycles in the acetate-based electrolyte. A stable CE of 99.8% was maintained for 2000 cycles, revealing that the deposited Zn could be essentially completely stripped during the subsequent charge process. Again, when compared to the acetate-based electrolyte, the Zn/Ti cells using the other three electrolyte salts showed far inferior CE and cycling stability (Figure 6.14). The obvious fluctuation of their CEs reflected the significant side reaction of H_2 evolution, resulting from their acidic solution environments.

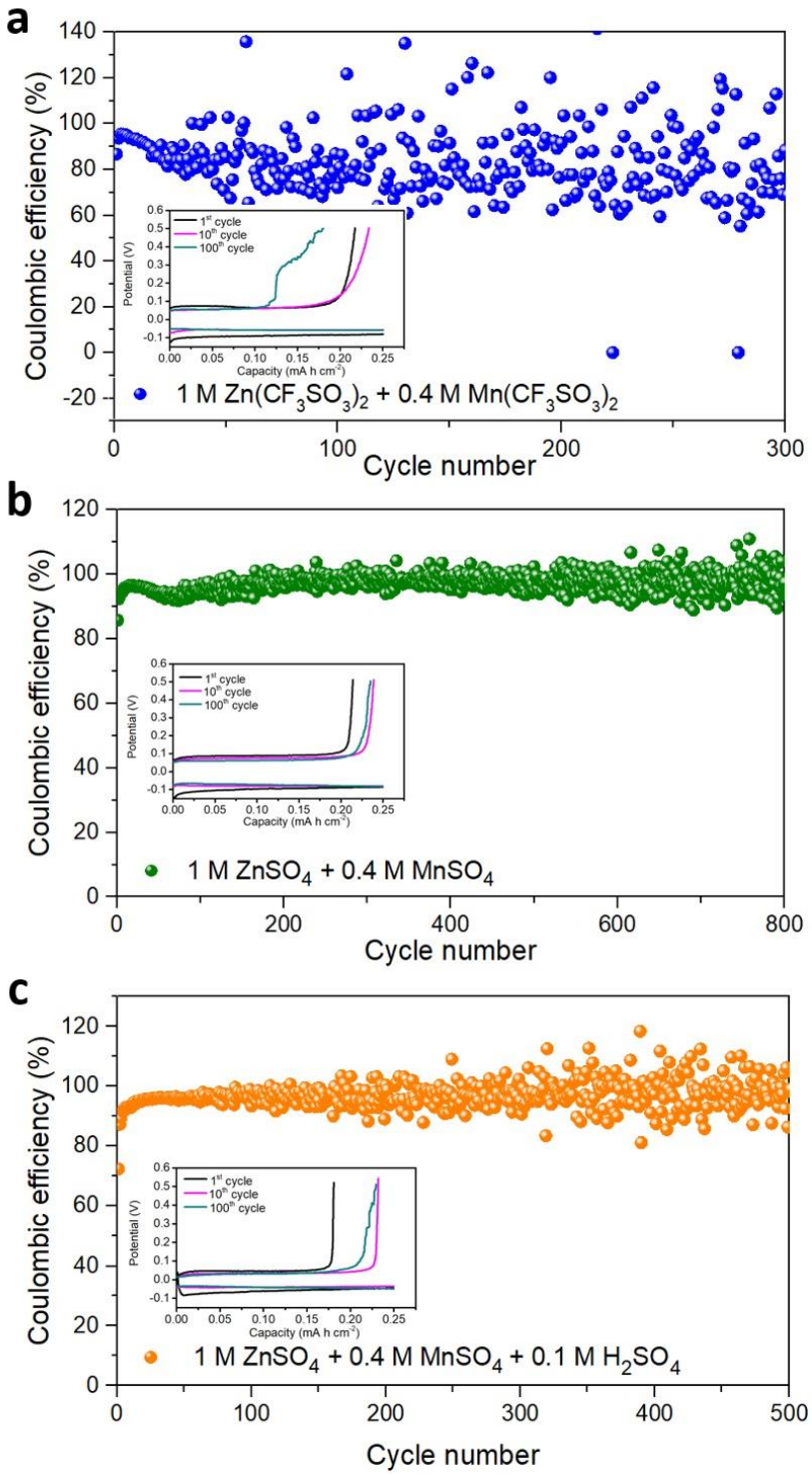

Figure 6.14 Coulombic efficiency of Zn/Ti cells at 1 mA cm^{-2} in different electrolytes. (a) The sulfonate-based electrolyte. (b) The sulfate-based electrolyte. (c) The sulfate-based electrolyte with 0.1 M H_2SO_4. The insets show the corresponding voltage profiles.

To further understand the effect of the electrolytes on Zn anode, the deposition

morphology of Zn metal was explored (Figure 6.15). In the acetate-based electrolyte, the electrodeposited Zn was compact and uniform, which was favorable for decreasing the local current density and thereby restraining the formation of dendrites during repeated plating/stripping processes.[33, 34] In contrast, discursive and agglomerated Zn was observed in the sulfonate-based and sulfate-based electrolytes.

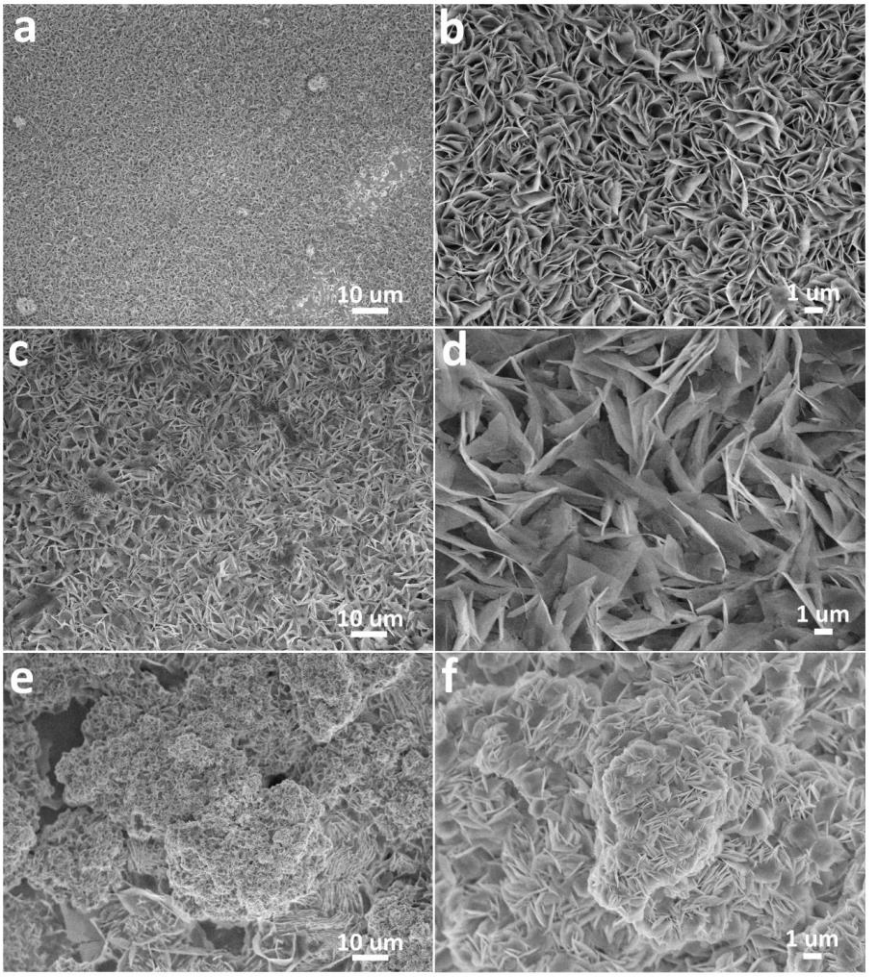

Figure 6.15 SEM images of electrodeposited Zn on Ti foil in different electrolytes. (a, b) The acetate-based electrolyte. (c, d) The sulfonate-based electrolyte. (e, f) The sulfate-based electrolyte.

Zn electrodes after plating/stripping in these aqueous electrolytes were also investigated by XRD and SEM. As shown in Figure 6.16, the peaks around 10 ° in the dashed box

could be assigned to the corresponding basic zinc salts, $Zn(CH_3COO)_{0.42}(OH)_{1.58}\cdot 0.31H_2O$ (JCPDS No. 00-056-0569), $Zn(CF_3SO_3)_a(OH)_b\cdot xH_2O$, $Zn_4(SO_4)(OH)_6\cdot 3H_2O$ (JCPDS No. 01-082-3605), and $Zn_4(SO_4)(OH)_6\cdot 5H_2O$ (JCPDS No. 00-060-0655), respectively. The formation of basic zinc salts could be attributed to the inevitable parasitic reaction of H_2 evolution and consequent pH change during long-term cycling. As shown in Figure 6.12c-f, the Zn anode still displayed a smooth, dense surface without Zn dendrites or "dead" Zn after plating/stripping for 100 h in the acetate-based electrolyte. Nevertheless, the Zn electrodes had non-compact and rough surfaces after plating/stripping in mildly acidic electrolytes, and some holes could even be observed in the electrolyte with H_2SO_4 addition, owing to serious corrosion.

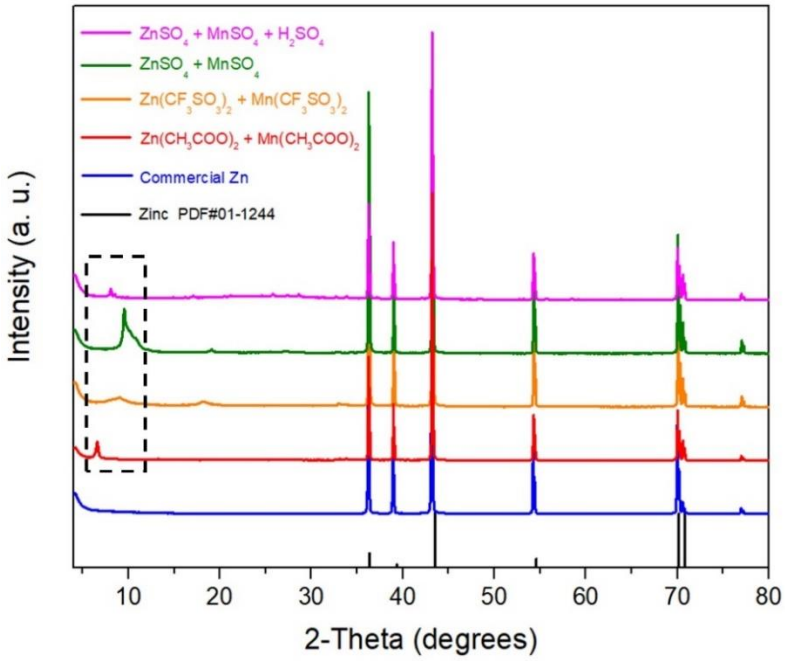

Figure 6.16 XRD patterns of Zn electrodes cycled in different electrolytes. The Zn electrodes were measured after plating/stripping in Zn/Zn symmetrical cells at 1 mA cm^{-2} for 100 h.

Optical images of the cycled Zn and the separators after cycling are displayed in Figure

6.17, where obvious dendrites/pulverization could be found in the sulfate-based electrolytes. To study the compatibility of Zn metal foil with these electrolytes, pieces of Zn foil were immersed in the electrolytes. After soaking for 20 days, the Zn metal in the acetate-based electrolyte still exhibited a smooth surface with a metallic luster, illustrating the excellent stability and compatibility of Zn in this near-neutral solution environment (Figure 6.18). In contrast, the Zn foil immersed in mildly/strongly acidic electrolytes displayed a dim surface and obvious corrosion. Zn corrosion has been shown to lead to an inhomogeneous surface texture and thus accelerates the formation of dendrites.

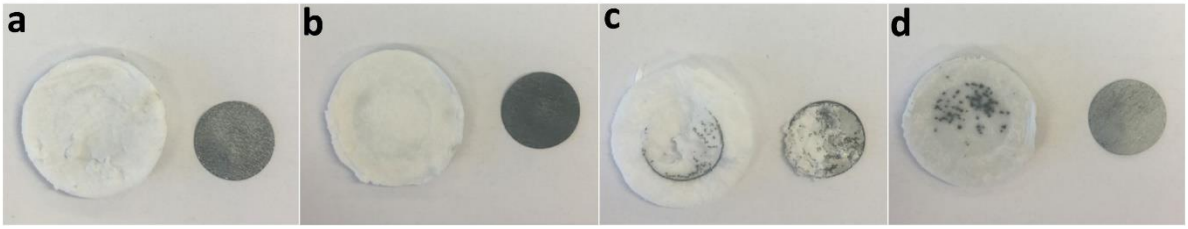

Figure 6.17 Optical images of Zn electrodes and separators after cycling in different electrolytes. (a) The acetate-based electrolyte. (b) The sulfonate-based electrolyte. (c) The sulfate-based electrolyte. (d) The sulfate-based electrolyte with 0.1 M H_2SO_4. The Zn/Zn symmetrical cells were cycled at 1 mA cm^{-2} for 100 h.

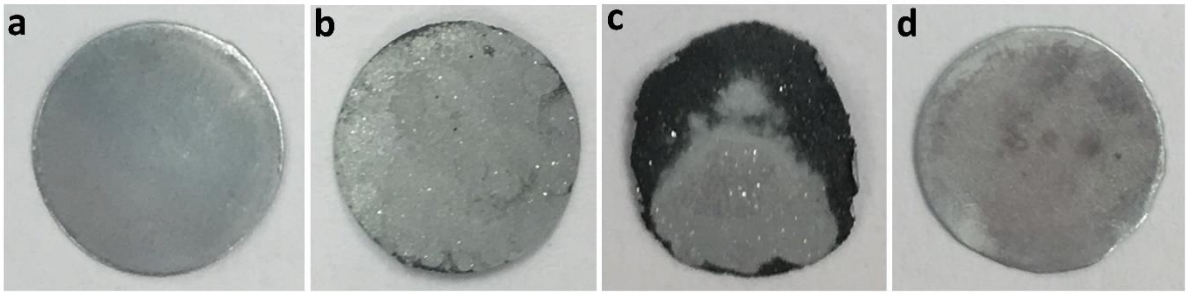

Figure 6.18 Optical images of Zn foil immersed in different electrolytes for 20 days. (a) The acetate-based electrolyte. (b) The sulfate-based electrolyte. (c) The sulfate-based electrolyte with 0.1 M H_2SO_4. (d) The sulfonate-based electrolyte.

In summary, the anode-friendly acetate-based electrolyte ensures a uniform Zn deposition morphology, and outstanding stability and compatibility of the Zn anode, thus enabling a dendrite-free and highly stable Zn anode with high CE. The excellent cycling stability and reversibility of Zn in the acetate-based electrolyte is of great significance for the long-lasting cyclability of Zn/MnO_2 batteries.

6.3.3 Electrochemical Performance of the Zn/MnO_2 Cell

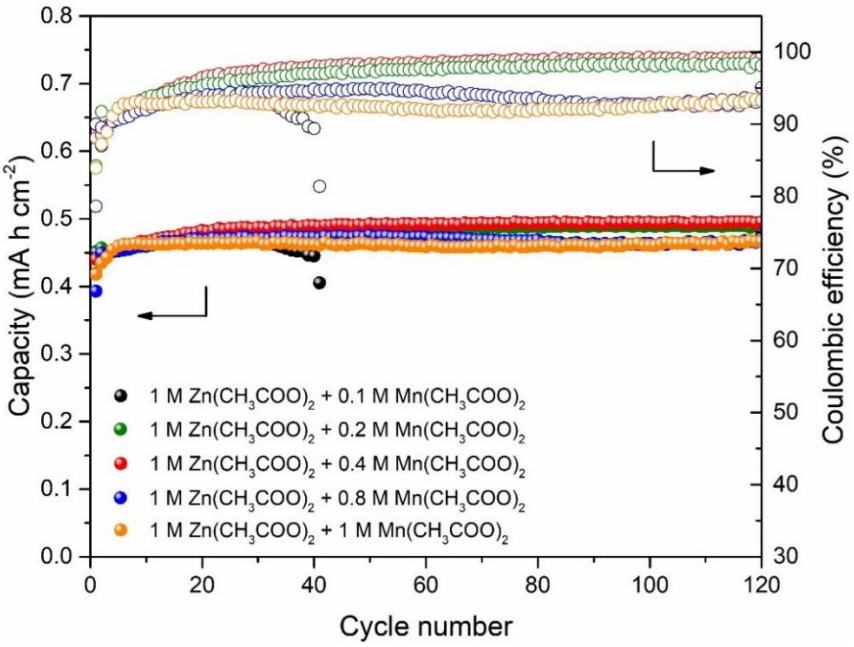

Figure 6.19 Electrochemical performance of the Zn/MnO_2 cell in electrolytes with different concentrations of $Mn(CH_3COO)_2$. All the cells were tested by charging at 1.8 V to 0.5 mA h cm^{-2} and discharging at 5 mA cm^{-2} to 1.0 V.

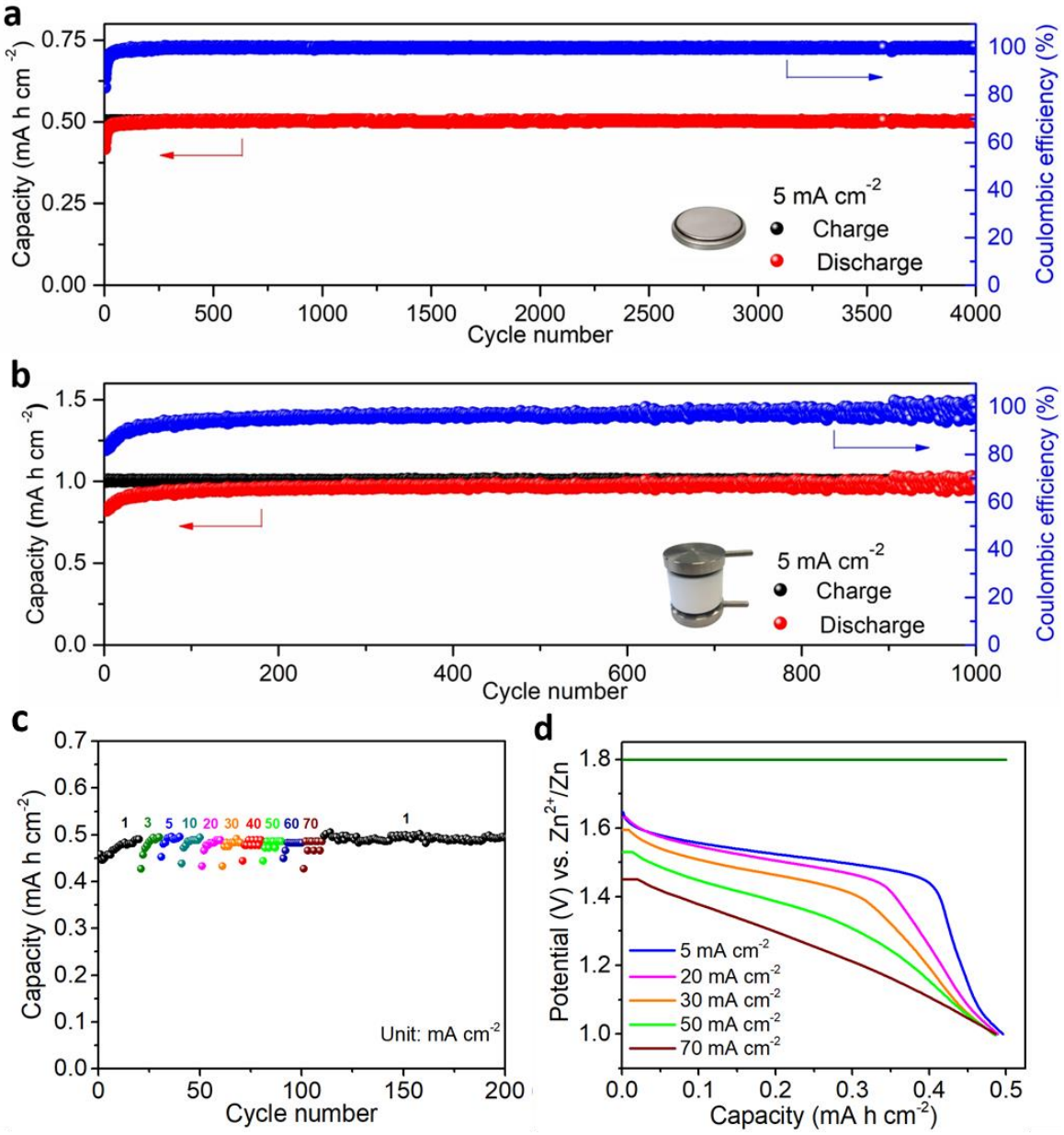

Figure 6.20 Electrochemical performance of the Zn/MnO_2 cell in the acetate-based electrolyte. (a) Long-term cycling performance of the Zn/MnO_2 coin cell at 5 mA cm^{-2} with an areal capacity of 0.5 mA h cm^{-2}. (b) Cycling stability test of the Swagelok-type Zn/MnO_2 cell at 5 mA cm^{-2} with an areal capacity of 1 mA h cm^{-2}. (c and d) Rate capability and charge/discharge curves of the Zn/MnO_2 coin cell with an areal capacity of 0.5 mA h cm^{-2} from 1 mA cm^{-2} to 70 mA cm^{-2}. All the cells were tested by charging at a constant potential (1.8 V) and galvanostatic discharging to 1.0 V.

The salt concentration of manganese acetate in the hybrid electrolyte was fixed at the optimized molarity of 0.4 M, based on the discharge capacity and CE (Figure 6.19). The long-term cycling performance and CE of the Zn/MnO_2 coin cell at 5 mA cm^{-2} are presented in Figure 6.20a. The cell exhibited a stable discharge capacity without noticeable decay for 4000 cycles at a charge capacity of 0.5 mA h cm^{-2}, reaching a high CE of nearly 100%. For comparison with previous reports, the areal specific capacity in Figure 6.20a has been converted to the mass specific capacity. The MnO_2 mass loading on carbon cloth was determined by the weight difference between the bare carbon cloth and that with the MnO_2 deposited after charge (see Experimental Section). The corresponding practical mass specific capacity was 556 mA h g^{-1}. Moreover, to scale up the areal energy storage capacity of the Zn/MnO_2 system, a Swagelok cell was constructed by simply replacing the carbon cloth with high-surface-area carbon felt (thickness of 3.18 mm). As shown in Figure 6.20b, the Swagelok cell delivered a highly reversible discharge capacity of 0.98 mA h cm^{-2} after 1000 cycles at a charge capacity of 1 mA h cm^{-2}. The cell with a higher areal capacity of 2 mA h cm^{-2} also showed a stable cycle life up to 200 cycles (Figure 6.21). The low CE in initial cycles could be attributed to residual MnO_2 cathode on the carbon cloth from the incomplete dissolution process.

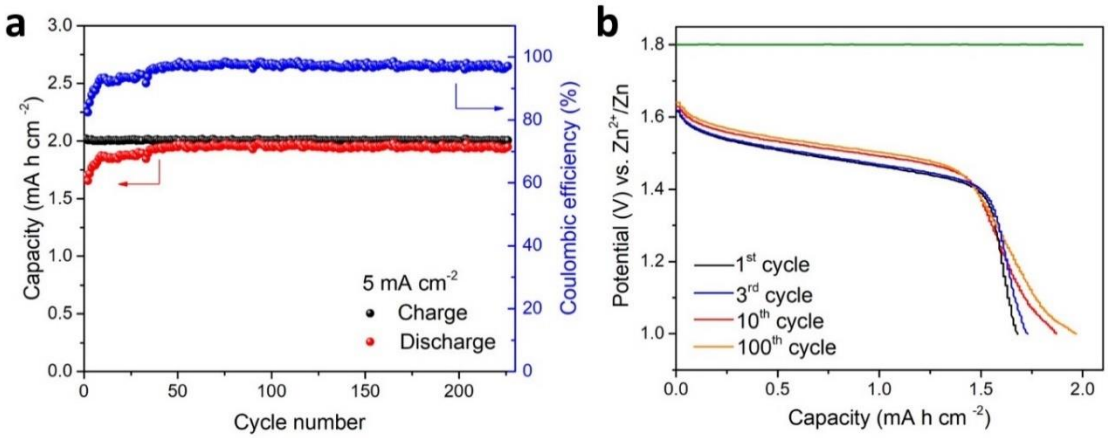

Figure 6.21 (a) Cycling performance of the Zn/MnO_2 cell with an areal capacity of 2 mA h cm^{-2} at 5 mA cm^{-2} and (b) corresponding voltage profiles.

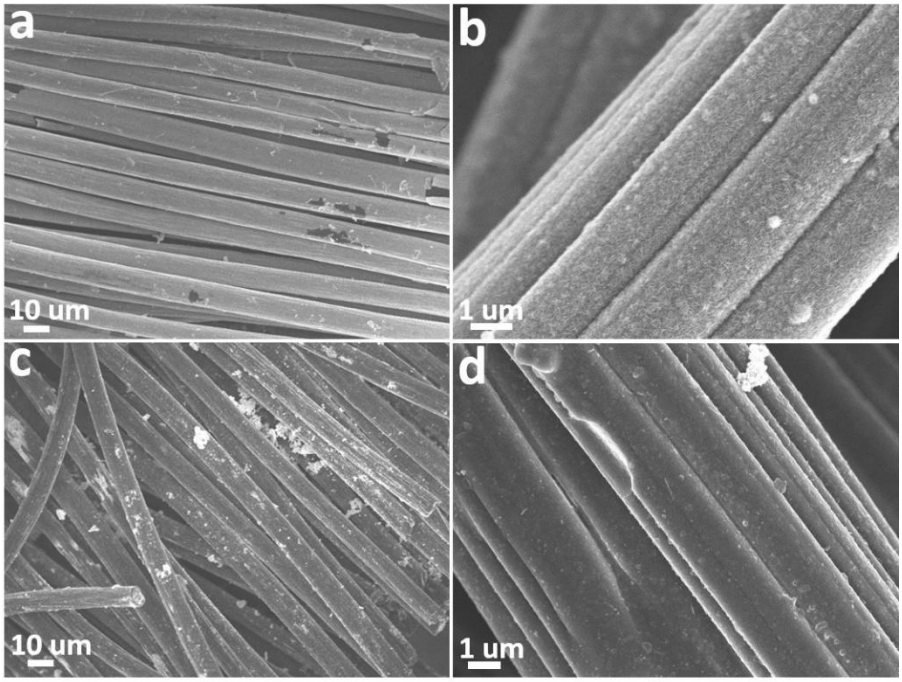

Figure 6.22 SEM images of the cathode after the 1000th cycle in the acetate-based electrolyte. (a, b) after the 1000th charge to 0.5 mA h cm^{-2}, and (c, d) after the 1000th discharge to 1.0 V.

SEM images of the cathode after 1000 cycles are shown in Figure 6.22, which reveal the deposition and dissolution process of MnO_2 on the carbon cloth. The Zn/MnO_2

system also exhibited superior rate performance. When the discharge rate was increased from 1 mA cm^{-2} to 70 mA cm^{-2}, the discharge capacity could still be maintained at almost 0.5 mA h cm^{-2} (Figure 6.20c). The corresponding discharge curves at different current densities in Figure 6.20d demonstrate that nearly 100% of the charge capacity could be preserved, even at the high current density of 70 mA cm^{-2} (discharge in ~25 s). The superior cycling stability and rate capability are attributable to the highly reversible MnO_2/Mn^{2+} deposition/dissolution reaction mechanism induced by the salt anion chemistry, which avoids phase transformation and structural collapse of the active materials during repeated cycles. Furthermore, the highly stable Zn anode in our near-neutral electrolyte environment is also critical for achieving superior electrochemical performance of the Zn/MnO_2 system.

6.4 Conclusion

We have proposed a new type of aqueous battery chemistry induced by electrolyte salts in rechargeable Zn/MnO_2 batteries. Acetate ions in the electrolyte have been shown to modify the surface properties of MnO_2 cathode and reduce the barrier for its dissolution process, through DFT calculations. Owing to the effect of CH_3COO^-, the two-electron Mn^{4+}/Mn^{2+} redox reaction is remarkably inspired, leading to higher capacity compared to the conventional Mn^{4+}/Mn^{3+} redox reaction and superior cycling reversibility. In addition, the near-neutral acetate-based electrolyte ensures outstanding stability and compatibility of the Zn anode, and consequently enables a dendrite-free Zn anode with a high plating/stripping CE. The combination of the two-electron reaction mechanism and the highly stable Zn anode yields high-performance Zn/MnO_2 batteries with high capacity, as well as excellent cyclability and rate capability. This new Zn/MnO_2 battery chemistry via manipulating the salt anions in the electrolyte provides a promising solution for large-scale energy storage applications.

6.5 References

[1] B. Dunn, H. Kamath, J.-M. Tarascon, *Science* **2011**, 334, 928.

[2] H. Kim, J. Hong, K. Y. Park, H. Kim, S. W. Kim, K. Kang, *Chem. Rev.* **2014**, 114, 11788.

[3] Z. Li, J. Zhang, Y. Lu, X. Lou, *Sci. Adv.* **2018**, 4, eaat1687.

[4] Q. Zhang, C. Didier, W. K. Pang, Y. Liu, Z. Wang, S. Li, V. K. Peterson, J. Mao, Z. Guo, *Adv. Energy Mater.* **2019**, 9, 1900568.

[5] L. Suo, O. Borodin, T. Gao, M. Olguin, J. Ho, X. Fan, C. Luo, C. Wang, K. Xu, *Science* **2015**, 350, 938.

[6] Q. Zhao, W. Huang, Z. Luo, L. Liu, Y. Lu, Y. Li, L. Li, J. Hu, H. Ma, J. Chen, *Sci. Adv.* **2018**, 4, eaao1761.

[7] L. Wang, K.-W. Huang, J. Chen, J. Zheng, *Sci. Adv.* **2019**, 5, eaax4279.

[8] J. Hao, J. Long, B. Li, X. Li, S. Zhang, F. Yang, X. Zeng, Z. Yang, W. K. Pang, Z. Guo, *Adv. Funct. Mater.* **2019**, 29, 1903605.

[9] H. Pan, Y. Shao, P. Yan, Y. Cheng, K. S. Han, Z. Nie, C. Wang, J. Yang, X. Li, P. Bhattacharya, K. Mueller, J. Liu, *Nat. Energy* **2016**, 1, 16039.

[10] M. Li, Q. He, Z. Li, Q. Li, Y. Zhang, J. Meng, X. Liu, S. Li, B. Wu, L. Chen, Z. Liu, W. Luo, C. Han, L. Mai, *Adv. Energy Mater.* **2019**, 9, 1901469.

[11] H. Zhang, U. Oteo, X. Judez, G. G. Eshetu, M. Martinez-Ibañez, J. Carrasco, C. Li, M. Armand, *Joule* **2019**, 3, 1689.

[12] G. G. Eshetu, X. Judez, C. Li, M. Martinez-Ibañez, I. Gracia, O. Bondarchuk, J. Carrasco, L. M. Rodriguez-Martinez, H. Zhang, M. Armand, *J. Am. Chem. Soc.* **2018**, 140, 9921.

[13] Y. Jin, L. Zou, L. Liu, M. H. Engelhard, R. L. Patel, Z. Nie, K. S. Han, Y. Shao, C. Wang, J. Zhu, H. Pan, J. Liu, *Adv. Mater.* **2019**, 31, 1900567.

[14] N. Zhang, F. Cheng, Y. Liu, Q. Zhao, K. Lei, C. Chen, X. Liu, J. Chen, *J. Am. Chem. Soc.* **2016**, 138, 12894.

[15] J. Hao, X. Li, X. Song, Z. Guo, *EnergyChem* **2019**, 1, 100004.

[16] D. Chao, W. Zhou, C. Ye, Q. Zhang, Y. Chen, L. Gu, K. Davey, S. Z. Qiao, *Angew. Chem. Int. Ed.* **2019**, 58, 7823.

[17] W. Chen, G. Li, A. Pei, Y. Li, L. Liao, H. Wang, J. Wan, Z. Liang, G. Chen, H. Zhang, J. Wang, Y. Cui, *Nat. Energy* **2018**, 3, 428.

[18] Z. Wang, J. Huang, Z. Guo, X. Dong, Y. Liu, Y. Wang, Y. Xia, *Joule* **2019**, 3, 1289.

[19] A. Naveed, H. Yang, Y. Shao, J. Yang, N. Yanna, J. Liu, S. Shi, L. Zhang, A. Ye, B. He, J. Wang, *Adv. Mater.* **2019**, 31, 1900668.

[20] N. Zhang, F. Cheng, J. Liu, L. Wang, X. Long, X. Liu, F. Li, J. Chen, *Nat. Commun.* **2017**, 8, 405.

[21] W. Sun, F. Wang, S. Hou, C. Yang, X. Fan, Z. Ma, T. Gao, F. Han, R. Hu, M. Zhu, C. Wang, *J. Am. Chem. Soc.* **2017**, 139, 9775.

[22] F. Wang, O. Borodin, T. Gao, X. Fan, W. Sun, F. Han, A. Faraone, J. A. Dura, K. Xu, C. Wang, *Nat. Mater.* **2018**, 17, 543.

[23] Z. Zhao, J. Zhao, Z. Hu, J. Li, J. Li, Y. Zhang, C. Wang, G. Cui, *Energy Environ. Sci.* **2019**, 12, 1938.

[24] X. Zeng, J. Hao, Z. Wang, J. Mao, Z. Guo, *Energy Storage Mater.* **2019**, 20, 410.

[25] X. Ji, *Energy Environ. Sci.* **2019**, 12, 3203.

[26] J. Huang, Z. Wang, M. Hou, X. Dong, Y. Liu, Y. Wang, Y. Xia, *Nat. Commun.* **2018**, 9, 2906.

[27] G. Liang, F. Mo, H. Li, Z. Tang, Z. Liu, D. Wang, Q. Yang, L. Ma, C. Zhi, *Adv. Energy Mater.* **2019**, 9, 1901838.

[28] J. Zhang，Y. Li，L. Wang，C. Zhang，H. He, *Catal. Sci. Technol.* **2015,** 5, 2305.

[29] V. Galakhov, M. Demeter, S. Bartkowski, M. Neumann, N. Ovechkina, E. Kurmaev, N. Lobachevskaya, Y. M. Mukovskii, J. Mitchell, D. Ederer, *Phys. Rev. B* **2002**, 65, 113102.

[30] M. Mautner, *J. Am. Chem. Soc.* **1988**, 110, 3854.

[31] A. R. Gandhe, J. S. Rebello, J. Figueiredo, J. Fernandes, *Appl. Catal. B* **2007**, 72, 129.

[32] K.-T. Lee, J.-F. Lee, N.-L. Wu, *Electrochim. Acta* **2009**, 54, 6148.

[33] A. Naveed, H. Yang, J. Yang, Y. Nuli, J. Wang, *Angew. Chem. Int. Ed.* **2019**, 58, 2760.

[34] S. Zhang, Q. Fan, Y. Liu, S. Xi, X. Liu, Z. Wu, J. Hao, W.K. Pang, T. Zhou, Z. Guo, *Adv. Mater.* **2020**, 2000380.

Chapter 7

Conclusions and Outlook

7.1 Conclusions

Rechargeable aqueous zinc-ion batteries have been revived as complementary to LIBs as a result of the intrinsic safety of aqueous electrolytes and the attractive properties of Zn metal anode, including high theoretical capacity, low redox potential, and abundant resources. Nevertheless, their practical application is largely impeded by the unsatisfactory reversibility and inferior cycling stability of the Zn anode, arising from notorious dendrite formation and side reactions. In this doctoral thesis, Zn anode issues and corresponding improvement strategies in different aqueous Zn-based batteries have been comprehensively summarized. Moreover, to further optimize Zn electrode towards the practical application of AZIBs, this thesis proposes both interfacial engineering and electrolyte salt strategy via deeply understanding Zn surface chemistry.

In the first case, a unique electrolyte design strategy for *in-situ* SEI construction is proposed in aqueous Zn chemistry to address the critical issues for Zn electrodes and promote the development of practical aqueous Zn-ion batteries. A robust and highly Zn^{2+}-conductive hopeite SEI layer is formed *in situ*, by simply introducing $Zn(H_2PO_4)_2$ salt into the aqueous electrolyte and taking advantage of the local pH increase originating from the competitive side reaction of water decomposition. Based on a combination of experimental results and computational analysis, we have demonstrated that the hopeite SEI layer stabilizes the Zn-electrolyte interface through guiding dendrite-free Zn plating/stripping and inhibiting continuous consumption of both Zn and aqueous electrolyte during cycling. Apart from the realization of high Zn reversibility and utilization, the exploitation of the *in-situ* SEI design also enables

significantly enhanced cyclability of Zn/V_2O_5 full cells under practical conditions, including lean electrolyte (9 μL mAh^{-1}), limited Zn excess, and a high-capacity cathode (2.52 mA h cm^{-2}). Thus, the new *in-situ* interfacial design in this work offers a promising strategy towards practical high-performance AZIBs. We believe that this strategy can also be extended to other aqueous battery systems facing the same issues, providing a brand-new route for the development of aqueous rechargeable energy-storage applications.

In the second case, the bio-inspired construction of a PDA SEI layer on Zn anode via an *in-situ* polymerization strategy has been successfully established, by simply introducing dopamine as an electrolyte additive to facilitate a highly stable Zn metal anode. The uniform PDA SEI layer possesses multifunctional features, strong adhesion to the surface of the Zn metal, remarkable hydrophilicity, and high Zn-ion conductivity, due to the abundant functional groups in its molecular chains. Such a robust SEI layer on Zn could alleviate interfacial side reactions via isolating Zn from the electrolyte. The favorable interaction of Zn^{2+} with the polymeric SEI layer was also verified by the combination of experimental characterizations and DFT computations. This SEI layer could promote a homogeneous Zn^{2+} flux at the electrode-electrolyte interface, and hence, effectively guide dendrite-free Zn deposition. Therefore, the Zn electrode in the electrolyte with DA additive exhibited tremendously improved Zn utilization (99.5 %) and stable Zn plating/stripping when cycling at high current densities and high areal capacities up to 30 mA cm^{-2} and 30 mA h cm^{-2}. The as-developed Zn anode further enables Zn/V_2O_5 full cells with high capacity, excellent rate performance, and long-term cycling capability, even with a practically relevant N/P ratio and lean electrolyte. This simple yet effective strategy for *in-situ* construction of a polymeric SEI layer in aqueous chemistry opens up a fresh route towards advanced energy storage systems for

practical applications.

In the third case, a new type of aqueous battery chemistry induced by electrolyte salts in rechargeable Zn/MnO_2 batteries has been proposed. Acetate ions in the electrolyte have been shown to modify the surface properties of MnO_2 cathode and reduce the barrier for its dissolution process, through DFT calculations. Owing to the effect of CH_3COO^-, the two-electron Mn^{4+}/Mn^{2+} redox reaction is remarkably inspired, leading to higher capacity compared to the conventional Mn^{4+}/Mn^{3+} redox reaction and superior cycling reversibility. In addition, the near-neutral acetate-based electrolyte ensures outstanding stability and compatibility of the Zn anode, and consequently enables a dendrite-free Zn anode with a high plating/stripping CE. The combination of the two-electron reaction mechanism and the highly stable Zn anode yields high-performance Zn/MnO_2 batteries with high capacity, as well as excellent cyclability and rate capability. This new Zn/MnO_2 battery chemistry via manipulating the salt anions in the electrolyte provides a promising solution for large-scale energy storage applications.

7.2 Outlooks

Although numerous strategies have also been proposed to enhance the performance of Zn electrode, the state-of-the-art AZIBs are still far from satisfactory and the related study is in its infancy. To pursue the goal of industrial application of AZIBs, the following aspects should be further considered.

Deep fundamental studies on Zn corrosion: In the alkaline systems, a ZnO by-product layer is generated on Zn electrode surface due to the electrode corrosion during battery rest. As the corrosion reaction goes on, the ZnO layer tends to be even and dense, which is likely to terminate the corrosion by blocking the electrolyte from reaching the Zn electrode. In addition, some electrode additives (such as Hg) have been used in

commercial alkaline Zn–based batteries to suppress the Zn electrode corrosion. No dense by-product layer is generated on the Zn electrode surface in mild electrolyte, however, indicating that the Zn corrosion cannot be stopped by itself. To date, no electrode additive has been proposed to alleviate Zn electrode corrosion in ZIBs, as Zn foil is the most commonly used electrode form. Overall, compared to the alkaline system, the effects of Zn electrode corrosion in mild systems are more serious, since it continually consumes electrolyte and active material and even damages the battery during the shelf time and transportation. Furthermore, it also increases the battery internal pressure by producing gas evolution, gravely affecting the battery performance. Thus, restraining the Zn electrode corrosion is the first step to achieving the actual application of ZIBs on a large scale. Fewer efforts in proportion to the problem have been spent, however, on studying the Zn corrosion behaviour and its by-products. Hence, more fundamental research should be conducted to deeply understand Zn corrosion in mild electrolyte, as well as the factors that affect it, such as the pH value of the electrolyte, the electrolyte salt types, the purity of the Zn electrode, Zn electrode forms, and the O_2 content in the electrolyte.

Depth of discharge (DOD) and CE measurements: The DOD of Zn electrode indicates the percentage of the Zn electrode that has been involved in the electrode reactions relative to the overall capacity of the electrode. Hence, the DOD can be regarded as a measure of the utilization of the Zn electrode. The Zn electrode's DOD is correlated with the capacity fade and energy density of the actual battery. Thus, it is an extremely important parameter for the battery and needs to be studied. Moreover, the CE is a critical indicator to evaluate the viability of Zn electrode in practical application. One has to keep in mind that the testing protocols can significantly impact on the results of CE measurements. High current densities are likely to produce the high CEs in Zn–Cu

or Zn–Ti cells, although testing under the high current density may make the CE results misleading. Some reports claimed very high CEs of Zn stripping and plating at a high current density. Unfortunately, the values of these CEs may be unreliable. This is because the fast testing would mask the issues induced by the side reactions occurring at low rates, such as the H_2 evolution. Apart from the current density, the testing time also affects the CEs of Zn electrode. Even under the same current density, the CE values are also different with different testing times. For example, even under the same current density of 1 mA cm^{-2}, the CEs with a testing time of 0.5 h are different from those with the testing time of 1 h. Therefore, there is no comparability between the CEs with different testing times, even under the same capacity. For instance, the CEs obtained at 1 mA cm^{-2} for 5 h are not comparable with these tested at 5 mA cm^{-2} for 1 h. Thus, choosing a suitable and reasonable testing protocol to evaluate the CE of a Zn electrode is of great importance. Overall, the CEs and DODs are of great importance for evaluating the performance of the Zn electrode. Currently, the CEs in most reports still were measured with low DODs, although the DOD effects have been neglected. What about CEs under a high DOD? What if CEs are measured under a high DOD but at different current densities? These problems should be understood before designing an actual Zn full cell with high energy density.

Study of the capacity ratio of the anode and cathode (N:P): For practical operation, the optimal capacity ratio of Zn anode to the cathode should be explored. Ideally, the N:P ratio in the battery should be 1 : 1. In practice, this condition cannot be achieved, especially for the metal-based batteries. We note that the current ZIBs reported in the majority of papers have a capacity ratio higher than 15 : 1, since the commercial Zn foil is very thick (≥ 10 μm). This indicates that most of Zn metal anode was not involved in the battery reaction, leading to a low DOD for the Zn electrode, which seriously reduces

the energy density of the battery and overestimates the electrochemical performance. Exploring the N:P ratio is of vital importance for developing industrial Zn-based batteries. In current ZIBs, the commercial Zn foil is the most commonly used Zn electrode form, and its thickness is usually greater than 10 μm. Therefore, developing a special battery assembly technique to fully use the Zn foil is highly desirable. In addition to the technique of using both sides of the Zn foil, other forms of Zn metal electrode may be developed.

Lean electrolyte study: A lean electrolyte design can be achieved by adding the minimum amount of electrolyte that makes the battery work normally to pursue high energy density. Adding the lean electrolyte is a critical step for the battery to achieve the goal of industrial application, which has not been achieved yet in Zn based batteries such as rechargeable alkaline Zn-air batteries and mild ZIBs. Currently, most of the rechargeable alkaline Zn-air batteries in past reports were tested in a beaker cell or other specially designed cells, in which an excessive amount of electrolyte was added to pursue the long cycle life. Although most of the ZIBs were assembled in small coin cells, the amount of added electrolyte (usually ≥ 100 μg) was still several times greater than for lean electrolyte. The excess electrolyte (> 150 mg Ah^{-1}) not only seriously reduces the energy density of the battery, but also masks the problem of electrolyte-induced side reactions that constantly consume the electrolyte. Thus, the lean electrolyte design in the aqueous Zn–based battery is significantly important to reveal if there are more battery issues before their large-scale application.

New separator exploration: Separators used in mild ZIBs are always composed of thick glass fibres (0.2-1.0 mm), which consumes more electrolyte and reduce the volumetric and gravimetric energy density of the battery. Exploring ultrathin hydrophilic

films/separators with enough mechanical strength to suppress Zn dendritic penetration would be a potential strategy for the practical application of mild ZIBs.

Configuration: A majority of studies on AZIBs were conducted on coin cells (2023 type), in which the size and mass of the cathode are limited (0.5-1.7 cm^2, and 0.5-2 mg for the cathode). In this case, it is imprecise to evaluate the energy density of the battery only based on the active materials. For practical application, the electrode materials need to be demonstrated on a large scale. Therefore, to meet the demands of the future energy market, different commercially available battery types, such as pouch cells, prismatic cells, and cylindrical cells (18650) should be assembled to evaluate the battery performance, including their reversible capacity, CE, cycling life, and energy density. On the other hand, developing flexible devices with gel electrolytes is also promising for the industrial application of aqueous Zn-based batteries. This is because the gel electrolyte has been claimed to inhibit the Zn dendrite growth and the water-induced side reactions, which contributes to enhancing the battery performance. Moreover, flexible aqueous Zn-based devices are a good choice for practical wearable applications, providing more options for the actual applications of aqueous Zn-based batteries. Nevertheless, to the best of our knowledge, the relevant data about the thickness and weight of gel electrolyte used in the flexible Zn-based batteries were not provided in past reports, However, the thickness and weight seriously affect the volumetric and gravimetric energy density of a battery, which should be considered in future flexible battery design.

Appendix A: Publications & Patent

Publications

1. **Xiaohui Zeng**, Kaixuan Xie, Sailin Liu, Shilin Zhang, Junnan Hao, Jiatu Liu, Wei Kong Pang, Pinhua Rao, Qinghong Wang, Jianfeng Mao, Zaiping Guo. Bioinspired Design of an In-Situ Multifunctional Polymeric Solid-Electrolyte Interphase for Zn Metal Anode Cycling at 30 mA cm^{-2} and 30 mA h cm^{-2}. ***Energy Environ. Sci.***, 2021, 14, 5947-5957.

2. **Xiaohui Zeng**, Jianfeng Mao, Junnan Hao, Jiatu Liu, Sailin Liu, Zhijie Wang, Yanyan Wang, Shilin Zhang, Tian Zheng, Jianwen Liu, Pinhua Rao, Zaiping Guo. Electrolyte Design for In Situ Construction of Highly Zn^{2+}-Conductive Solid Electrolyte Interphase to Enable High-Performance Aqueous Zn-Ion Batteries under Practical Conditions. ***Adv. Mater.***, 2021, 2007416.

3. **Xiaohui Zeng**, Jiatu Liu, Jianfeng Mao, Junnan Hao, Zhijie Wang, Si Zhou, Chris D. Ling, Zaiping Guo. Towards a Reversible Mn^{4+}/Mn^{2+} Redox Reaction and Dendrite-Free Zn Anode in Near-Neutral Aqueous Zn/MnO_2 Batteries via Salt Anion Chemistry. ***Adv. Energy Mater.***, 2020, 1904163.

4. Junnan Hao[#], Xiaolong Li[#], **Xiaohui Zeng[#]**, Dan Li, Jianfeng Mao, Zaiping Guo. Deeply Understanding the Zn Anode Behaviour and Corresponding Improvement Strategies in Different Aqueous Zn-Based Batteries." ***Energy Environ. Sci.***, 2020, 13, 3917-3949.

5. **Xiaohui Zeng[#]**, Junnan Hao[#], Zhijie Wang, Jianfeng Mao, Zaiping Guo. Recent Progress and Perspectives on Aqueous Zn-Based Rechargeable Batteries with Mild Aqueous Electrolytes. ***Energy Storage Mater.***, 2019, 20, 410-437.

6. Chen Wu[#], **Xiaohui Zeng[#]**, Pingge He, Libao Chen, Weifeng Wei. Flexible

WS_2@CNFs Membrane Electrode with Outstanding Lithium Storage Performance Derived from Capacitive Behavior. ***Adv. Mater. Interfaces***, 2018, 5, 1701080.

7. Yanyan Wang, Zhijie Wang, Liang Zhao, Qining Fan, **Xiaohui Zeng**, Sailin Liu, Wei Kong Pang, Yan-Bing He, Zaiping Guo. Lithium Metal Electrode with Increased Air Stability and Robust Solid Electrolyte Interphase Realized by Silane Coupling Agent Modification. ***Adv. Mater.***, 2021, 2008133.
8. Junnan Hao, Bo Li, Xiaolong Li, **Xiaohui Zeng**, Shilin Zhang, Fuhua Yang, Sailin Liu, Dan Li, Chao Wu, Zaiping Guo. An In-Depth Study of Zn Metal Surface Chemistry for Advanced Aqueous Zn-Ion Batteries. ***Adv. Mater.***, 2020, 32, 2003021.
9. Junnan Hao, Xiaolong Li, Shilin Zhang, Fuhua Yang, **Xiaohui Zeng**, Shuai Zhang, Guyue Bo, Chunsheng Wang, Zaiping Guo. Designing Dendrite-Free Zinc Anodes for Advanced Aqueous Zinc Batteries. ***Adv. Funct. Mater.***, 2020, 30, 2001263.
10. Junnan Hao, Jun Long, Bo Li, Xiaolong Li, Shilin Zhang, Fuhua Yang, **Xiaohui Zeng**, Zhanhong Yang, Wei Kong Pang, Zaiping Guo. Toward High-Performance Hybrid Zn-Based Batteries via Deeply Understanding Their Mechanism and Using Electrolyte Additive. ***Adv. Funct. Mater.***, 2019, 29, 1903605.

Patent

1. Zaiping Guo, Jianfeng Mao, **Xiaohui Zeng**; Electrochemical cell and manufacturing method, Application number: 2019904131

Appendix B: Conferences & Activities

1. The 2019 International Symposium on Future Materials, North Wollongong, Australia, Jan. 30th -Feb. 1st, 2019
2. 2019 UOW-USTC Joint Research Workshop, North Wollongong, Australia, Aug. 19th – 21st, 2019

Appendix C: Awards

1. 2020 ISEM Postgraduate Student Excellence Award

2. 2018 International Postgraduate Tuition Award (IPTA), University of Wollongong.